2018

LAMINAR AND TURBULENT STUDY OF COMBUSTION IN STRATIFIED ENVIRONMENTS USING LASER BASED MEASUREMENTS

Stephen William Grib
University of Kentucky, sgrib38@gmail.com
Digital Object Identifier: https://doi.org/10.13023/etd.2018.269

STUDENT AGREEMENT:

I represent that my thesis or dissertation and abstract are my original work. Proper attribution has been given to all outside sources. I understand that I am solely responsible for obtaining any needed copyright permissions. I have obtained needed written permission statement(s) from the owner(s) of each third-party copyrighted matter to be included in my work, allowing electronic distribution (if such use is not permitted by the fair use doctrine) which will be submitted to UKnowledge as Additional File.

I hereby grant to The University of Kentucky and its agents the irrevocable, non-exclusive, and royalty-free license to archive and make accessible my work in whole or in part in all forms of media, now or hereafter known. I agree that the document mentioned above may be made available immediately for worldwide access unless an embargo applies.

I retain all other ownership rights to the copyright of my work. I also retain the right to use in future works (such as articles or books) all or part of my work. I understand that I am free to register the copyright to my work.

REVIEW, APPROVAL AND ACCEPTANCE

The document mentioned above has been reviewed and accepted by the student's advisor, on behalf of the advisory committee, and by the Director of Graduate Studies (DGS), on behalf of the program; we verify that this is the final, approved version of the student's thesis including all changes required by the advisory committee. The undersigned agree to abide by the statements above.

Stephen William Grib, Student

Dr. Michael Renfro, Major Professor

Dr. Alexandre Martin, Director of Graduate Studies

LAMINAR AND TURBULENT STUDY OF COMBUSTION IN STRATIFIED ENVIRONMENTS USING LASER BASED MEASUREMENTS

DISSERTATION

A dissertation submitted in partial fulfillment of the requirements for the degree of Doctor of Philosophy in the College of Engineering at the University of Kentucky

By
Stephen William Grib

Lexington, Kentucky

Director: Dr. Michael Renfro, Professor and Chair of Mechanical Engineering

Lexington, Kentucky

2018

ABSTRACT OF DISSERTATION

LAMINAR AND TURBULENT STUDY OF COMBUSTION IN STRATIFIED ENVIRONMENTS USING LASER BASED MEASUREMENTS

Practical gas turbine engine combustors create extremely non-uniform flowfields, which are highly stratified making it imperative that similar environments are well understood. Laser diagnostics were utilized in a variety of stratified environments, which led to temperature or chemical composition gradients, to better understand autoignition, extinction, and flame stability behavior. This work ranged from laminar and steady flames to turbulent flame studies in which time resolved measurements were used.

Edge flames, formed in the presence of species stratification, were studied by first developing a simple measurement technique which is capable of estimating an important quantity for edge flames, the advective heat flux, using only velocity measurements. Both hydroxyl planar laser induced fluorescence (OH PLIF) and particle image velocimetry (PIV) were used along with numerical simulations in the development of this technique. Interacting triple flames were also created in a laboratory scale burner producing a laminar and steady flowfield with symmetric equivalence ratio gradients. Studies were conducted in order to characterize and model the propagation speed as a function of the flame base curvature and separation distance between the neighboring flames. OH PLIF, PIV and Rayleigh scattering measurements were used in order to characterize the propagation speed. A model was developed which is capable of accurately representing the propagation speed for three different fuels. Negative edge flames were first studied by developing a one-dimensional model capable of reproducing the energy equation along the stoichiometric line, which was dependent on different boundary conditions. Unsteady and laminar negative edge flames were also simulated with periodic boundary conditions in order to assess the difference between the steady and unsteady cases. The diffusive heat loss was unbalanced with the chemical heat release and advective heat flux energy gain terms which led to the flame proceeding and receding. The temporal derivative balanced the energy equation, but also aided in the understanding of negative edge flame speeds. Turbulent negative edge flame velocities were measured for extinguishing flames in a separate experiment as a function of the bulk advective heat flux through the edge and turbulence level. A burner was designed

and built for this study which created statistically stationary negative edge flames. The edge velocity was dependent on both the bulk advective heat flux and turbulence levels. The negative edge flame velocities were obtained with high speed stereo-view chemiluminescence and two dimensional PIV measurements.

Autoignition stabilization was studied in the presence of both temperature and species stratification, using a simple laminar flowfield. OH and CH_2O PLIF measurements showed autoignition characteristics ahead of the flame base. Numerical chemical and flow simulations also revealed lower temperature chemistry characteristics ahead of the flame base leading to the conclusion of lower temperature chemistry dominating the stabilization behavior. An energy budget analysis was conducted which described the stabilization behavior.

KEYWORDS: Laser Diagnostics, Edge Flames, Autoignition, Flame Stabilization, Extinction

Stephen Grib

7/13/18

Date

LAMINAR AND TURBULENT STUDY OF COMBUSTION IN STRATIFIED ENVIRONMENTS USING LASER BASED MEASUREMENTS

By

Stephen William Grib

Dr. Michael Renfro

Director of Dissertation

Dr. Alexandre Martin

Director of Graduate Studies

7/13/18

Date

Acknowledgements

This dissertation would not be possible without the help of many people. First and foremost I want to thank my parents; without your support on this (long) journey I would not have been able to get through this. I hope I've made you proud. I also want to thank my loving fiancée for taking this journey with me. The weekend trips to and from Philly and Storrs and even longer move to Kentucky were certainly not easy, but hey we made it! I cannot thank you enough for being okay with the long nights, early mornings, and constant research thoughts I've put in our lives. Without your support, this thesis certainly would not be possible.

A special thanks goes out to my advisor, mentor, and friend Mike Renfro. Thank you for guiding me to be a better researcher and person. Most importantly, thank you for getting me into beer and golf! To my co-advisor at UConn, Prof. Baki Cetegen, thank you for helping me at the early stages of my research career and always being available to help. To my committee members; Profs. Saito, McDonough, and Yang, thank you all for asking the tough questions and broadening my thought process to think outside the box. I also want to thank Prof. Grana-Otero for his insight and combustion help and Dr. Ahmad Salaimeh for broadening my research experience.

I also want to thank my lab-mates (both UK and UConn) for providing laughs, assistance, and friendship. Starting with the "old" Renfro lab; Marc, Kathryn, James, and Martin I thoroughly enjoyed working with you. To the Cetegen crew, Jason, Bikram, and George: I cannot thank you enough for putting up with me while I was beginning to grasp what we were doing. I certainly made the most leaps and bounds as a researcher while working you guys. To the "new" Renfro lab, Jake and Tyler, thank you for being great coworkers and embracing the frequent lab events (ah, the barrel room, I will miss you).

Table of Contents

List of Figures

1 Introduction

Combustion technology is used in a variety of applications due to high energy density of most fuels. Some typical combustion applications are electric energy production and aerospace propulsion which use gas turbine engines. Figure 1.1 [1] shows that approximately two-thirds of the electricity production in the United States is generated through coal and natural gas. Of the natural gas consumption, it is expected that there will be a 1% annual increase, leading to 34 trillion cubic feet being consumed in the United States alone by 2040, shown in Figure 1.2 [2]. Harmful pollutants, such as NO_x, can be produced in the burning process which can significantly affect the atmosphere by creating smog and acid rain [3]. Therefore, cleaner combustion is needed to reduce such emissions.

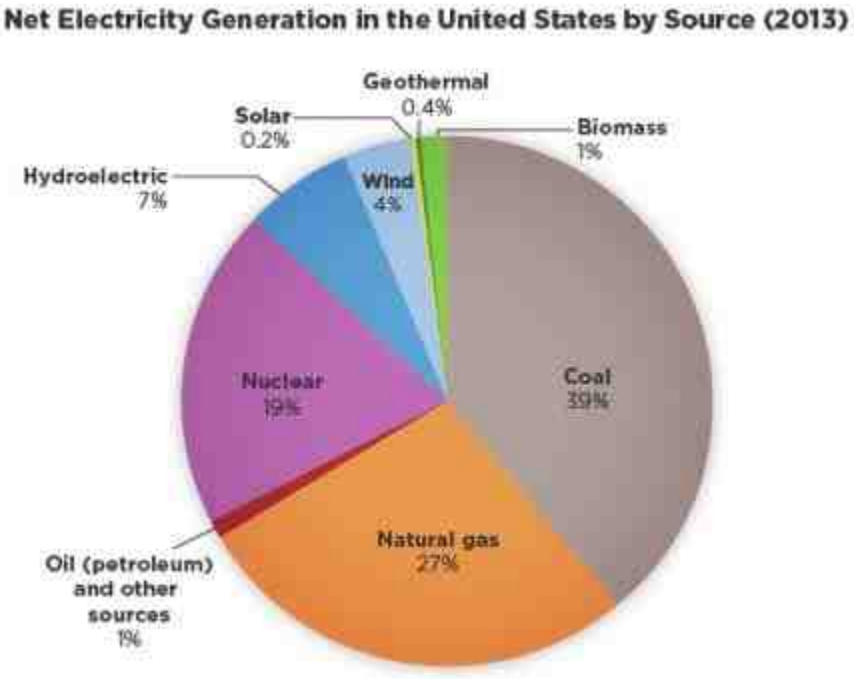

Figure 1.1: United States electric generation breakdown by type of production [1].

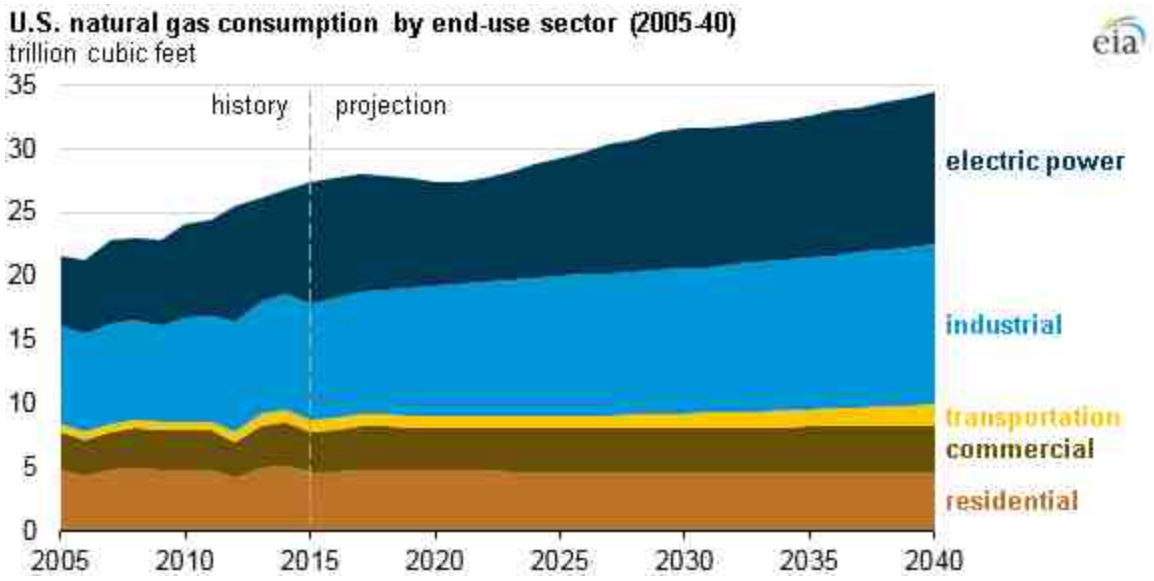

Figure 1.2: Historical and projection of natural gas consumption broken down by sector [2].

Combustor technology relies on a stable flame to prevent engine failure. Thus, most combustors historically utilized non-premixed combustion modes, where fuel and oxidizer are not mixture prior to reacting. However, non-premixed combustion leads to high peak flame temperatures which reside at stoichiometric conditions and therefore produce more pollutants [4]. Premixed combustion, where fuel and oxidizer are mixed prior to reacting, allows the peak flame temperature to be varied by changing the fuel-to-air ratio which can greatly decrease pollutant production [5]. Fully premixed combustion systems are rarely used in combustors because of the inherent stability issues, such as instabilities associated with pressure oscillations [6] and flashback which can create safety concerns since hardware can be damaged and ultimately the engine could fail. Partially-premixed combustion has emerged in application and is often accomplished by injecting fuel and oxidizer separately but stabilizing a flame at a location downstream of the injector nozzles which allows the fuel and oxidizer to slightly mix before burning, creating a fuel-

air gradient ahead of the flame base. This burning mode has better stability behavior and also has characteristics of both premixed and non-premixed combustion.

The burning modes in combustors also changes how flames are stabilized. For instance, premixed flames are stabilized by how quickly the reactants can be heated and react given a homogenous mixture, which is highly dependent on the fuel to air ratio. Partially-premixed combustion is stabilized by similar premixed flame behavior, however, the mixing layer ahead of the flame has a fuel-air ratio gradient ahead of the flame base which significantly changes the behavior of the flame. Design changes can also be implemented which change how flames are stabilized as well. Higher pressure ratios increases the cycle efficiency, so future combustors may inject premixed fuel and air mixtures into sufficiently hot environments such that the mixture may spontaneously ignite prior to the premixed flame base. Other designs such as the one used in the current TALON X [7] combustor injects air into a fuel rich mixture which quickly crosses stoichiometric conditions to avoid high temperature burning via extinction. This dissertation has many studies to emulate these conditions which ranges from fully non-premixed studies, focused on extinction fronts, to fully premixed systems where autoignition may be a dominant stabilization mechanism. These studies have direct implications into gas turbine engine applications and further our understanding of how flames ignite, stabilize, and extinguish in well-defined experiments.

This dissertation studies a variety of burning modes which are either presently used, or may be used, in combustors. The common theme between the studies is that the flow is stratified by either species, temperature, or both. Many fundamental combustion studies have conducted homogenous flow studies, as opposed to those with gradients, for

simplicity to understand the physical phenomena. However, flows with gradients need to be better understood to create more efficient and safer combustor technology.

The focus of this dissertation is to understand how these gradients impact each respective study. Chapter 2 will provide a literature review of relevant studies. Chapters 3 and 4 will give technical details regarding the burners and laser diagnostics used throughout this dissertation. The four main sections of this dissertation are as follows which will subsequently be explained in slightly more detail:

1. Novel diagnostic development to estimate the advective heat flux (Chapter 5)
2. Propagation speeds of interacting triple flames (Chapter 6)
3. Negative edge flames (Chapter 7)
4. Stabilization of a premixed jet injection into a hot coflow (Chapter 8)

1.1 Advective Heat Flux Estimation

Flame hole dynamics are important in gas turbine engine combustors because flame holes can lead to inefficiencies and increased pollutant production. Local extinction in flame sheets can create unwanted flame holes that can grow or heal depending on local flow conditions. Edge flames reside at the boundaries of flame holes, shown in Figure 1.3, which can be classified into two main categories. Negative edge flames are extinction fronts which are typically formed at the beginning stages of flame hole development which work to increase the flame hole area. Conversely, positive edge flames are propagating edge flames which attempt to close the flame hole and heal the flame back to a two-dimensional flame sheet.

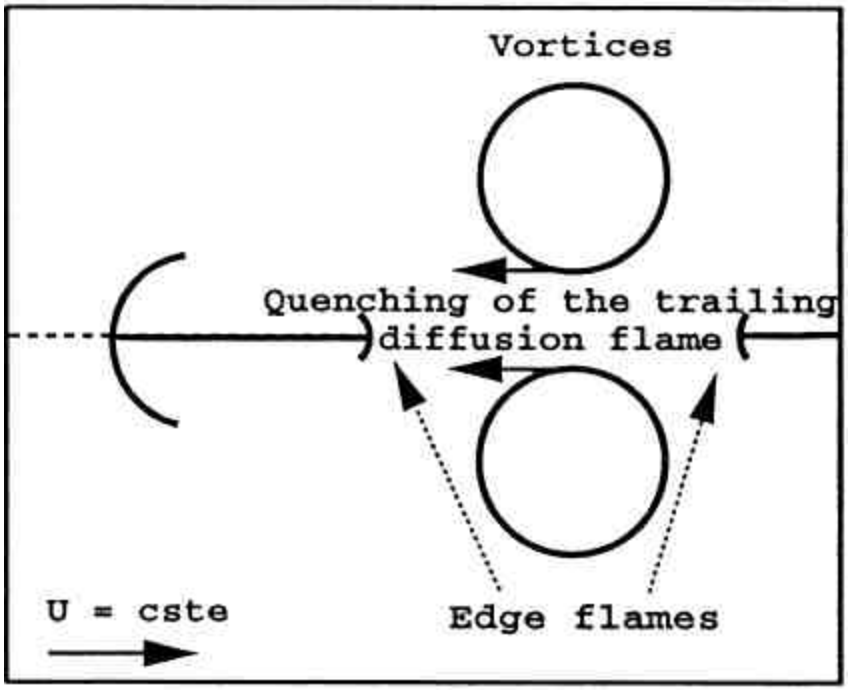

Figure 1.3: Diffusion flame undergoing local extinction which creates edge flames [8].

The advective heat flux, $\rho c_p v \cdot \nabla T$, is an important quantity in edge flames because the sign of $v \cdot \nabla T$ characterizes relative propagation direction of the edge flame, and its magnitude gives information regarding strength of the resulting propagation or extinction front. Modern laser techniques can measure the velocity and temperature fields simultaneously within a flame, but accurate measurements of temperature simultaneous with velocity outside the high temperature region of the flame are more difficult and time-resolved measurements of velocity and temperature simultaneously for unsteady flows require complex measurement systems. In this work, the theoretical framework to show that the flow dilatation can be used to directly estimate a scaled advective heat flux is presented. Numerical simulations of both a positive (propagating) and negative (extinguishing) edge flame were studied to assess the relationship between dilatation and advective heat flux. Experimental measurements of the two-dimensional component of dilatation in positive and negative edge flames were also made and compared to the

simulations. The full advective heat flux was well represented by the dilatation in the simulations, and the experimental data demonstrates that the measured dilatation is useful for estimating advective heat flux. Flames with varying positive and negative flame speeds are examined with the technique.

1.2 Propagation Speed of Interacting Triple Flames

Partially premixed combustion creates environments with fuel gradients ahead of the flame base. In relatively low gradients, triple (or tribrachial) flames can be produced. Triple flames propagate through mixtures faster than the premixed laminar flame speed due to streamline divergence ahead of the flame base that decelerates the flow into the leading edge of the flame. When multiple triple flames are in close proximity, the bulk propagation speed of the structure can be even faster due to additional streamline divergence. Turbulent flames in partially-premixed conditions can encounter these situations, where multiple stoichiometric crossing are in close proximity, leading to multiple interacting triple flames being formed. Propagation speeds of the flame structure with respect the bulk flow for individual triple flames have been well characterized in previous studies, and the local flame speed of interacting triple flames have been reported; however, characterization of the propagation speed for the overall flame structure of interacting triple flame speeds has not been reported. The present work utilizes a laminar five slot burner, which allows both the concentration gradients and stoichiometric separation distance of two interacting triple flames to be varied. The bulk propagation speed of the multiple edge flames has been characterized as a function of the distance between the flame bases (or stoichiometric locations) and the local flame curvatures in order to better understand the conditions which lead to larger streamline divergence and

faster propagation speeds. Interaction between multiple edge flames has been found to play an essential role in this propagation speed. Interacting edge flame speeds were modeled by modifying the relationship for single triple flame propagation speed with an added term for the interaction between the two flames to account for the increased effective divergence.

A second set of experiments were conducted to determine how different fuels effect the propagation speeds. Previous work with partially-premixed ethylene from the first study showed that multiple triple flames can interact resulting in even larger propagation speeds. In this work, propagation velocities for interacting triple flames of partially-premixed methane and propane were measured with different levels of triple flame interaction. For both fuels, the interacting triple flames propagate faster than a single triple flame with similar equivalence ratio gradients. The interacting triple flames can be described with an effective curvature, allowing the linear relationship between propagation speed and curvature from single triple flames to be used to describe the interacting flame speed. The aerodynamic effects of the interaction maximize the propagation speed and achieve the theoretical maximum velocity for single triple flames. For all fuels studied, the interacting flames reach this asymptotic limiting propagation speed. The observations and model developed for different fuels were consistent and it was concluded that interacting triple flames are dominated by aerodynamic effects.

1.3 Negative Edge Flames

Negative edge flames, representing a propagating extinction front, are typically found in the early stages of flame hole development and aid in expanding the flame hole. In practical combustors, extinction events create regions of unburnt fuel and air mixtures.

These unburnt mixtures can potentially leave the combustor section which leads to the system being less efficient. Negative edge flames need to be better understood in order to prevent flame holes from growing to undesirable sizes. Three studies were performed in this section related to negative edge flames.

Previous studies related to steady negative edge flames characterized the energy budget through a negative edge flame. Typical counterflow diffusion flames along the centerline are a simple balance of chemical heat release and diffusive heat loss. Negative edge flames, however, have flow through the edge with decreasing temperatures. Therefore, there is an additional advective heat flux energy gain term which becomes important and allows negative edge flames to stabilize at higher scalar dissipation rates than the typical one-dimensional counterflow extinction scalar dissipation rate. Previous work relied on using two-dimensional flow simulations to calculate negative edge flames. However, the simple geometry and the fact that only three energy terms control the behavior along the stoichiometric line leads to the potential for a one-dimensional model which can predict negative edge flame behavior. Initial work used two-dimensional simulations to develop a model for each term in the energy equation which was used to calculate one-dimensional simulations of negative edge flames along the stoichiometric line. Further work utilized one-dimensional centerline counterflow simulations to similarly calculate the negative edge flame along the stoichiometric line without the need to run two-dimensional flow simulations. This work allows simple one-dimensional calculations to be performed which fully characterizes negative edge flames along the stoichiometric line.

Most relevant studies related to negative edge flames have been limited to steady conditions. Although there have been many observations of unsteady negative edge flame behavior, there has not been an extensive study of unsteady negative edge flames. This work attempts to bridge the gap between steady negative edge flame understanding and unsteady, and even turbulent, observations of negative edge flames. Negative edge flames were simulated with similar conditions to previous steady negative edge flame work. However, the simulations imposed periodic boundary conditions which oscillated the negative edge extinction point. The edge oscillation was tracked in time and the energy balance found similar findings from previous studies, however, the unsteady term in the energy equation had a significant influence at the edge. This study examined the effect of different boundary condition frequencies which characterized the response time of the negative edge. The negative edge flame speed was also characterized with different frequencies. A new physical interpretation of the negative edge flame speed was determined which changes our understanding of the negative edge flame speed.

Because of their transient nature and short time scales, negative edge flames have not been studied extensively in turbulent flows. This section presents an experimental study of statistically stationary negative edge flames in a turbulent flow. High speed diagnostics were performed in order to extract flame velocities with respect to the flow and develop an understanding of how negative edge flame respond to turbulent fluctuations. Results show that bulk advective heat flux plays a crucial role in the magnitude of the negative edge flame speeds. Turbulence also modifies the negative edge flame speed, with increased turbulence levels leading to decreased edge speeds. This effect is proposed to be a result of time history effects on the flame, through local fluctuation in the scalar

dissipation rate leading to flame weakening prior to the flame edge, or a result of altered scalar dissipation rate fields.

1.4 Flame Stabilization of a Premixed Jet in Vitiated Coflow

Next generation combustor technology for gas turbine engines may include lean premixed mixtures injected into high temperature vitiated products such that autoignition can become a potential stabilization mechanism. Fundamental understanding of when autoignition occurs in these complex flowfields is crucial to model future combustors. A simplified flowfield of a premixed jet in vitiated coflow was used in this work to understand how mixing between the two flows can stabilize a steady, laminar autoignition stabilized flame. Both an experimental and numerical study was performed in this section to help determine the stability behavior in this geometry.

Formaldehyde and hydroxyl planar laser induced florescence measurements were performed for experimental observations. The flow time to reach the peak levels of hydroxyl was inconsistent with the chemical simulation time scales. Numerical flow simulations with detailed chemistry were conducted to better understand the stability behavior of such flames. Time scales to the high temperature reaction layer similarly had longer delay times than what the chemical simulations suggested. Chemical flow simulations were re-examined which suggested that autoignition with moderate temperatures, and therefore long ignition delay times, have high concentrations of hydrogen peroxide (H_2O_2) which may serve as an indicator for this chemical regime. Numerical flow simulations had larger concentrations of H_2O_2 upstream of the stabilization point which suggests that moderate temperature chemistry may be dominating the stability behavior. Delay times to the reaction layer were consistent with larger mixture fractions

which also provides evidence that moderate temperature chemistry is dominant. An energy balance in the streamwise direction was calculated for different regions of the flame. Premixed flame behavior was found downstream of the high heat release region. Streamlines which flowed through moderate heat release rates also showed premixed flame behavior, but was heated from the coflow. A critical streamline was found which had characteristics of autoignition. This work advances our understanding of next generation combustor technology by identifying how autoignition helped stabilize a premixed flame which issued into a hot environment.

2 Literature Review

The following sections will review studies which are relevant to this research in order to assess the current state of the field. Flame holes are first discussed to motivate and introduce edge flames. Edge flames are then discussed with regard to both ignition and extinction fronts. Finally, jet in coflow experiments will be reviewed to understand flame stability mechanisms and will lead into flame stabilization in hot environments.

2.1 Flame Holes

Practical combustors typically rely on turbulent flow fields for rapid mixing between fuel and oxidizer or for increasing flame surface area to increase burning rates. When the turbulent fluctuations are sufficiently large, locally extinguished holes in the flame sheet can arise, for example in Figure 2.1, due to non-uniformities in strain rate, curvature, and scalar dissipation rates. Depending on the local conditions at the flame hole, the hole can either close back to a fully burning state or grow leading to global extinction or a decrease in combustion efficiency. Therefore, flame hole dynamical evolution needs to be well understood. For instance, in combustor design it is crucial to understand what conditions lead to flame hole development and in particular know what conditions lead to global extinction.

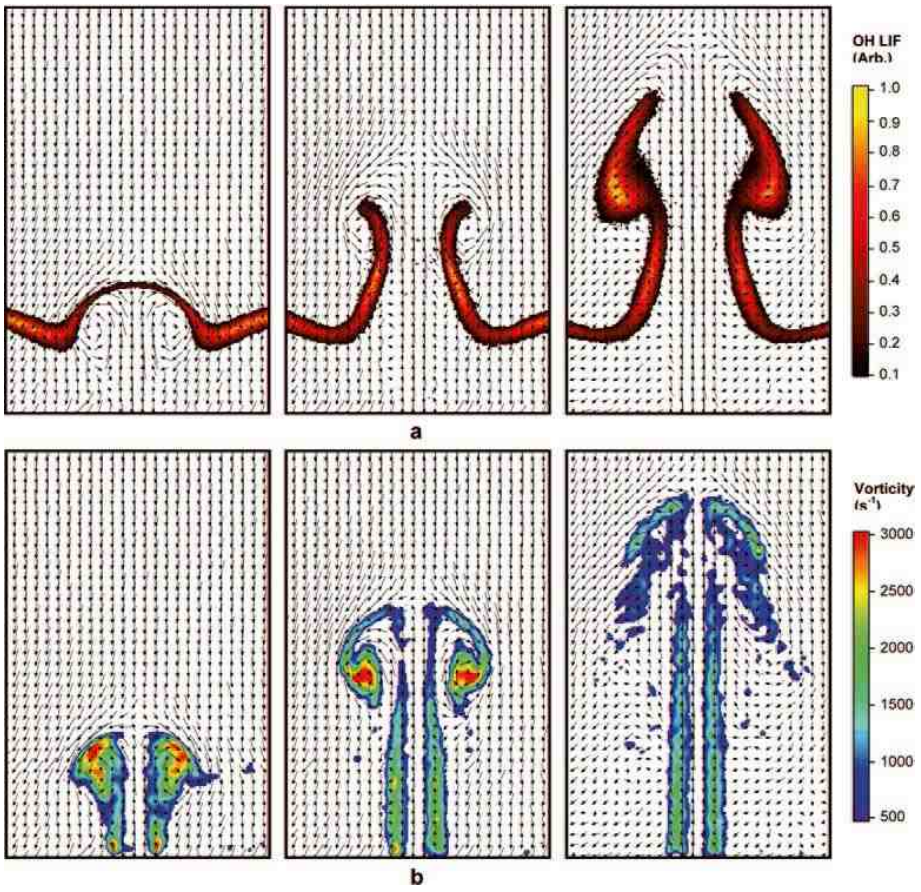

Figure 2.1: Example of a local extinction as vortex impinges on flame sheet [9].

2.1.1 Global Extinction

An inherent problem of understanding flame hole dynamics is the extremely transient behavior of such processes. Extinction studies have been performed in order to understand how global parameters affect the flame structure and eventually lead to extinction. Many studies used opposed-flow geometries where one nozzle issued fuel and the other oxidizer [10], shown in Figure 2.2. The centerline of opposed-flow, or counterflow, geometries can be treated as a one-dimensional flow which dramatically simplifies calculations and understanding of such flames. Along the centerline, the energy balance is simple, shown in Eq. (2.1), where the left hand side is the diffusive heat loss and the right hand side is the chemical heat release [10]. λ refers to the thermal conductivity,

T is the temperature, $\dot{\omega}'''$ is the volumetric kinetic rate of reaction, and Δh is the enthalpy of combustion. From an energy standpoint, these terms must balance up until extinction. As extinction is approached the diffusive heat loss increases and leads to higher reaction rates. At a critical value, the reaction rate can no longer keep up with the heat loss, and extinction occurs.

$$\lambda \nabla^2 T = \dot{\omega}''' \Delta h \tag{2.1}$$

The bulk strain rate can be characterized for these geometries as $\frac{2V}{H}$ where V is the velocity and H is the separation distance between the nozzles, shown in Figure 2.2. For a given nozzle separation distance, the strain rate can be nearly linearly increased by increasing the gas velocity from the nozzles. Increasing the strain rate decreases the fuel-oxidizer mixing layer and subsequently effects the flame structure. Another quantity which is often referred to is the mixture fraction, Z, defined such that $Z = 1$ in the fuel stream and $Z = 0$ in the oxidizer [10]. Similarly, as the velocity increases, the mixture fraction gradient decreases.

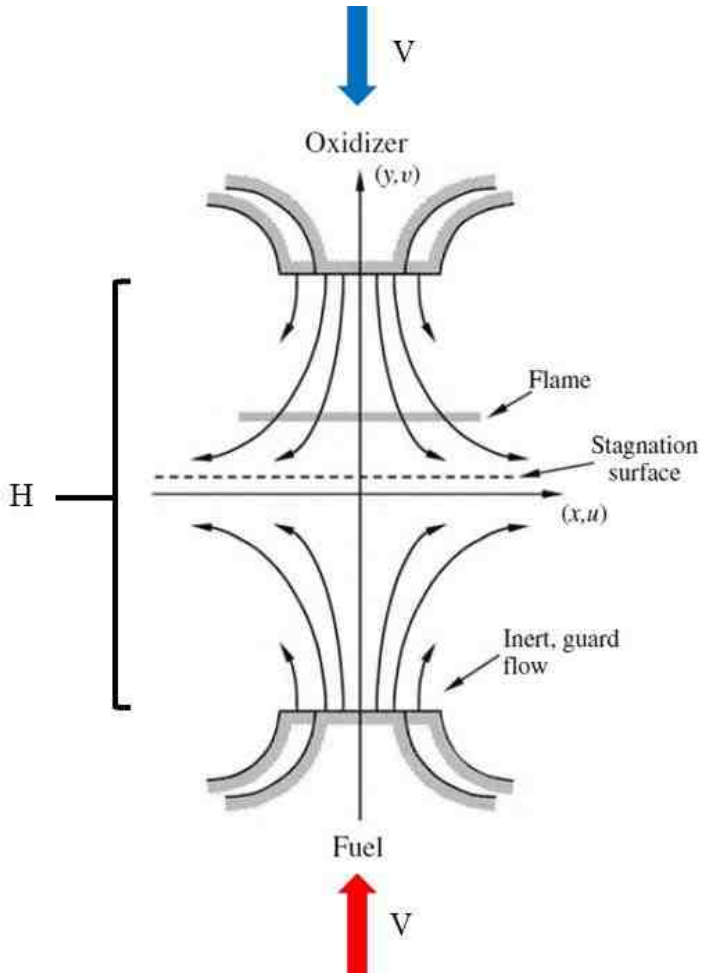

Figure 2.2: Opposed-flow, or counterflow, geometry depiction. This image was edited from [10].

Two main parameters are often used to describe extinction. The Damkohler number is a non-dimensional number which is simply a ratio of the flow and chemical timescales. As the strain rate or mixture fraction gradient increases, the diffusive timescale decreases and therefore the Damkohler number does as well. Near extinction, the diffusive time scale becomes short enough that reactions cannot be sustained and extinction eventually occurs. The other parameter which is often referred to is the scalar dissipation rate, shown in Eq. (2.2), where χ is the scalar dissipation rate, D is the species diffusion, and Z is the mixture fraction [10]. The scalar dissipation rate is particularly useful for numerical simulations since this can be directly calculated, however, is more difficult to

quantify experimentally. The scalar dissipation rate will be used extensively in Chapters 7.1 and 7.2. Similarly, as the velocity is increased for counterflow flames, the mixture fraction gradient increases, and likewise the scalar dissipation rate increases. One-dimensional scalar dissipation rates are often used to describe extinction [10] in realistic flowfields and is even used in models to determine when local extinction will occur [8].

$$\chi = 2D(\nabla Z \cdot \nabla Z) \tag{2.2}$$

2.1.2 Flame Hole Dynamics

Flame holes dynamics have been observed in turbulent diffusion flames in numerous studies (e.g., [11–15]), where laser techniques have been used to measure breaks in the flame front, for example in Figure 2.3. Boxx *et al.* [14] gave a detailed analysis using high speed three-component particle image velocimetry (PIV) and hydroxyl planar laser induced fluorescence (OH PLIF) to study a turbulent diffusion jet flame and assess whether breaks in the flame front were actual flame holes. The paper identified images that appear to represent flame holes individually, but when examined in sequence at high speed were shown to result from other mechanisms such as out of plane convection. The authors show that even with the high speed, three dimensional measurement, it can be difficult to correctly characterize the nature of discontinuities in the flame, for example in Figure 2.4.

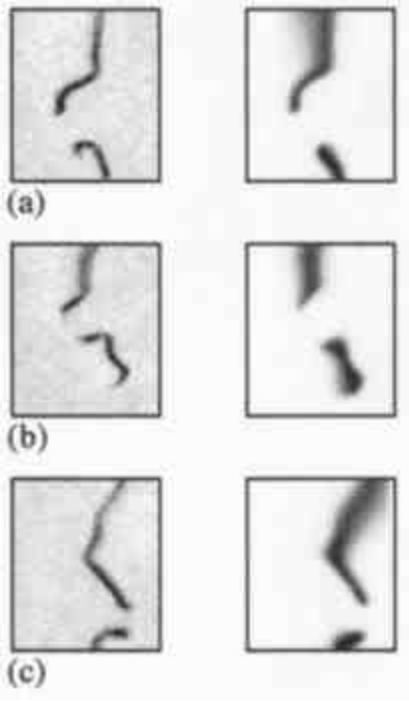

Figure 2.3: Break in CH (left) and OH (right) PLIF measurements in a turbulent jet diffusion flame [12].

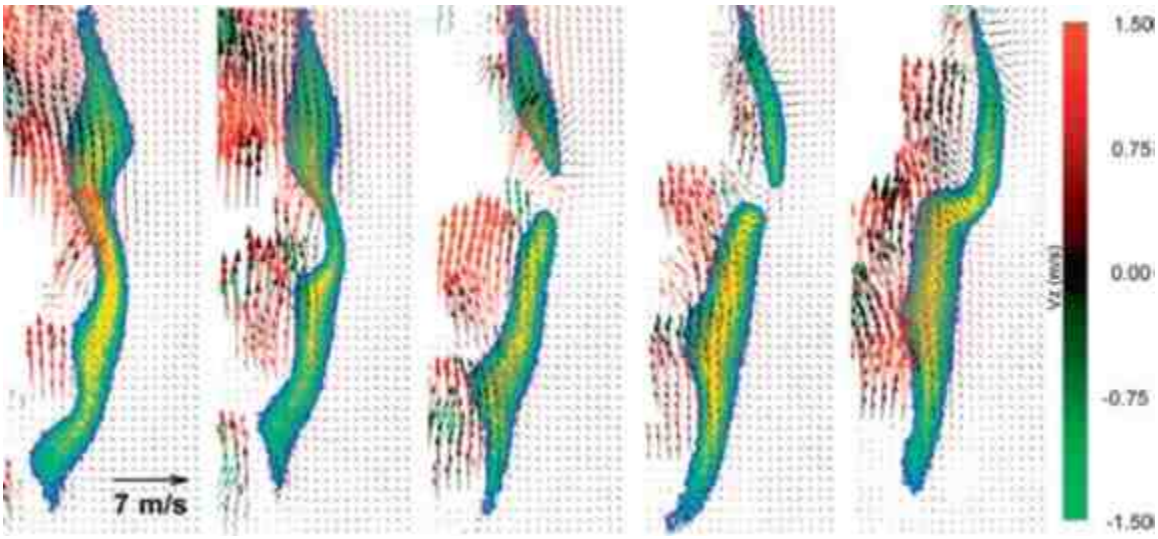

Figure 2.4: Time resolved velocity measurements with OH PLIF contour [14] showing flame discontinuities.

Limited studies of flame hole dynamics have been conducted in simplified flowfields. Rolon *et al.* were among the first to develop a burner which was able to produce flame holes in a repeatable manner [16]. Their burner consisted of a standard counterflow

flame with a piston actuator to pass a vortex through the center of the flat flame. Once the vortex reached the flame, locally large magnitudes of vorticity and strain rate were imposed on the flame. In situations where the strain rate was less than a critical extinction strain rate, the flame would wrinkle and extinction did not occur. Conversely, if the strain rate was larger than the critical extinction strain rate, then a local flame hole was formed. After the flame hole formed, the flame was observed to either heal back to the initial state or lead to global extinction. Other groups created similar burners and further studied the vortex-flame interaction [9,17] which will be further discussed in Chapter 2.2.2. Favier *et al.* examined a flame hole numerically by introducing a vortex into a triple flame which led to local extinction of the diffusion tail at the one dimensional extinction scalar dissipation rate [8]. Once the flame hole was created, the hole responded differently to the scalar dissipation rate compared to the unbroken flame. Understanding flame hole behavior from these studies are challenged by the unsteady propagation of the flame hole in a time-varying flow field.

2.2 Edge Flames

When a flame hole is locally produced, the boundary between the hole and the remaining flame sheet results in edge flames that vary depending on the velocity of the flame edge relative to the bulk flow. A depiction of a flame hole is given in Figure 2.5 in which only two edges are shown, a positive edge and a negative edge. Positive edges, shown as the upper edge flame of Figure 2.5 (a), are characterized by the relative flame velocity propagating into unburned fuel and oxidizer. For a stationary positive edge flame, the bulk flow is from cold reactants to hot products. This produces a velocity and temperature gradient that results in a positive advective heat flux, $\rho c_p v \cdot \nabla T$, through the

edge since $v \cdot \nabla T > 0$. Negative edge flames, shown as the lower edge of Figure 2.5 (b), are characterized by the relative flame velocity propagating away from unburned fuel and oxidizer and toward products. For a stationary negative edge flame, the bulk flow is from hot products to cold reactants causing an opposite sign for the velocity and temperature gradient and resulting in a negative advective heat flux since $v \cdot \nabla T < 0$. A special case where the velocity is perpendicular to the temperature gradient, not shown in Figure 2.5, would result in an edge flame that is simply convected with the bulk velocity and has no advective heat flux through the edge [18]. Although the three edge flames have relatively simply definitions, they are very difficult to experimentally observe since simultaneous velocity and temperature measurements are problematic from an experimental point of view.

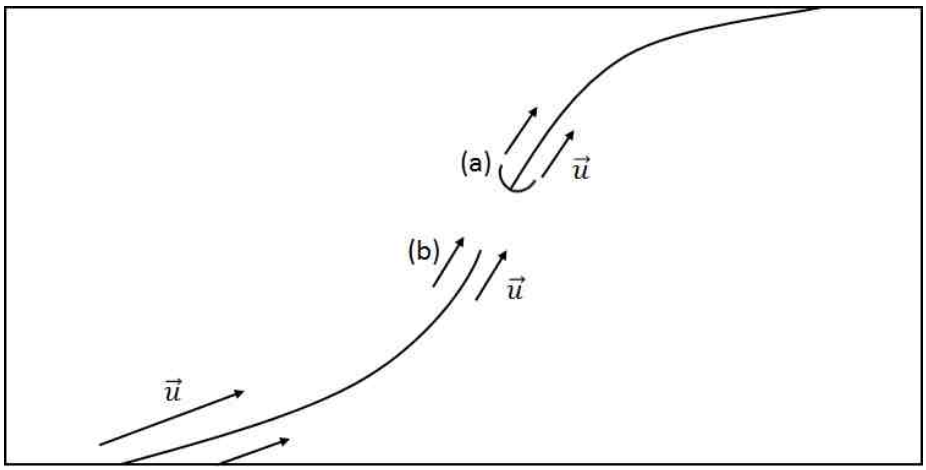

Figure 2.5: Side view of simplified break in flame sheet where (a) is a positive edge flame and (b) is a negative edge flame.

2.2.1 Positive Edge Flames

Positive edge flames represent partially-premixed flame propagation and in Figure 2.5 would result in the closing of the flame hole. These flames are relatively easy to study because they can be formed by nonpremixed or partially premixed lifted flames and can be

stabilized by matching the flow velocity to the edge flame propagation velocity, which is in the opposite direction. Since they are relatively easy to create, they have been extensively studied both numerically and experimentally [19–29]. Positive edge flames can have a triple flame structure, first observed by Phillips [30]. Triple flames have three distinct burning regions, as shown in Figure 2.6, a rich premixed branch, lean premixed branch, and diffusion tail. The three distinct burning regions occur because of the stratification of fuel and oxidizer which creates an equivalence ratio gradient ahead of the flame base. Because the equivalence ratio varies from lean to rich, both lean and rich premixed branches are present. The remaining fuel and oxidizer from the rich and lean respective sides diffuse in a hot region which then leads to a downstream diffusion tail. The three branches are connected at the triple point, which led to the naming of the triple flame that separates the lean and rich side of the mixture. One of the first significant observations was that triple flame propagation speeds were as much as five times faster than the laminar flame speed.

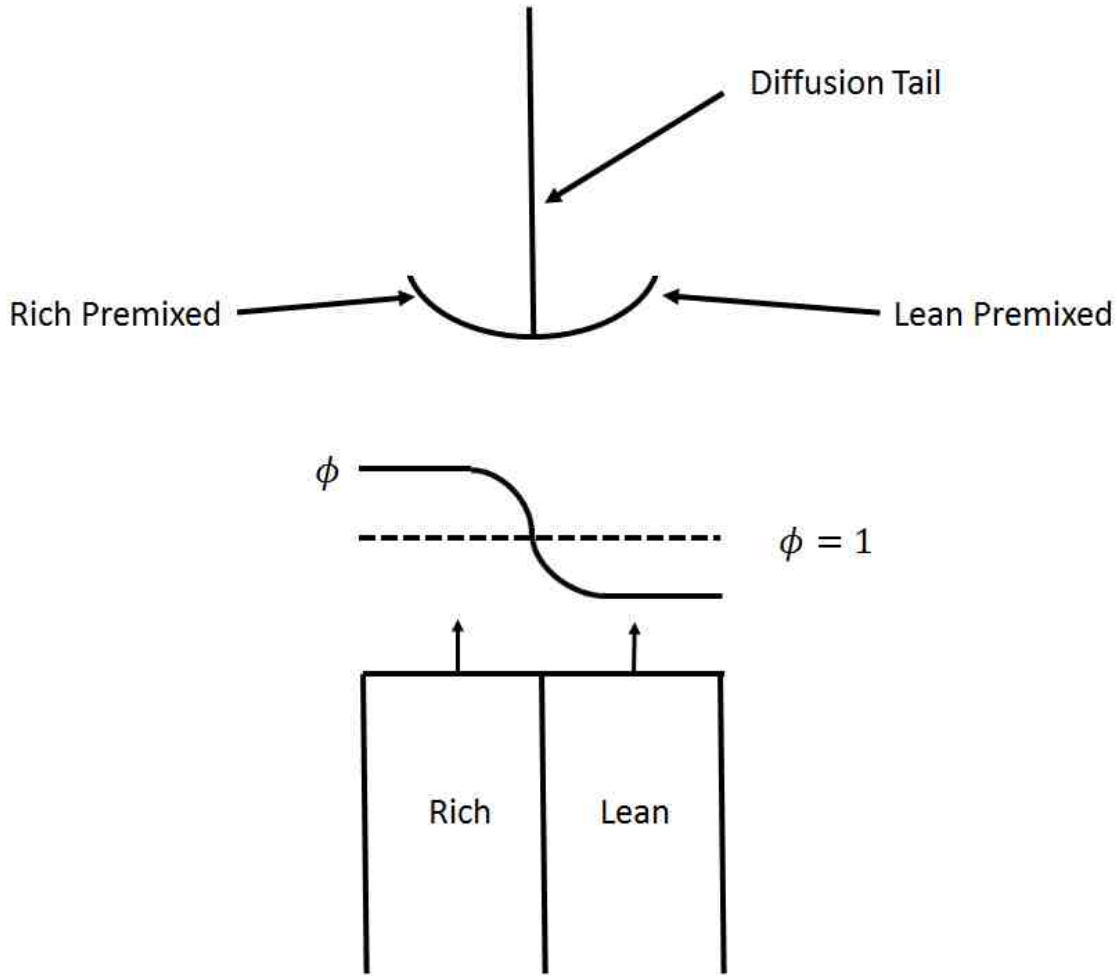

Figure 2.6: Positive edge flame showing the characteristic triple flame structure.

Kioni *et al.* [19,20] performed positive edge experiments in a diverging duct, which caused a stream-wise reduction in velocity. PIV and OH PLIF were conducted in conjunction with numerical simulations to study the propagation velocity. The authors found that the minimum velocity just upstream of the flame base was approximately the laminar flame speed of a stoichiometric mixture. The numerical simulations confirmed this and also showed that the flame base location was approximately at a location of local stoichiometric mixture fraction. The triple point was further confirmed experimentally to be at the stoichiometric mixture fraction [31]. One of the major flow field effects observed was the divergence of streamlines ahead of the flame base, which could be attributed to the

heat release. This is an important feature because it allows the triple flame structure to create a locally low velocity and effectively propagate through the incoming fresh reactants at greater than the laminar flame speed. Santoro *et al.* [21] found that strain rate had an influence on the triple flame structure and used a thermal diffusive model in order to correlate Damkohler number to the propagation velocity, which describes how strain rate leads to a smaller triple flame structure and subsequently lower flow divergence ahead of the flame base.

Work by Ruetsch *et al.* [28] found that the heat release from the flame not only diverges the streamlines allowing the flame to stabilize at lower velocities, but also aids in creating a smaller mixture fraction gradient. This enhances the width of the premixed region. It was also shown that the curvature of the premixed branches and flame heat release induces a pressure gradient that causes flow divergence ahead of the premixed flame base, which allows the velocity to locally reduce in the stream-wise direction. An analytical asymptotic limit was also derived which was proportional to the square root of the density ratio between upstream reactants and downstream products, where the equivalence ratio gradient was zero.

The equivalence ratio gradient ahead of the flame base was further shown to affect the propagation speed by changing the flame curvature at the leading edge [32–35]. With very low equivalence ratio gradients, the flame is wide and has large streamline divergence. As the equivalence ratio gradient is increased, the flammable mixture width decreases, leading to a smaller flame base, higher local curvature and subsequently smaller streamline divergence, depicted in Figure 2.7 where ρ is the radius of curvature. Hirota *et al.* [36] further characterized this relationship and showed that the fuel concentration gradient was

linearly related to the flame curvature ahead of the flame base, similar to [34,35]. Ko and Chung derived the dependence between curvature and the fuel concentration gradient and showed that it was linear [32].

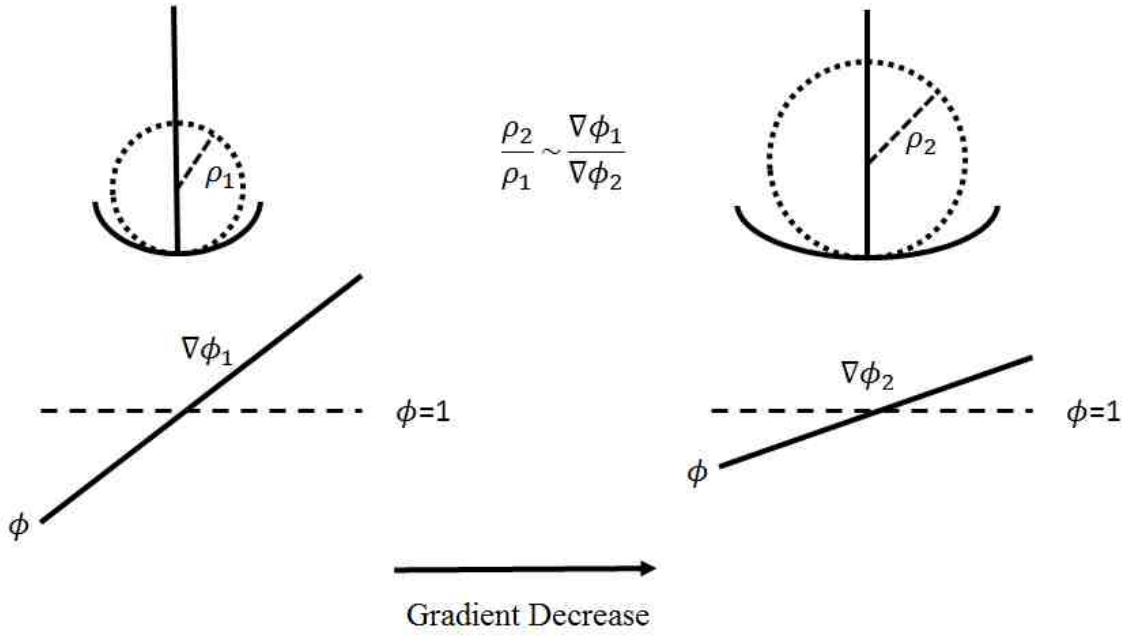

Figure 2.7: Individual triple flame curvature response to equivalence ratio gradient.

Kim *et al.* [33] characterized the propagation speed of a single triple flame through the bulk flow for different concentration gradients using a lifted, steady, laminar flame. The largest speed before blowoff, where the flame could no longer propagate through the flow, was taken as the freestream propagation speed of the triple flame with respect to the bulk flow. This approach was used since the effect of flow divergence will persist all the way to the burner exit if the flame structure is stabilized at a fixed lift off height and this can affect the boundary conditions, leading to an inaccurate description of the propagation speed. When the flame just blows off, the flame structure can no longer diverge the streamlines quickly enough to allow stabilization, leading to a well characterized speed. At relatively high equivalence ratio gradients, reduction in the gradient led to linearly

higher propagation speeds due to larger diverging streamlines. A critical concentration gradient was shown to exist at very low gradient magnitudes where the propagation speed is maximum, first observed in [37], and it was speculated that this point represents the transition from a triple flame to a laminar premixed flame [33]. Further reduction in the equivalence ratio gradient no longer sustained a triple flame structure as the diffusion tail sufficiently weakened, leading to lower propagation speed. At low equivalence ratio gradients, the propagation speed varied linearly with equivalence ratio gradient [33], but over a larger range the propagation speed varies inversely with equivalence ratio gradient [32,38]. Propagation speeds in highly strained conditions, to the point where the premixed wings of the triple flame structure collapse into a bibrachial or monobrachial structure have also been studied [21,39,40]. Individual triple flame velocities have been well characterized with respect to the upstream fuel-air gradient, however, there has been little work related to characterizing the propagation speed of multiple triple flames in close proximity, which is relevant to turbulent partially premixed stabilization where multiple stoichiometric crossings may be relatively close.

2.2.2 Negative Edge Flames

Negative edge flames represent an extinguishing front with a negative advective heat flux, $\rho c_p v \cdot \nabla T$, and in Figure 2.5 would act to increase the size of the flame hole. These edges are significantly more difficult to study due to typically rapid transient behavior of extinction events. Negative edge flames have been reported in numerous experiments [8,17,39,41–46], but each of these studies were performed during a transient process where a local flame hole was formed and the negative flame edge quickly receded away from the region of high gradients creating the hole, for example in Figure 2.8. This

led to limited characterization of the negative edge. Amanatini *et al.* [17,41] conducted experiments and numerical simulations similar to the Rolon burner [16]. In the experimentally phase locked data, the negative edge velocities could not be measured during the extinction process due to its short time scale. When the authors conducted numerical simulations, negative edge velocities were found where the velocity was approximately six times faster than the laminar flame speed.

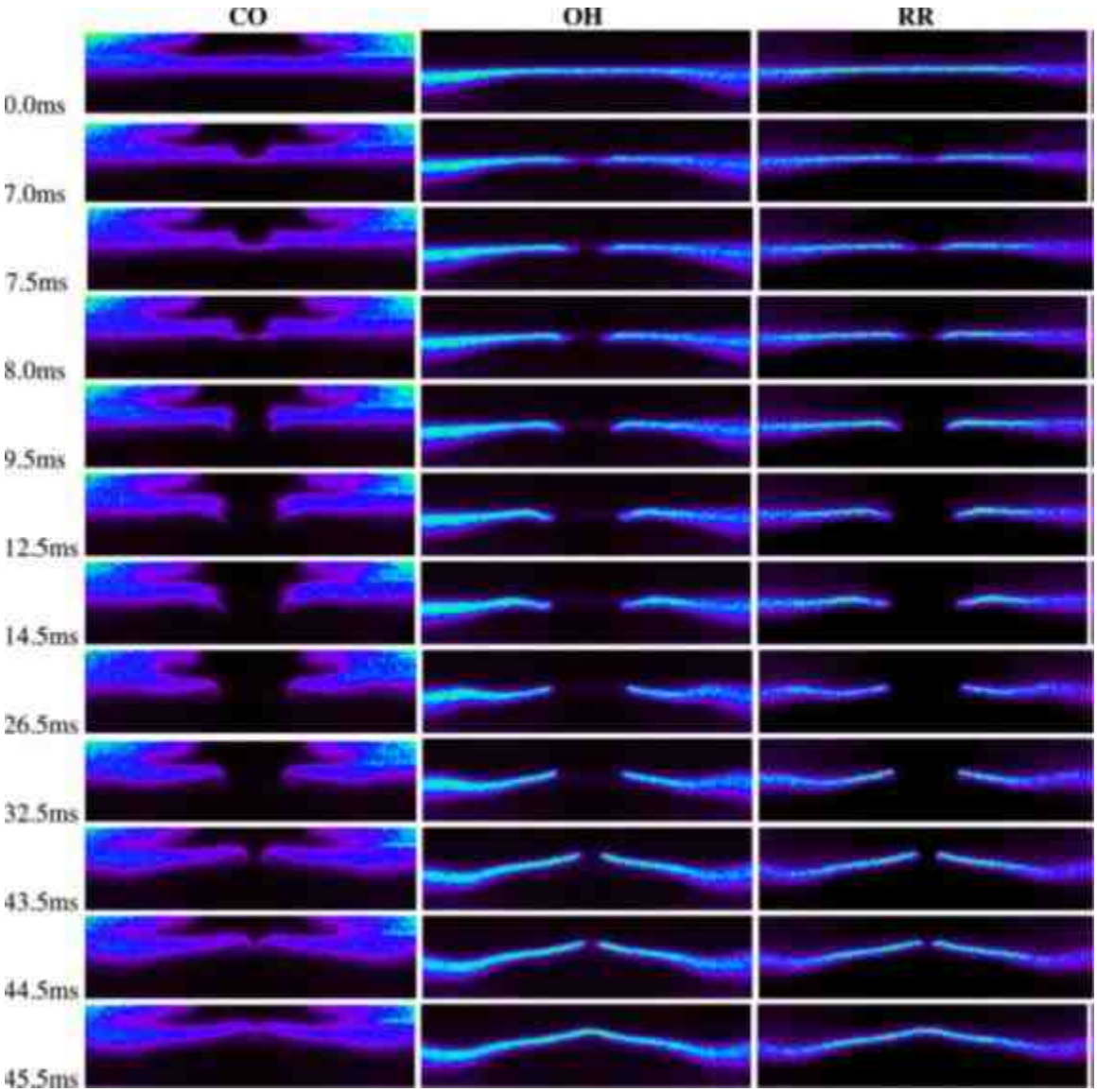

Figure 2.8: Flame hole formation and closing process [17].

Karami *et al.* [15] studied flame hole dynamics in a turbulent jet diffusion flame and found evidence of negative edge flames expanding the flame hole surface area. When the flame hole was able to recover, positive edge flames were observed even though the flame hole area was still expanding due to tangential strain rates continuing to dominate over the positive edge flame propagation speed. Negative edge flame velocities were observed, and were found to be dependent on scalar dissipation rate.

An important characteristic of negative edge flames is the negative edge flame speed, which controls how quickly a flame hole expands and ultimately may determine whether global extinction occurs. Amantini *et al.* [41] found negative edge flame speeds which were as much as six times faster than the laminar flame propagation speed of a premixed flame. Cha and Ronney [39] observed negative edge flames, referred to as retreating edge flames, which were found to be in excellent agreement with numerical simulations [43]. Yang *et al.* [45] also studied propagation speeds of negative edge flames and correlated the results using a local Karlovitz number.

Carnell *et al.* [47,48] conducted experiments and numerical simulations of a steady and stable negative edge flame utilizing a modified counterflow geometry. In this burner, coannular outer nozzles, which are typically used as a nitrogen guard, were used at a higher velocity, to create a radial increase in scalar dissipation rate resulting in an off axis extinguishing edge. This specific geometry is useful because it creates a situation where the negative flame speed can be balanced against the outward flow from the centerline resulting in a stationary negative edge flame. Experimental diagnostics and steady simulations have been conducted on this flame in order to better understand the fundamental mechanism of negative edge flames [48]. An energy balance [48] along the

stoichiometric contour through the negative edge showed that the advective heat flux at the edge aided the stability of the flame, leading to stabilization at higher scalar dissipation rates than the one dimensional extinction scalar dissipation rate. Further analysis showed that the excess scalar dissipation rate above the 1-D value was linearly proportional to the advective heat flux at the edge. Since the one dimensional extinction scalar dissipation rate does not include the process of advective heat flux, it cannot predict the negative edge extinction scalar dissipation rate behavior.

No single negative edge flame speed existed as a function of scalar dissipation rate because both the velocity and temperature gradient at the edge impacts the advection [48]. The edge velocity was linearly proportional to the excess scalar dissipation rate with a constant flame strength, however. Therefore, if a flame with a given flame strength decreases in velocity, the negative edge will stabilize at a lower scalar dissipation rate, and therefore have a lower edge velocity. Likewise, if a negative edge has a constant velocity but is weakened, it will stabilize at a lower scalar dissipation rate and have a lower edge velocity.

The analysis from [48] has been vital to understanding negative edge flames, but has been limited to steady and laminar cases. However, practical applications will create unsteady and turbulent negative edge flames which still need to be analyzed to further understand the implications of negative edge flames in gas turbine engine combustors.

2.2.3 Stationary Edge Flame

Zero velocity edge flames with no advective heat flux have been rarely studied, but was hypothesized by Buckmaster [18]. Shay *et al.* [49] produced edge flames by misaligning a counterflow slot burner. The edge was found to exist in near zero velocity

low strain regions. This flame represents a special case between forward and negative edge flames, but has received little additional study.

2.3 Jet in Coflow

Jet in coflow experiments provide simple flowfields which make it easier to understand flames in different conditions without complex flowfield structures forming. Jet in coflow experiments typically consist of coannular nozzles in which the outer nozzle (coflow) is much larger in diameter than the inner jet. The coflow studies typically are either run in cold ambient or hot vitiated conditions. Many jet in coflow studies involve high velocity fuel jets being injected into oxidizer environments such that the flame is lifted. In cold environments, the stabilization behavior becomes dominated by the mixing between the fuel jet and oxidizer coflow in which the fuel and oxidizer must mix to become ignitable and the flame will propagate against the incoming flow. When the coflow is sufficiently hot, mixing between the jet and coflow still must occur in order to reach an ignitable mixture, however, instead of propagating against the incoming flow, autoignition may occur and the flame base may not rely on heat from the flame to preheat the reactants. In both cases however, the flow field is quite simple and can provide insight into the physics of how these flames stabilize.

2.3.1 Lifted Jet in Cold Environments

Lifted laminar jet flames have been found to stabilize by positive edge flames, which have a triple flame structure. These have been discussed extensively in 2.2.1. Although Chapter 2.2.1 was motivated by flame hole dynamics, the information is relevant to laminar lifted flame stabilization.

Flame stabilization of lifted turbulent diffusion jets have become a fundamental point of interest over the years. In most practical applications, fuel is injected into an oxidizing environment which subsequently mixes and burns. Therefore, fundamental understanding of lifted turbulent jet diffusion flame stabilization can give insight into how flames stabilize in applications. Although this geometry is incredibly simple, it was not well understood how turbulent jet diffusion flames stabilize. There were two main theories for the stabilization mechanism; the extinction and premixed mechanisms.

The extinction stabilization model uses laminar flamelets to explain the stabilization. The model implies that the diffusion flame ends at the flame base by extinction at the laminar flamelet model scalar dissipation rate. Peters and Williams [50] developed this concept which theorized that the flame will stabilize as a diffusion flame sheet anchored by a point at which reaction could no longer occur. The main downfall of this concept is that there is no mechanism that allows significant premixing ahead of the flame base which would allow a flame to be sustainable. Work in [49] showed a triple flame which stabilized in regions below the critical one dimensional extinction strain rate, concluding that the edge flames can occur in regions where extinction is not the limiting phenomena. Everest *et al.* [51] measured the scalar dissipation ahead of a lifted turbulent diffusion flame base and found the scalar dissipation to be higher than the critical extinction value. However, Watson *et al.* [52] conversely observed the lifted flame base to reside in a region lower than the critical scalar dissipation rate. Over the years it seems that this concept has received less attention as more data was collected.

The premixed stabilization model assumes that the flame is suitably mixed upstream of the flame base such that the flame can propagate against the flow [53,54]. In

this model, the lifted flame base chemical flame speed locally balances the local flow speed, similar to the laminar triple flame [20]. This model was extended slightly to include a diffusion tail, which gives the flame base a propagating triple flame structure [18]. A large amount of data has been provided to support the likelihood of this stabilization mechanism, and Lyons [55] seems to support this idea. Upatnieks *et al.* [56] performed experiments using cinema PIV (CPIV) in order to measure the velocity upstream of the flame base. The authors provided analysis showing that the propagation speeds were not consistent with the turbulent intensities, concluding the flame base is unaffected by turbulent premixed flame propagation. However, the results indicate that edge flames were present since the upstream flow velocity near the flame base was nearly the laminar flame speed dependent on the local conditions, consistent with edge flame behavior. Instantaneous snapshots near the flame base showed significant divergence of the streamlines, shown in Figure 2.9, which is also typical of positive edge flames.

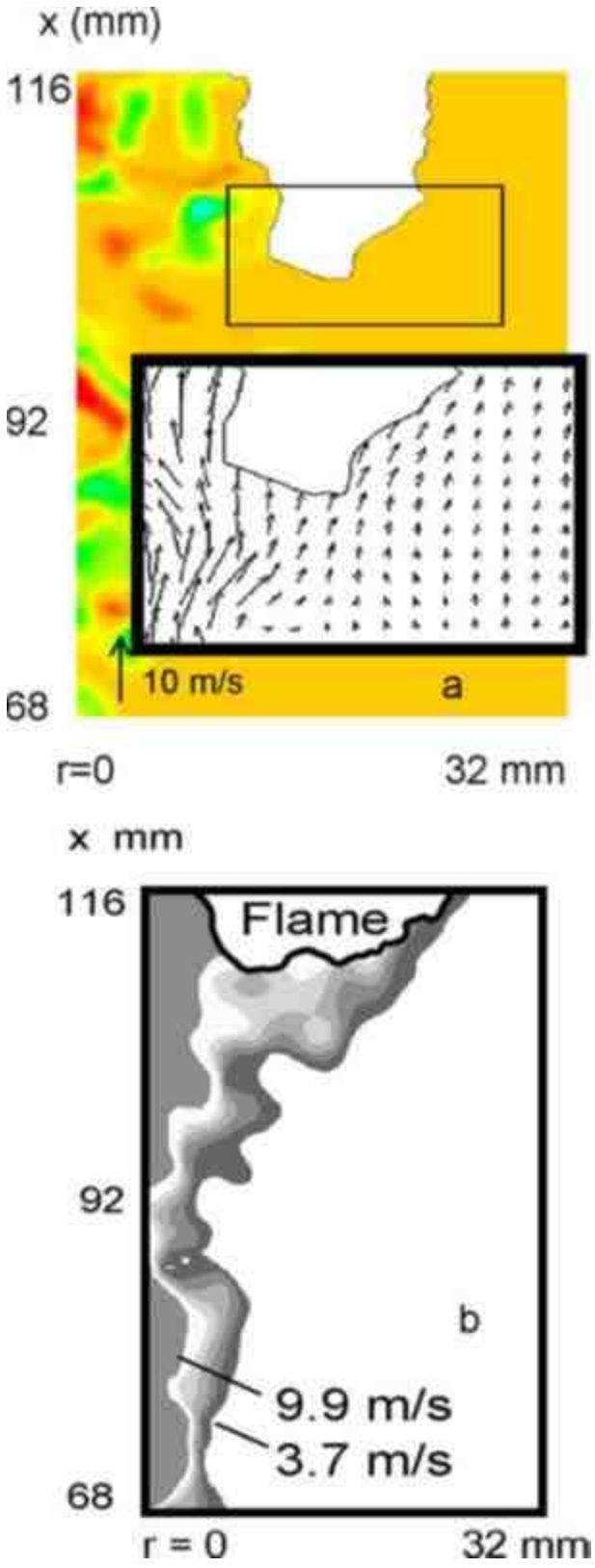

Figure 2.9: Flame base depiction from [56] showing divergence of streamlines ahead of flame base.

A separate study used a direct numerical simulation (DNS) to simulate hydrogen injection into quiescent air [57]. The flame index, which describes whether reactions are burning in premixed or non-premixed mode, was used in order to understand what propagation mode was occurring at the flame base. The flame index is defined in Eq. (2.3), where FI is the flame index, Y_F is the fuel mass fraction, and Y_O is the oxidizer mass fraction. This parameter is often used to determine the propagation mode with a relatively easy definition. In non-premixed burning modes, the fuel and oxidizer diffuse from opposing directions, and therefore have mass fraction gradients in opposing directions. Conversely, premixed flames start with a given fuel and oxidizer mass fraction and subsequently burn, therefore have an alignment of the respective mass fraction gradient directions. Thus, the flame index is positive for premixed flame stabilization and negative for diffusion, or non-premixed, flame behavior. An example of the flame index at the leading edge of the flame is shown in Figure 2.10. The dark black line represents the stoichiometric line which has positive flame indexes on either side representing a premixed flame base. Downstream of the premixed structures is regions of negative flame index, and therefore is a diffusion tail. Thus, the leading edge has clear characteristics of a triple flame structure. Near this flame base, it was found that the incoming flow was balanced by the laminar burning velocity. This further confirms that edge flames, or the premixed model, is the stabilization mechanism for standard jet diffusion flames.

$$FI = \nabla Y_F \cdot \nabla Y_O \tag{2.3}$$

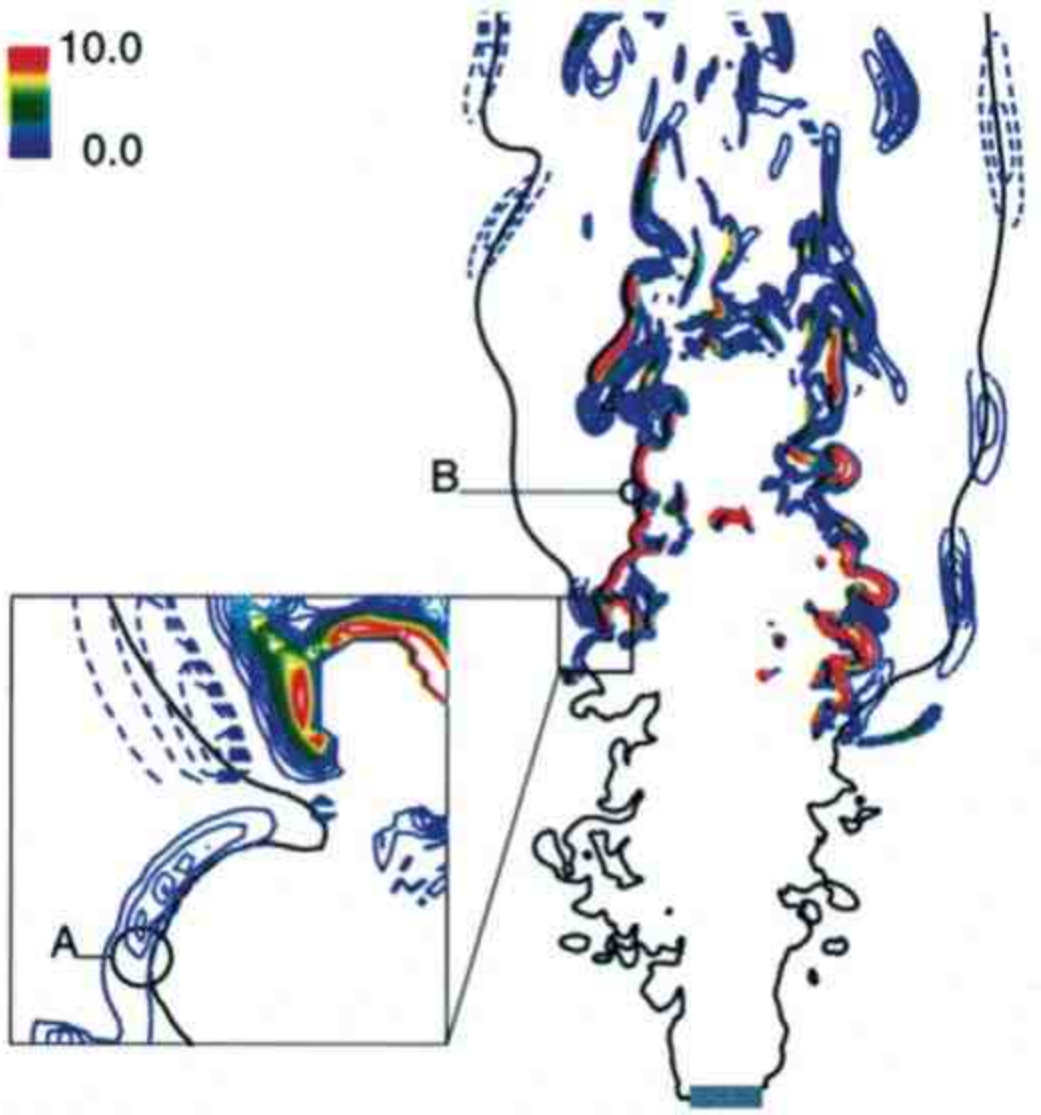

Figure 2.10: Flame index of a turbulent jet diffusion flame [57]. The zoomed in window shows a triple flame structure. The dark black represents the stoichiometric line. Solid blue lines represent positive flame index contours and dashed lines are negative.

Studies have been performed with coflowing air at high velocities. Work by Han and Mungal [58] showed that the flame base, determined by CH PLIF, was near the stoichiometric velocity, where the stoichiometric velocity was defined as the laminar propagation speed of a stoichiometric mixture. Therefore the flame is propagating against the mixture and also supports the premixed stabilization mechanism.

2.3.2 Lifted Jet in Hot Coflow

Lifted jets in sufficiently hot environments such that autoignition can occur are fundamentally different than jets in cold environments. In cold environments, the flame must propagate against the flow at the flame speed, however, when the mixture can potentially autoignite, the flow characteristics may allow autoignition to occur prior to the lifted flame base stabilizing by propagation speed.

Homogeneous autoignition studies typically examine specific fuel to air ratios at fixed temperatures where a defined ignition delay time is characterized [59–61]. Higher temperatures and mixtures closer to stoichiometric typically lead to decreased ignition delay times because the reaction rate is exponentially increased with temperature. In heterogeneous flows, where mixing occurs between a jet and hot oxidizing coflow, a most reactive mixture fraction can be present where there is a minimum ignition delay time based on homogeneous chemical kinetics [62]. Most relevant work regarding autoignition in non-homogeneous high temperature flows has been conducted with pure fuel jets issuing into a hot environment with a sufficient amount of oxygen such that combustion can take place [63–71]. In these experiments, not only is there a gradient in temperature between the two streams, but there is also a correlated gradient in mixture fraction. Low mixture fractions have high temperatures but low fuel concentration, while large mixture fractions have low temperatures. This leads to a tradeoff between the impact of temperature and deficient species on the ignition delay time. While the autoignition delay time is shortest in low mixture fractions, very little heat release occurs because there is not much fuel present; thus these heterogeneous conditions significantly complicate the problem of defining the location where autoignition will first occur. Autoignition relies on a localized

region where a sufficient amount of fuel, oxidizer, and heat are present for a sufficiently long time to ignite, however once the flame is formed, partially premixed propagation can also occur with a lifted flame front propagating against the non-homogeneous fuel and air mixture [30]. Since the flame is lifted, mixing occurs between the fuel and oxidizer environment which leads to an equivalence ratio gradient ahead of the flame base which can lead to edge flame propagation [19,20,28]. Most studies with fuel jets injected into hot environments identified whether partially premixed propagation or autoignition was the dominant stabilization mechanism but did not address autoignition location or its local conditions.

In situations where the oxidizing environment is sufficiently hot and the flame is lifted about the fuel injection point, either autoignition or partially-premixed flame propagation are potential stabilization mechanisms. Cabra *et al.* [63,64] were among the first to study such flames in a laboratory setting. A turbulent fuel jet was issued into a 1045 K coflow where multiscalar point measurements were conducted and compared against several turbulent combustion models. Although the measurements were inconclusive whether autoignition was the dominant stabilization mode, a direct numerical study (DNS) study using similar conditions as in [63] confirmed that autoignition was occurring due to the production of preheating radical pools ahead of the flame base [72]. Gordon *et al.* [68] performed hydroxyl (OH) and formaldehyde (CH_2O) planar laser induced fluorescence (PLIF) on similar conditions as [64] in which radical pools of CH_2O were found ahead of the high burning region, followed by OH production with low levels of CH_2O in both laminar simulations and turbulent flame experiments. An example is

shown in Figure 2.11, which indicated that autoignition was occurring in the experiment where ignition kernels develop and initiate reactions ahead of the steady burning flame.

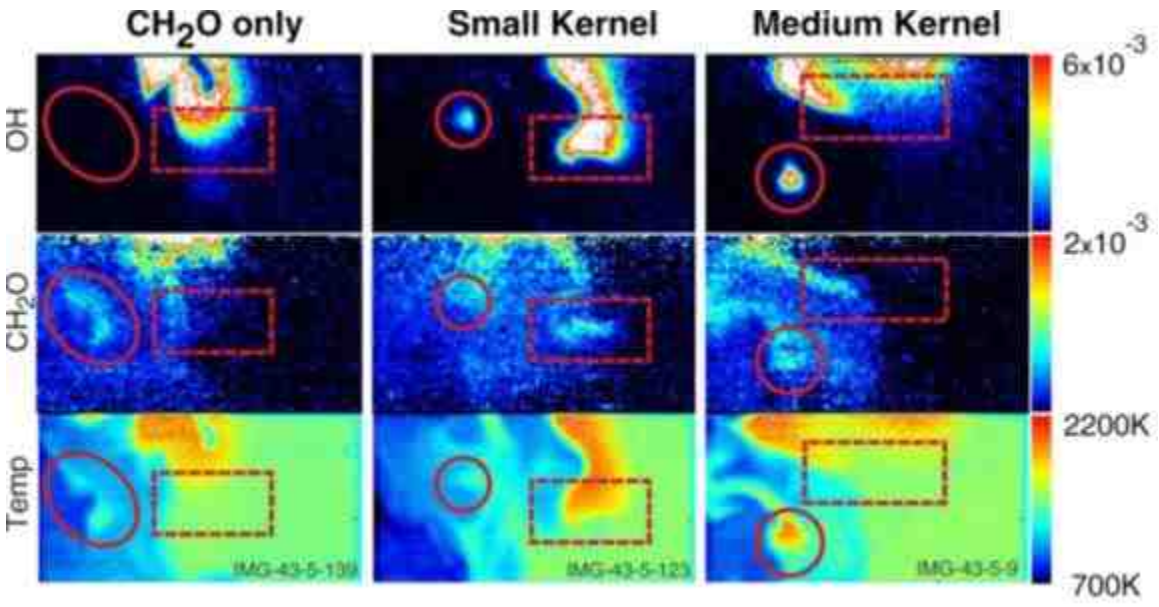

Figure 2.11: Simultaneous OH and CH_2O PLIF with Rayleigh scattering measurements for temperature from [68]. Three regimes are shown; CH_2O only flames, small kernels, and medium kernels.

Arndt *et al.* [67] studied the transient process of a turbulent fuel jet injection into a vitiated coflow. High speed Rayleigh scattering was used to quantify the mixture fraction and temperature at the initiating kernel development. The sudden fuel injection first occurred until a steady flowfield was established. After the flowfield stabilized, the leading autoignition kernel was found to be in regions of low scalar dissipation rate and mixture fraction, shown in Figure 2.12, in agreement with chemical simulations of the most reactive mixture fraction due to the high temperature. In the premixed jet in vitiated coflow situation, only heat needs to be transferred from the vitiated products to ignite the mixture; thus different conditions for autoignition are expected compared to a pure fuel jet.

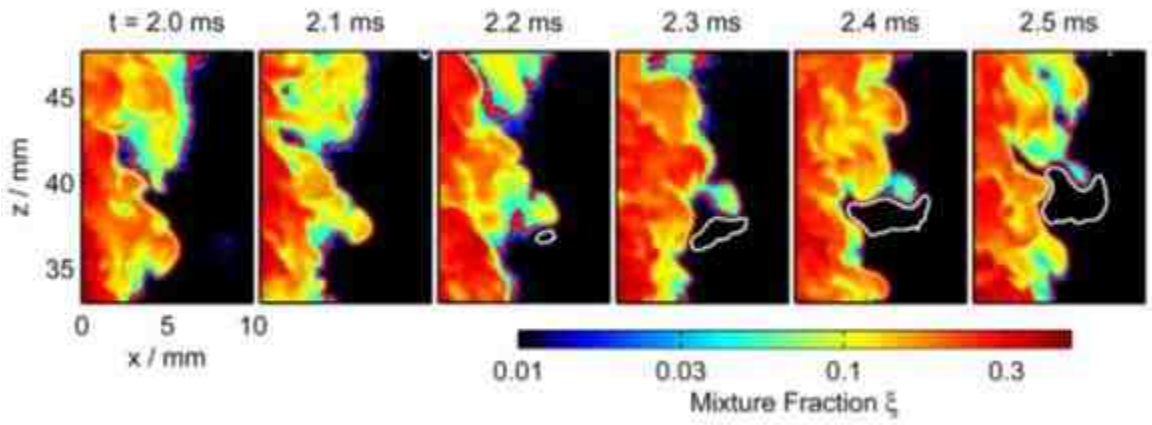

Figure 2.12: Ignition kernel development sequence. The white contour is a 1500K contour, indicative of an ignition kernel. Note the mixture fraction colorbar is logarithmic [67].

Premixed jets in hot coflow and crossflows are relevant to future gas-turbine engine design but have been studied less frequently [73–76]. Schmitt *et al.* [73] examined a premixed jet into vitiated crossflow and found that the jet immediately ignited upon entering the test section. They attributed this to a horseshoe vortex penetrating into the jet tube, which ignited inside the jet tube. Wagner *et al.* [74] studied similar conditions which instead led to lifted and unsteady flames where the flame was found to be autoignition assisted. Later work [75] used simultaneous particle image velocimetry (PIV) with OH and CH_2O PLIF and found three burning regimes. In one of the regimes, CH_2O was found to be produced well upstream of the OH flame base, similar to [68] where a radical buildup occurred ahead of the reaction zone, suggesting that autoignition was important in the flame stabilization behavior. Although there has been many observations of autoignition type behavior, no study thus far has attempted to understand how and why autoignition is occurring as opposed to premixed propagation.

2.4 Research Objectives

There has been significant contributions from various researchers regarding these topics. This Chapter will briefly describe what is currently missing from the literature and how each Chapter in this dissertation addresses the respective question.

2.4.1 Advective Heat Flux Estimation

Edge flames have relatively simple definitions which can be easily calculated using numerical simulations, but are difficult to identify experimentally. Each edge flame is characterized by the sign of the advective heat flux $v \cdot \nabla T$ at the flame boundary and the magnitude gives information regarding the strength of the edge flame. Although the velocity and temperature can be easily measured, it is very difficult to do this simultaneously and with sufficient resolution to accurately compute gradients. A simple technique to estimate the advective heat flux using the flow dilatation is presented in Chapter 5 which will outline the theoretical background and provide validation.

2.4.2 Positive Edge Flames

Propagation speeds for positive edge flame have been well characterized in the literature for a single triple flame. However, practical applications can create flowfields with many stoichiometric crossings, and therefore positive edge flames, in close proximity. Since the edge flames are near one-another, they may begin to interact and lead to increased propagation speeds. The propagation speed of two steady and laminar interacting triple flames were characterized and modeled based on the flame curvature, or equivalence ratio gradient, and level of interaction to give an accurate representation of the propagation speed. Three fuels were tested to validate the model with different fuel diffusivities in Chapter 6.

2.4.3 Negative Edge Flames

Steady negative edge flames were well characterized in several studies. Two-dimensional simulations were needed to calculate the conditions at the flame. However, only three terms were non-negligible in the energy equation which could be modeled such that a reduced order one-dimensional calculation could be performed to provide the same information, and is described in Chapter 7.1. Unsteady negative edge flames have not received the same attention as the steady cases, but are extremely relevant to better understand negative edge flames in practical applications. Unsteady negative edge flames were studied in Chapter 7.2 with respect to different boundary condition oscillations. The energy equation was reanalyzed in order to better characterize the unsteady energy term. The negative edge flame speed was also evaluated in the unsteady flow which gave better insight into how edge flame velocities are interpreted. Negative edge flame velocities were also measured in a turbulent flow in Chapter 7.3 to better understand differences between laminar and turbulent negative edge flames.

2.4.4 Premixed Jet in Vitiated Coflow

There has been an effort to better understand jets in vitiated flows throughout the literature. However, most studies simply determined whether autoignition was the dominant stabilization mechanism rather than understanding why and where autoignition occurred. In order to better understand the stabilization behavior from a fundamental level, a premixed jet in vitiated coflow was simulated in laminar and steady conditions to understand the stabilization behavior in Chapter 8.

3 Combustors

Four burners were used in this dissertation which created environments with different types of stratification. Each burner will be described in the following sections and the relevance to each problem will be described. The burners will also be described in the respective Chapters since they are used slightly differently in each study. This Chapter serves as an introduction for each burner geometry and the respective utility.

3.1 Multiple Slot Burner

Chapters 5, 6.1, and 6.2 used this burner to create positive edge flames. Chapter 5 utilized this burner to create a flowfield suitable to stabilize a laminar and steady triple flame, while Chapters 6.1 and 6.2 created both single and interacting triple flames.

Triple flames were created using a five slot burner used in a past study [29] and shown in Figure 3.1. The burner is symmetric in the out of plane direction which allowed the flowfield to be simplified into a two dimensional problem. The five 14 mm wide inlets were separated by metal plates which allowed the velocity and mixture to be independently controlled. The flow went through several mesh pieces to uniformly distribute the flow across each slot. A 1/2" thick, 1/8" cell size aluminum honeycomb flow straightener was placed at the exit of the slots which entered a converging nozzle without separators between the slots. This allowed neighboring slots to mix which helped create smooth gradients across the combustor. The converging nozzle created a near plug flow velocity profile at the burner exit. The exit of the burner was equipped with a 1/4" thick 1/16" cell steel honeycomb to straighten the flow exiting the burner and act as a flame arrestor. The nozzle had a 9:1 contraction ratio, 3:1 in each direction, which transitioned the flow area from 75 x 120 mm to 25 x 40 mm. Converging nozzles with large contraction rations have been

implemented to create a near plug flow velocity profile, which was verified in [47]. Velocity measurements will be examined in this burner in a later Chapter which verified that the velocity profile was nearly flat. A 5mm nitrogen guard was used around the burner exit to separate room air from the combustor.

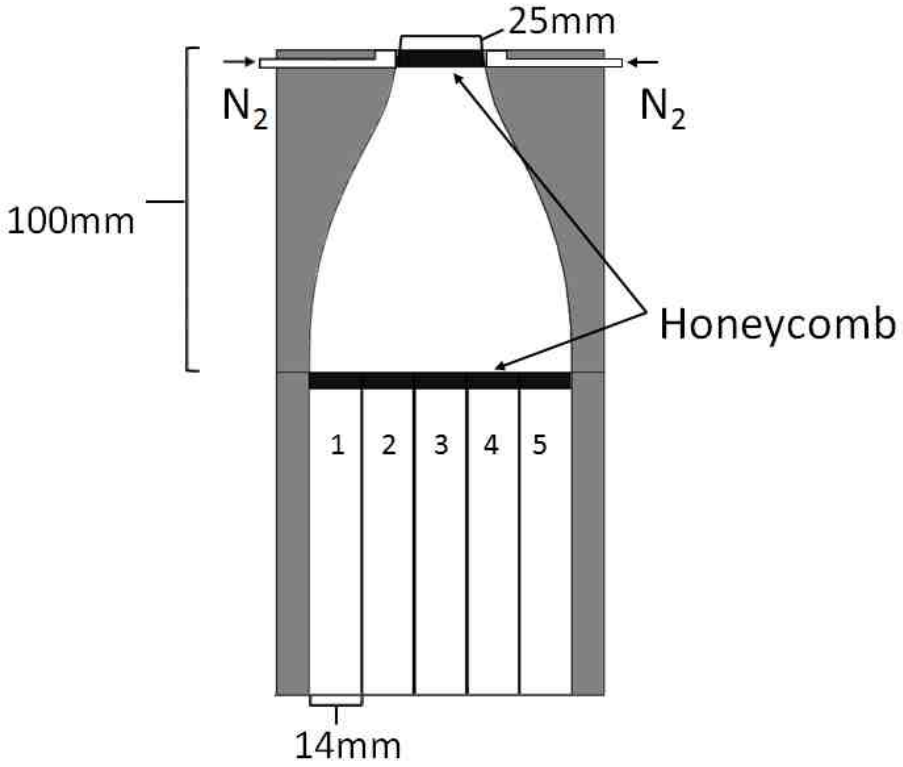

Figure 3.1: Experimental five slot burner schematic.

The two-dimensionality of the burner was verified by observing both the flatness of the flames in the out-of-plane direction and how straight the flames were in the out-of-plane direction. If the flame(s) were not flat, then the velocity field may not be uniform, whereas if the flame(s) were not straight in the out-of-plane direction, then the fuel was likely not distributed well. In the beginning stages of the tests, these were checked and the steel mesh flow distributers were reoriented until the flames were two-dimensional.

For each study in this dissertation, the velocity in each slot was held constant while the equivalence ratio was varied. Though, the burner has the capability to produce both velocity in conjunction with equivalence ratio gradients. The burner was capable of producing either one or two triple flames by creating one or two stoichiometric crossings. To create a single stoichiometric crossing, a single equivalence ratio gradient was created by flowing nitrogen through slots 1 and 2, a rich equivalence ratio mixture through 3, a lean equivalence ratio mixture through 4, and air through 5. Two create two stoichiometric crossings, two equivalence ratio gradients were created by supplying air through slots 1 and 5, a lean mixture through 2 and 4, and a rich mixture through slot 3. These mixtures provided the capability to alter the gradient by changing the equivalence ratio through slot 3; higher equivalence ratios resulted in higher fuel concentration gradients. Moreover, when multiple triple flame were created, the stoichiometric location was able to be controlled by changing the lean equivalence ratio through slots 2 and 4. Leaner equivalence ratios moved the two triple flames closer together while higher equivalence ratios separated them.

This burner was used in this dissertation to measure the flow dilatation through a single triple flame which was compared to the advective heat flux. Simulations were computed which gave full access to both the advective heat flux and dilatation, and subsequent experimental dilatation measurements were then compared to the simulated trends. The burner was also used in a separate study to compare the propagation speeds of interacting triple flames to individual triple flames. Interacting triple flames allow larger divergence ahead of the flame base which allows even faster propagation than single triple

flames, which was characterized and modeled. This study was expanded to include multiple fuels.

3.2 Modified Counterflow Burner for Steady Negative Edge Flame Studies

This burner was used primarily in Chapter 5 but was also modeled using numerical simulations in Chapters 7.1 and 7.2. In Chapter 5 the burner created a variety of negative edge flames which was used to compare the flow dilatation to the advective heat flux. In Chapter 7.1 the stoichiometric line of negative edge flames was modeled in numerical flow simulations. The goal from that Chapter was to model the energy equation along the stoichiometric line in this geometry and be able to calculate negative edge flame characteristics without two-dimensional simulations. Lastly, Chapter 7.2 simulated this burner but differed from previous studies by using periodic boundary conditions in the outer nozzle to make the negative edge flame unsteady in a well-defined way. The details of each study will be explain in the respective Chapter. The following provides a description of the experimental modified counterflow burner.

A modified laminar counterflow burner was used to create a steady, axisymmetric negative edge flame which was used in several prior studies [47,48,77]. A typical counterflow diffusion flame is produced using opposed flowing jets where oxidizer is flowing from one nozzle and fuel from the other. Each flow decelerates eventually reaching a stagnation plane in which the velocity reaches zero along the centerline, creating a one-dimensional problem. Because of the one dimensionality of the problem, there have been many studies related to this geometry. Molecular diffusion occurs between the fuel and oxidizer streams which create a local region with a stoichiometric mixture fraction, which allows a flame to be created. Typical counterflow burners have an outer coannular

nozzle which supplies a nitrogen curtain to separates the experiment from the room air. This burner instead, flows the same concentration mixture from the coflowing nozzles but at higher velocity. The increased velocity locally raises the scalar dissipation rate which locally extinguishes the flame and stabilizes a steady negative edge flame.

The burner schematic is shown in Figure 3.2. Flow entering both the center and outer nozzles flow through a contoured converging nozzle, with a contraction ratio of 10:1, to create a plug flow velocity profile at the nozzle exits. Flow distributors were placed at the nozzle inlets with honeycomb pieces to straighten the flow, while 1/2" thick 1/8" cell size aluminum honeycomb pieces were placed at the nozzle exits. A 1 mm wall separated the inner and outer nozzles. The inner and outer nozzles had diameters of 20 and 48 mm respectively, which were 15 mm separated. The burner was attached to metal plates which were attached to four metal rods which aligned the nozzles.

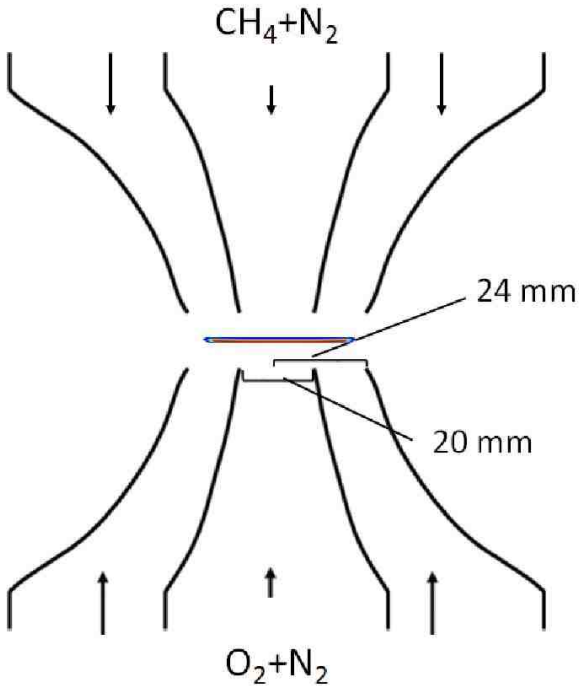

Figure 3.2: Experimental schematic of the modified counterflow burner. The counterflow flame reaction rate is shown in color between the opposed flowing nozzles.

Chapters 7.1 and 7.2 simulated this burner but also expanded the inner nozzle diameter, which was not capable in the experiment since this would require multiple burners. The inner nozzle diameter was increased in order to keep the same flame strength while increasing the gas flow velocity through the negative edge which changed the energy through the edge. The flow velocity through the edge can be increased by changing the inner nozzle velocity, however, the negative edge flames are highly dependent on both the velocity and the temperature gradient through the edge. If the inner nozzle velocity is increased the velocity increases through the edge, but the temperature gradient is no longer held constant. For this reason, the turbulent negative edge burner was designed in built, which is described in the next Chapter.

3.3 Turbulent Negative Edge Burner

The major limitations of the negative edge counterflow burner described in Chapter 3.2 are the ability to reach higher edge velocities, reach turbulent conditions, and separate the flame strength and velocity through the negative edge. For these reasons a burner was built which is able to reach higher velocities through the negative edge and also isolate the stabilization flame strength and velocity through the edge. It should be mentioned that the burner in Chapter 3.2 could reach turbulent conditions, however, not in a stable way. Turbulence generating grids were 3-D printed and placed in the burner. The flame was highly unsteady, however, the flame would penetrate outside the burner at times which significantly increased the temperature of the burner and could potentially melt the grid. For this reason, the burner could not reliably reach unsteady and turbulent conditions. Also, the stability of the counterflow flame significantly changed as well. It is believed

that the large fluctuations may have flowed back towards the centerline and dramatically affected the flame near the centerline.

The turbulent burner schematic is shown in Figure 3.3 and was able to create statistically stationary negative edge flames in flows with varying levels of turbulence. The main channel cross sectional area was 15.7 mm deep (into the page along the z-direction) by 34.8 mm wide in the x-direction. Fuel and air flowed from the bottom of the burner on opposing sides of a 9.5 mm wide splitter plate in the x-direction which was 50.4 mm in the y-direction and was placed in the center of the channel. While flowing on the respective side of the splitter plate, the gases went through steel mesh pieces to distribute the flow and subsequently a 3.2 mm cell size, 12.7 mm thick aluminum honeycomb to straighten the flow. The flow exiting either side of the splitter plate is referred to as the "slot flow". The fuel and air mixed in an 88.9 mm long (y-direction) test section where the splitter plate ended, leading to the formation of a two dimensional flame sheet stabilized in the wake of the splitter plate. Square jets with 15.7 mm sides were introduced perpendicular to the flame sheet 19 mm downstream of the splitter plate, which supplied the same fuel and air mixtures from the respective sides but at higher velocities. The jets introduced perpendicular to the flame sheet will be referred to as "side jets". The side jets caused an increase in scalar dissipation rate along the flame sheet in the flow direction and led to local extinction. The flow then went through an exhaust section, shown in Figure 3.4, to vent the products and allow laser access to the test section.

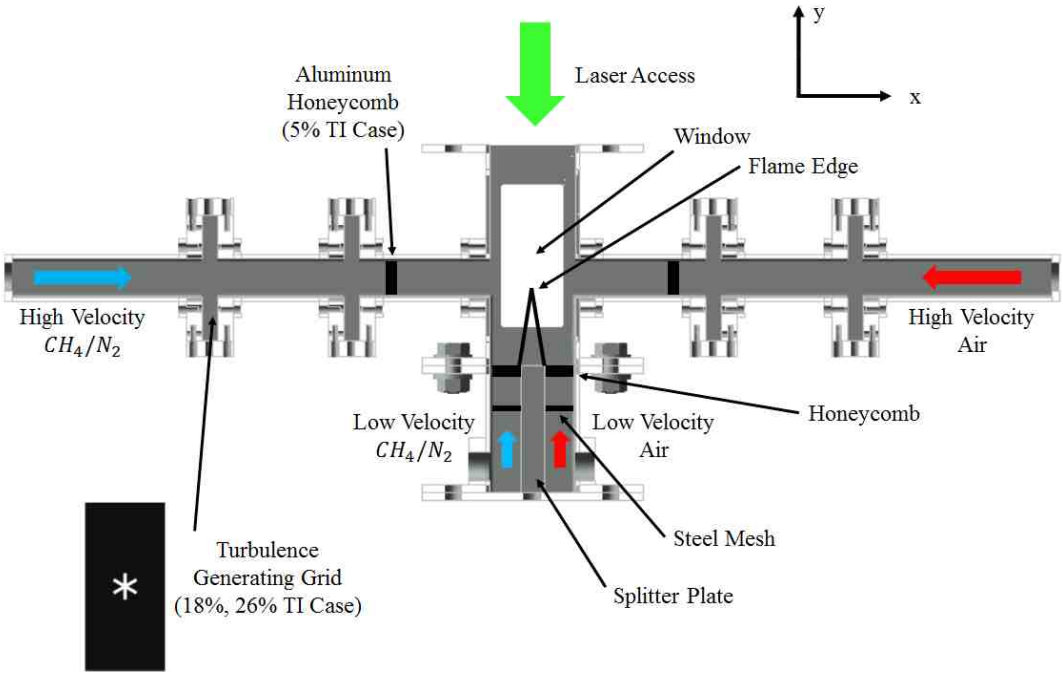

Figure 3.3: Turbulent negative edge burner detailed schematic.

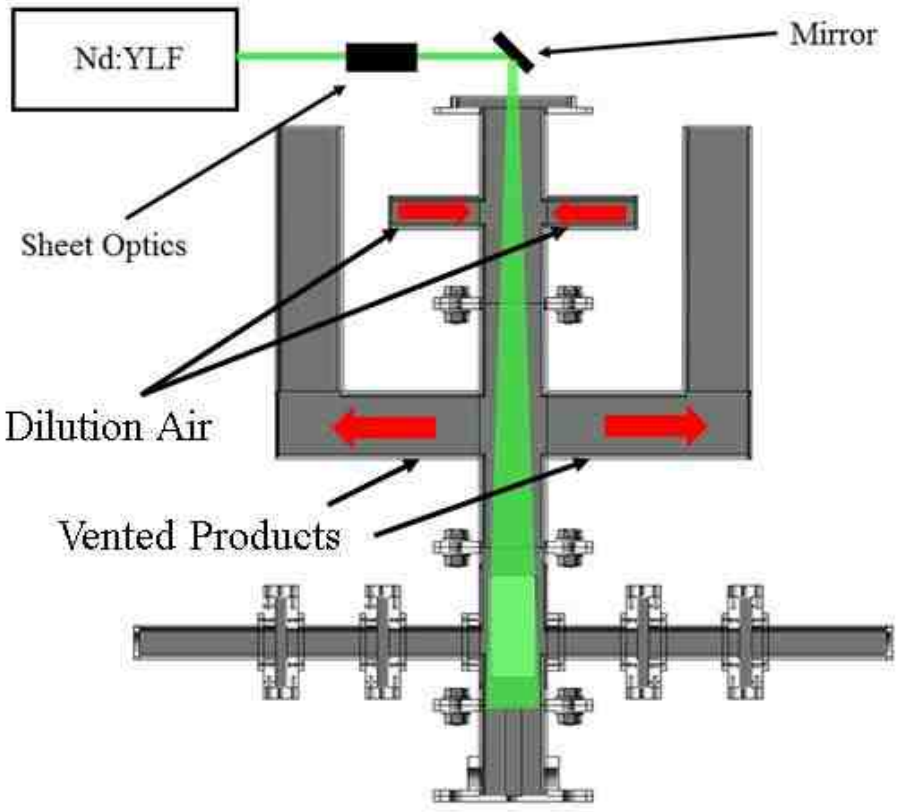

Figure 3.4: Negative edge flame burner with exhaust section depicting the laser access.

The side jets had varying levels of turbulence intensities. Low (~5%) turbulence intensities were achieved by simply placing an aluminum honeycomb flow straightener in the channel. Higher turbulence intensities (18 and 26%) were achieved by removing the honeycomb and instead placing turbulence generating grids in the flow, which were 3D printed using polylactic acid (PLA) filament. The turbulence generating grid, shown inset in Figure 3.3, was designed to have a central jet with 6 slots extending outward, similar to the design used in [78,79]. The grids each had 1 mm wide slots and were 7 mm and 3 mm long from the center of the jet, leading to 84% and 94% blockage ratios, which generated 18 and 26% turbulence intensities, respectively. The integral length scales were measured to be approximately 5 mm for each case. The turbulence properties were measured using particle image velocimetry (PIV), which will be introduced later in this dissertation, with a side jet separately flowing air into the room at the set velocities used in the experiments.

Variations in both the fuel concentration and slot velocity led to different bulk advective heat fluxes flowing through the negative edge. Higher fuel concentrations led to stronger flames, and therefore higher bulk advective heat flux; likewise higher velocities also led to higher advective heat fluxes.

This burner was used in this dissertation to study how turbulence effects flame hole development and negative edge velocities, in Chapter 7.3. Different turbulence intensities were used with similar bulk scalar dissipation rates to study these effects. A stereo-view chemiluminescence experiment was used to obtain the flame velocities and the flow velocity was measured with PIV.

3.4 Premixed Jet in Vitiated Coflow

This burner was designed and built to study stabilization of premixtures being injected into hot vitiated environments such that autoignition may be a dominant stabilization mode. This burner is directly relevant to future combustor technology where premixed fuel-air mixtures are injected into a hot vitiated mixture, in a staged-combustion style. This burner was used in Chapter 8 to perform preliminary experiments, and was further simulated to provide more information about the stabilization.

The burner consists of two coannular nozzles in which the outer nozzle provides vitiated products, while the inner nozzle provides premixed cold reactants, shown in Figure 3.5. A 264.7 mm diameter cylinder was refractory lined with Kast-O-Lite 97L to form a converging nozzle for the coflow. The fuel and air entering both the jet and coflow were well mixed before entering the bottom of the burner. A connector which held the jet and perforated plates in place allowed different jet diameters to be used. The current study utilizes a 3.81 mm diameter jet which runs straight through the burner. The coflow fluid enters through four ports on the bottom of the burner and flows through a series of flow distributors before passing through a final steel perforated plate with an 87% blockage ratio and 1.5 mm diameter holes to stabilize a coflow flame and to act as a flame arrestor. The coflow diameter is 122.5 mm in this region, which then passes through a converging nozzle to create a nearly plug flow velocity profile at the jet exit. The coflow diameter is 50 mm at the exit, leading to a contraction ratio of 6:1 over 70 mm in length. After passing through the converging nozzle, both the jet and coflow exit the burner and are allowed to mix, and the jet was initially autoignited by the hot coflow. The burner is unconfined in the laboratory. All cases in this experiment produced a laminar and steady lifted flame

allowing low speed diagnostics to be used, although parameters can be altered to create turbulent flames.

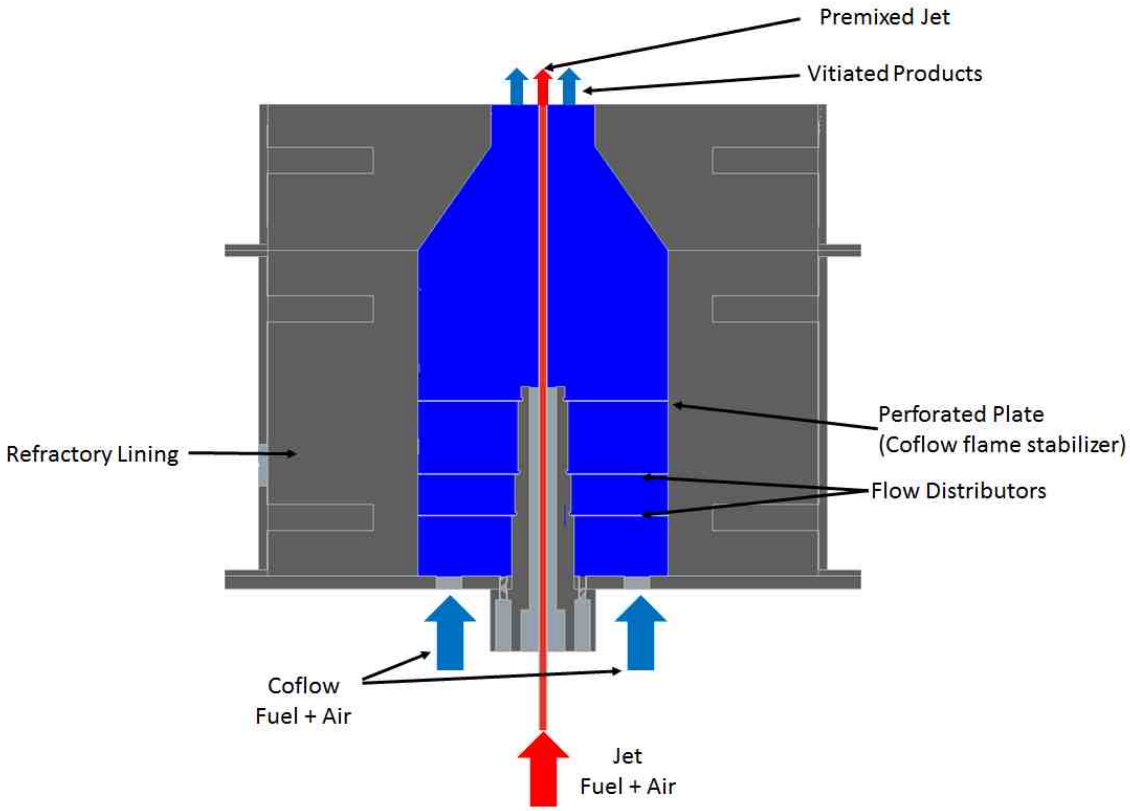

Figure 3.5: Premixed jet in vitiated coflow experimental burner design.

Several boundary conditions were varied in the experiments including ϕ_J and V_J. Ethylene was used as the jet fuel due to the molecular weight being similar to air, while propane was used to create the vitiated products in the coflow. Rayleigh scattering has been used to measure the coflow temperature with ϕ_{Co} at 0.7, which is nominally 1500 K. It should be noted that the coflow temperature was relatively difficult to accurately measure. Accurate temperature measurements were taken with the jet removed which nearly were the adiabatic flame temperature for the coflow upstream conditions. However, when the jet is placed in the burner, the measurements change for two reasons. The jet continuously flows air through it in order to prevent the plastic tubing from melting.

Therefore, the hot coflow transfers heat to the jet which decreases the coflow temperature. Moreover, there is a temperature gradient in the jet and in the coflow near the jet exit and temperature measurements via Rayleigh scattering rely on knowing the local species composition. Near the jet exit this is known, but where the air and coflow fluid begin mixing the species composition is unknown without more complicated measurements. Therefore, the temperature very close to the jet wall cannot be accurately measured since the species composition changes in this mixing layer.

4 Laser Diagnostics

One of the most important developments for understanding reacting flows has been the laser and associated diagnostics, since non-intrusive measurements can be made. For instance temperature measurements can be made by laser scattering, whereas a physical temperature probe, such as a thermocouple, would otherwise be needed and disturb the flow.

Several diagnostic techniques were used throughout this dissertation to provide valuable qualitative and quantitative information. Qualitative measurements were performed using laser induced fluorescence (LIF) in order to determine the boundary between reactants and products, while quantitative measurements were performed for velocity through particle image velocimetry (PIV), and temperature or species concentration via Rayleigh scattering. The background of each of the aforementioned diagnostics will be provided in detail in the following sub-chapters.

4.1 Particle Image Velocimetry

Flow visualization was historically at the forefront of advancing knowledge of fluid dynamics. In the early stages, flow visualization was used purely for qualitative observations, such as flow separation [80] using smoke generators, but with modern equipment can be used for quantitative measurements.

Velocity measurements provide useful information when observing flame-flow interactions, such as strain rates locally extinguishing flames, or more transient turbulent vortices interacting with the flame. PIV measurements performed in this dissertation were all done in a single plane, therefore only two dimensional velocity components were measured. By having a single plane velocity field measurement, velocity component

derivative quantities were calculated in plane leading to strain rate, vorticity, and dilatation measurements in two dimensions.

The working principle in PIV is to seed the flow with small particles which have a sufficiently small Stokes number in order to follow the flow. A visualization of the PIV process is shown in Figure 4.1. A planar light source with a very short pulse, usually a Q-switched laser expanded into a sheet, is used to create Mie scattering off the particles. Mie scattering is an elastic light scattering interaction which occurs when the size of the particle is larger than the wavelength of incident light. Mie scattering signal is directionally dependent [80] and scatters at the same wavelength as the incoming photons. Two subsequent images of the Mie scattering signal, referred to as Mie images, are taken with a known time delay and processed to give particle displacements vectors using cross correlation algorithms which can then be converted into velocity vectors. Modern commercial software is available to calculate the cross correlation in relatively small interrogation windows to produce a vector in each window. The windows therefore makeup the velocity field in a single plane.

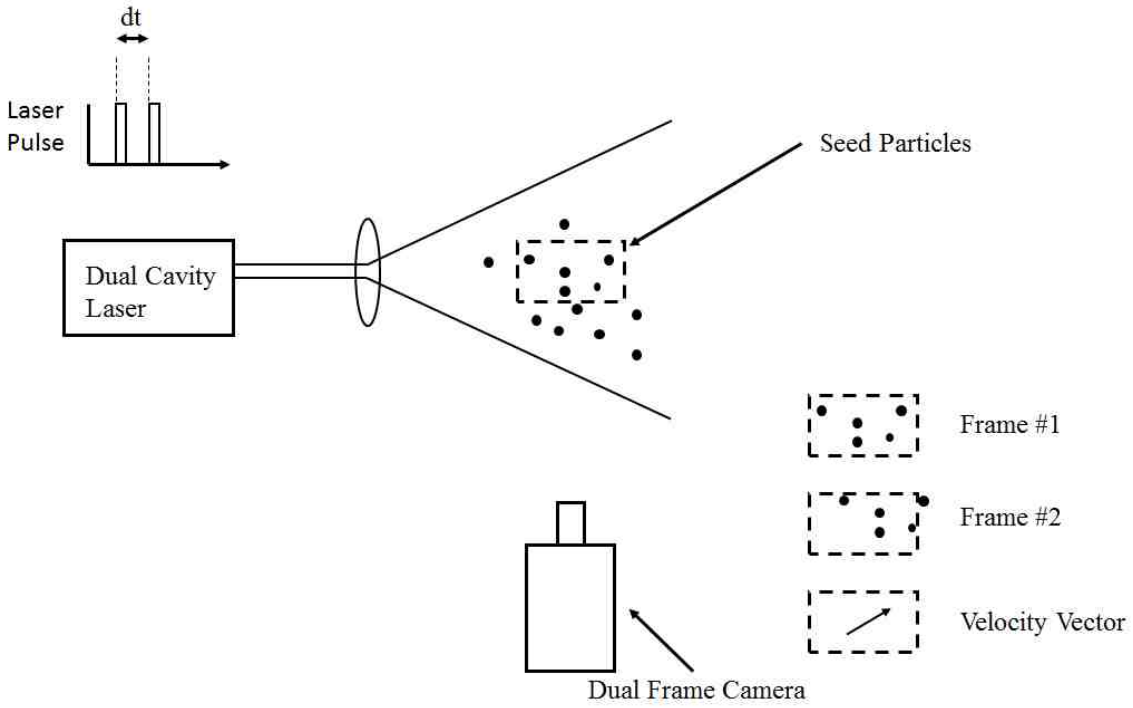

Figure 4.1: PIV principle visualization.

Three dimensional PIV (or tomographic PIV, TPIV) can be conducted, however, much higher laser powers are required since the laser sheet is expanded into a light volume. Although three dimensional vectors are obtainable, there is a significant tradeoff in terms of spatial resolution. For instance 2-D PIV can have spatial resolutions near the Kolmogrov length scale, while TPIV typically has spatial resolutions on the order of 1 mm. Also, multiple high speed cameras are also needed to reconstruct the volume which significantly increases the price of such measurements since eight views are often required to obtain high quality velocity vectors. It should be mentioned that since the large number of views are required, large optical access is often also needed, which is difficult to obtain in enclosed burners and therefore is typically only used in open burner configurations. At times, the fully reconstructed flowfield is not needed, but rather the full strain rate tensor is in a single plane. This situation often calls for dual-plane stereo-PIV (SPIV). SPIV uses

two cameras to resolve the three velocity components in a single plane. Therefore, two SPIV measurements can be conducted in close proximity to one-another to resolve the three velocity components in two dimensions. Thus, the out-of-plane velocity gradient and full three dimensional velocity gradient can be resolved. Since these measurements are more complicated and are not conducted in this dissertation, they will not be further discussed.

There are several details which need to be considered when conducting PIV. Small seed particles are crucial to ensure that the particles sufficiently follow the flow, however, Mie theory predicts that larger particles scatter more light. Therefore, a compromise needs to be made in order to obtain the best contrast between a dark background and the scattered light so high correlations are calculated between neighboring frames to obtain accurate velocity vectors while also having particles which sufficiently follow the flow. The second challenge is having uniform seed density. In order to calculate reliable vectors, approximately 4 particles are needed in each interrogation window [80]. Therefore, interrogation windows with less seed, or none at all, are subject to inaccurate velocity measurements. Over-seeding also becomes an issue since the large amount of seed can disturb the flowfield, and specifically in combustion application can change the stability behavior of flames. Seed can also create problems in confined environment windows since the seed tends to stick to windows which creates an optically thick media such that light rays can no longer easily penetration through the window. Particles also need to be appropriately chosen especially in combustion environments so that the particles can pass through the flame without evaporating or melting. In all experiments conducted in this dissertation, 1 μm diameter particles of Al_2O_3 were used as seed particles. In non-reacting

experiments, water vapor or oil droplets are often used. It should be mentioned that these droplets can be used for combustion experiments, however, the droplets will evaporate and mark a specific temperature prior to the flame. The last detail to consider in PIV measurements is the time delay between subsequent laser pulses. It is recommended that the particles, on average, travel a quarter of the interrogation window length [80] to allow enough particle movement, while not travelling out of the respective interrogation window. Typically, a velocity scale can be used in conjunction with the desired camera spatial resolution and interrogation window size to determine a time delay. However, experiments often have a range of velocities in a single flowfield which can complicate the time delay scaling.

Classic PIV experiments setups consist of two laser cavities with a single camera. Modern PIV lasers are dual cavity lasers, either neodymium doped yttrium aluminum garnet (Nd:YAG), typically for low speed application, or neodymium doped yttrium lithium fluoride (Nd:YLF), typically for high speed application, equipped with a doubling crystal to convert the laser wavelength into the visible range. Low speed systems (<10 Hz) often use charged coupled device (CCD) cameras which utilize interline chip designs which allow two images to be stored on-chip before transferring the image data to a computer. High speed systems (>1 kHz) on the other hand typically use complementary metal-oxide-semiconductor (CMOS) cameras which image at double the sampling frequency to obtain a dual-frame image. In both of these systems the exposure times are relatively large and the laser pulses are offset within the camera exposure. Prior to interline CCD cameras, a camera would expose for the duration of two laser shots which captured

both of the Mie images. In this case autocorrelation algorithms were used instead to calculate the seed particle displacement [80].

PIV was conducted in this dissertation in order to calculate the two dimensional flow dilatation, $\nabla \cdot v$, which was shown to be a scaled advective heat flux in Chapter 5. The propagation velocity of neighboring triple flames with different levels of interaction was measured in Chapter 6, and negative edge flame velocities were measured in Chapter 7.3.

4.2 Laser Induced Fluorescence

LIF is a nonintrusive technique which can be used to qualitatively or quantitatively measure a particular species, and a typical experimental setup is shown in Figure 4.2. The working principle is to excite a particular species to an upper electronic state using a laser. The upper electronic state is more energetic, therefore the molecule absorbs an incoming photon which has energy resonant with a specific electronic energy transition. While in the upper electronic state, the molecule will spontaneously return back to a ground electronic state. In order to return to a ground state, energy must be lost, which can be through the loss of a fluorescence photon with an energy defined by Eq. (4.1), where E is the photon energy, h is Planck's constant, and ν is the photon frequency. Likewise, the laser incident photons must also be resonant with a particular species absorption energy transition defined from Eq. (4.1). A detector can be used to collect the fluoresced photons, which gives information regarding the specific molecule. For imaging application, the laser light can be expanded into a sheet such that planar laser induced fluorescence (PLIF) can be conducted, where a two-dimensional sheet of molecules can be excited and therefore imaged to determine the species location, depicted in Figure 4.2.

$$E = h\nu \tag{4.1}$$

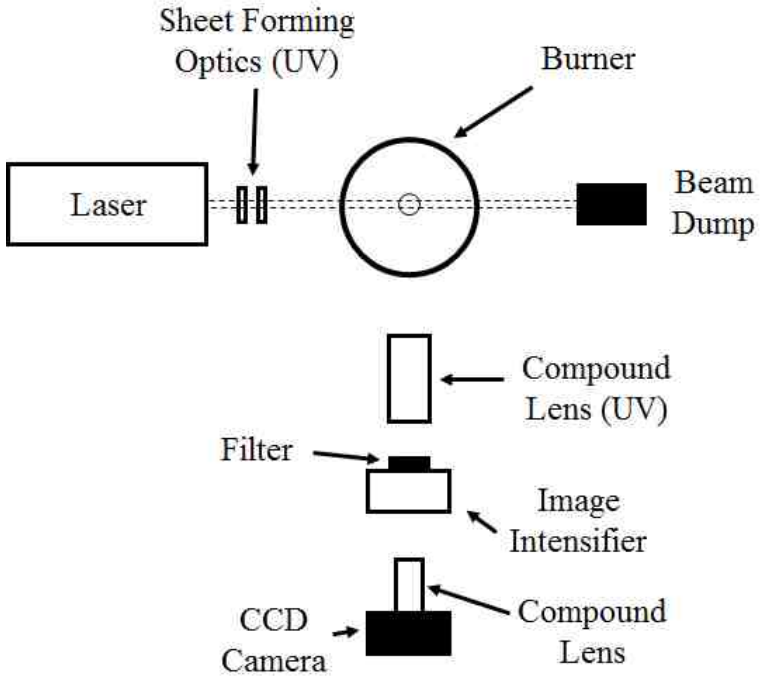

Figure 4.2: Typical optical setup for PLIF.

The previous description is a simplified two step model, but in reality is much more complicated. In the previous description, the incident photons are the same frequency as the fluorescence photons, which is not necessarily the case. The fluorescent photon is dependent on the initial and final electronic, rotational, and vibrational quantum state. The incident photon is well-defined to have the required energy to transition a specific molecule from a ground to excited electronic, vibrational, and rotational quantum state which are all determined before-hand. Once the photon is absorbed, the energy can be redistributed into different vibrational and rotational levels, and even electronic states if excitation is to an upper third or fourth electronic state, which all occur due to either molecular collisions or photon losses. The collisions exchange energy between neighboring molecules which impacts the quantum state of the molecule. Also, the electronic de-excitation can return to

a different ground rotational and vibrational state than the initial one. Each of these processes can affect the fluorescent initial and final states, and therefore changes the energy and therefore frequency of the emitted photon. For this reason, fluorescence is typically collected over a broad range to collect light over many emission transitions to improve the amount of light collected.

Typical PLIF setups require a tunable light source, several optical pieces to redirect and form a laser sheet, and an imaging unit. First and foremost, the optical pieces need to be chosen. Most molecular transitions reside in the ultraviolet (UV) range, and therefore require UV optical components, shown in Figure 4.2. BK-7 glass is often the material in optical pieces which is transparent in the visible range, however, is a strong absorber of UV light. Therefore, other materials such as silica fused quartz is often used for PLIF experiments throughout the experiment, including sheet forming optics, windows, and imaging optics. The tunable light source used in this dissertation was a tunable dye laser which was pumped with an external second laser. Other tunable light sources are used in the literature, for instance optical parametric oscillators (OPO) which uses nonlinear optical setups to change the laser frequency, but will not be further discussed in this dissertation. Typical LIF light sources are Q-switched lasers which only emit light on the order of 10 ns which leads to short snapshot measurements. Without inclusion of other effects, the absorption energy transition is a discrete energy, and therefore is a single photon energy. However, Doppler and collisional broadening make the linewidths of the transition larger, which are dependent on the velocity, temperature, and pressure of the experiment. For most atmospheric combustion application, the spectral absorption linewidth is on the order of tens of picometers. Typically, a single energy absorption

transition is desired, so therefore the laser must have a sufficiently small linewidth such that one energy transition is excited, although, is not always necessary for all experiments.

Extreme laser spectral precision is needed to know which absorption line the laser is tuned to. Dye lasers often need to be calibrated to ensure the correct transition is being probed. Simple flames can be used to sweep the dye laser across a few absorption transitions to calibrate the laser. This can be rather tedious since fairly high spectral resolution is needed. Using the available dye laser and a photo-multiplier-tube (PMT) equipped with a 320 ± 20 nm filter, such a calibration was conducted with 1 picometer precision across half-of-a-nanometer and is shown in Figure 4.3. Although the relative signals are not perfectly aligned it is apparent that the dye laser, shown in green lines, is slightly off from the LIFBASE [81] simulations. Therefore, this known offset can be applied to the subsequent measurements. On a daily basis this is much easier, for instance a few points along the transition of interest can be checked.

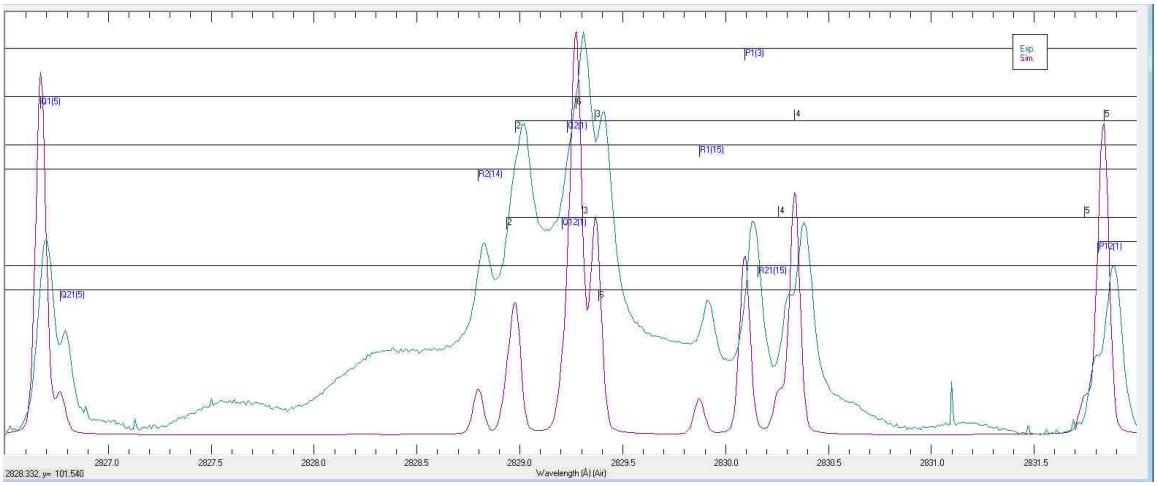

Figure 4.3: OH A-X simulated and experimentally probed transitions using a dye laser. The cyan line represents the experimentally measured signal and the purple line is the simulated signal.

Two dimensional fluorescence is usually imaged using an image intensifier since the relative fluorescence signal is not large enough to be detected with a point-and-shoot

camera, but also transitions the light from the UV spectrum to the visible. Imagine intensifiers typically use the photoelectric effect to create more photons via a high voltage source. Fluorescence signal is typically the only desired signal, which lasts on the order of tens of nanoseconds. Therefore the intensifier is usually gated to small enough time scales (typically 100 – 500 ns) to collect mostly fluorescence signal, as opposed to chemiluminescence or other background signals. On most occasions the intensifier gate width is set to be wide enough to reliably capture each PLIF signal in a day, but also day-to-day. PLIF timing uncertainty on a given day often stems from both the timing unit which syncs the laser and intensifier gate, but also the laser jitter. Typical Nd:YAG time jitter is on the order of 10 ns. On a daily basis the laser delay can change, on average, less than 100 ns. However, in environments with large temperature changes daily may have significant changes. In combustion application, chemiluminescence is always emitted and can be imaged by simply increasing the exposure time. Spectral filters are often used to only collect light over a certain wavelength range to only collect signal from a fluorescence, but also is chosen such that the laser frequency is not collected either to eliminate Mie scattering off of surfaces and particles (therefore reject signal from PIV if conducted simultaneously).

PLIF imaging can provide both qualitative and quantitative information. Qualitative PLIF is used to mark the location of a specific molecule. For instance hydroxyl (OH) PLIF gives information about the boundary between reactants and hot (~1500K) products. Methylindyne (CH) on the other hand is only present in the reaction layer of flames and is useful for giving information regarding where the reaction layer resides. This has advantages over OH PLIF since it is not detectable in the products, but provides much

less signal. Although qualitative PLIF does not directly give quantitative information, image post processing can be performed to obtain quantitative measurements. For instance, the stretch rate and curvature of flames is very useful for fundamental understanding of the flame surface. Other information such as relative flame motion (and therefore velocities) are capable of being measured with qualitative PLIF by determining the distance the flame boundary moved.

Quantitative PLIF is significantly more difficult to perform. The fluorescence equation is given in Eq. (4.2), where F is the fluorescence signal, h is Planck's constant, ν is the laser frequency, c is the speed of light, Ω is the solid collection angle, V is the excited volume, I_ν is the laser energy, N is the population, A and B are the Einstein absorption and emission coefficients respectively, and Q is the quenching coefficient. Because many of the terms are constant in a given experiment, the fluorescence signal is only proportional to I_ν, N, and the LIF efficiency, $\frac{A}{A+Q}$. Although most of these quantities are measureable, Q is very difficult to determine hindering most quantitative LIF measurements. There are ways to estimate Q, but is outside the scope of this dissertation.

$$F = \frac{h\nu}{c}\frac{\Omega}{4\pi}VI_\nu NB_{12}\frac{A}{A+Q}$$
$$F \sim VNI_\nu B_{12}\frac{A}{A+Q} \tag{4.2}$$

Most of the quantitative PLIF measurements obtain either species concentration or temperature. Because the LIF signal is dependent on the population and the transitions are dependent on the temperature, it is a relatively easy to measure concentrations and temperatures in theory. Two line thermometry, which compares the relative LIF signal at two different transitions, gives the ability to measure temperature by comparing peak fluorescence signals over two absorption lines which can be compared to simulations, such

as LIFBASE [81]. Line scanning techniques [82], are techniques similar to line-peak techniques but instead compare the fluorescence area over the entire absorption width which obtains more accurate measurements.

In this dissertation, OH PLIF was used qualitatively to determine the boundary between reactants and products. OH PLIF was used in Chapter 5 to identify the flame position, Chapter 6 to measure triple flame curvatures, and Chapter 8 to identify the high heat release region.

4.3 Rayleigh Scattering

Rayleigh scattering is often used to measure either temperature or species concentration in an entire field. This is different than LIF since LIF can only measure temperature or species concentration where the particular species is located, whereas Rayleigh scattering interacts with all molecules in the flow leading to whole-field-of-view measurements. Similar to Mie scattering, Rayleigh scattering is an elastic light-molecule scattering interaction. However, Mie scattering occurs when the incident light wavelength is smaller than the object size (particles), while Rayleigh scattering occurs when the objects are smaller than the incident wavelength (molecules). Raman scattering occurs in the same size regime as Rayleigh scattering, but is an inelastic scattering process which leads to different scattered wavelengths than the incident one. Therefore, Raman and Rayleigh scattering occur simultaneously, but Rayleigh scattering will scatter at the same frequency as the incident light, while Raman will have shifted frequencies. Mie scattering signal is often orders of magnitude larger than Rayleigh and Raman scattering, and Rayleigh scattering is larger than Raman. For this reason it is important to perform Rayleigh and Raman scattering in clean environments and away from enclosed walls since Mie scattering

can overwhelm the signal and interfere with the Rayleigh and Raman scattering signals, leading to inaccurate measurements.

Rayleigh scattering signal for a single wavelength with multiple species can be expressed in Eq. (4.3), where S is the Rayleigh scattering signal, I_ν is the laser energy at a frequency ν, n is the number density, σ_{mix} is the mixture averaged Rayleigh cross-section, Ω is the collection solid angle, l is the sample length, and ϵ is the collection efficiency. The mixture Rayleigh cross section can then be defined in Eq. (4.4), where X_i is the mole fraction and σ_i is the Rayleigh cross section, where i refers to the ith species. Most applications use Rayleigh scattering to obtain either temperature or species concentration measurements. In Eq. (4.3) for a constant Rayleigh cross section and laser intensity, the scattered signal is proportional to the number density. In constant pressure environments, the temperature is linearly proportional to the number density. Often times, a mixture can be created such that the Rayleigh cross section is nearly constants across the fuel, oxidizer, and combustion products (usually by using various amounts of inert species) and therefore the temperature is proportional to the scattered signal. In other situations, if the pressure and temperature is held constant, then the Rayleigh signal is proportional to the mixture Rayleigh cross section. This is often useful for mixing studies where two streams with differing Rayleigh cross sections are mixed and the respective mole fractions can be extracted. In combustion application, mole fraction measurements are typically only able to be accurately measured on either the unburnt or burnt side of the reaction layer, since the temperature is no longer constant.

$$S = I_\nu n \sigma_{mix} \Omega l \epsilon \tag{4.3}$$

$$\sigma_{mix} = \sum_i X_i \sigma_i \tag{4.4}$$

Unlike LIF, but similar to PIV, the collection wavelength needs to be the same as the laser wavelength. Therefore, Mie scattering needs to avoid walls, seed particles, and dust particles to ensure accurate measurements. For this reason the flow must be free of particles and in most cases be in an open environment without windows. Not only that but measurements need to be taken sufficiently far from burner exits (or metal tubes) so that surface scattering does not interfere with the Rayleigh signal.

Typical Rayleigh scattering experiments consist of a single laser and standard CCD or CMOS camera. Continuous wave (CW) lasers are useful for Rayleigh scattering, but will lead to averaged signals, similar to chemiluminescence. Therefore, Q-switched or diode lasers are superior because the laser pulse durations can be from nanoseconds to femtoseconds which leads to short duration snapshots of the measurements, similar to PLIF. Experiments in this dissertation were taken with a Q-switched Nd:YAG which delivered approximately 300 mJ/pulse. Rather inexpensive cameras and lenses can be used for collection in these experiments since chromatic aberrations are not an issue (since the incident light is a single wavelength) and there is enough signal for a typical camera to capture. However, signal levels are rather low especially with low power lasers, and therefore can be problematic.

In this dissertation, fuel concentration measurements were obtained which subsequently led to fuel concentration gradients and stoichiometric separation distance measurements with respect to interacting triple flames in Chapter 6.

5 Advective Heat Flux Estimation from Velocity Information

5.1 Motivation

5.1.1 Advective Heat Flux Measurements

In order to characterize the type of edge flame, the sign of the advective heat flux through the edge must be measured. Additionally the magnitude of the advective heat flux has been shown to impact the strength of the extinction process and alter the extinction scalar dissipation rate. Thus, local measurements of advective heat flux upstream of and through edge flames is important to understanding flame hole behavior. Direct advective heat flux measurements require knowledge of both velocity and temperature fields as well as the local density and specific heat. Velocity measurements in two dimensions is relatively easy to perform via PIV where imaging of Mie scattering from seed particles in the flow tracks the particle motion [83]. However, many temperature measurements that would be suitable for characterizing temperature gradients, such as Raman or Rayleigh scattering, in the region upstream of a flame edge rely on scattering methods which are weaker than Mie scattering [84]. Two line thermometry can instead be performed simultaneously with velocity measurements, but this usually relies on the presence of intermediate species, such as OH, therefore only giving temperature information within the flame [85]. Moreover, simultaneous PIV and two-color PLIF is a significantly more complicated experimental arrangement.

Omrane *et al.* [86] has developed a technique utilizing thermographic phosphor particles, Mg_4FGeO_6:Mn, to obtain both temperature and velocity measurements simultaneously. In this experiment, two cameras and three lasers were used. One camera was used to capture a double frame image of the particles being illuminated by two

frequency doubled Nd:YAG lasers, which were used for PIV measurements. The second camera was used to capture an image of the seed particles being illuminated by a third harmonic Nd:YAG laser. The fluorescence between 632-657 nm was collected and calibrated to a temperature ratio. One issue with this experiment for application to flame edges is that the flow was only mildly heated, therefore there were not any temperatures near typical flame temperatures, and no large temperature gradients. The second issue is that the temperature was only sampled at the particles leading to limited spatial resolution.

Elliott *et al.* [87] were able to conduct simultaneous temperature and velocity measurements by performing filtered Rayleigh scattering. The experiment was conducted on a variety of different burners to show the applicability across many geometries. The setup consisted of two laser systems; a typical PIV setup and a filtered Rayleigh scattering setup. The filtered Rayleigh system used an injection-seeded frequency doubled Nd:YAG which could deliver up to 650 mJ per pulse with as low as 100 MHz linewidth. An iodine vapor filter was introduced which filtered out the Mie scattering signal while still passing the edges of the Rayleigh signal. The remaining Rayleigh signal could then be recorded for temperature measurements. With each of these techniques $v \cdot \nabla T$ could be measured, but the full advective heat flux would also require estimation of local density and specific heat.

The main focus of this chapter is to examine a technique which can estimate the advective heat flux from PIV without directly measuring temperature or local properties. Each of the other methods described require more complicated setups to measure temperature and velocity simultaneously and have limited utility in terms of spatial

resolution or range of temperature. Moreover, a technique using only PIV can be more easily extended to three dimensional and unsteady applications.

5.1.2 Theory

The flow dilatation can be computed starting from the continuity equation applied to an ideal gas, shown in Eq. (5.1), where p is the absolute pressure, R is the mixture gas constant, T is the temperature, and v is the velocity vector. Under steady state conditions, this simplifies, as shown in Eqs. (5.2) and (5.3) where M is the mixture molar mass. Thus, the flow dilatation is a sum of three terms, an advective temperature, molar mass, and pressure gradient term. Under the low Mach number approximation and by assuming low molar mass changes, the flow dilatation is just impacted by the temperature gradient term as shown in Eq. (5.4). The appropriateness of neglecting pressure and molecular weight terms will be examined using the numerical results, subsequently. It should also be noted that in this derivation, steady state was assumed, but is not necessary in general. If an unsteady flow is examined, the dilatation will include a $\frac{1}{T}\frac{\partial}{\partial t}(T)$ term as well.

$$\frac{\partial}{\partial t}\left(\frac{p}{RT}\right) + \nabla \cdot \left(\frac{pv}{RT}\right) = 0 \tag{5.1}$$

$$\nabla \cdot v = -v \cdot \nabla\left(\frac{1}{T}\right)\Big/\left(\frac{1}{T}\right) - v \cdot \nabla\left(\frac{1}{R}\right)\Big/\left(\frac{1}{R}\right) - v \cdot \frac{\nabla p}{p} \tag{5.2}$$

$$\nabla \cdot v = v \cdot \frac{\nabla T}{T} - v \cdot \frac{\nabla M}{M} - v \cdot \frac{\nabla p}{p} \tag{5.3}$$

$$\nabla \cdot v = v \cdot \frac{\nabla T}{T} \tag{5.4}$$

The term measured by dilatation, $v \cdot \frac{\nabla T}{T}$, referred to here as a scaled advective heat flux, is similar to the full advective heat flux, $\rho c_p v \cdot \nabla T$, but scaled by $\left(\rho c_p T\right)^{-1}$. The relationship between the scaled and advective heat flux and limitations of both molecular weight variations and in using this scaled advective heat flux for assessing edge flames is examined in Chapter 5.3.2.

5.1.3 Dilatation

To the authors' knowledge, there have been no experiments which attempt to use dilatation as a marker for advective heat flux. However, significant theoretical, numerical, and experimental work in the literature has attempted to correlate dilatation to heat release [74,88–103]. In certain experiments, the dilatation was shown to correlate well with the flame shape and used to further process the data assuming this was the flame region [74,97,99]. In work by Mungal *et al.* [99], Mie scattering images used for PIV measurements were shown and there was a clear distinction between the cold reactants and hot products where seed density dramatically dropped. In contour plots of the dilatation, there was a clear Bunsen flame shape which seemed to capture the heat release region. Mueller *et al.* [97] created a premixed flat flame and injected a vortex into the flame in order to observe extinction events. By using dilatation as a flame marker, the initial flat flame was tracked well and was able to give a shape that corresponded to a vortex impinging on the dilatation field. Towards the end of the vortex impingement, there was a clear break in the dilatation field which was attributed to extinction and subsequently led to little dilatation in regions where extinction was observed. In their analysis, there was a similar derivation as presented in this paper which showed that the dilatation is the

convection portion of the energy equation, but the analysis was then used to relate dilatation to chemical heat release and diffusive heat loss.

Najm *et al.* [100] studied dilatation numerically with regards to heat release by injecting a vortex into a premixed V-flame configuration to observe possible extinction events. The authors show that dilatation should be a good flame marker in both magnitude and location for a freely propagating flame. These calculations showed a linear relationship between heat release and peak dilatation rate. In the full numerical calculations, the fully burning flame was well represented by dilatation except that the dilatation field was wider than the heat release. As the vortex impinged on the flame, a region of high curvature locally weakened the flame. Analysis of the largest curvature region of the flame showed that the heat release was lowered slightly below the fully burning rate, but the dilatation significantly dropped in magnitude, concluding that dilatation did not track the heat release region well in high curvature regions. In their analysis of the dilatation field, the authors noted a similar relationship as given in Eq. (5.4) and they showed that the dilatation is a scaled flame displacement speed.

In this sub-chapter, the use of dilatation was examined to characterize the advective heat flux directly via Eq. (5.4). For the application of studying edge flames, this advective heat flux is of particular interest, thus this analysis can apply to studies of propagating and extinguishing flame edges.

5.2 Setup

5.2.1 General Setup

Two burner geometries were used to study the correlation between dilatation and advective heat flux in edge flames. One geometry used a multi-slot burner to enable the

stabilization of a lifted triple flame and the other geometry used a modified counterflow burner to enable the stabilization of an extinguishing edge flame. The lifted triple flame was expected to give positive advective heat flux through the positive edge as in the top edge of Figure 2.5 (a). The modified counterflow burner was used to create a stationary negative edge flame which was expected to give a negative advective heat flux through the edge as in the bottom edge of Figure 2.5 (b).

The positive edge geometry was a slot burner, shown in Figure 5.1 was used in previous work reported in [29] and consisted of five slots to independently control the velocity and mixture concentrations. These five slots were controlled using a ten channel electronic flow bench which could set the flow rate of fuel and air independently in each slot using electronic pressure transducers and commercially available calibrated choked orifices. Each slot had steel mesh and a 1/2" thick, 1/8" cell aluminum honeycomb to distribute and straighten the flow. The five slots were then sent into a 100 mm converging mixing channel which brought the cross section from 75 x 120 mm to 25 x 40 mm. The mixing channel was used to smooth any concentration discontinuities between adjacent slots. The channel was contoured in such a way to create a plug flow velocity profile. The exit of the burner also had a 1/4" thick, 1/16" cell steel honeycomb to straighten the flow and also act as a flame arrestor. In the current study, the five slots were set such that slots 1, 4, and 5 contained pure nitrogen and slot 2 contained a lean, $\phi = 0.4$ methane-air mixture. The third slot was varied between two cases of $\phi = 2.25$ and 4.5, producing two different concentration gradients. The bulk velocity at the outlet was 65 cm/s for both cases. The concentration gradient was varied to produce lifted triple flames with different scalar dissipation rates, and therefore different propagation velocities. Since the mixture was

constant in each slot and laminar, this geometry is two dimensional leading to no out of plane gradients allowing comparisons to two-dimensional simulations.

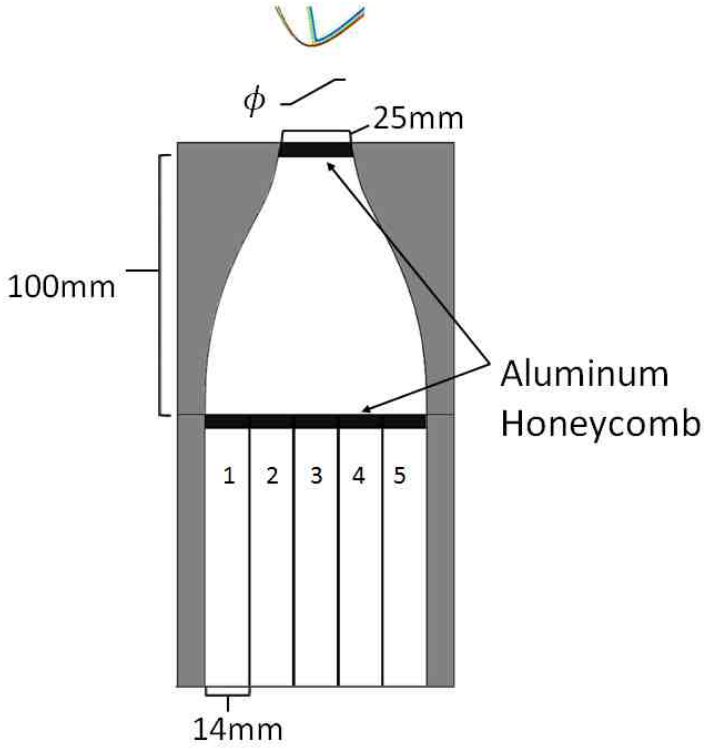

Figure 5.1: Experimental schematic of positive edge slot burner.

The negative edge flame was created using a modified counterflow burner, shown in Figure 5.2, which was used in previous work in [47]. The flow of fuel and oxidizer from the inner nozzles produced a stable counterflow diffusion flame. Typical counterflow burners utilize a nitrogen guard to isolate the flow from boundary effects, while this burner used an outer nozzle to supply the same concentration flows but at a higher velocity to create a radial increase in scalar dissipation and an off-axis extinction point [47]. Flow to this burner was supplied in a similar fashion to the slot burner by the use of the same electronic flow bench. The opposed nozzles were identical with the inner nozzle being 20 mm in diameter, while the outer diameter was 48 mm. There was a 1 mm wall which separated the two flows. A 1/8" cell aluminum honeycomb was placed at the exit of each

nozzle to straighten the flow. The separation distance between the two nozzles was 15 mm. The top nozzles supplied 20% methane, 80% nitrogen by volume, while the bottom nozzles supplied air. The inner nozzle velocity was varied to produce different strength stable burning flames. The three cases examined were 10:40, 15:40, and 20:40, where the notation $V_i{:}V_O$ represents inner (V_i) and outer (V_O) velocities in cm/s. Since the geometry was axisymmetric and laminar, it was compared to two-dimensional simulations as well.

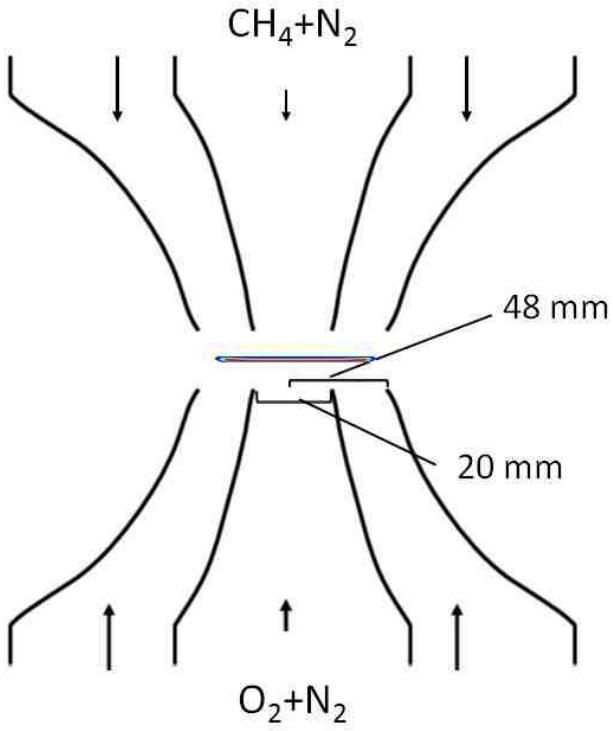

Figure 5.2: Experimental schematic of negative edge counterflow burner.

5.2.2 Numerical Formulation

To assess the validity of the neglected terms in Eq. (5.3) and to compare the full dilatation to full advective heat flux, numerical simulations were conducted for each burner geometry. The simulation methods were similar to work conducted by Carnell *et al.* [48]. Simulations were calculated using ANSYS Fluent 16.1 [104] using a steady, segregated, implicit solver. One step chemistry was modeled using the exponents suggested by

Westbrook and Dryer [105] for the volumetric reaction rate of methane. One-step-chemistry was previously used to simulate these negative edge flames and was shown to sufficiently capture the extinction and edge location. The analysis of dilatation and advection in these simulations is sensitive to the temperature and velocity field but does not require a full kinetic simulation of the internal flame structure. As long as the simulation produces a flame edge in the correct location, the temperature and flow are expected to be well represented. The Semi-Implicit Method for Pressure Linked Equations (SIMPLE) [106] scheme with PREssure STaggering Option (PRESTO!) [104] for pressure interpolation was used for pressure-velocity coupling. Multicomponent and thermal diffusion were utilized, solving the Maxwell-Stefan equations for the diffusive mass flux vector. Mass fluxes were calculated based on binary mass diffusion coefficients, while thermal diffusion was modeled empirically using the composition dependent equation derived from Kuo *et al.* [107]. Fluid properties were modeled as laminar incompressible ideal gases, so mixture thermal conductivity, viscosity, and specific heat capacity were calculated based on ideal gas mixing. Mass and thermal diffusivities, thermal conductivity, and viscosity of individual species were calculated via kinetic theory. This required information of L-J characteristic length and energy parameter which were supplied from the GRI transport database [108]. One step chemistry has a tendency to over predict flame temperatures because intermediate species are neglected, so the specific heat capacity can be altered to give more realistic flame temperatures. The polynomial for the specific heat capacity suggested by Rose and Cooper [109] was used.

The positive edge flame was computed on a two-dimensional domain which was 65 mm wide x 100 mm high centered above the burner exit. Adaptive meshing was used

based on a percentage of the maximum reaction rate to give finer resolution along the triple flame structure, including the diffusion tail. This gave a non-reacting grid spacing of 0.125 mm and a spacing of 32.25 μm near the reaction zone. The boundary condition at the burner exit used a constant velocity of 65 cm/s at 300K to match the experiments. A linear gradient of equivalence ratio was applied as a boundary condition at the slot exit to model the mixing between the adjacent lean and rich slots. Since the goal of this work is to assess how well flow dilatation can be used to predict advective heat flux, it is necessary that the simulated flame shape matches the experiments. Hirota *et al.* [36] showed that the curvature of a triple flame is directly proportional to the concentration gradient below the flame. The linear profiles for the equivalence ratio gradient was varied until the curvature of the predicted flame matched the curvature of the flame in the experiments. This led to fuel mass fraction gradients of 25 and 54.2 m^{-1} for the ϕ = 2.25 and 4.5 case boundary conditions, respectively. Constant pressure boundary conditions were used along the sides and top of the domain at 300K.

The negative edge flame was computed with an axisymmetric grid. The momentum, species, and energy equations were solved using second order upwind discretization. The domain size was 15 mm axially x 38 mm radially. The center 5 mm in the axial direction of the domain, was meshed with cell sizes of 62.5 micron sizes, while the remaining domain transitioned to 0.25 mm mesh size. The inlet velocities were modeled as plug flow profiles at the same velocities as the experiments. The flows were given the same mixture concentrations as the experiments with a temperature of 300 K. The outflow was modeled as a constant pressure outlet. Further details of the

computational methods can be found in work by Carnell *et al.* [48], where this approach was shown to adequately capture the flame shape and extinction location.

5.2.3 Experimental Measurements

Simultaneous PIV and OH PLIF measurements were conducted on both burners, as shown in Figure 5.3. The PIV laser light source was a Photonics neodymium-doped yttrium lithium fluoride (Nd:YLF) dual cavity, high repetition rate laser. The burners were translated in and out of the laser path so that the same laser/imaging setup was used in all cases. An adjustable telescoping assembly was used to focus the beam to a thickness of approximately 1 mm. A diverging ($f = -10\ mm$) lens was attached to the telescoping assembly, which was used to expand the laser beam into a sheet. Mie scattering images were collected using a Vision Research Phantom v611 CMOS camera equipped with an f/2.8, $f = 105\ mm$ compound Sigma f-mount lens. The Mie scattering spatial resolution was approximately 35 pixels/mm. 600 images were captured at 10 Hz to match the speed of the OH PLIF system and time spacing between dual images was varied from 200 to 500 μs apart for the positive and negative edge flames in order to account for flow velocity changes between the different experiments. LaVision Davis 8.2 software was used to control the timing between the camera and laser for the PIV system.

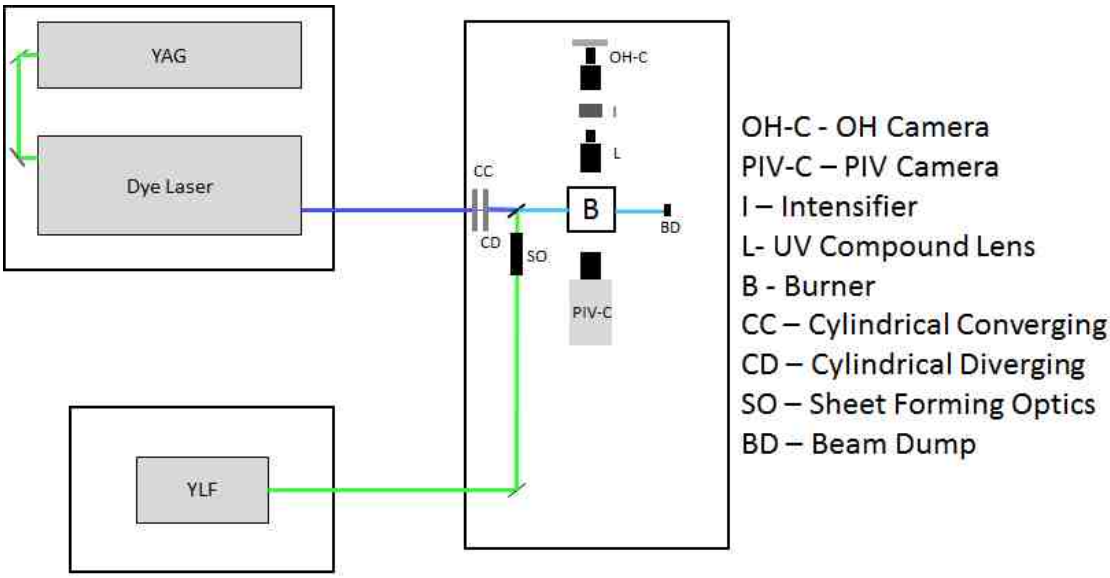

Figure 5.3: Top view of experimental setup.

Mie scattering images were processed with the Davis 8.2 software. The vectors were calculated using a multi-pass cross correlation algorithm. For both the positive and negative edge cases, the algorithm successively worked down from 128 x 128 to 32 x 32 interrogation windows, with 50% overlap giving a vector approximately every 400 μm. This led to an overall spatial resolution of approximately 1 mm. Each velocity field was calculated and subsequently averaged due to small shot-to-shot variations. For the positive edge case, a vector field was calculated for each of the 600 images and subsequently averaged, while the sum of correlations function was used in the negative edge case due to much lower seeding density. The negative edge flame is sufficiently steady to enable correlation averaging.

Aluminum oxide particles were used to seed the flows of interest. The particles were about 1 μm in diameter. In the positive edge case, only the rich and lean slots were seeded, while only the inner nozzles were seeded in the negative edge case. All of the flow

that passes through the flame edge originates from the inner nozzle so this is sufficient for analysis of the advective heat flux at the flame edge.

OH PLIF measurements were simultaneously conducted with PIV measurements. A 282.67 nm beam was produced by pumping a Sirah Cobra-Stretch dye laser with a 300 mJ, 532-nm beam from a frequency doubled SpectraPhysics QuantaRay neodymium-doped yttrium aluminum garnet (Nd:YAG) LAB 170-10 laser. This beam was used to excite the $Q_1(5)$ transition in the $A^2\Sigma^+ \leftarrow X^2\Pi(1,0)$ band of OH. The $Q_1(5)$ transition was chosen due to the low temperature sensitivity from 1000 – 2500 K. The beam was formed into a sheet with less than 1 mm thickness. The beam was then sent through a dichroic mirror to overlap the PIV laser sheets. The PLIF signal was imaged using a Photonis XX1950LP image intensifier, which had a spectral range from approximately 230 to 800 nm. The light was directed to the intensifier using a Universe Kogaku (America) Inc. UV 1054B lens. A filter was attached to the intensifier which had a spectral range of 320+/- 20 nm. A Mightex CGN-B013-U camera acquired images from the intensifier which was triggered with the laser.

The imaging cameras were on opposite sides of the burner and a thin calibration plate was aligned with the laser sheet and imaged from both sides. Davis 8.2 was used to obtain a spatial grid for both cameras, allowing the PIV and PLIF images to be overlapped.

5.3 Results

5.3.1 Qualitative Observations

5.3.1.1 Positive Edge Flame

The positive edge flame is stabilized by partially premixed flame propagation against a concentration gradient in which the lowest point of the flame resides at the

stoichiometric mixture fraction. Figure 5.4 shows the simulated temperature field of the ϕ = 2.25 case with overlaid streamlines. The typical triple flame structure of two premixed branches and a diffusion tail was observed in the heat release distribution. The advective heat flux field, $\rho c_p v \cdot \nabla T$ shown in Figure 5.5 (a), can be compared against the temperature distribution to gain a more complete understanding of the flame. Since this is a forwardly propagating flame front, similar to the upper edge flame in Figure 2.5 (a), a positive advective heat flux and therefore a positive dilatation are expected. Moreover, the advective heat flux at the lowest point on the triple flame has the largest advective heat flux due to this being the point with the largest temperature gradient. Going outward along the two premixed branches, the advective heat flux decreases as both the temperature gradient and the velocity through the flame decreases. Downstream of the flame base, there is little advective heat flux due to the negligible temperature gradients along the streamlines. Although there is additional heat release from the diffusion branch, the streamline that originates from the stoichiometric triple point follows along this stoichiometric contour such that the diffusion branch also has negligible advective heat flux. Overall, the only advective heat flux is along the flame base and is positive with a maximum at the stabilization point and decreasing values along the lean and rich premixed branches.

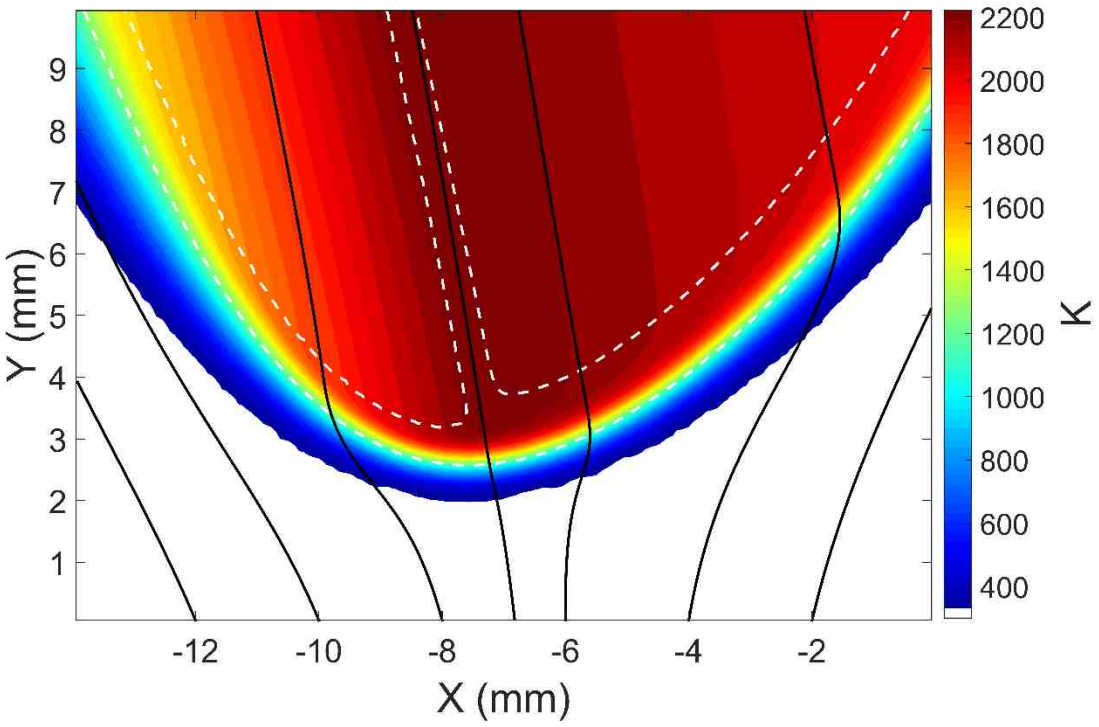

Figure 5.4: Numerical temperature field of positive edge, $\phi = 2.25$ case with streamlines. The white, dashed contour represents the 1% reaction rate contour to indicate the triple flame structure.

The advective heat flux and dilatation for the positive edge flame is shown in Figure 5.5 (a) and (b) respectively for the ϕ = 2.25 case. In these plots, streamlines are included to show how the flow goes through the flame. The 1% contour of reaction rate is also plotted to show the relative location of heat release to both the advection and dilatation. There are clear structural similarities between the advective heat flux and the dilatation. First, the advective heat flux, and therefore dilatation, are positive everywhere due to the fact that along the flame base the streamlines pass from cold reactants to hot products. The largest magnitude dilatation and advective heat flux are on the upstream side of the peak heat release and the location of largest dilatation also produces the largest advective heat flux along the streamline which passes through the triple point on the tribrachial flame structure. This point along the flame base corresponds to a stoichiometric mixture fraction,

and therefore the maximum temperature. Looking outward along the premixed flame branches, there is a decrease in advective heat flux and dilatation due both to the temperature decreasing away stoichiometric conditions and to the lower velocity through the flame. Downstream of the flame base there is no dilatation, consistent with the advective heat flux being zero.

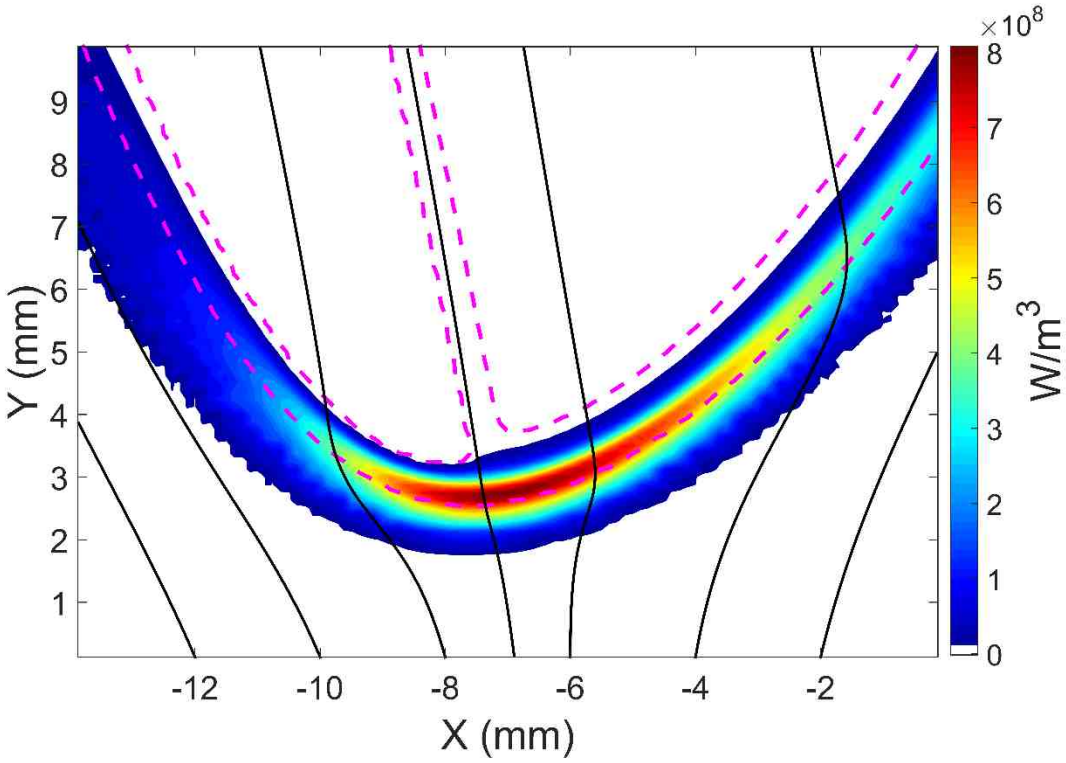

(a)

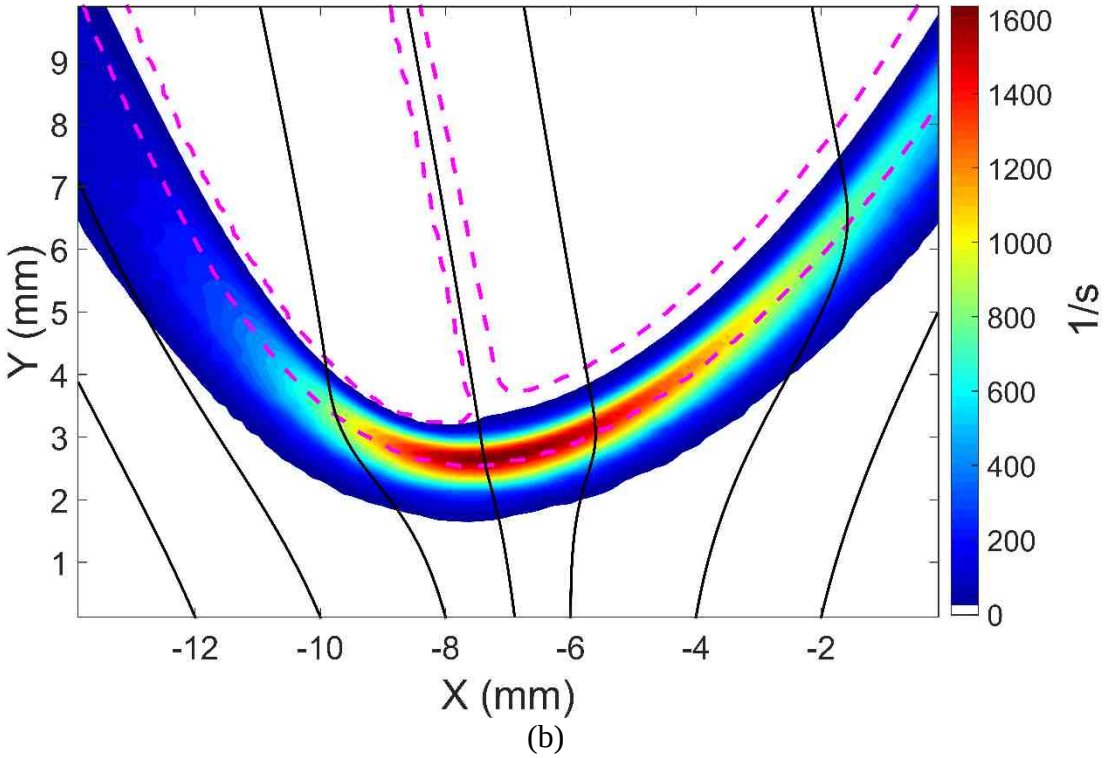

(b)

Figure 5.5: Calculations of (a) advective heat flux and (b) dilatation from numerical results in positive edge, ϕ = 2.25 case, with 1% of the maximum reaction rate plotted with a dashed contour and solid lines representing streamlines.

5.3.1.2 Negative Edge Flame

For the negative edge case, the inner nozzles use low velocity flow to produce a standard counterflow diffusion flame. The outer nozzles use the same mixture composition but at a higher flow rate. This produces a radial increase in scalar dissipation creating an off-axis extinction point as shown in the simulated temperature field of Figure 5.6 for the 15:40 case. The advective heat flux field can be compared, shown in Figure 5.7 (a). This can be identified as an extinguishing front, similar to the lower edge of Figure 2.5 (b). There are three major regions with an advective heat flux component which can be described by either flow into or out of the flame. The flow going into the flame from the inner nozzles produces a positive advective heat flux because the streamlines are passing from cold reactants to hot products. Also, the bottom of the domain, where the oxidizer is entering the flame, had a larger magnitude in advective heat flux than the top due to where the flame sits relative to the stagnation plane. Radially outward, as the streamlines flow through the negative edge, the flow is from hot products to a colder region, which produces a negative advective heat flux.

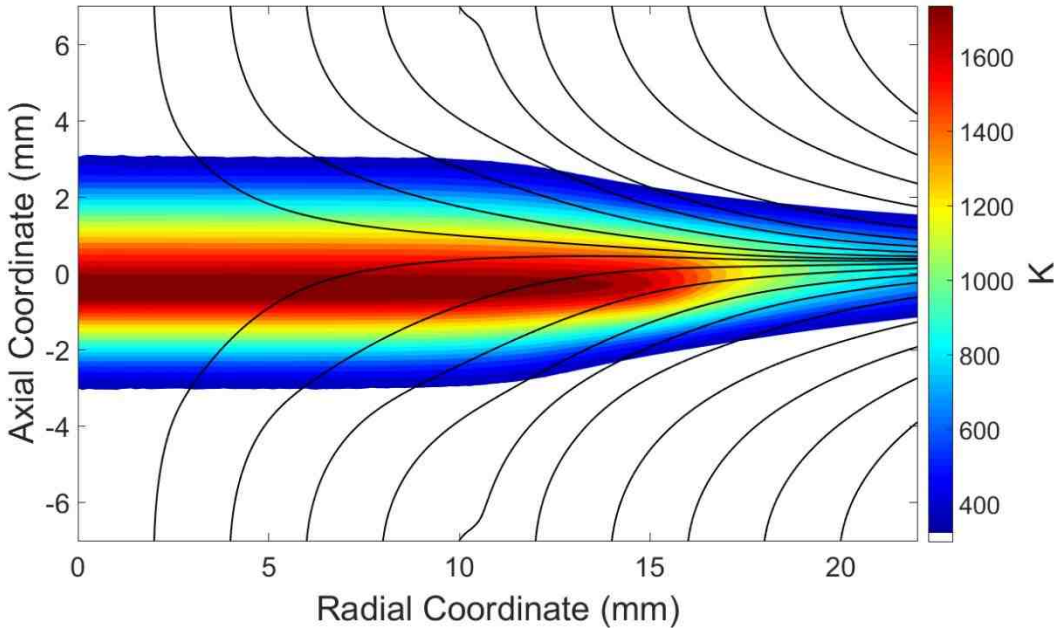

Figure 5.6: Numerical temperature field of negative edge 15:40 case in the counterflow burner with streamlines.

The advective heat flux and dilatation were calculated in the whole numerical domain of the 15:40 case and shown in Figure 5.7 (a) and (b) with streamlines and a 1712 K contour representative of where the extinction edge occurs [48]. There are clearly two signs of advective heat flux and dilatation in different regions of the flame, either entering or exiting the flame. Above and below the flame resides positive advective heat flux and dilatation. Radially outward towards the negative edge there is a clear transition to a negative advective heat flux due to the flow going from hot products to cold reactants at the extinction point. Similarly, there is a transition to a large negative dilatation structure. Clearly, the qualitative structures of the advective heat flux are well represented by the dilatation in this counterflow diffusion flame and through the negative edge.

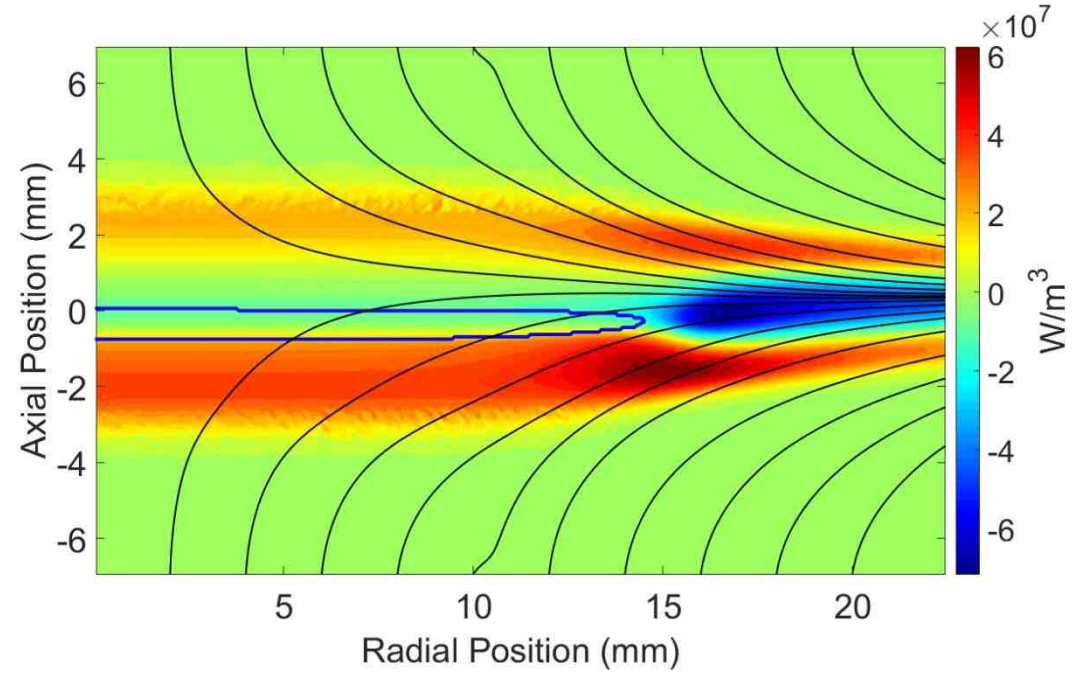

(a)

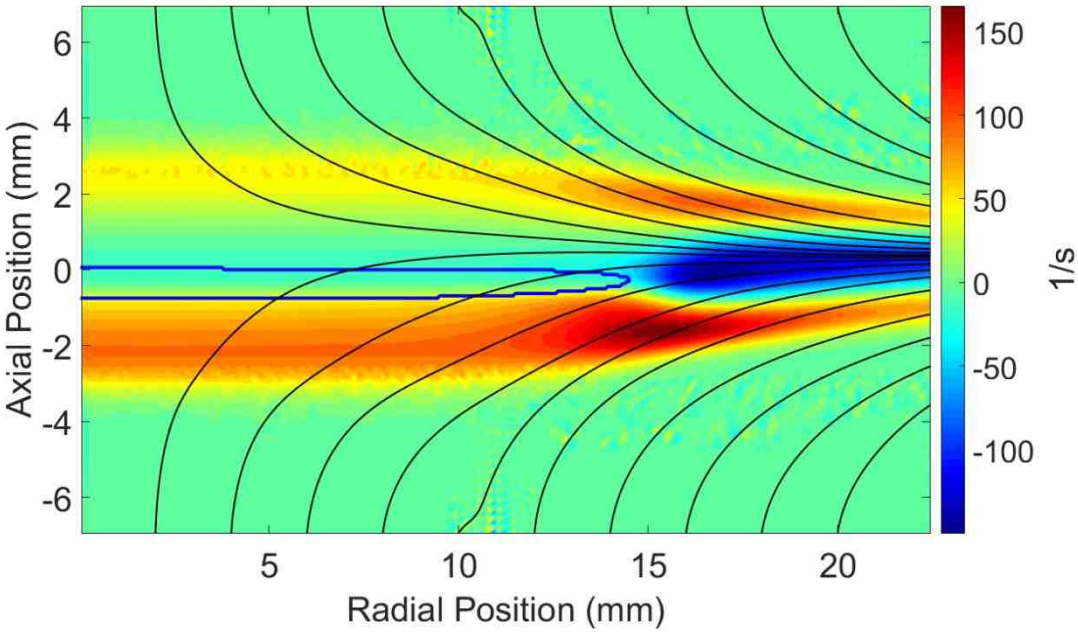

(b)

Figure 5.7: Calculations of (a) advective heat flux and (b) dilatation plotted with streamlines and a 1712 K temperature contour in the numerical negative edge 15:40 flame domain.

Negative dilatation is an interesting observation that had not been given much attention in the literature. Gamba et al. [94] performed an experiment using volumetric

PIV and OH PLIF on a turbulent jet in coflow. The OH PLIF measurements provided a two dimensional end view slice of where flame was located, while the volumetric PIV gave the full three velocity components allowing all nine of the velocity gradient terms to be calculated. In particular, the full dilatation was calculated experimentally. Some useful observations could be made as to possible flame holes or flow going through the flame in the dilatation image. However, the sign of the dilatation at flame boundaries along with the velocity was not discussed in detail.

5.3.2 Negligible Terms

In Chapter 5.1.2, the dilatation was shown to be directly related to a scaled advective heat flux by assuming that gradients in the molecular weight and pressure were negligible in comparison to the scaled advective heat flux. The numerical simulations give the ability to directly calculate the four terms in Eq. (5.3) to show the relative importance of each, validating Eq. (5.4). Figure 5.8 (a) shows the calculation of terms in Eq. (5.3) along the streamline which passes through the maximum dilatation in the positive edge flame with an equivalence ratio of 2.25, while Figure 5.8 (b) shows the same calculation in the negative edge burner along the maximum temperature radial line for the 15:40 case.

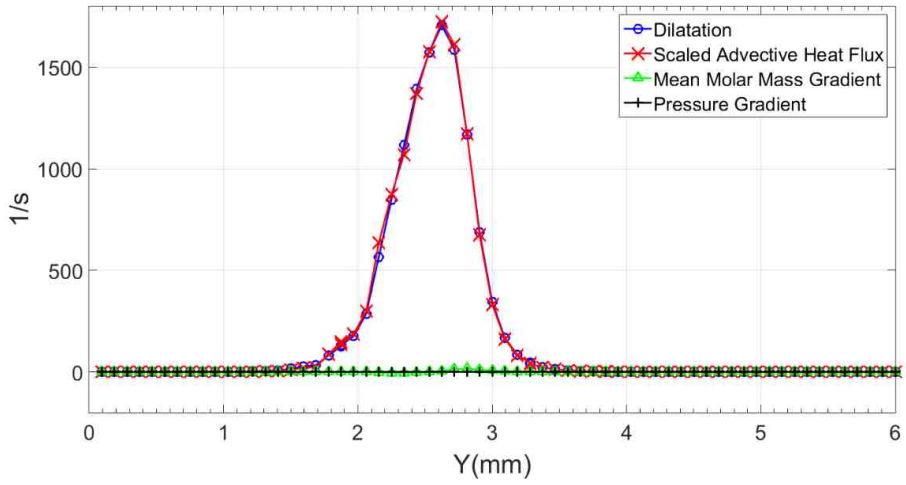
Dilatation
Scaled Advective Heat Flux
Mean Molar Mass Gradient
Pressure Gradient
1/s
Y(mm)

(a)

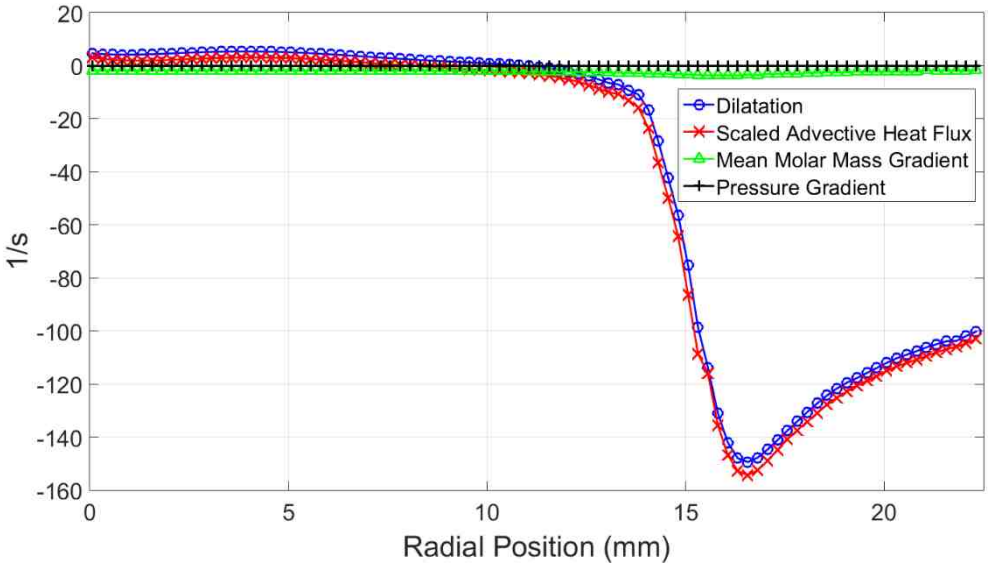
Dilatation
Scaled Advective Heat Flux
Mean Molar Mass Gradient
Pressure Gradient
1/s
Radial Position (mm)

(b)

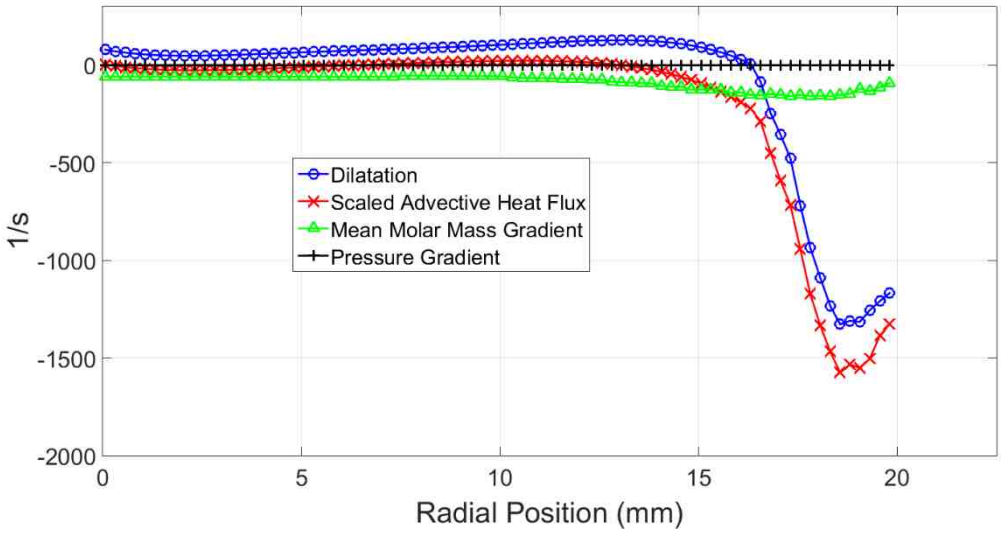

(c)

Figure 5.8: Calculation of four terms in Eq. (5.3) in the (a) positive edge along the streamline passing through the maximum dilatation point, (b) negative edge along the maximum temperature radial line of methane diluted with nitrogen, and (c) negative edge flame along the maximum temperature radial line with undiluted methane.

In Figure 5.8 (a) there are no spatial gradients in any of the four terms upstream of the flame base, therefore each term will be zero. As the streamline passes through the flame, the scaled advective heat flux and dilatation increase. The mixture molar mass and pressure gradient terms are negligibly small compared to the dilatation and scaled advective heat flux terms in the calculations. The peak dilatation value differed from the scaled advective heat flux by less than one percent. The maximum molecular weight and pressure gradient terms were each less than 1% of the peak scaled advective heat flux term. As the streamline passes through the flame and continues along the diffusion flame branch there is no advective heat flux or dilatation.

Figure 5.8 (b) shows the terms from Eq. (5.3) along the maximum temperature contour going radially outward in the negative edge flame. The flame is burning in a stable state near the centerline, which is simply a balance between heat release and diffusive heat loss leading to very small advective heat flux. This is true until a radial position

approximately 15 mm from the centerline where the flame begins to extinguish. After this region, there is a negative advective heat flux and dilatation. In this case, the mixture molar mass and pressure gradient terms are again negligible. The minimum dilatation was found to differ from the scaled advective heat flux by 3%. The minimum mixture molar mass and pressure gradient terms were approximately 2.5% and 0.2% of the minimum scaled advective heat flux term, respectively.

In the current study, the positive edge flame uses undiluted fuel that partially premixes with air upstream of the flame base. Thus it represents a practical partially premixed flame. However, the negative edge flame is highly diluted with nitrogen such that the molecular weight does not vary significantly throughout the flowfield. In order to assess the magnitude of molecular weight changes in undiluted fuels, a negative edge flame simulation was computed with pure methane from the fuel stream with the inner velocity set to 1 m/s and the outer velocity to 4 m/s in order to create a negative edge flame. Note that these conditions cannot be run in the experiment due to flame unsteadiness, but the simulation results can still be useful to examine larger variations in molecular weight. Figure 5.8 (c) shows a radial slice, similar to Figure 5.8 (b), with the undiluted fuel. In this case, the approximately 80% difference in the fuel and air molecular weights results in a 10% difference between the maximum dilatation and scaled advective heat flux.

5.3.3 Quantitative Observations

5.3.3.1 Positive Edge Flame

Since the qualitative structures and related terms of the dilatation matched the scaled advective heat flux well, a quantitative comparison to the full advective heat flux was also studied. The streamline passing through the maximum dilatation was sampled for

both positive edge numerical studies. For this comparison, the dilation (1/s) as would be measured is compared to the advective heat flux including density and specific heat (W/m^3). These quantities from the simulation were normalized by the maximum respective value in the field between both cases to compare profiles and the streamlines were sampled at the same distance upstream of the flame base for both cases as shown in Figure 5.9. The magnitude of the normalized quantities show excellent correlation. The widths of the advective heat flux are slightly thinner than the dilatation. The magnitudes at the peak location show a similar trend between the advective heat flux and dilatation. Note that the increase in concentration gradient between the ϕ = 2.25 and 4.5 case results in a higher curvature at the flame base and a thinner triple flame structure. However, since the streamline through the triple point is still at a stoichiometric mixture fraction for both cases, the peak temperature, the local flame speed, the advective heat flux and the dilatation show no differences between the two cases. In both cases, the dilatation is an excellent marker for advective heat flux in the positive edge numerical flame.

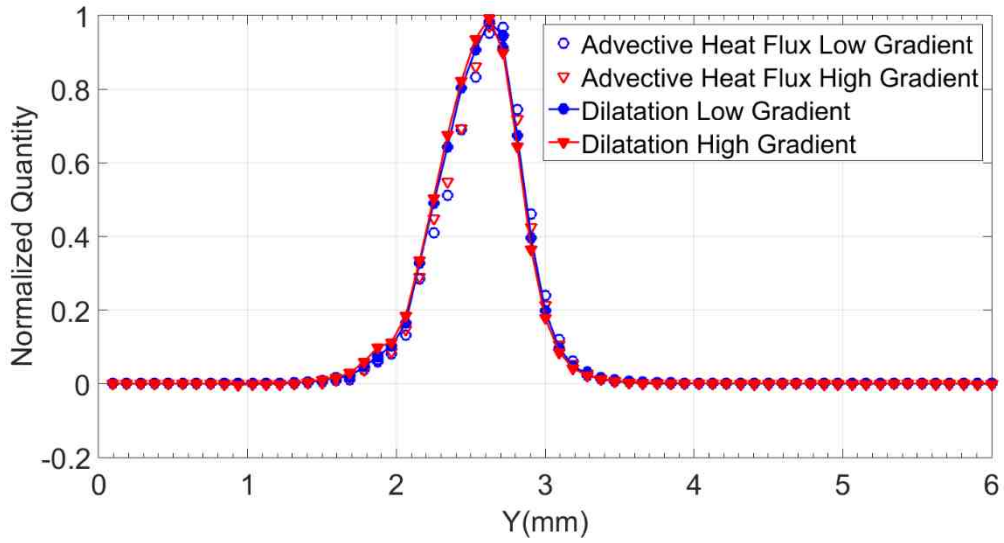

Figure 5.9: Normalized advective heat flux and dilatation sampled along a streamline passing through the maximum dilatation point in both of the positive edge numerical studies.

5.3.3.2 Negative Edge Flame

Profiles of the full advective heat flux and dilatation in the negative edge flame were next quantitatively compared in both the axial and radial directions, shown in Figure 5.10 (a) and (b) respectively. An axial slice of the advective heat flux and dilatation at a radial position of 8 mm from the centerline were sampled and compared for the three boundary conditions. All of the profiles were normalized by the maximum value in each of the three cases, which was the oxidizer side (negative values of axial position) peak magnitude in the 20:40 case. The profiles show excellent agreement between the two quantities in all three cases. The largest advective heat flux and dilatation magnitudes occurs in the 20:40 case and decreases as the inner velocity is decreased, likely due to the lower strain rate broadening the preheat regions. The magnitudes of the advective heat flux and dilatation are larger on the oxidizer side than the fuel side in all cases, which again shows consistent results. The profiles on the oxidizer side also seem to be wider for the

10:40 case and decrease in width as the inner velocity is increased. The largest difference is that the dilatation has a slightly larger slope in the regions near the flame for each case. This could be due the negligible terms being slightly more important in those regions, but still negligibly small.

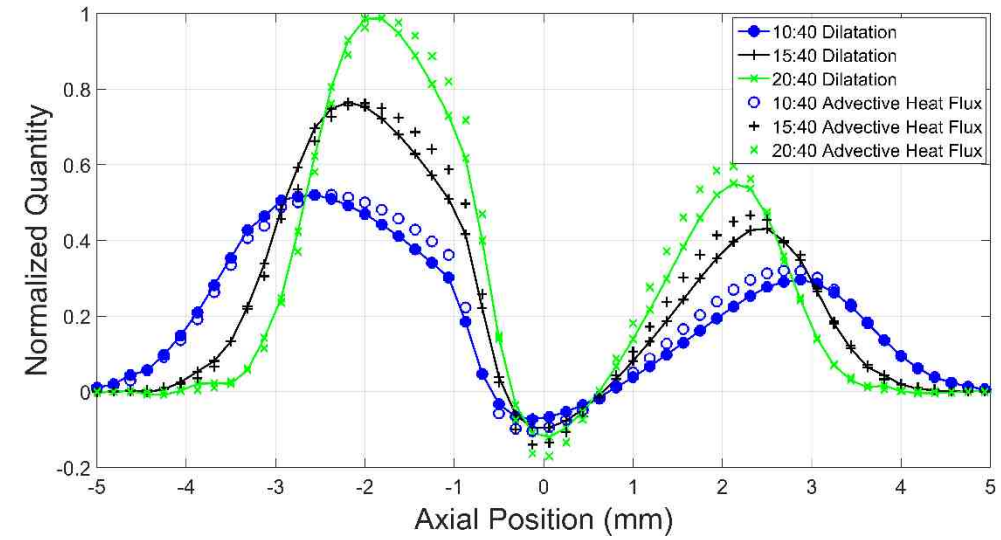

(a)

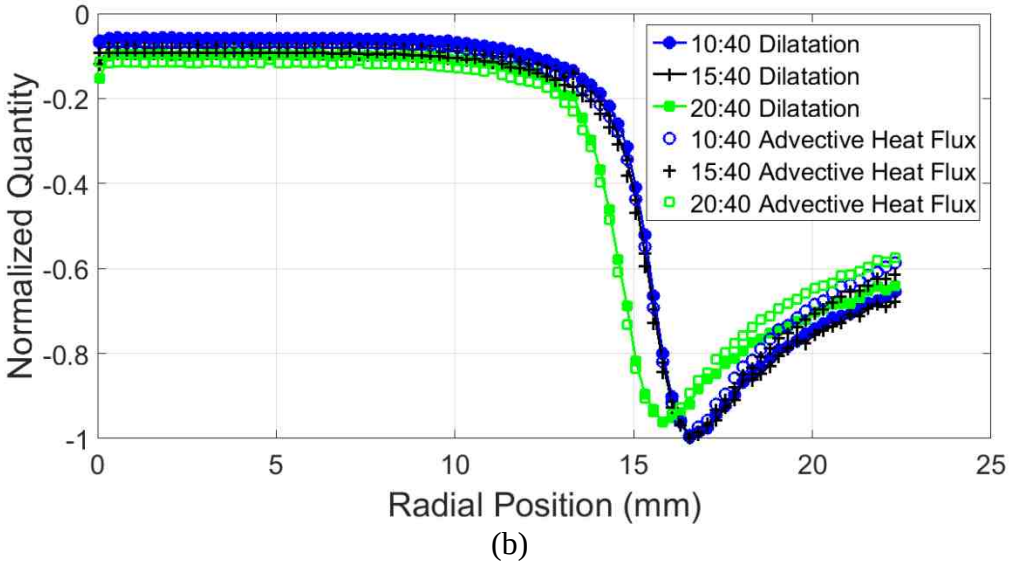

(b)

Figure 5.10: Profiles of (a) axial and (b) radial slices of advective heat flux and dilatation in the negative edge 10:40, 15:40, and 20:40 cases normalized by the (a) maximum and (b) minimum value in all of the cases.

For each case, a radial slice was taken along a line of minimum dilatation at each radial position, shown in Figure 5.10 (b). This sampling technique was chosen (as opposed to sampling along a stoichiometric contour) because it can be easily replicated in the experimental profiles compared subsequently. The profiles were normalized by the minimum respective value across all three cases. The figure again shows excellent agreement between advective heat flux and dilatation. Near the fully burning region (radial positions less than 10 mm) there is a small negative dilatation, but as the radial position gets closer to the negative edge near 15 mm there is a large drop in both advective heat flux and dilatation, since flow is going from hot products to cold reactants in this region. As the inner flame is weakened by increasing the inner velocity (for the 20:40 case), extinction occurs sooner in the outer flow thus the negative edge recedes towards the centerline. Overall, the numerical advective heat flux and dilatation show excellent qualitative and quantitative agreement, leading to the dilatation being a sufficient marker for advective heat flux in the negative edge flames as well. Note that the agreement between dilatation, which was shown to be related to scaled advective heat flux, and the full advective heat flux from the simulations implies that the scaling factor, $\left(\rho c_p T\right)^{-1}$, does not significantly vary. In fact, this scaling factor is constant within 5% for conditions where the temperature is greater than 1000 K, including through the flame edge. Where the scaling factor has larger variations into the fuel and air streams, there is little advective heat flux. This suggests that the simple measurement of dilatation can be used for assessing advective heat flux through a flame edge qualitatively and that only a calibration would be needed to make the measurement quantitative within the uncertainties caused by the impact of molecular weight and smaller variations in $\left(\rho c_p T\right)^{-1}$.

5.3.4 Experimental Results

5.3.4.1 Positive Edge Flame

The numerical simulation showed that dilatation can represent advective heat flux within better than 3% for the case of a diluted fuel. In this sub-chapter, PIV measurements were examined for the flame edge cases to test the accuracy of applying this approach experimentally. Simultaneous OH PLIF was used to identify the flame edge location. The dilatation field from PIV with streamlines and an OH edge contour set at 30% of the maximum OH fluorescence signal is shown in Figure 5.11 for the ϕ = 2.25 case. The OH measurements here are not needed for the determination of dilatation, but are used only to help identify the flame edge and interpret the resulting velocity gradient measurements. The dilatation structure is similar to that shown in Figure 5.5 (b). The flame base where the triple point is likely located has a peak dilatation value due to this being the largest advective heat flux. Going outward from the flame base along the premixed flame branches there is a decrease in dilatation, similar to previous advective heat flux observations, due to the temperature decreasing and the velocity through the flame also decreasing. Downstream of the flame base, there is no dilatation structure including in the region of the diffusion flame branch as previously discussed.

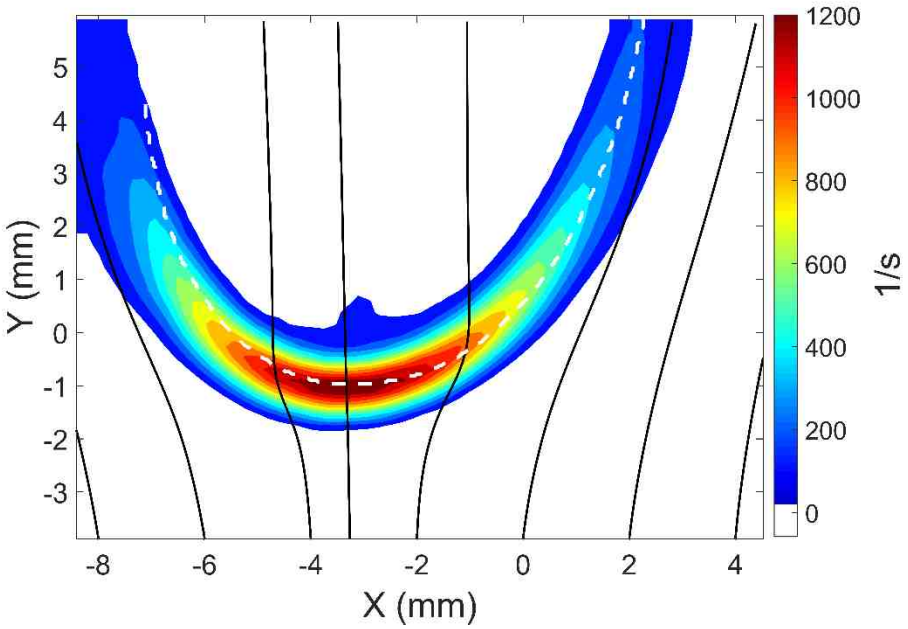

Figure 5.11: Dilatation field of positive edge ϕ = 2.25 case with streamlines in solid black and 30% OH contour in dashed white.

The location of the dilatation can be compared the OH contour as well. The beginning of the OH contour should show approximately where the reaction zone is beginning. In the dilatation field shown in Figure 5.11, there is clearly a dilatation structure just upstream of the OH edge. This shows that there is preheating upstream of the flame base, due to diffusion heat loss from the reaction zone. Thus, the measured dilatation shows good structural correlation to the advective heat flux, especially near the triple point.

Figure 5.12 shows the dilatation sampled along the streamline which passes through the maximum dilatation point for both positive edge flame cases. The peak dilatation magnitude differs by approximately 15% between the two cases. Downstream of the large dilatation region should produce no dilatation because there is no advective heat flux, though there is a clear slightly positive dilatation downstream of the flame base. Since the flame lift off height oscillate slightly and these measurements are averaged, the peak dilatation is affected by this small motion. If the dilatation is integrated across the flame,

the two cases differed by 2%, leading to the total dilatation being similar between the two flame curvature cases.

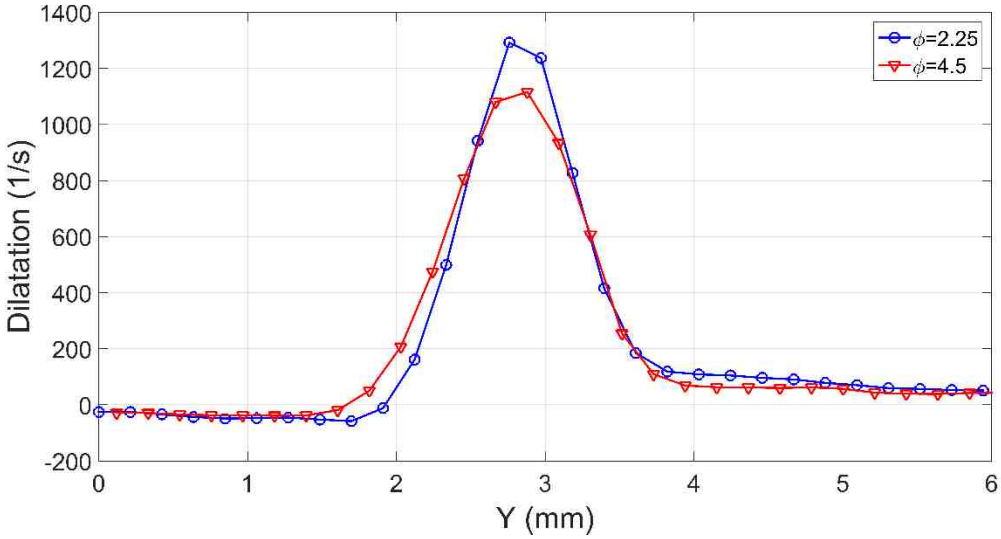

Figure 5.12: Dilatation sampled along the streamline passing through the maximum dilatation point in the experimental positive edge ϕ = 2.25 case.

5.3.4.2 Negative Edge Flame

Experimental dilatation measurements were compared in the negative edge 15:40 case by using PIV and OH PLIF. The dilatation field with streamlines and the 30% OH contour is shown in Figure 5.13. It was noted earlier than only two flows were seeded, both inner nozzles, due to these being the only flows which passed through both the positive and negative dilatation regions. Thus, the data is truncated along the streamline that borders the inner and outer nozzles. Qualitatively, there is good agreement between the structures shown in the numerical results and experiment. As flow comes from the two nozzles it creates a diffusion flame with two positive dilatation regions surrounding it axially. The dilatation represents heating of the respective flow entering the flame. Looking farther outward in the radial direction, there is a clear extinction edge flame

occurring along the OH contour near 20 mm radially outward from the centerline with negative dilatation present through the edge. This is consistent with the numerical results.

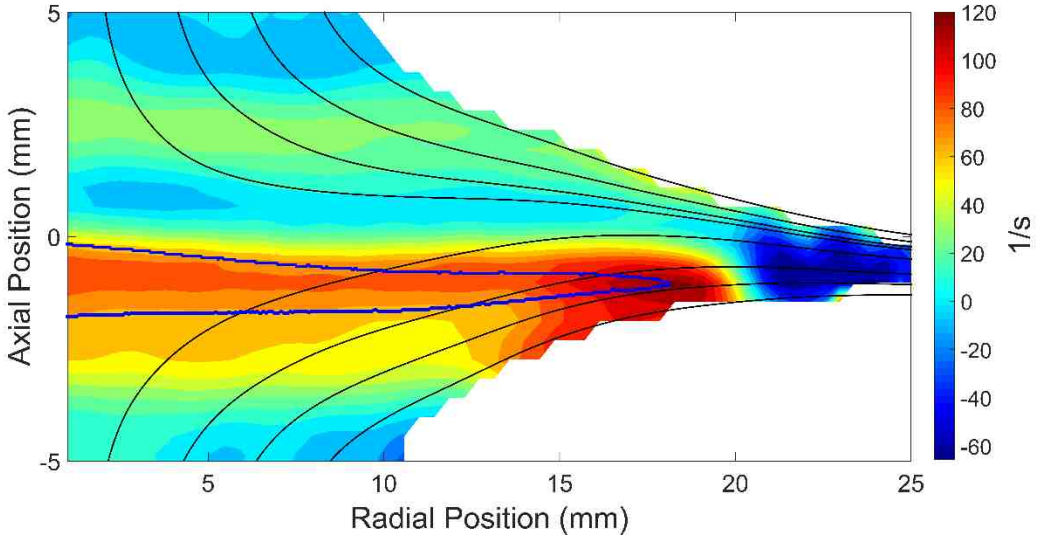

Figure 5.13: Experimental 15:40 dilatation field with streamlines and OH contour plotted in the negative edge counterflow diffusion flame.

One valid technique to measure the advective heat flux in this geometry would be two line OH thermometry. This technique relies on OH being present in order to measure the temperature. Based on the Figure 5.13 the only region that has sufficient OH is along the oxidizer side near the large positive advective heat flux region. Thus only the positive advective heat flux would be measured and the negative advective heat flux through the extinction point would be missed. For this reason, dilatation computed just from the velocity measurements provides a more complete picture of the advective heat flux throughout the flame.

Next, profiles of the dilatation in the axial and radial directions were compared for quantitative agreement across the three cases. The axial profiles are shown in Figure 5.14 (a) while the radial profiles in Figure 5.14 (b). The axial profile is an average of the profiles from 4 to 7 mm radially outward. The oxidizer side (negative axial position values)

magnitudes are larger than the fuel side, which is consistent with the numerical study. Also, on the oxidizer side, the peak magnitude of the dilatation increases as the inner velocity is increased. One slight disagreement is the larger value in dilatation as the position nears the stagnation plane. The profiles on the oxidizer side are also wider for the 10:40 case and become thinner as the inner velocity is increased by the same reasoning given in the numerical work. On the fuel side, the 10:40 case has the lowest dilatation in this region which is consistent with the numerical work, but the 15:40 and 20:40 cases show almost no change in peak magnitude.

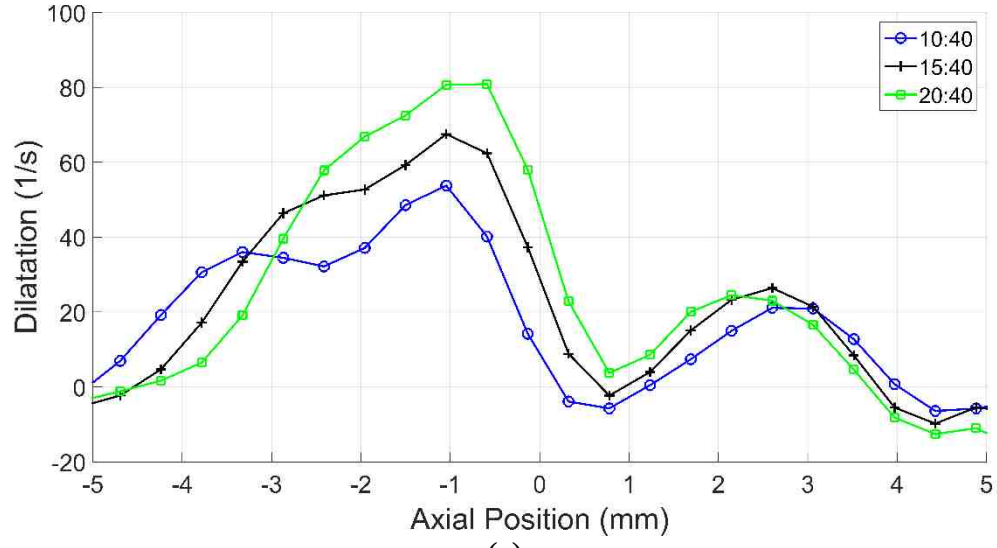

(a)

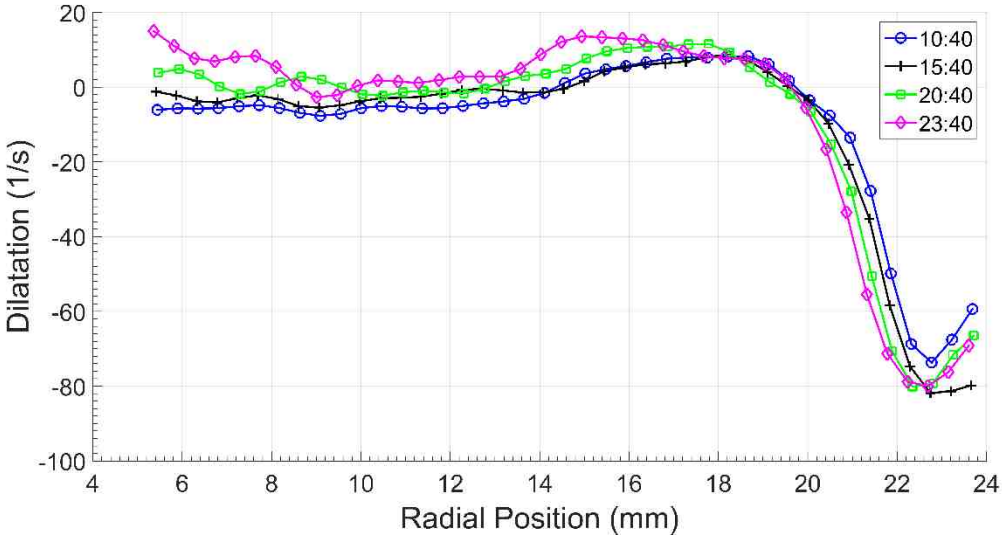

(b)

Figure 5.14: Profiles of (a) axial and (b) radial slices of dilatation in the negative edge 10:40, 15:40, 20:40, and 23:40 cases.

The radial slice was sampled by taking a two point sliding average and subsequently sampling the minimum dilatation at each radial position, similar to the numerical study. Near the centerline the magnitude of the dilatation is relatively low, but as the radial position nears the extinction region, there is a quick transition to large negative dilatation, consistent with the numerical study. Near the centerline of the burner, there are some fluctuations in the dilatation sampling. These oscillations can mostly be attributed to

boundary conditions effects, such as honeycomb spacing and inlet velocity profile non-uniformities. The honeycomb spacing seems to be the most likely solution to the fluctuations because the fluctuations in the profiles grow with inner velocity and also seem to occur near the same regions in each case. By performing a first approximation of the uncertainty, the dilatation uncertainty was 2.5 $\frac{1}{s}$ which was much smaller than the fluctuations found near the centerline. The trends between the cases are very similar to those found in Figure 5.10 (b). The 20:40 case begins to drop prior to the other two cases, with the 10:40 and 15:40 cases having very similar profiles. The peak negative magnitudes are very similar between the three cases. In the numerical work the peak magnitudes of the 10:40 and 15:40 case differ from the 20:40 case by 3%, while in the experimental differed by 4% showing good agreement. One more case was run in order to emphasize the trend that as the inner flame is weakened the flame recedes, and therefore the transition from near zero to large negative dilatation recedes towards the centerline as well. Overall, the experimental observations seem to match the numerical work quite nicely.

5.3.5 Summary and Conclusions

In edge flames representing propagating or extinguishing flame fronts, knowledge of the advective heat flux is important to characterizing the edge and quantifying the strength of the extinction process. A simple diagnostic using only flow dilatation to characterize the edge was explored and the theory describing how the flow dilatation could be interpreted as a scaled advective heat flux in combusting flows was derived. The theory shows that under the low Mach number and small molar mass gradient assumption with respect to temperature gradients, the dilatation is directly a scaled advective heat flux. Numerical and experimental studies were performed on both positive and negative edge

flames in order to assess how well the dilatation represented the advective heat flux both qualitatively and quantitatively at flame edges. Numerical results also assessed the accuracy of using dilatation for advective heat flux.

For each of the cases studied, the dilatation structures matched very well with the advective heat flux structures. All terms in the dilatation were calculated and it was shown that the molar mass and pressure gradient terms were negligible compared to the dilatation and scaled advective heat flux, leading to a difference of no more than 3% in the case of a highly diluted fuel. For the case of undiluted methane where the fuel and oxidizer differ in molecular weight by 80%, variations in molecular weight across the flame lead to a 10% different between the dilatation and scaled advective heat flux. Quantitative agreement was also found to exist between the dilatation and full advective heat flux since variations in the combined property $\left(\rho c_p T\right)^{-1}$ throughout the flame were less than 5% at temperatures for which there was significant advective flux.

Experimentally, the dilatation structure and quantitative trends in dilatation were in good agreement to those from simulations for both cases of positive and negative edge flames. OH PLIF measurements further showed the location of the dilatation relative to the flame in agreement with advective heat flux calculations. Comparisons between experiments and numerical simulations showed good agreement for all cases.

Overall, the dilatation is a suitable marker for advective heat flux and can ascertain whether an edge flame represent a point of propagation or extinction. The magnitude of the dilatation can also provide semi-quantitative values of advective heat flux (requiring a calibration) to understand the strength of the extinction. This paper examined steady flames where the comparisons could be more easily made. Unsteady flows in either

experimental or numerical simulations should be conducted to assess the effects of the out of plane motion that would not be captured in two-dimensional PIV measurements.

6 Positive Edge Flame Studies

Turbulent partially premixed combustion leads to non-uniformities in species concentrations, allowing multiple stoichiometric crossings in close proximity [110]. Since the stoichiometric crossings are close in length, multiple neighboring edge flames may stabilize. If the crossings are close enough, aerodynamic interactions may occur which change the stabilization of one or both flames. Domingo *et al.* [111] simulated a complex flowfield which led to numerous triple flames, many of which were in close proximity and interacting. In order to take a step towards understanding flame propagation through a more complex partially-premixed flowfield with the potential for many interacting triple flames, the propagation characteristics of interacting triple flames need to be further studied.

Wason *et al.* [112] studied steady laminar neighboring and interacting edge flames by constructing a five slot burner to create two stoichiometric crossings. Different flame stabilization modes were observed with interacting triple flames [112], similar to the twin flames from a concentric jet burner in [113]. With high equivalence ratio gradients, the flames were symmetric and acted as two individual triple flames that were not interacting. As the gradient decreased, interaction occurred, which led to a bifurcation where one flame was lifted higher than the other. The structure could be switched between two stable states with either triple flame at the lower liftoff height. The bifurcation was suggested to occur by small perturbations in the incoming diverging streamlines allowing the divergence of one flame base to dominate slightly over the other and the other flame being pushed to a higher lift off location. Once this structure is created, lowering the equivalence ratio gradient led to the inner premixed branches merging and the formation of a single

continuous premixed structure with alternating rich and lean sections and multiple trailing diffusion flame branches. Further reduction in equivalence ratio gradient caused the triple flame structure to no longer exist, but instead create a large premixed flame.

In prior work [112], interacting triple flames were also found to stabilize at lower heights compared to a single triple flame with the same equivalence ratio gradient, suggesting larger propagation speeds than for single triple flames. However, these faster propagation speeds were not quantified. The local edge propagation speeds for the interacting triple flames in [113] were measured, but the overall free-stream propagation speed of the two triple flames together was not studied. The increased propagation speed of the interacting triple flame structure was proposed in [112] to be due to a larger streamline divergence ahead of the flame base caused by the effectively wider flame structure of two triple flames. This can be observed in Figure 6.1, which shows streamlines of both a single and interacting triple flame under similar equivalence ratio gradients. These streamlines are computed from velocity fields measured in each flame as discussed later in this paper. The leading edges of the two flames have been overlapped to directly compare the differences in the streamlines. Clearly interacting triple flames have increased divergence which is likely the cause of increased propagation speed.

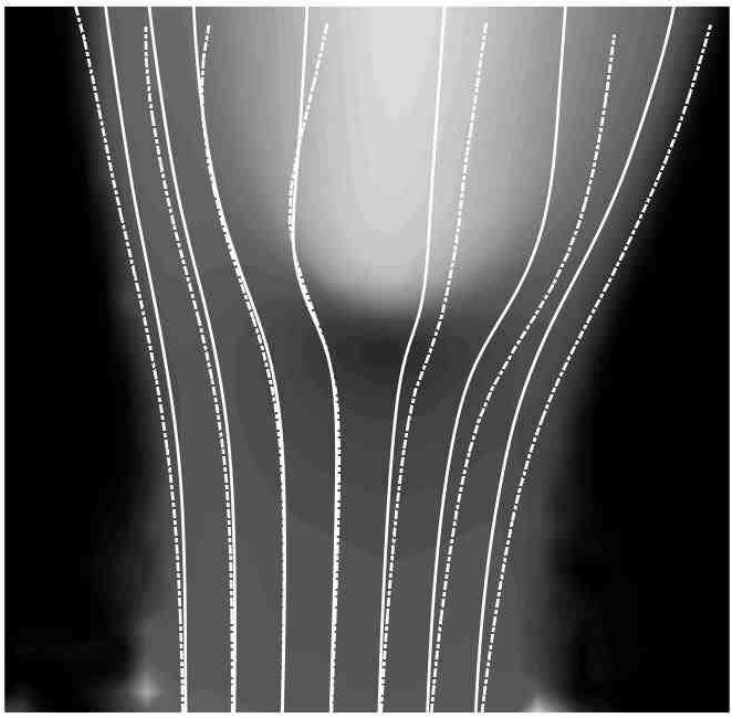

Figure 6.1: Streamline effect from a single (solid) and interacting (dashed) triple flame. The color scale represents the velocity magnitude of the single triple flame

Later work by Kostka *et al.* [29] performed both Rayleigh scattering imaging for fuel concentration and combined hydroxyl (OH) and formaldehyde (CH_2O) planar laser induced fluorescence (PLIF) to identify whether chemical interactions existed between two interacting triple flames. Relative heat release measurements were made, which showed that no chemical interaction occurred between the interacting flames, concluding that the interaction was only due to aerodynamic effects. It was also shown that both triple flames in the interacting case, even with significantly different liftoff heights, had similar concentration gradients below each triple point. A linear relationship between curvature of the flame base and concentration gradient was shown to exist for the interacting triple flames [29] over the range of conditions studied, which was similar to the results found in [32,34–36] for individual triple flames. This led to the conclusion that each triple flame base in an interacting triple flame structure stabilizes at the same conditions as that of a

single triple flame. However, the aerodynamic interaction creates the overall bifurcation between the two triple flames and permits the flame structure to stabilize at even faster speeds than for a single triple flame. However, these speeds were not quantified in this study. The radii of curvature and the distance between the two interacting flame stoichiometric locations was found to be the controlling parameters which determined when the flames were separated or merged. If the sum of the radii of curvature exceeded the stoichiometric separation distance, then the flames were interacting which impacted liftoff heights (and therefore propagation speeds), otherwise the flames were separated.

The following Chapter will show measurements and characterize the propagation speeds for interacting triple flames. The curvatures and level of interaction between neighboring flames will be varied in order to assess the impact of each on the propagation speed. Chapter 6.1 is a study which characterizes the propagation speed with respect to a single fuel, ethylene (C_2H_4) diluted with nitrogen (N_2). The experimental procedure details are rigorously described in this sub-chapter in each phase of the experimental measurements. Observations and a model are shown for the given fuel. Chapter 6.2 focuses on fuel effects on interacting triple flame propagation speeds. Since observations in Chapter 6.1 could be interpreted as unique to the fuel used, two different fuels (methane (CH_4) diluted with argon and propane (C_3H_8) diluted with helium) were used with similar experimental measurements and procedures as in Chapter 6.1 to determine the similarities and differences in observations and how the propagation speed model is affected when different fuels are used.

6.1 Positive Edge Flame Velocities with Multiple Concentration Gradients

6.1.1 Motivation

In this sub-chapter, interacting edge flames were studied to characterize how these interactions impact the overall propagation speed of the flame structure. These results impact our understanding of the overall consumption speed for flame structures propagating through mixtures with significant equivalence ratio gradients as will occur in partially premixed turbulent flows. The propagation speeds are measured as a function of fuel concentration, or equivalence ratio, gradient and separation distance for interacting triple flames, and a model to compute the effect of triple flame interactions on propagation speed is proposed.

6.1.2 Experimental Setup

The same five slot burner as in [29] was used in the current study, which is shown in Figure 6.2. Each slot was independently controlled giving the ability to change both the velocity and mixture content. For the current study, each slot issued the same velocity but with different equivalence ratios. The flow to each slot was individually controlled by choked orifices using a ten channel electronic flow bench. After exiting the five slots, the flow was sent into a 100 mm long converging nozzle to allow mixing between neighboring slots, which smoothed out large species gradients. The nozzle transitioned from a cross section of 75 × 120 mm to 25 × 40 mm, leading to an overall contraction ratio of 9:1 (3:1 in each direction) to provide a uniform velocity profile at the burner exit. The inlet and outlet of the converging nozzle had a 1/2" thick, 1/8” cell aluminum honeycomb and 1/4” thick, 1/16” hastelloy honeycomb, respectively. A 5 mm wide nitrogen guard was also used surrounding the burner exit to lessen boundary effects.

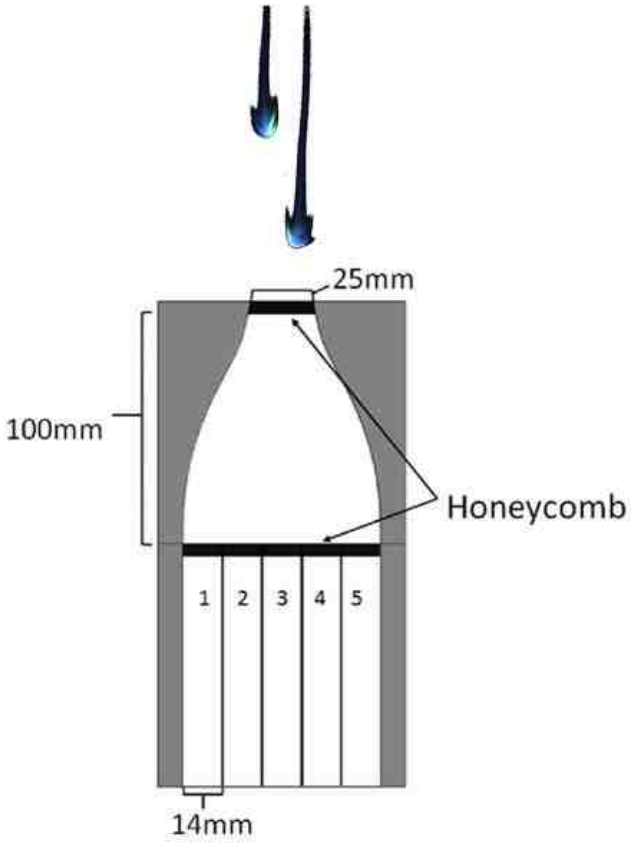

Figure 6.2 Schematic of experimental five-slot burner.

Two flame configurations were used in this study, one created a single triple flame while the other created two interacting triple flames. To create a single triple flame, only one stoichiometric crossing was produced by supplying slots 1 and 2 with nitrogen, 3 with a rich mixture, 4 with a lean mixture, and 5 with air. To create interacting edge flames, two stoichiometric crossing were created. In this case, slots 1 and 5 were supplied with air, 2 and 4 the same lean mixture, and 3 a rich mixture. For the single triple flame, the lean equivalence ratio was fixed at 0.75 and the rich equivalence ratio was varied between 1.25 and 8. This maintained one stoichiometric crossing but varied the equivalence ratio gradient ahead of the single triple flame. Three sets of cases were run for interacting edge flames. The lean mixture in slots 2 and 4 was set at 0.5, 0.75, and 1 while the rich mixture

was varied between 1.25 and 8. This permitted variation of both the equivalence ratio gradient ahead of the flame and the separation distance between stoichiometric crossings. A typical interacting triple flame with a different liftoff heights is shown in Figure 6.2. In this case, one triple flame stabilizes at a lower height, even though the flowfield is symmetric. As discussed in the previous sub-chapter, this lower triple flame is of interest as its conditions describe the overall propagation speed of the two triple flames together. The measurements reported in this paper focus on the propagation speed, equivalence ratio gradient and curvature of this leading triple flame in the structure. For all cases, the fuel consisted of 16.7% ethylene diluted with 83.3% nitrogen by volume in order to keep the flame speed low enough to be laminar. Ethylene was chosen because its molecular weight is similar to air which minimizes density variations throughout the burner.

Simultaneous OH PLIF and particle image velocimetry (PIV) were used in one experiment to measure the flame curvature and free stream propagation speed. The OH PLIF laser beam was formed by pumping a Sirah Cobra-Stretch tunable dye laser with the frequency doubled output of a Spectra Physics LAB 170 series Nd:YAG. The PLIF beam was tuned to excite the $Q_1(5)$ transition in the $A^2\Sigma^+ \leftarrow X^2\Pi(1,0)$ band of OH at 282.67 nm. The fluorescence signal was imaged onto a Photonis XX1950LP image intensifier using a Universe Kogaku UV 1054B lens and recorded using a Mightex CGN-B013-U camera. A 320 ± 20 nm filter was placed ahead of the intensifier to collect fluorescence from bands away from the beam wavelength to eliminate scattering signal. The PLIF images had a projected resolution of approximately 15 pixels/mm.

Aluminum oxide particles with nominal diameters of 1 μm were seeded into the flow. Only the slots with fuel were seeded because the streamlines from these slots were

the only ones which passed through the flame structure. Therefore, only two slots were seeded for a single triple flame case, and three slots were seeded for interacting triple flames. A Photonics Nd:YLF high repetition rate laser was used to illuminate the particles in the flow. The Mie scattering images were imaged using a Phantom V611 CMOS high speed camera equipped with a f = 105 mm Sigma lens. The PIV timing and recording was controlled by LaVision Davis 8.3. The Mie scattering images had a projected resolution of approximately 18 pixels/mm. The images were processed using Davis 8.3 with a multipass algorithm and a final 32 × 32 interrogation window with 50% overlap, leading to an overall vector spacing of 0.85 mm.

Both beams were formed into sheets by a combination of cylindrical lenses and telescoping lenses, and combined using a dichroic mirror. The sheets were subsequently overlapped and sent into the flowfield, depicted in Figure 6.3. 300 images of both PLIF and PIV were recorded, processed, and subsequently averaged for each case.

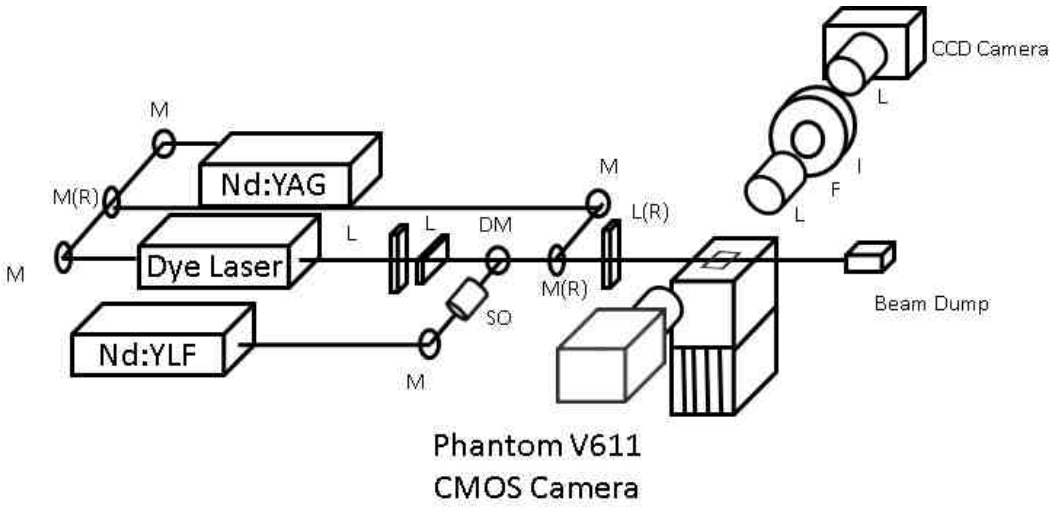

Figure 6.3 Experimental OH PLIF, PIV, and Rayleigh scattering setup, where items marked (R) refer to items that were placed in the optical path for only the Rayleigh scattering measurements. M: mirror, DM: dichroic mirror, L: lens, SO: sheet forming optics, F: filter, and I: intensifier. The intensifier unit was removed for Rayleigh scattering imaging.

In a separate experiment, Rayleigh scattering was performed to measure the fuel concentration gradient and stoichiometric separation distance at the burner exit. The approximate 300 mJ per pulse frequency doubled output of the Spectra Physics Nd:YAG bypassed the dye laser and was directed towards the burner as shown in Figure 6.3, where items marked (R) were placed in the optical path for Rayleigh scattering. The beam was shaped with only a single f = 500 mm cylindrical lens to form a sheet. The beam was not expanded in order to keep a high power density in the combustor section. The beam height was approximately 9 mm in which the center 5 mm was used for measurements. A pair of apertures were used on either side of the burner in order to eliminate any scattering off the burner. Images were captured using a Mightex CGN-B013-U camera and gated down to 50 μs to minimize any background signal. 300 images were taken near the burner exit and averaged for each case studied with the flame not lit to quantify the free stream fuel concentration gradient, which is similar to the equivalence ratio gradient. The pixel resolution was approximately 35 pixels/mm.

A similar processing scheme for the Rayleigh scattering signal was used as in [29] to extract the fuel concentration gradient, as given in Eq. (6.1), where SP is the processed signal, S_{Signal} is the Rayleigh signal from the test case, $S_{Background}$ is measured using only nitrogen flow from each of the five slots, and $S_{C_2H_4}$ is measured using only fuel from each slot. This ratio, SP, is related to the mole fraction, X_i, and the Rayleigh scattering cross section, σ_i, of the respective species. As discussed in [29], if the difference in the Rayleigh scattering cross sections of oxygen and nitrogen are neglected, SP can be taken to approximate just the mole fraction of ethylene as given in Eq. (6.1). Oxygen and nitrogen do have differing Rayleigh cross sections by approximately 1.5%, which causes a slight

difference between the measured and actual fuel mole fraction [114]. In order to correct this, a calibration was conducted against flows with known homogeneous equivalence ratios. This calibration was used to correct each case, similar to the technique used in [29]. The calibration resulted in $X_A = 0.94X_M + 0.0066$ where X_A and X_M are the actual and measured fuel concentrations. A correlation coefficient (R^2) of 0.999 was obtained for this calibration.

$$SP = \frac{S_{Signal} - S_{Background}}{S_{C_2H_4} - S_{Background}} = \frac{[X_{O_2}\sigma_{O_2} + X_{N_2}\sigma_{N_2} + X_{C_2H_4}\sigma_{C_2H_4}] - [(1)\sigma_{N_2}]}{[(1)\sigma_{C_2H_4}] - [(1)\sigma_{N_2}]} \approx X_{C_2H_4} \quad (6.1)$$

6.1.3 Results and Discussion

6.1.3.1 Curvature Observations

In order to characterize the propagation speed of the flame structure at a given equivalence ratio gradient, a stable and steady flame was produced and the velocity was increased with the same slot equivalence ratios until blowoff occurred. Once blowoff occurred, the velocity was lowered by 1 cm/s, relit to create the last steady flame which could stabilize, and PIV and OH PLIF measurements were then taken at those conditions. This condition was used as representative of the freestream case since it was the maximum speed at which the flame could stabilize, similar to the procedure used in [33], to ensure that the flow divergence does not affect the exiting flow. The bulk flow speed exiting the nozzle was used to characterize the maximum propagation speed of the flame structure. Although the local velocity at the triple point is balanced by the local laminar flame speed, the overall flame structure propagates at the bulk flow velocity exiting the burner. For this

reason, the freestream propagation speed, blowoff speed, and propagation speed are all interchangeable.

Both PIV and OH PLIF were used in order to measure the freestream propagation speed and the flame front curvature, respectively. An example of a typical velocity field around the lower triple flame is shown in Figure 6.4 (a) with the raw OH PLIF signal (left), which has a lean equivalence ratio (ϕ_L) of 0.75 and rich equivalence ratio (ϕ_R) of 2.25 for an interacting edge flame case. The X-coordinate is perpendicular to the flow with an origin at the burner centerline, and the Y-coordinate origin is defined at the burner exit with the positive direction being in the flow direction. It should be noted again that only the center three slots were seeded for PIV measurements because these were the only ones which passed through the flame bases. Therefore, in Figure 6.4 (a), the regions with apparently a zero velocity are simply unseeded regions. There is no shear layer near the flame stabilization region. The upper triple flame, as shown in Figure 6.2, is present but outside the field of view of the PIV and PLIF systems. Immediately after recording the measurements with the flame burning, the flame was forced out and the non-reacting velocity field was also recorded under the same flow conditions as the reacting case. This was done to ensure that the flame structure's diverging streamlines were not influencing the velocity profile at the burner exit and thus the characterized propagation speed was truly the freestream propagation speed. The velocity profiles 1 mm above the burner exit for both reacting and non-reacting conditions are shown in Figure 6.4 (b). The two cases are nearly identical and are also constant across the burner exit, verifying that there is negligible effect from the flame. The reacting profiles were averaged to obtain a single propagation speed. The OH PLIF contour at 30% of the signal maximum is also plotted in

Figure 6.4 (a) in white, which identifies the flame boundary in the interacting edge flame configuration. Only one of the two triple flames was recorded in most cases because the downstream triple flame was significantly lifted above the lower flame, similar to measurements in [29]. The bottom edge of the PLIF contour was used to determine the curvature of the flame. It was shown in [29] that both the upper and lower flames exhibited nearly identical concentration gradients and curvatures, leading to one flame curvature being sufficient to characterize each case. The center 3 mm of the flame base was isolated and curve fit to determine the radius of curvature. This best fit circle representing the radius of curvature is plotted in black in Figure 6.4 (a). The flame curvature is an important parameter because it has been shown to be linearly proportional to the fuel concentration gradient upstream of the flame base [29,32,34–36]. This gives the ability to characterize the propagation speed of the flame structure with respect to a scaled fuel concentration gradient.

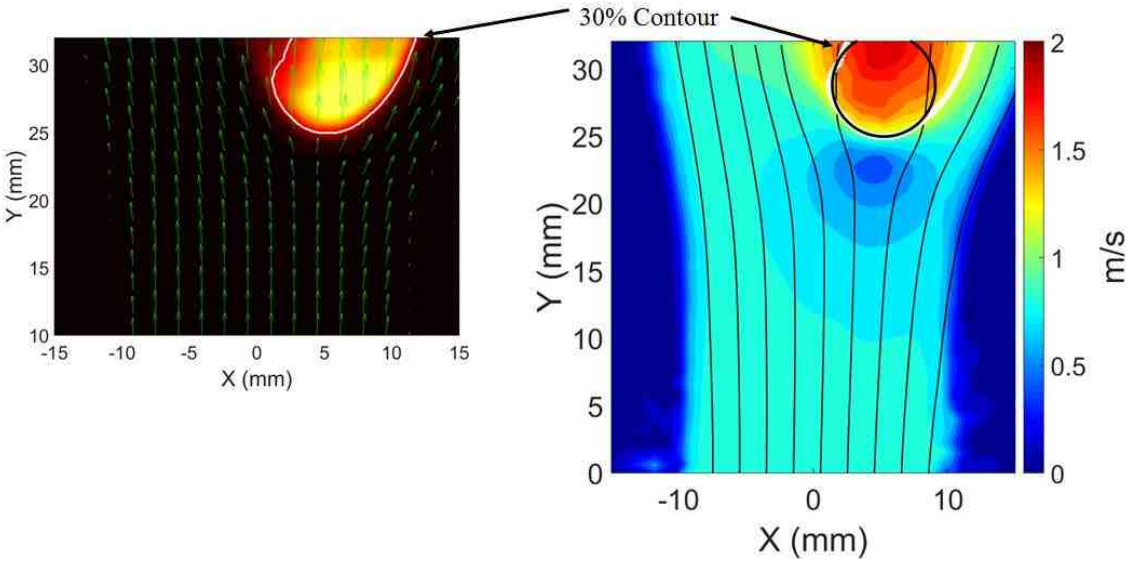

(a)

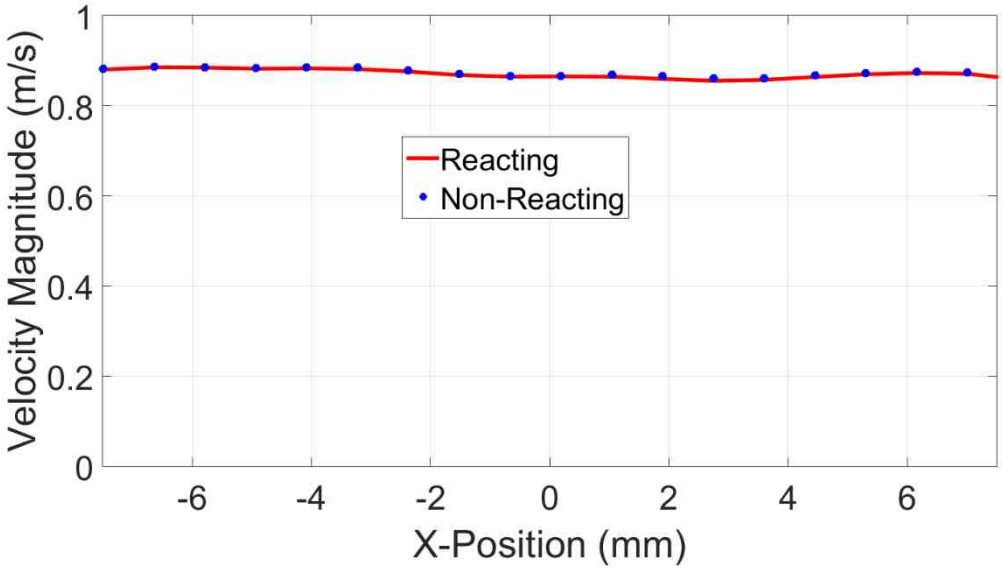

(b)

Figure 6.4: Velocity field (right) and raw OH PLIF signal (left) with 30% OH PLIF contour plotted in white and circle of best fit along the center 3 mm shown in black (a) and inlet velocity profile (b) of two triple flames with ϕ_L = 0.75 and ϕ_R = 2.25. The Y-coordinate begins are the burner exit in the direction of the flow, and the X-coordinate is centered at the burner exit.

Note that it is important to ensure the flame is near blowoff to use the burner exit velocity as representative of the freestream propagating speed of the flame structure with respect to the bulk flow. To demonstrate this, an interacting case with ϕ_L = 0.75 and ϕ_R = 4 was recorded with several inlet velocities approaching the blowoff speed. Both reacting

and non-reacting velocity data were taken at each setpoint and profiles were examined 1 mm above the burner exit. Figure 6.5 shows the maximum difference between the reacting and non-reacting at each point along the velocity profiles. For slower bulk velocities, the triple flame liftoff height decreases and the flow divergence ahead of the flame base perturbs the flow all the way to the burner exit leading to a difference in the burner exit profile with and without the flame. As the velocity magnitude is increased toward blowoff at 79.5 cm/s, the difference between the reacting and non-reacting velocity profiles become negligibly small. Therefore, it is demonstrated that this procedure is necessary and the characterized speed used in this procedure is nearly the freestream propagation speed with respect to the bulk flow.

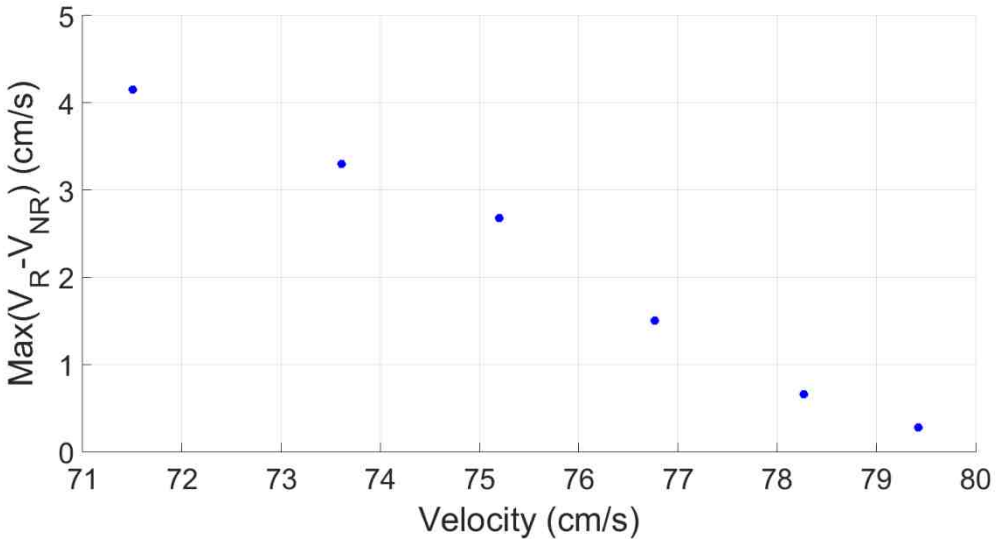

Figure 6.5: Maximum sampled difference between reacting and non-reacting velocity profiles as the velocity magnitude is increased to blowoff.

Each case was processed using this procedure outlined above, by pushing the flame towards blowoff, and the velocity magnitudes are shown versus the respective flame curvatures in Figure 6.6. Error bars shown in the figure were determined by one standard deviation of the velocity variation across the burner exit and by the spatial resolution of

one pixel in the PLIF measurement. The single triple flame case was used as a basis to compare against interacting edge flames. The single triple flame follows a similar trend as in [33] where decreases in equivalence ratio gradient lead to a broader flame base. This results in a smaller curvature (larger radius of curvature) and larger divergence of the flow around the flame base. The larger flow divergence permits a faster bulk propagation speed, which has been well documented in the literature for single triple flames. The propagation speed reaches a maximum at a limiting curvature [33,37]. When the gradient is decreased further, the flame no longer sustains a diffusion tail, which leads to a transition to premixed flame propagation and a decrease in propagation speed [33,37], shown as open symbols in Figure 6.6. Ruetsch *et al.* [28] showed that in the asymptotic limit of a triple flame with zero equivalence ratio gradient (zero curvature) the free stream propagation velocity, U_F, is related to the laminar flame speed, S_L, and the density of the unburned and burned states. Using ideal gas law, the zero gradient speed can be defined in Eq. (6.2), where T_b is the burnt products temperature and T_u is the reactant temperature as,

$$U_F \sim S_L \sqrt{T_b/T_u} \tag{6.2}$$

Kim *et al.* [33] showed if the linear portion of the flame speed versus fuel concentration gradient was extrapolated to the zero intercept, this intercept speed correlated well with the theoretical value from [28] using undiluted methane, which was also shown by Ko and Chung [32]. Kim *et al.* [33] found with propane the extrapolated value from measurements exceeded the value from Eq. (6.2). but Lee *et al.* [34] showed that propane extrapolated to the correct asymptotic value in microgravity conditions, leading to the conclusion that buoyancy had a significant influence on this limiting propagation speed. Further work by Seo *et al.* [115] showed that undiluted methane correlated well with the asymptotic limit,

but when methane was diluted with nitrogen, the zero intercept speed decreased below the asymptotic limit. For the present experiments with diluted ethylene, the laminar flame speed and adiabatic flame temperature for a stoichiometric mixture were calculated using Cantera Chemical Solver [116] with GRI-Mech 3.0 [108]. The values in Eq. (6.2) predict an asymptotic limiting speed of 116 cm/s. The measured value from extrapolating the linear portion of Figure 6.6, was approximately 93 cm/s, plotted as an open diamond in Figure 6.6. Similar to [115], the diluted zero intercept propagation speed was lower than the asymptotic limit.

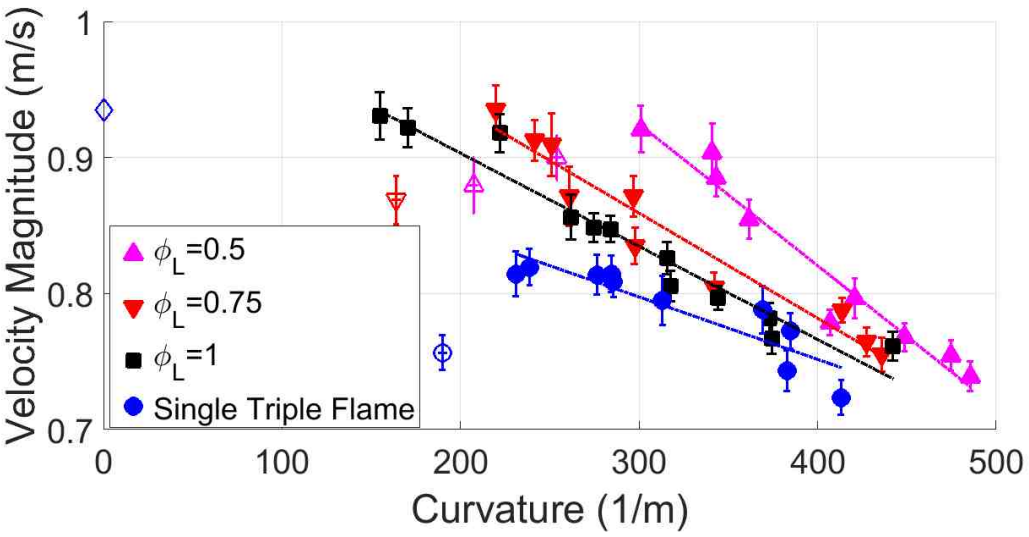

Figure 6.6: Propagation speeds of flame structure with respect to curvature. The open diamond symbol represents the zero intercept speed of a single triple flame. Open symbols represent cases below the critical curvature value where the flame transitions from a triple flame to a premixed flame. Closed symbols were used to calculate the linear relationship for each case.

Interacting triple flames follow a similar behavior as shown in Figure 6.6; as the equivalence ratio gradient is decreased the propagation speed increases. However, in all cases, the propagation speed of the interacting triple flames is larger than a single triple flame with the same curvature. For the interacting flame cases with ϕ_L = 0.5 and 0.75, a critical curvature exists, as with the single triple flame, such that further decrease in

curvature leads to lower flame speeds. The ϕ_L = 1 case does not exhibit this behavior, likely due to the diffusion tail not being sufficiently weakened for the cases studied; i.e., the flame cannot be made wide enough in the present burner to achieve this limiting condition. Interestingly, the maximum speed of each respective interacting triple flame is nearly the zero intercept propagation speed for a single triple flame, as seen in Figure 6.6. It is feasible that the maximum propagation speed for interacting triple flames is limited by the zero-gradient limit for single triple flames. This zero-gradient velocity for single triple flames occurs in the limit of an infinitely wide triple flame. Single triple flames cannot become wide enough to reach this limit without sufficiently weakening the diffusion tail. Interacting triple flames, however, can become effectively wider under low gradients without losing the triple flame structure. Thus the divergence at the flame base can be increased. While not conclusive, it is feasible that the limitation of this divergence is the same as occurs for an infinitely wide single triple flame.

The three interacting edge flame cases exhibit similar behavior as a single edge flame, but at higher propagation speeds. Clearly, the slope of the flame speed with respect to curvature of the single triple flame is smaller than each of the interacting flames. The slopes of each case were calculated using the solid symbols in Figure 6.6. The slope for the single triple flame is – 459 mm^2/s. It should be noted that propagation speeds vary with curvature inversely, but the range being examined is linear and can therefore be processed accordingly. The interacting triple flames permit a larger flow divergence ahead of the leading (lower) triple flame which has the same effect as a wider triple flame base. Thus, the interacting flames enable an even faster flame structure propagation. As the equivalence ratio in the lean slots are decreased, the stoichiometric locations will move

closer together resulting in more flame interactions [29]. That is, for the same flame curvature but with a closer interacting edge flame, the speed of the structure is faster. As the lean equivalence ratio is decreased, or more interaction occurs, the magnitude of the slope of the flame speed with respect to curvature increases. The slopes are – 685, – 773, and – 1041 mm^2/s for ϕ_L = 1, 0.75, and 0.5, respectively.

6.1.3.2 Fuel Concentration Observations

In order to extract the fuel concentration gradient and stoichiometric separation distance, Eq. (6.1) in conjunction with the linear calibration was used to measure the fuel distribution. An example of the fuel concentration field, approximately 5 mm above the burner exit, is shown in Figure 6.7 (a) with ϕ_L = 0.5 and ϕ_R = 7. The same coordinates as used in Figure 6.4 was used in Figure 6.7. The concentration was then averaged in the Y-direction to obtain a line Rayleigh signal. The signal was then Gaussian fit on either side of the maximum point, shown in Figure 6.7 (b). The analytical derivative of the fit was then taken and sampled at the stoichiometric locations to determine the relevant fuel concentration gradient. In all interacting edge flame cases, the derivatives at either stoichiometric location were sufficiently similar to be averaged and obtain a single characteristic fuel concentration gradient ahead of each flame base. The stoichiometric separation distance was also measured using the curve fit. For single triple flame cases, only one half of the fuel concentration profile was sampled, and the derivative was taken to obtain the fuel concentration gradient. Several samples were tested at 5 different heights, with 1 mm averaging windows to ensure that there were no significant gradient changes in the Y- direction. It was confirmed that at each height the fuel concentration gradient varied by less than 1%.

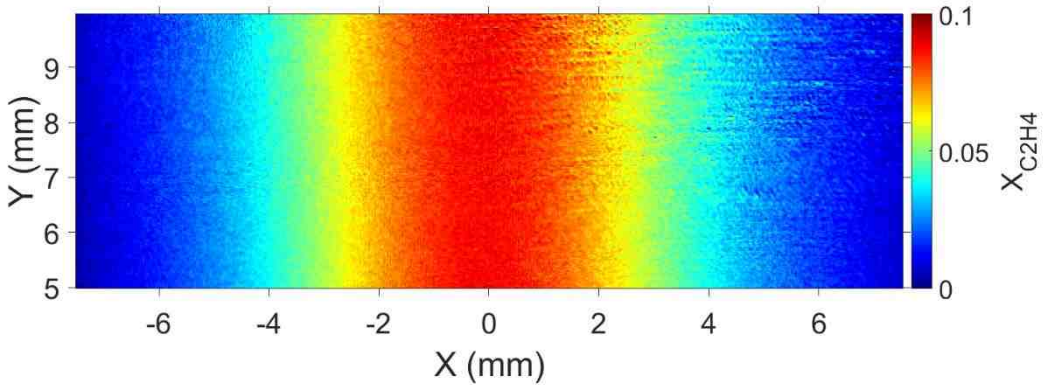

(a)

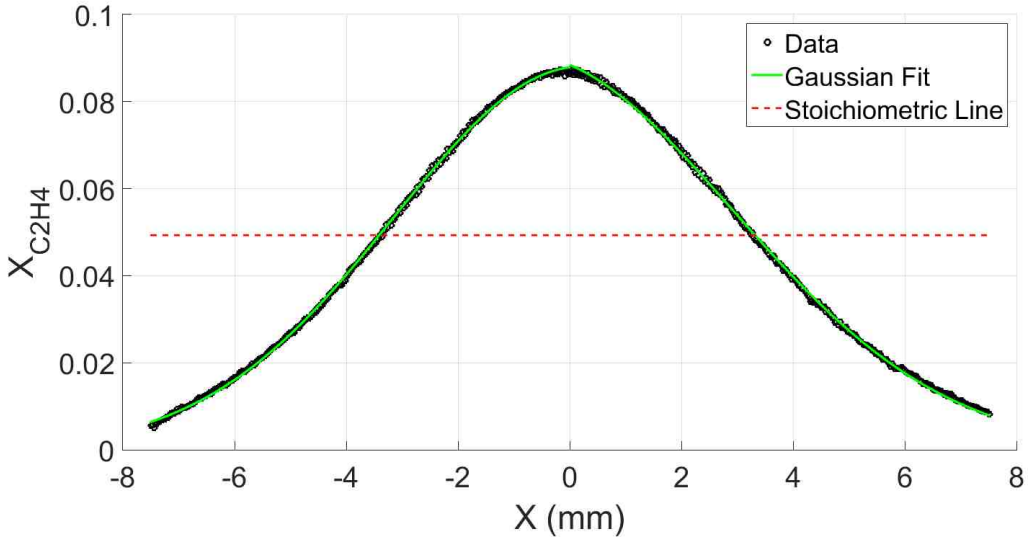

(b)

Figure 6.7: (a) Corrected fuel concentration signal using Eq. (6.1) and calibration, and (b) the mean signal in the Y-direction with Gaussian fit and stoichiometric line where analytical derivative was taken.

Previous work has shown that both single and interacting triple flame curvatures are linearly proportional to the fuel concentration gradient [29,36], which is also demonstrated here as shown in Figure 6.8. The same trend of a linear correlation exists between curvature and fuel concentration gradient regardless of the level of the flame interactions.

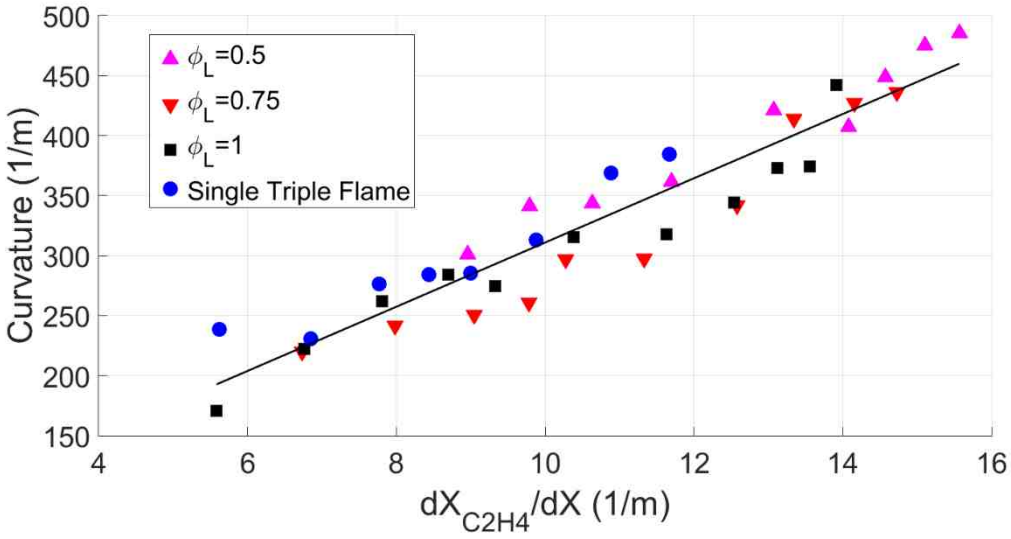

Figure 6.8: Curvature plotted against fuel concentration gradient demonstrating a linear correlation.

Clearly, interaction has a significant influence on the propagation speed of the triple flame structure. Kostka *et al.* [29] developed a simplified interaction parameter to determine when interacting edge flames would be merged as opposed to being separated. This interaction parameter, ψ, is given in Eq. (6.3), where ρ is the radius of curvature and δ_{stoich} is the stoichiometric separation distance in the X-direction. Kostka *et al.* [29] showed that the stabilization modes were only a function of stoichiometric distance in the X-direction, and therefore the Y-direction liftoff height difference need not be characterized. In order to characterize the level of interaction between the interacting triple flames, the stoichiometric distance was also measured from the fuel mole fraction profile fits, as shown in Figure 6.9. As intended, when ϕ_L is increased the stoichiometric separation distance is increased which should lead to less interaction between the interacting edge flames.

$$\psi = \frac{\rho_1 + \rho_2}{\delta_{stoich}} \sim \frac{2\rho}{\delta_{stoich}} \tag{6.3}$$

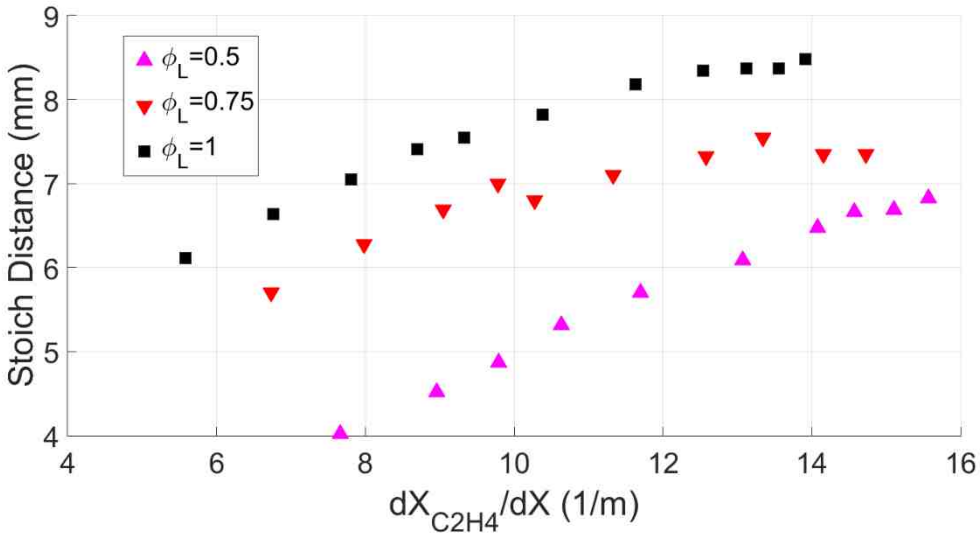

Figure 6.9: Stoichiometric separation distance between interacting edge flames plotted against fuel concentration gradient.

6.1.3.3 Model for Interacting Triple Flames Speed

A single triple flame has a propagation speed, V, that can be approximated as,

$$V = mC + b \tag{6.4}$$

where C is the curvature of the lifted flame base (or this could be related to the local equivalence ratio gradient as discussed with Figure 6.8), m is the slope of the linear portion of the speed versus curvature for a single triple flame discussed with Figure 6.6, and b is the zero-speed intercept that is related to the asymptotic limit of a zero gradient triple flame as discussed in [28]. The linearity of the propagation speed with respect to curvature for a single triple flame is limited, however, to lower curvatures. At higher curvatures, an inverse relation may instead be needed [32]. For the interacting triple flame, the effect of the interaction is to increase the flow divergence in a way that makes the flame behave as if it is wider than measured by flame curvature alone. We therefore propose to estimate the speed by defining an effective curvature $C_{eff} = C \times f(\psi)$, where the function $f(\psi)$ accounts for the ratio of the effective curvature to the true curvature as a function of the

interaction parameter. The effective curvature can then be input into Eq. (6.4) to obtain the propagation speed.

In order to find the functional form of $f(\psi)$, the effective curvature ratio, $\frac{C_{eff}}{C}$, was calculated and plotted against ψ, where C_{eff} is calculated for each case by using the single triple flame linear relationship in Eq. (6.4) and computing the curvature that would be required in a single triple flame case to achieve the same velocity as measured from the interacting flame. This ratio is shown in Figure 6.10 for all cases. The open symbol represents the single triple flame case itself, where no interaction is occurring, or $C_{eff} = C$. The data suggests there is a range where interaction has little influence on the effective curvature until approximately ψ = 0.5 where there is then a decrease in the effective curvature ratio due to increased propagation speed. Beyond ψ = 1.5 there is little data, but 0 is a limiting value for the curvature ratio and from the fit through the data of Figure 6.6 it is suggested that each of the interacting cases reach nearly the zero intercept speed. Therefore, for interactions above ψ = 1.5, the interacting triple flames appear to have maximized the impact of interactions on aerodynamic increases in propagation speed and to have achieved the theoretical maximum speed for a propagating triple flame. This point was further emphasized by supplying slots 1, 3, and 5 with air while 2 and 4 with a rich equivalence ratio. This provides four stoichiometric crossings surrounding the two rich slots, and therefore four triple flames. The maximum achievable speed with this configuration was the same zero intercept speed. Although this could not be further characterized due to limitations in the burner, it shows that further increase in interaction did not lead to higher propagation speeds.

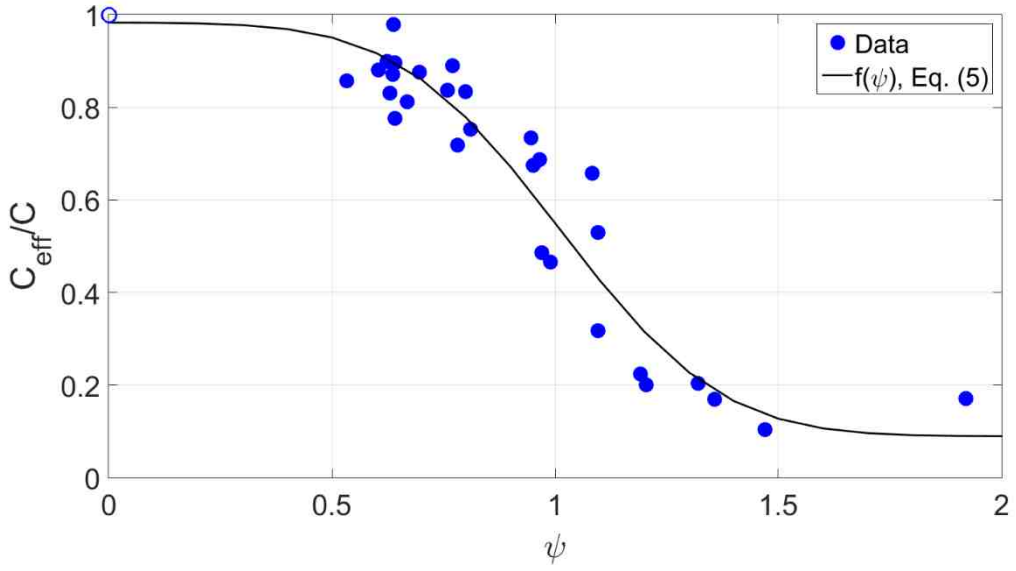

Figure 6.10: Effective curvature ratio, $\frac{C_{eff}}{C}$, plotted against ψ showing the functional form of how interaction changes the effective curvature. The open symbol represents the single triple flame case.

Figure 6.10 also includes a fit to the data in order to predict the effective curvature from only the interaction parameter. An error function was chosen based on the shape of the data and the resulting fit is given in Eq. (6.5) using a nonlinear least-squares method. This model was then used to calculate each of the propagation speeds based on the interaction and curvature. The measured propagation speeds were plotted against the calculated speeds from this model as shown in Figure 6.11. The model is able to describe each propagation speed with a maximum error of 2.5 cm/s and works in the limit of both non-interacting and interacting triple flames. The full model is shown in Eq. (6.5), including the linear fit for the propagation speed, where m and b are from the single triple flame fit. The effective curvature relationship is also given along with the functional form of the effective curvature.

$$V = mC_{eff} + b$$

$$C_{eff} = C \times f(\psi) \tag{6.5}$$

$$f(\psi) = -0.45\,\mathrm{erf}\big(2.49(\psi - 1.01)\big) + 0.54$$

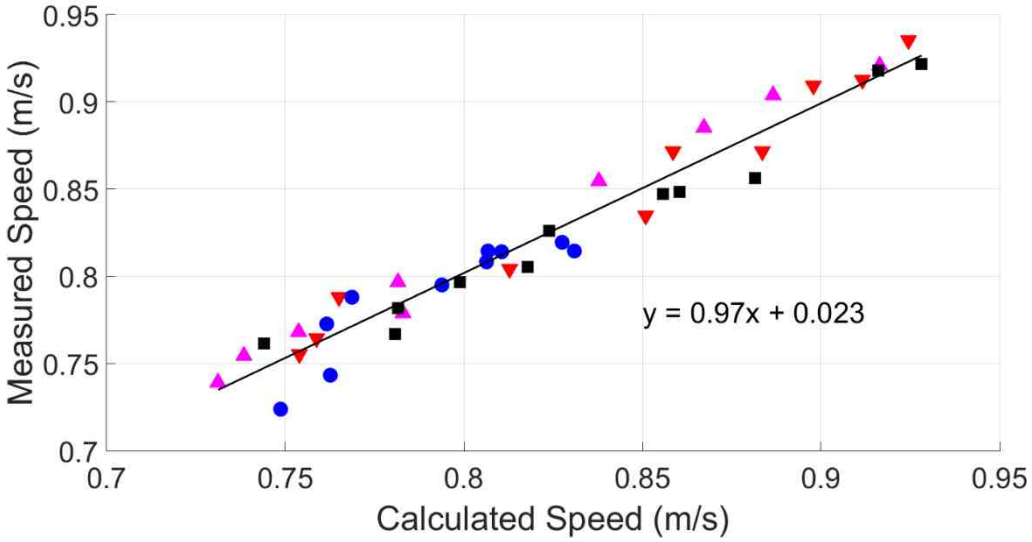

Figure 6.11: Measured propagation speed with respect to calculated propagation speed using Eq. (6.5).

6.1.4 Summary and Conclusions

Interacting edge flame speeds were measured and compared to speeds for a single triple flame with respect to the flame curvature, or equivalence ratio gradient. Propagation speeds, defined as the speed at which the flame structure propagates with respect to the bulk flow, for the single triple flame were observed to increase with lower equivalence ratio gradients, consistent with prior work in the literature. With interacting edge flames, aerodynamic interactions between the individual triple flame structures enabled the flame structure to propagate at even larger speeds. The level of interaction between interacting edge flames was varied by changing the separation distance between the triple points and the local equivalence ratio gradients. As the flames interacted more, the sensitivity to curvature and equivalence ratio gradient was increased. Stoichiometric separation

distances were measured to calculate an interaction parameter. The interaction parameter was found to impact the propagation speed of the interacting triple flame structure and even reached the limiting theoretical speed of a single triple flame, which was consistent for each interacting triple flame case.

A model was then developed to estimate the propagation speed of interacting edge flames, which utilized the linear relation for the propagation speed of a single triple flame along with a defined effective curvature that only depends on the interaction parameter. This simple model is able to describe the propagation speeds for all flames studied, within the measured curvature range.

6.2 Fuel Effect on Interacting Positive Edge Flame Velocities

6.2.1 Motivation

The propagation speed for interacting triple flames of ethylene was characterized in [117] (and in Chapter 6.1) and it was shown that all interacting triple flames propagate faster than a single triple flame at the same equivalence ratio gradient. The equivalence ratio gradient displayed a critical value, similar to [33,37], that resulted in a maximum interacting flame propagation speed. However, this maximum speed of each interacting case was nearly the zero gradient speed for single triple flames, suggesting that the flame interactions may achieve the same effect as an infinitely wide single triple flame. The propagation speed of interacting ethylene triple flames was modeled utilizing a linear relationship between the propagation speed with respect to curvature of a single triple flame, but with a modified effective curvature that accounts for the level of interaction between the two flames. The prior study focused primarily on effects with respect to a given fuel. However, the observations are only valid for the given fuel which may not

account for different effects, in particularly changes in fuel diffusivity, and therefore a similar study is needed for differing fuels. The goal of this sub-chapter is to examine interacting triple flames for other fuels and to verify or alter the model formed in [117] to understand impact of fuel type on interacting triple flame velocities. In particular this paper will examine whether different fuel properties, such as thermal and mass diffusion, change the observations in [117].

6.2.2 Experimental Setup

The same burner used in [29,117] was used in this study, shown in Figure 6.2. The burner consists of five independently controlled slots with the same velocity issuing from each, but with different equivalence ratios. The slots issued into a 100 mm long converging nozzle, which smoothening the discrete gradients between neighboring slots. The nozzle had a 9:1 contraction ratio (3:1 in each direction) which transitioned from 75 × 120 mm to 25 × 40 mm to create a near plug flow velocity profile. A 12.7 mm thick, 3.175 mm cell aluminum honeycomb was inserted at the inlet of the nozzle, while a 6.35 mm thick, 1.6 mm cell steel honeycomb was inserted at the exit. A 5 mm nitrogen guard surrounded the burner exit to lessen effects from room air. Additional details are available in [117].

Two cases were studied, creating either one or two stoichiometric points. In the case of a single stoichiometric point, only one triple flame was produced by supplying slots 1 and 2 with nitrogen, 3 with a rich mixture, 4 with a lean mixture, and 5 with air. To create two stoichiometric points, and therefore two triple flames, slots 1 and 5 were supplied with air, 2 and 4 with a lean mixture, and 3 with a rich mixture. The rich equivalence ratio (ϕ_R) slot was changed to adjust the equivalence ratio gradient ahead of the flame base, while the lean equivalence ratio (ϕ_L) was changed to move the

stoichiometric locations of the two triple flames. For a single triple flame, ϕ_L was kept constant at 0.75 while ϕ_R was varied from 1.25 – 8. For interacting triple flames, ϕ_L was 0.5, 0.75, or 1, while ϕ_R varied from 1.25 – 8. Both propane diluted with helium and methane diluted with argon were used in this study, with fuel percentages of 62% and 45%, respectively. These diluents and dilution ratios were chosen to obtain the same mean mixture molecular weight as air. This allowed different fuels and varying equivalence ratio gradients to be tested in the burner with minimal change in the density field. Thus, the upstream flowfield for all cases were similar.

Planar laser induced fluorescence (PLIF) was used to measure the flame curvature at the flame base. The curvature has been found to be linearly correlated to the fuel concentration gradient ahead of the flame base [32] and verified in other works [29,34–36,117]. A Sirah Cobra-Stretch dye laser was pumped with the frequency doubled output of a Spectra Physics Quanta Ray LAB 170 Nd:YAG laser, shown in Figure 6.12. The dye laser was tuned to excite the $Q_1(5)$ transition of the $A^2X^+ \leftarrow X^2\Pi(1,0)$ band of OH at 282.67 nm. The beam was formed into a sheet using an f = 500 mm converging lens and an f = -30 mm diverging lens. The fluorescence was imaged onto a Photonis XX1950LP imaging intensifier with a Universe Kogaku UV 1054B lens. A 320 $\pm$ 20 nm filter was placed in front of the intensifier to avoid scattering from the burner walls. The intensifier phosphor screen was imaged using a Mightex CGN-B013-U camera. 300 images were collected, averaged, and processed for each case. The curvature was extracted by obtaining the 30% of the maximum intensity contour of the image and curve fitting a circle of best fit to the center 4 mm of the leading edge of the lower triple flame. The projected resolution was approximately 13 pixels per millimeter.

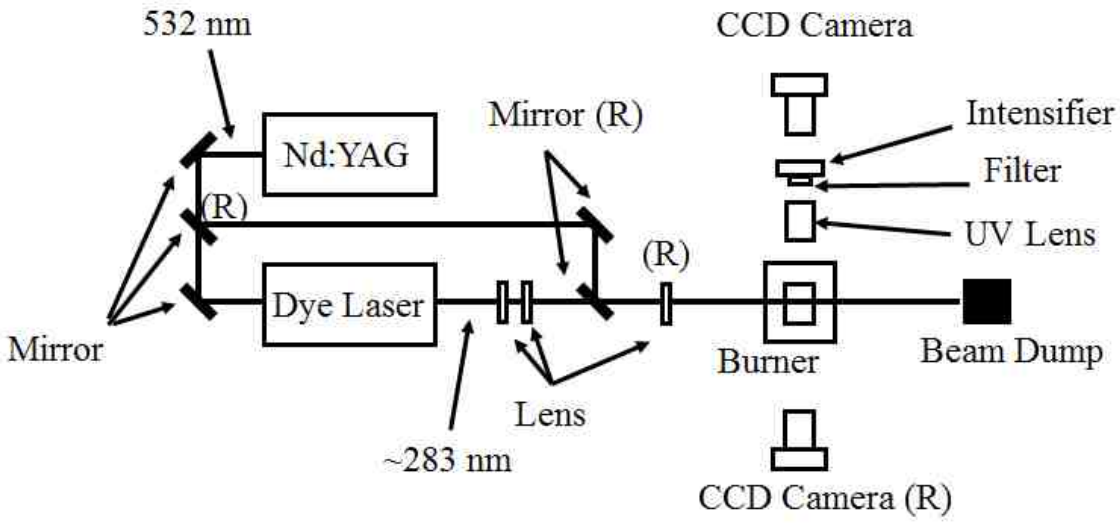

Figure 6.12: Experimental laser setup. Items marked (R) were used for Rayleigh scattering.

Rayleigh scattering was separately conducted on interacting triple flames to measure the fuel distribution upstream of the flame and compute the stoichiometric separation distance between the two triple flames. The 300 mJ per pulse frequency doubled output of the Spectra Physics Nd:YAG bypassed the dye laser and was rerouted to the combustor section, shown in Figure 6.12. The beam was formed into a 9 mm sheet by using a single f = 500 mm cylindrical lens. Images were collected using a Mightex CGN-B013-U camera and gated for 200 μs. The projected resolution was approximately 36 pixels per millimeter. Fuel concentration gradients were extracted by taking both a nitrogen background image and fuel only image and utilizing Eq. (6.6) to obtain the fuel concentration field, assuming that the diluent, oxygen, and nitrogen all have similar Rayleigh cross sections [29,117], where S_P is the processed Rayleigh signal, S is the mixture signal, S_{N_2} is the nitrogen background, S_F is the fuel background, and X_F is the fuel mole fraction. Although, these species do have differing Rayleigh cross sections [114], the signal can be calibrated to obtain a linear relationship using known equivalence

ratios [29]. In past studies [29,117] nitrogen was used as the fuel diluent, leading to only a difference in nitrogen to oxygen scattering cross-sections. In the current study, both argon and helium are used as diluents, which adds another species to the mixture. However, helium has a very small Rayleigh cross section, and argon is sufficiently similar to both oxygen and nitrogen such that a single linear calibration curve was observed to describe all of the mixtures studied. The calibration led to linear relationships via Eq. (6.6) with R^2 values greater than 0.99, leading to sufficiently accurate mole fraction measurements.

$$S_P = \frac{S - S_{N_2}}{S_F - S_{N_2}} \approx X_F \tag{6.6}$$

The characteristic propagation velocity for this flame structure was defined as the velocity far enough upstream of the flame base to be unperturbed by the diverging streamlines that are characteristic of triple flames. Similar to [33,115,117], the propagation velocity was characterized by beginning with a steady, laminar, lifted, flame and increasing the velocity by small increments while keeping the slot equivalence ratio unchanged until blowout occurs. When blowoff occurred, the velocity was lowered by 1 cm/s, (as this was the smallest velocity change controllable by the flow system) the flame was relit and measurements were taken. This ensured that the flame structure did not affect the burner exit velocity profile, and therefore the characterized propagation speed. Therefore, the blowoff velocity is the speed at which the streamlines can no longer diverge sufficiently to allow the flame to stabilize. This was demonstrated in [117] by obtaining the burner exit velocity profile at velocities leading to blowoff. Far from blowoff, the diverging streamlines affected the velocity profile at the burner exit. When the flame was pushed

closer to blowoff, the effect was lessened until the last stabilization velocity which had a negligible effect on the velocity profile. Velocity measurements were not conducted in this study because in [117] it was found that the velocity profiles were flat with less than 1 cm/s differences along the burner exit. Also, the mean measured velocity profiles and set velocities were a maximum of 3 cm/s different across all cases leading to the same trends and observations using velocity measurements or velocity set points. Flames were always checked prior to measurements to be uniform in the out-of-plane direction at the measurement location to ensure an accurate curvature measurement.

6.2.3 Results and Discussion

6.2.3.1 Curvature, Velocity, and Stoichiometric Distance Measurements

Examples of PLIF images for both methane and propane cases are shown in Figure 6.13 with the 30% maximum intensity contour and circle of best fit for curvature for each case. The circle of best fit was fit to data along the leading edge of the flame which spanned 4 mm in the X-direction. In past work [29], it was shown that for symmetric equivalence ratio gradients, the curvature of the leading edge is sufficient to characterize the interacting flame structure. Flames shown in Figure 6.13 are at different liftoff heights. In [117] velocity measurements were sampled using non-reacting data at different heights which showed less than 1 cm/s changes. Therefore, the exit velocity magnitude sufficiently characterized the propagation speed regardless of the liftoff height.

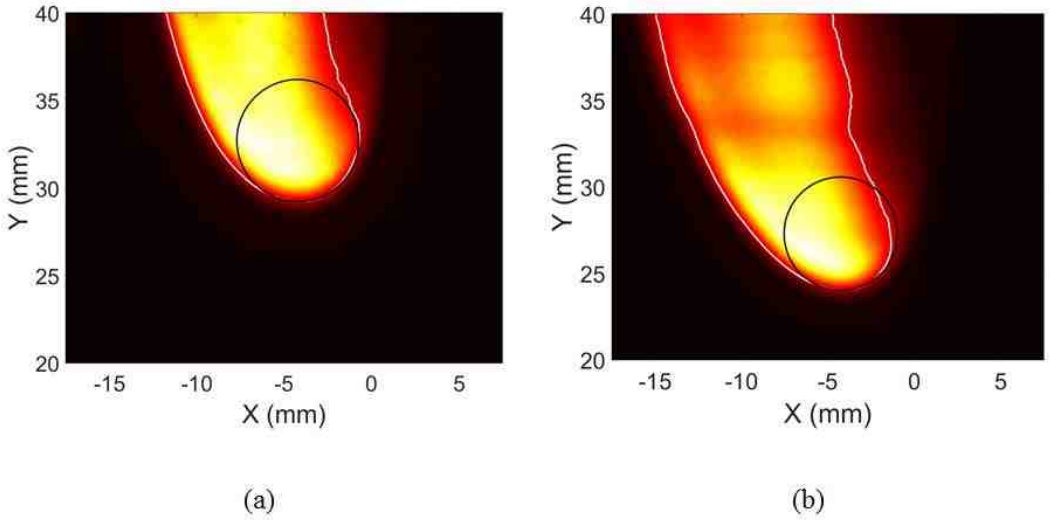

Figure 6.13: Example of averaged PLIF images of (a) methane and (b) propane with ϕ_L = 0.75 and ϕ_R = 2.25. The colormap represents the OH PLIF intensity, white line is the 30% maximum intensity contour, and black line is the circle of best fit to the leading edge curvature.

The curvatures were measured for each case using both methane and propane and are shown in Figure 6.14 versus the respective propagation velocities. Both the methane and propane cases show similar trends as found in [33,115,117]; for sufficiently high equivalence ratio gradients (or curvatures), a decrease in the gradient leads to linearly faster propagation speeds because the flame base is larger, which increases the diverging streamlines ahead of the flame base. There exists a critical gradient, except for the ϕ_L = 1 cases, for which a reduction in the gradient leads to slower propagation speeds. This is likely the case where the diffusion tail is sufficiently weakened and does not keep the triple flame structure [33,117]. Points which were below the critical concentration gradient were shown as open symbols in Figure 6.14. For both methane and propane, the single triple flame always propagates slower than the interacting triple flames for a given curvature, consistent with [117]. Also, with increasing interaction, or decrease ϕ_L, the slopes of the

propagation speeds increase, due to the flames being closer and therefore having increased interaction.

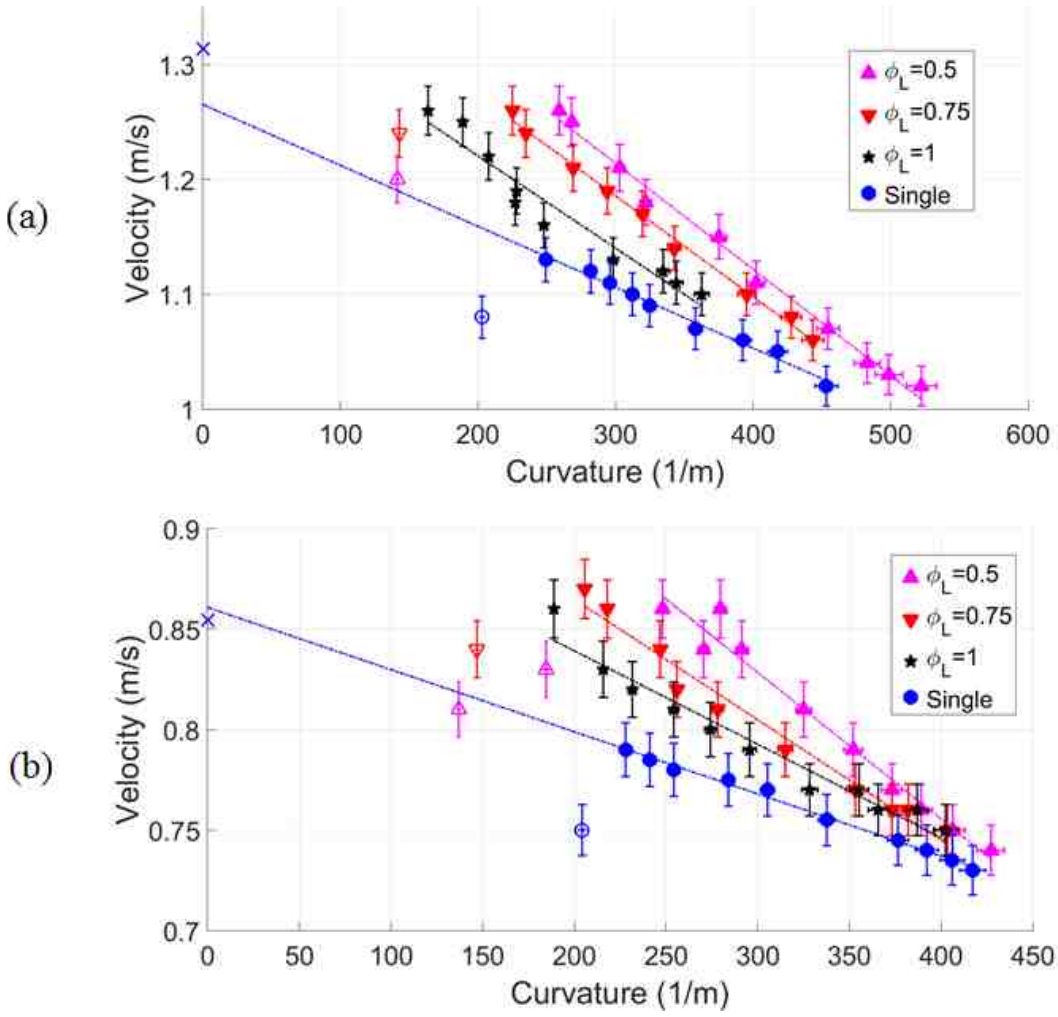

Figure 6.14: Propagation velocities versus curvatures for (a) propane and (b) methane for both the single and interacting triple flames. The single triple flame linear relation was plotted as a diamond at zero curvature for reference. The squares at zero curvature is the calculated asymptotic limit from Eq. (6.7). Closed symbols represent the points which were used in the linear regression calculations.

The asymptotic limiting propagation speed that occurs at zero equivalence ratio gradient was calculated using the relationship developed by [28] and using the ideal gas law, shown in Eq. (6.7) where U_F is the triple flame propagation speed, S_L is the flat premixed laminar flame speed, T_b is the adiabatic flame temperature, and T_u is the unburnt

reactants temperature. S_L and T_b were calculated using Cantera [116] with chemistry, transport, and thermodynamic data from GRI Mech 3.0 [108]. The calculated propagation velocities are shown as squares in Figure 6.14 to compare against the extrapolated zero gradient velocity. Methane exhibits similar zero gradient propagation speeds when diluted with argon, similar to [33]. Interestingly, in other work by the same group [115], it was found that methane diluted with nitrogen had lower propagation speed than the calculated asymptotic limit. Findings in this work show that using even 65% argon as the diluent did not alter the zero gradient velocity. Though, propane diluted with helium was found to have a lower measured propagation speed compared to the calculations. Experiments in microgravity [34] showed that buoyancy also effected triple flame propagation speeds. Zero intercept propagation speeds which did not follow the asymptotic analysis in normal gravity conditions did in microgravity. Therefore, the propane zero gradient propagation speed may be effected by buoyancy, but it is not clear from this work.

Each interacting triple flame case was found to have a maximum propagation speed within 1 cm/s of the zero gradient velocity extrapolated from the single triple flame. This is similar to findings in [117], where it was suggested the extra flow divergence obtained from the interacting flames was enough to approach what would be obtained by a wider triple flame potentially reaching the limiting zero equivalence ratio gradient case. The findings from this work confirm that interacting triple flames with different fuels have the same limiting velocity; the single triple flame relationship extrapolated to zero equivalence ratio gradient. This gives more evidence to support the idea that the interacting triple flames are able to mimic an infinitely wide triple flame reaching the asymptotic limiting velocity. This also supports the conclusion made by Kostka *et al.* [29], which showed that

the interaction between neighboring triple flames is only via aerodynamic interactions, as opposed to chemical interactions, because each fuel shows similar results in regards to the interacting triple flames.

$$U_F = S_L(T_b/T_u)^{\frac{1}{2}} \tag{6.7}$$

In order to further characterize the interactions with different fuels, the interaction parameter defined in [29] was measured for each case, similar to [117]. The interaction parameter, ψ, is given by Eq. (6.8) where ρ_i is the radii of curvature of the two interacting flame fronts, and δ_{st} is the stoichiometric separation distance between the two triple flames. Since the two equivalence ratio gradients are the same, the curvature of the leading triple flame, ρ, was used for both flames.

$$\psi = \frac{\rho_1 + \rho_2}{\delta_{st}} \sim \frac{2\rho}{\delta_{st}} \tag{6.8}$$

A sample fuel concentration profile from both the methane and propane case is shown in Figure 6.15. The profiles were obtained from the two dimensional Rayleigh scattering field utilizing Eq. (6.6), the linear calibration to fuel concentration, and subsequently averaging 5 mm in the Y-direction to obtain the profiles. A Gaussian fit was applied to the data to obtain a smooth line and the stoichiometric distance was then measured using the fit.

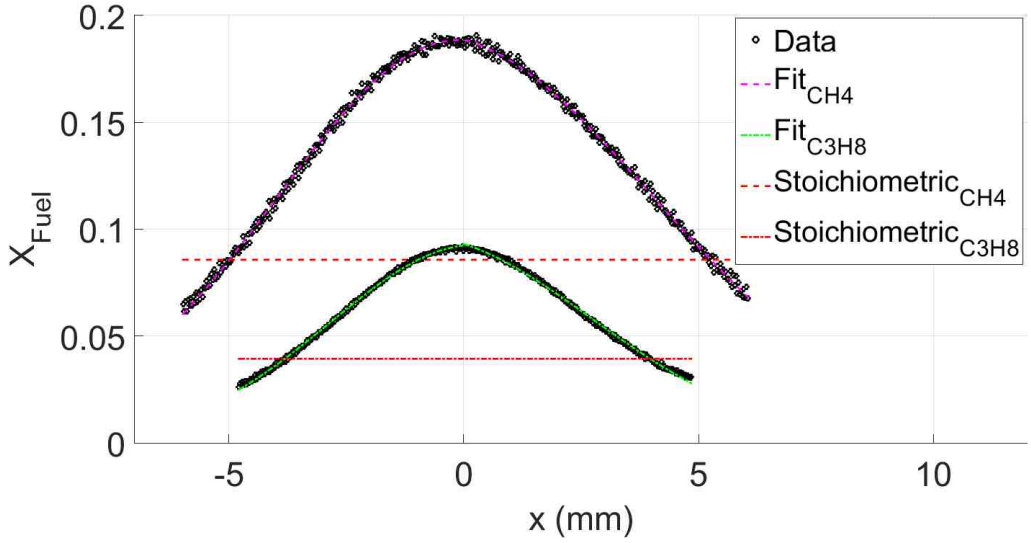

Figure 6.15: Example fuel mole fraction profiles of propane ϕ_L = 0.75, ϕ_R = 2.5 and methane ϕ_L = 0.75, ϕ_R = 6.

6.2.3.2 Propagation Speed Model

Previous work in [117] modeled the propagation speed of ethylene diluted with nitrogen using the idea that triple flame interactions increase the flow divergence in the same way as a wider single triple flame, thus altering the effective width (or curvature) of the flame structure. This concept was used to take advantage of the known behavior between flame curvature and propagation speed for single triple flames and to capture limiting behavior such that with zero interaction, multiple triple flames should propagate at the single triple flame speed. Conversely, infinite interaction nearly leads to zero effective curvature, or the zero gradient propagation speed for a single triple flame. Single triple flames have been shown to be linearly proportional to the equivalence ratio gradient ahead of the flame base, or curvature, and therefore can be used in this work. Equation (6.9) shows the linear relationship where V is the propagation speed, m is a linear constant, and b is the zero gradient propagation speed for a single triple flame. An effective curvature, C_{eff}, was defined as $C_{eff} = C \times f(\psi)$, where C is the measured curvature, and

f is the degree of interaction defined by ψ. The same approach was used in this work for both methane and propane. The interacting triple flame effective curvature, C_{eff}, was computed using the linear relationship for a single triple flame. For the actual measured velocity of the interacting flame, the curvature required to achieve this velocity for a single triple flame was computed from the data in Figure 6.14. The ratio of this effective curvature to the actual measured curvature was then computed to determine $f(\psi)$ as found in [117]. These results are shown in Figure 6.16 using points above the critical concentration gradient, and it appears that the same error function shape can be used as found in [117], which ensures correct limiting behavior. An error function was fit to each of the data sets with three different fuels as also shown in Figure 6.16 by the dotted lines. The three different fuels show very similar results as the ethylene case, but there is a slight difference between the three cases. Ethylene displays a slightly larger effective curvature ratio for a given interaction parameter, followed by propane, and finally methane. A fit to all of the fuel data together are shown as a solid line in Figure 6.16 and the parameters for this fit is given in Eq. (6.9).

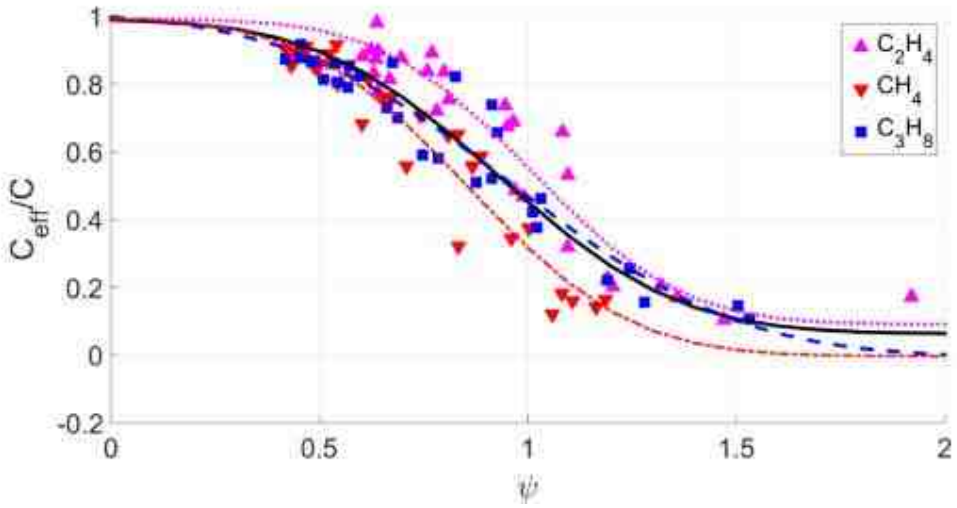

Figure 6.16: Effective curvature ratio plotted against the interaction parameter to obtain a functional shape, $f(\psi)$. The line represents the modeled line, given in Eq. (6.9).

$$V = mC_{eff} + b \tag{6.9}$$

$$C_{eff} = C \times f(\psi)$$

$$f(\psi) = -0.46\,\mathrm{erf}\big(2.1(\psi - 0.93)\big) + 0.53$$

The ability of this single curve to describe the interacting flame propagation speeds for all three fuels is shown in Figure 6.17. For each case the measured flame curvature and interaction parameter were used to compute an expected propagation speed which was compared to the actual measured value. This model is able to calculate each of the measured velocities with a maximum error of 3.5 cm/s, regardless of the fuel being used. This confirms that the interacting triple flames have essentially only aerodynamic effects, as suggested by Kostka *et al.* [29], because each fuel shows similar results in regards to the interacting triple flames. Differences in chemistry or fuel diffusivity are negligible on altering the flame interactions. Differing fuel properties do alter the laminar premixed flame speed; however, modification to this speed caused by triple flame interactions can be considered independent of the fuel.

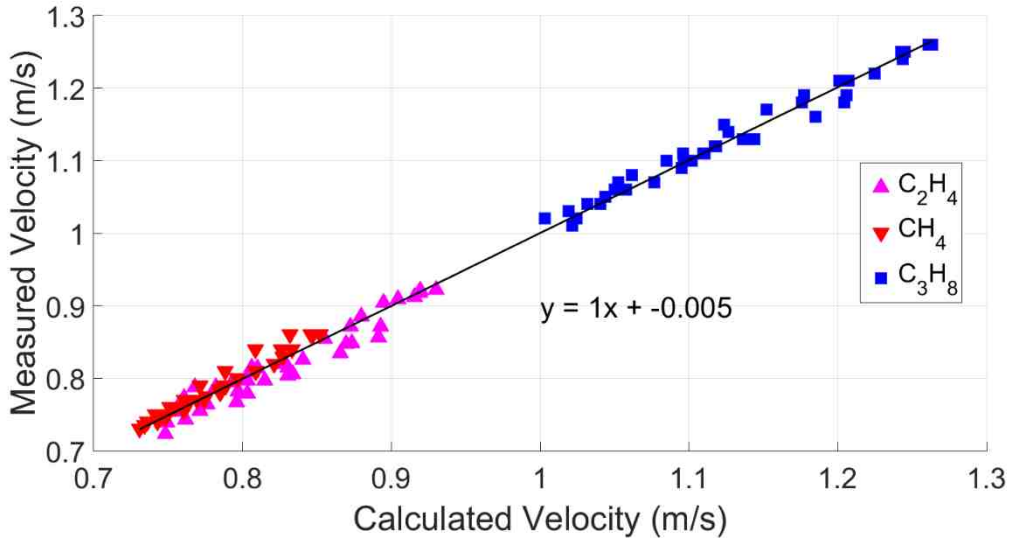

Figure 6.17 Measured propagation speed plotted against calculated speed using Eq. (6.9).

6.2.4 Conclusions

Propagation velocities for single triple flames and interacting triple flames were measured for methane diluted with argon and propane diluted with helium. Similar results were observed as found in [117] for ethylene, where interacting triple flame propagation speeds were larger than a single triple flame resulting from the effectively larger width of the flame structure. Both new fuels studied here also showed that the asymptotic limiting velocity at zero equivalence ratio gradient for a single triple flame was the maximum velocity achieved for all interacting cases with a given fuel mixture. These results indicate that the aerodynamic effects associated with interacting triple flame maximizes the single triple flame velocity by adding an effective width (or curvature) until the zero gradient velocity is reached. Reduction in the equivalence ratio gradient beyond the zero intercept velocity led to a reduction in propagation speed.

The interaction between the two triple flames was also measured. An effective curvature, using the single triple flame linear relationship between curvature and

propagation speed was computed and a similar functional form as developed in [117] for both fuels was found to describe this effective curvature as a function of the triple flame interaction and curvature. The model was shown to describe all interacting flame velocities for ethylene, methane, and propane within 3.5 cm/s. Therefore, the model is sufficient to predict interacting triple flame propagation velocities given the single triple flame propagation velocity versus curvature relationship and the stoichiometric separation distance. The results indicate that only aerodynamic effects are found between interacting triple flames, because a single model based on the interaction parameter can be used to model the propagation speeds for three different fuels. Thus, fuel properties do not affect the interacting triple flame model, but differences are captured in the single triple flame propagation speed relationship.

7 Negative Edge Flames

In work by Carnell and Renfro [48] negative edge flames were studied in a diffusion flame. Classic counterflow diffusion flames studies have been used to characterize extinction with given boundary conditions, which leads to a balance between heat release and diffusion heat loss. Negative edge flames in [48] found that the advective heat flux also plays a crucial role in the physics of negative edge flames. The authors found that along the fully burning diffusion flame the energy equation was just a balance between chemical heat release and diffusive heat loss, similar to classic counterflow diffusion flames. Near the extinguishing edge however, there was an additional important term, the advective heat flux. It was found that the advective heat flux acted as an energy gain term which allowed the flame to stabilize at higher scalar dissipation rates than the 1-D extinction scalar dissipation rate. Numerical simulations were performed with larger inner nozzle diameters which produced larger advective heat flux through the edge while keeping the stable diffusion flame constant. The additional scalar dissipation rate at the extinction point was also linearly proportional to the advective heat flux at the edge.

The findings from [48] helped understand the role each term in the energy equation had at the edge, in particular the role of the radial advective heat flux through the edge. Chapter 7.1 in this dissertation expands upon this work by understanding that only three energy terms are important at and through the negative edge flame. Therefore, a simple model was produced that simulated the stoichiometric contour in the radial direction to predict when and where extinction occurs. Furthermore, centerline numerical simulations were also used which nearly replicated the same profiles through the negative edge.

While steady negative edge flames were well understood from [48], unsteady negative edge flames have not been extensively explored. In particular, the dynamical behavior and the influence of each energy term at the edge have not been previously examined. Chapter 7.2 simulates similar conditions as [48] but instead introduces unsteady periodic outer nozzle flows to create transient negative edge flame behavior. The energy terms were examined in the periodic environment to determine the role of the unsteady energy term with different frequencies at the boundary. Negative edge flame velocities were also examined and a new physical interpretation of the edge velocity was derived.

Lastly, Chapter 7.3 uses a burner which was recently designed and built to measure the negative edge velocity at different turbulence intensities. Although most work to this point with respect to negative edge flames have been performed in laminar environments, most applications will use turbulent flowfields which may produce negative edge flames. Therefore, negative edge flames need to be better understood in turbulent environments. A stereo-view setup was used to extract the flame and flow velocity in the center plane of the burner to measure negative edge flame velocities in a turbulent flow. The advective heat flux and turbulence intensity was varied which effected the negative edge flame velocity which will be presented in Chapter 7.3.

7.1 Steady Negative Edge Flame Model

Work by Carnell and Renfro [48] numerically examined negative edge flames in a modified counterflow configuration which created steady and laminar negative edge flames. In most cases, only three terms in the energy equation were non-negligible to characterize the conditions at the edge. Although the energy physics is dominated by three terms, two-dimensional flow simulations are still primarily used to calculate negative edge

flame behavior. With the limited number of variables, a simplified model can be produced which could predict the negative edge flame behavior without using full two-dimensional flow simulations.

The goal of this work is to develop a simplified model capable of predicting when and where a negative edge flame may form in a similar environment as [48], but without full flow simulations. The model will be capable of calculating each non-negligible term in the energy equation along the stoichiometric line to predict the behavior upstream and through the negative edge. First, the model will be developed using negative edge flame two-dimensional flow simulations to better understand each important energy term and help identify how to calculate each term in a simple way. The second step of this work is to use one-dimensional information along the centerline of a counterflow flame to predict the modeled terms without computing a two-dimensional negative edge flame simulation.

7.1.1 Numerical Setup

A model will be developed using the same modified counterflow burner as the one shown in Figure 3.2. Multiple two-dimensional flow simulations of similar geometries were also performed in this sub-chapter in order to provide data along the stoichiometric line to aid in the model development. A brief description of the burner and numerical domain setup will be given here, but additional details are provided in Chapter 5.2. The burner consists of two opposed flow coannular nozzles. The top nozzles supply nitrogen diluted methane while the bottom nozzle supplies air. The inner nozzles provide low velocities of the given mixtures to establish a stable and steady counterflow diffusion flame. The outer nozzles provide the same concentration mixtures, but at higher velocities which leads to an increase in scalar dissipation rate in the radial direction which locally

extinguishes the flame via heat loss, as opposed to species deficiency. This geometry creates steady negative edge flames.

The negative edge flame model has been designed for a single geometry, however multiple counterflow geometries were used to provide sufficient information at the negative edge to model the terms in the energy equation. The following details describe the two-dimensional computational domain which provided multiple negative edge flames and is shown in Figure 7.1. Although Figure 7.1 shows the domain being constant size, the inner nozzles radius was varied in order to provide different advective heat fluxes through the edge, similar to [48]. The inner nozzles provide low velocity flow which stabilize a steady counterflow diffusion flame while the outer nozzles supply high velocity gas which radially increases the scalar dissipation rate and locally extinguishes the flame. The inner nozzle radius was varied using 10, 20, 40, 60, and 80 mm radii. Larger inner nozzle radii holds the flame strength nearly constant by providing a similar scalar dissipation rate upstream of the outer nozzle, however, the velocity through the negative edge increases and therefore the advective heat flux increases as well. This provides more data through the edge to provide a more generalized model of each individual term in the energy equation. The inner nozzle also provides varying inner nozzle velocities ranging from 8 to 22 cm/s to change the advective heat flux through the edge. The increased velocity will provide more bulk flow through the edge, but will also weaken the flame leading to lower flame temperatures and likely lower temperature gradients through the edge. Therefore, the simple increase in inner nozzle velocity will not necessarily increase the advective heat flux. The outer nozzle was held geometrically constant by maintaining a 25 mm long exit in the computational domain. Several outer nozzle velocities were also

used in the simulations which varied from 24 to 72 cm/s. The fuel concentration was also changed from 18% to 25% methane by volume which was diluted with nitrogen. A cooling jacket wall present in related experiments was also included in the simulations at the end of the outer nozzle domain and was simulated as walls. The boundary condition on the far right of Figure 7.1 is a pressure outlet and was modeled as 300 K nitrogen flow. All inlet boundary conditions and walls were modeled at 300 K.

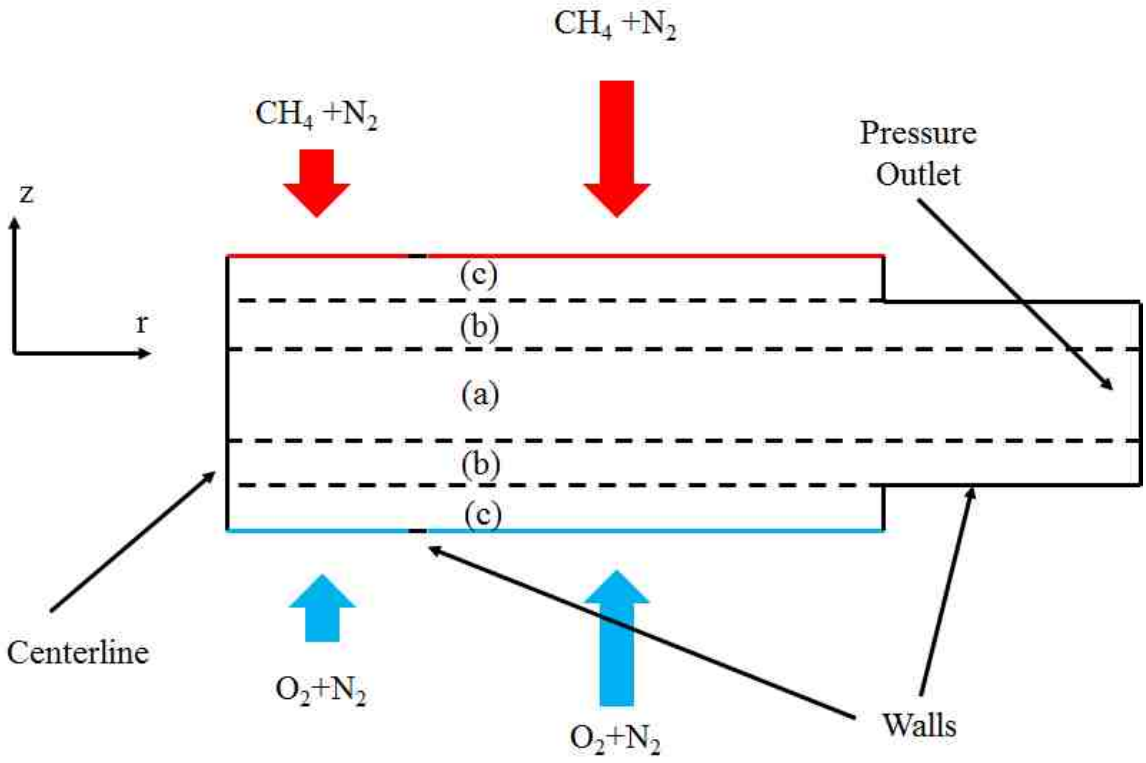

Figure 7.1: Two-dimensional computational domain of the modified counterflow diffusion flame burner to produce laminar and steady negative edge flames.

Three mesh resolutions were used in order to resolve different regions of the flow. The mesh in each respective region was designed to be square and uniform. Regions labeled (c) in Figure 7.1 were 2.5 mm long in the z-direction and maintained 0.25 mm grid resolution to simply resolve the nearly uniform species flow. Regions (b) extended another 2.5 mm toward the center of the burner in the z-direction and had a grid resolution of 0.125

mm which was used to resolve the region with a temperature gradient. Region (a) comprised the center 5 mm of the burner in the z-direction and had the highest grid resolution of 62.5 μm which was meant to fully resolve the reaction layer. These grid resolutions have been verified in [48] to be sufficient to resolve each of the respective regions. The same numerical scheme used in Chapter 5.2.2 was also implemented in this work.

7.1.2 Results and Discussion

7.1.2.1 Model Development Using Negative Edge Flames

The stoichiometric line was determined by calculating the mixture fraction field, and the contour of a stoichiometric mixture was sampled. The mixture fraction was derived using Bilger's definition [118], defined in Eq. (7.1), and applied using methane, shown in Eq. (7.2). In these equations, Y_i refers to the respective element mass fraction, the superscript F and O refer to the values at the fuel and oxidizer side respectively, n and m to the number of hydrogen and carbon atoms in the fuel, and ν'_{O_2} to the stoichiometric coefficient of oxygen. The energy equation, given in Eq. (7.3), must be satisfied at each point in the numerical simulation, and each term can be individually calculated along the stoichiometric contour. In Eq. (7.3) ρ is the density, c_p is the specific heat capacity at constant pressure, V_r is the radial flow velocity, V_a is the axial velocity, T is the temperature, λ is the thermal conductivity, h_i is the i^{th} species enthalpy, $\vec{J_i}$ is the diffusive flux of the i^{th} species, $\dot{\omega}'''$ is the volumetric kinetic rate of reaction, and Δh is the enthalpy of combustion for the given chemical reaction.

$$Z = \frac{\frac{Y_C}{mW_C} + \frac{Y_H}{nW_H} + \frac{Y_O^O - Y_O}{\nu'_{O_2} W_O}}{\frac{Y_C^F}{mW_C} + \frac{Y_H^F}{nW_H} + \frac{Y_O^O}{\nu'_{O_2} W_O}} \tag{7.1}$$

$$Z = \frac{\frac{2Y_C}{W_C} + \frac{Y_H}{2W_H} + \frac{Y_O^O - Y_O}{W_O}}{\frac{2Y_C^F}{W_C} + \frac{Y_H^F}{2W_H} + \frac{Y_O^O}{W_O}} \tag{7.2}$$

$$0 = -\rho c_p \left(V_r \frac{\partial T}{\partial r} + V_a \frac{\partial T}{\partial a}\right) + \lambda \left(\frac{\partial^2 T}{\partial r^2} + \frac{\partial^2 T}{\partial a^2} + \frac{1}{r}\frac{\partial T}{\partial r}\right) + \frac{\partial \lambda}{\partial r}\frac{\partial T}{\partial r} + \frac{\partial \lambda}{\partial a}\frac{\partial T}{\partial a} - \sum_i \nabla \mathrm{h}_i \cdot \vec{J_i} + \dot{\omega}''' \Delta h \tag{7.3}$$

The individual terms from Eq. (7.3) can be calculated and assessed through the negative edge. Similar to [48], many energy terms are negligibly small. Effects of energy by species transport, $\sum_i \nabla \mathrm{h}_i \cdot \vec{J_i}$, is negligible since the diffusive velocities are small with respect to the local flow velocities. Furthermore, the geometrical term, $\frac{1}{r}\frac{\partial T}{\partial r}$ is negligible indicating that the burner geometry does not affect the negative edge flame behavior. Terms arising from the thermal conductivity gradient, $\frac{\partial \lambda}{\partial r}\frac{\partial T}{\partial r}$ and $\frac{\partial \lambda}{\partial a}\frac{\partial T}{\partial a}$, are also negligible. The axial advective term, $-\rho c_p V_a \frac{\partial T}{\partial a}$, was also shown to be negligible until downstream of the extinction event. Therefore, a simplified energy equation can be used, given in Eq. (7.4), which is simply a balance between the axial and radial diffusive heat losses with the radial advective heat flux and chemical heat release. The remaining terms were calculated and shown in Figure 7.2. Often times, the radial diffusive heat loss is negligible, but is included in this analysis.

$$0 = -\rho c_p V_r \frac{\partial T}{\partial r} + \lambda \frac{\partial^2 T}{\partial a^2} + \lambda \frac{\partial^2 T}{\partial r^2} + \dot{\omega}''' \Delta h \tag{7.4}$$

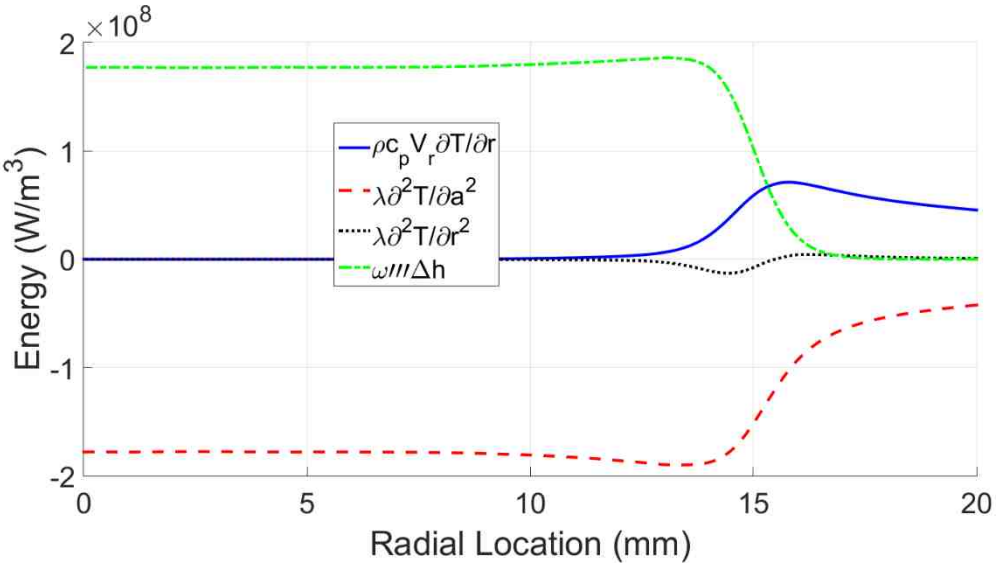

Figure 7.2: Energy balance of remaining four energy terms along the stoichiometric line with an inner and outer nozzle velocity of 20 and 40 cm/s respectively in a burner geometry with an inner nozzle radius of 10 mm.

A parameter often used in the combustion community is the so-called scalar dissipation rate which is defined in Eq. (7.5), where χ is the scalar dissipation rate, D is the species diffusion coefficient, and Z is the mixture fraction. A scaling parameter also often used is the Lewis number which is the ratio of the thermal diffusion (α) to the species diffusion (D). Methane has a Lewis number of approximately unity which allows the scalar dissipation rate to be rewritten with α to replace D. Although Eq. (7.4) is important, it does not directly have χ included. Therefore, a coordinate transformation was performed on Eq. (7.4) to include χ in the governing equation, shown in Eq. (7.6).

$$\chi = 2D(\nabla Z \cdot \nabla Z) = 2D\left(\left(\frac{\partial Z}{\partial r}\right)^2 + \left(\frac{\partial Z}{\partial a}\right)^2\right) \tag{7.5}$$

$$0 = \frac{\partial^2 T}{\partial Z^2}\rho c_p \chi - \rho c_p V_r \frac{\partial T}{\partial r} + \dot{\omega}'''\Delta h \tag{7.6}$$

Equation (7.6) is a relatively simple equation which may be modeled and can therefore predict the behavior through a negative edge flame. Since this model is being created along the stoichiometric line, the species composition is pre-determined and is constant. First, ρ is easily calculated if the temperature is known, via the ideal gas law since the molecular weight is constant. Similarly c_p values are tabulated with respect to temperature for all the species used in this work, and therefore is known if the temperature is known. Thus, $\frac{\partial^2 T}{\partial Z^2}$, χ, V_r, and $\dot{\omega}'''\Delta h$ are still unknown. However, if these terms can be sufficiently modeled, then only the radial temperature gradient is unknown and therefore the temperature profile can be numerically calculated.

The radial velocity, V_r, can be modeled using a hybrid between mass conservation and empirical fits. Three distinct regions were modeled and connected at the boundaries for continuity, which is fully modeled in Eq. (7.7) where V_r is the radial velocity, X_f is the fuel mole concentration, r is the radial location in meters, V_o is the outer nozzle velocity in cm/s, and V_i is the inner nozzle velocity in cm/s. The first thing to consider is where the stoichiometric line resides relative to the stagnation plane. The stagnation plane will have the largest radial velocity and will be lower as the stoichiometric line moves closer to either boundary. Other effects such as the flame temperature and density are also controlled by the fuel concentration as well. Therefore, the radial velocity through each section should be a function of the fuel molar concentration. Also, the stoichiometric point relative to the stagnation point is also controlled by the inner nozzle velocity, and therefore should be included in the overall velocity model.

In the radial direction, beginning at the centerline the radial velocity must be zero by symmetry and linearly increases with radial location until reaching the outer nozzle;

therefore should be a function of the radius, and is shown in the second line of Eq. (7.7). Outside the transition region from the inner to outer nozzle region, mass conservations dictates that the radial velocity should follow the functional form shown in the last line of Eq. (7.7). To smoothen out the transition region a $r^2 + r$ function was used to match the boundaries and create a smooth matching, shown in the third line in Eq. (7.7). Only a single burner geometry with an inner nozzle radius of 10 mm was used to obtain the velocity model. The percent error using this model is shown in Figure 7.3 (a) using inner nozzle velocities ranging from 8 to 22 cm/s, outer nozzle velocities from 24 to 72 cm/s, and fuel concentrations from 18 to 26%. Most errors are under 5%, however there are a few conditions which have almost 15% error. An example of the velocity profile with the second most error is shown in Figure 7.3 (b). Overall, this model sufficiently captures the radial velocity through the edge.

$$V_r = \left(2.927 \times X_f + 2.256\right) \times V_i \times G(r)$$

$$G(r) = \begin{cases} r, & r < 9 \text{ mm} \\ r + 104 \times \left(\frac{V_o}{V_i} - 1\right) \times (r - 0.09)^2, & 9 < r < 15 \text{ mm} \\ \left[\frac{V_o}{V_i} + \left(1 - \frac{V_o}{V_i}\right) \times \left(\frac{0.013}{r}\right)^2\right] \times r, & r > 15 \text{ mm} \end{cases} \tag{7.7}$$

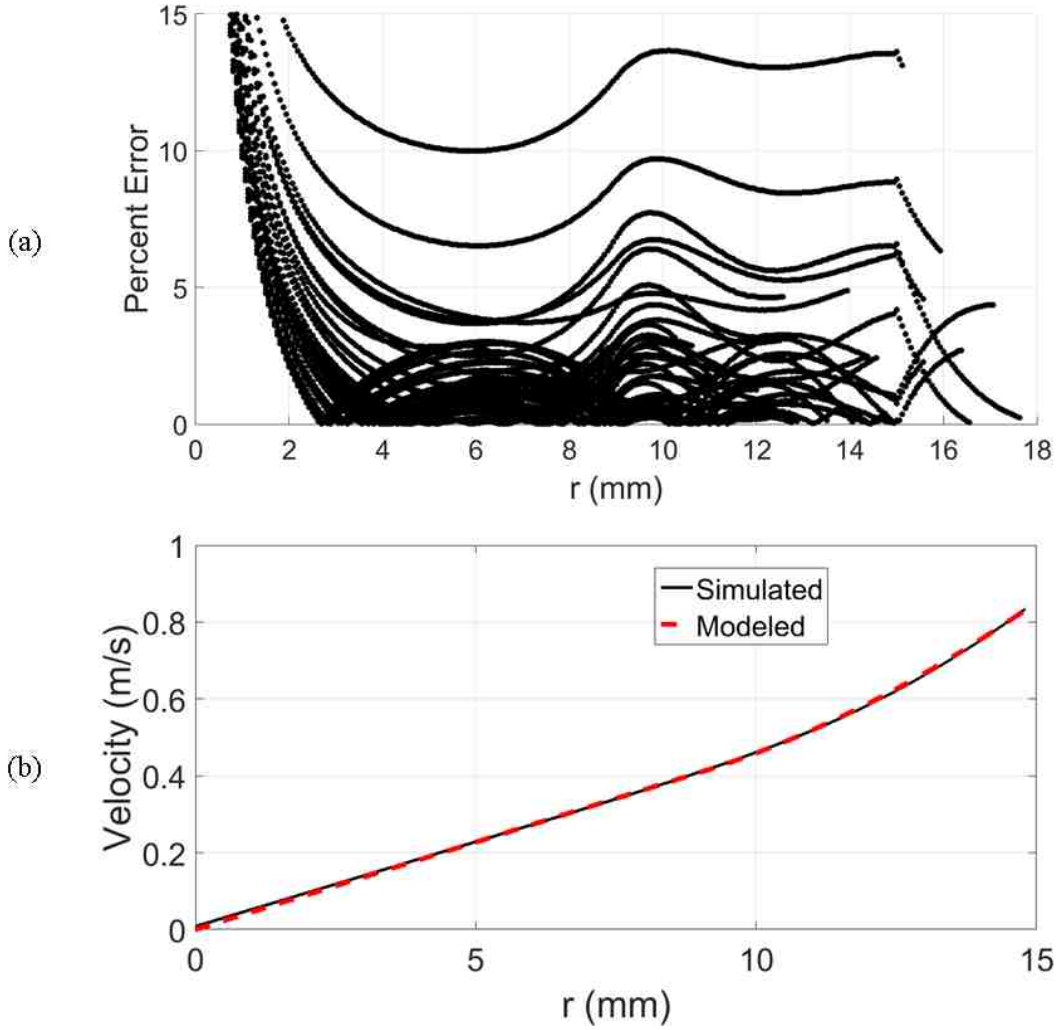

Figure 7.3: (a) Percent error between Fluent and the modeled velocity profiles in the radial direction using a range of velocities and fuel concentrations. 42 different simulations were used in this analysis. (b) Example velocity profiles with V_i = 16 cm/s, V_o = 32 cm/s, and X_f = 0.2.

The scalar dissipation rate is rather easy to approximate. At radial positions less than the inner nozzle radius, the scalar dissipation rate is constant until reaching the outer nozzle radius. If the outer nozzle radius is approximated as infinitely wide, the scalar dissipation rate will again be constant. Therefore, there is only a transition region between the inner and outer nozzle which needs to be modeled to approximate the scalar dissipation rate field. An error function was chosen as the functional form to capture the transition

from the inner and outer nozzle scalar dissipation rates since the error function is constant prior to the change, reaches the desired change and continues to be constant beyond the transition. The same cases were used to fit the scalar dissipation rate and the errors were plotted in Figure 7.4 (a) using the model in Eq. (7.8), where χ is the modeled scalar dissipation rate, χ_{CL} is the centerline scalar dissipation rate, r is the radial location in meters, and V_o and V_i are the outer and inner nozzle velocities in cm/s. An example profile which has the second most average percent error is plotted in Figure 7.4 (b). Therefore, only the inner and outer nozzle velocities are needed with the centerline scalar dissipation rate to model the scalar dissipation rate along the stoichiometric line for the modified counterflow negative edge flame.

$$\chi = \frac{\chi_{CL}}{2}\left[\left[\mathrm{erf}\left(\frac{r-0.0154}{0.00483}\right)+1\right]\left[\frac{V_o}{V_i}-1\right]+1\right] \tag{7.8}$$

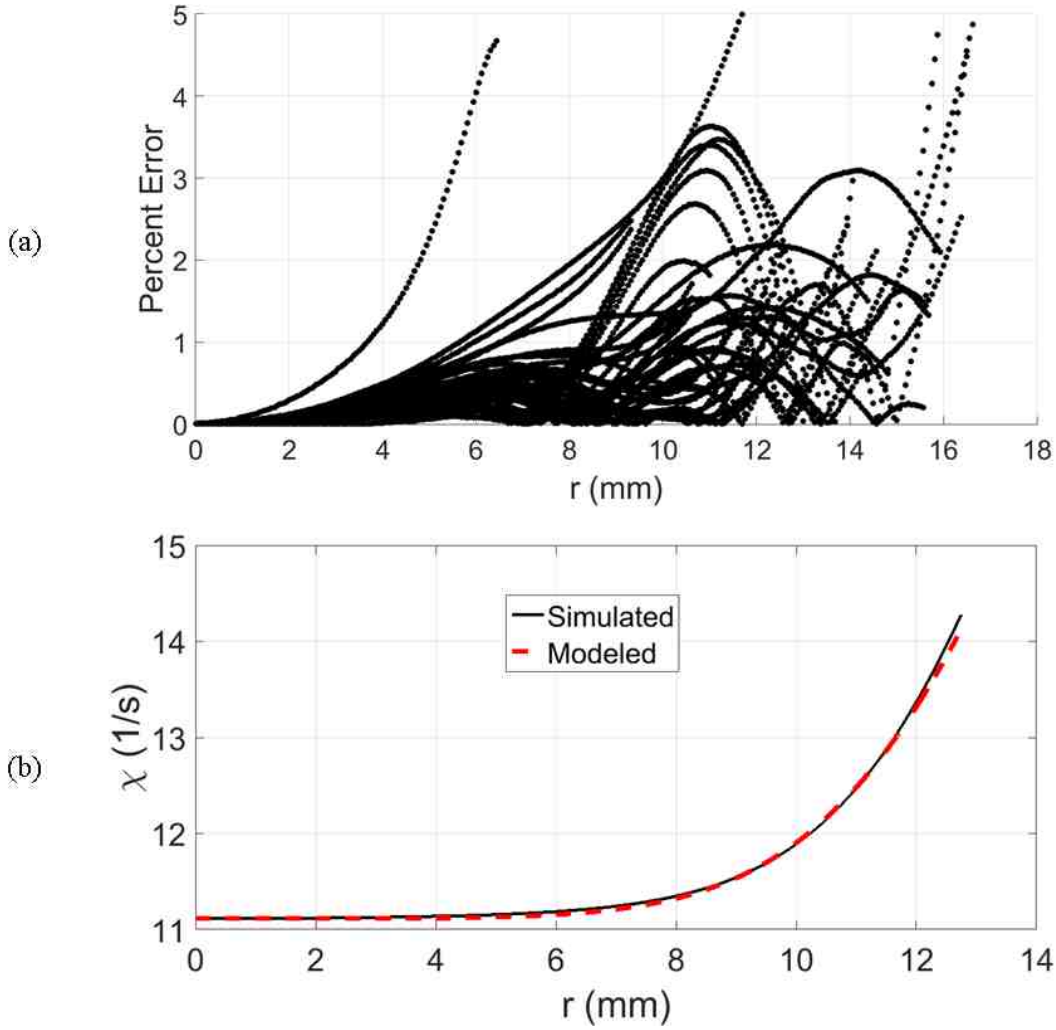

Figure 7.4: (a) Percent error between Fluent and the modeled scalar dissipation rate plotted along the radial direction over a variety of boundary conditions. 42 simulations were compared. (b) Example of the simulated and modeled scalar dissipation rates.

The remainder of the model development only used 20% fuel concentrations but different inner and outer nozzle velocities as well as inner nozzle diameters. Chemical kinetics determine the heat release rates and are highly dependent on temperature and species composition. The analysis is conducted along the stoichiometric line, so the species composition is known, however the temperature is not. Therefore, the heat release should be dependent on temperature. With this in mind, the heat release for a single fuel dilution of 20% methane and 80% nitrogen was calculated in Fluent with varying inner nozzle

velocities and diameters and outer nozzle velocities. For the purposes of understanding how the heat release behaves through the negative edge, the heat release was only analyzed from 1600 K and above since this is well below the extinction temperature of 1712 K from centerline counterflow diffusion flame studies [48]. The heat release for different temperatures along the stoichiometric line is shown in Figure 7.5. The plotted Fluent results are those for several different inner and outer nozzle velocities. Simply plotting the heat release with respect to the local temperature collapsed the data onto a fairly smooth line for all the different cases with the single fuel dilution. Therefore, a third order polynomial was fit through the data to characterize the heat release response with respect to different temperatures. It is interesting to note that as the temperature decreases from the maximum temperatures (~ 1830 K) there is a fairly sharp increase in heat release until reaching the extinction temperature (~1712 K), where the heat release becomes nearly constant. Past extinction the heat release decays rather smoothly, and therefore is not symmetric about the extinction temperature. For this reason a second order polynomial was not chosen, since it would maintain symmetry about the extinction temperature.

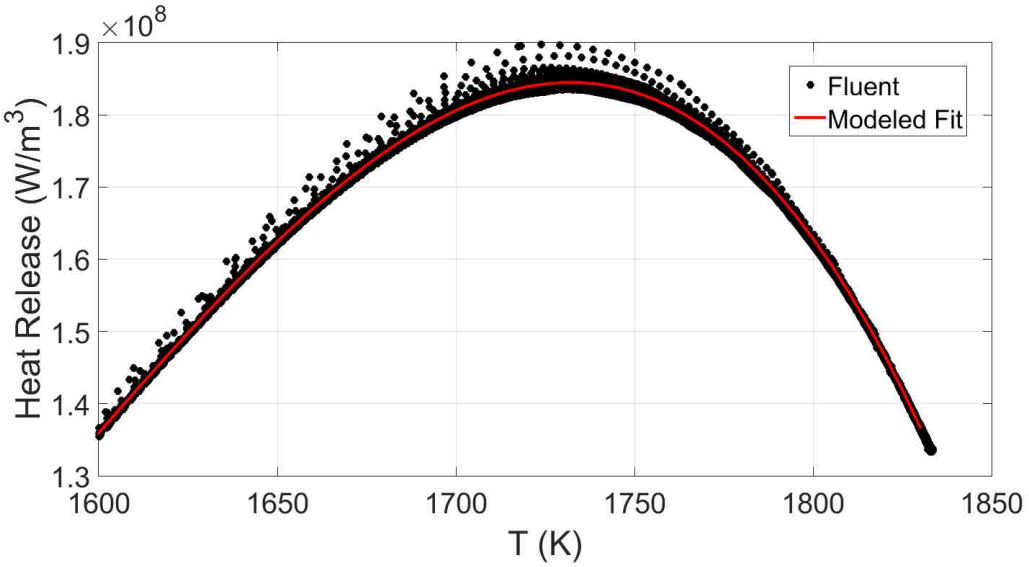

Figure 7.5: Heat release plotted versus temperature for multiple inner nozzle diameters and velocities and outer nozzle velocities for temperatures greater than 1600 K. The data points, labeled Fluent, were sampled along the stoichiometric contour. A third order polynomial was fit through the data as a model. 30 simulations were used to create this model which had varying inner nozzle diameters, inner nozzle velocities, and outer nozzle velocities.

There is only one term remaining that needs to be modeled before the radial temperature profile can be calculated, namely $\frac{\partial^2 T}{\partial Z^2}$. This term can be interpreted physically as the temperature diffusive response in mixture fraction space. This term can be instead written as $T\frac{\partial^2 f}{\partial Z^2}$, where f can be physically interpreted as the temperature diffusivity functional form in mixture fraction space. This diffusive term can also be interpreted as the thermal width of the flame, and therefore should be a function of scalar dissipation rate. This quantity was calculated along the stoichiometric line, and similarly limited to temperatures greater than 1600 K. The calculations were plotted in Figure 7.6 with respect to χ. There is very good agreement with this term across different scalar dissipation rates, and therefore a second order polynomial was fit through the data.

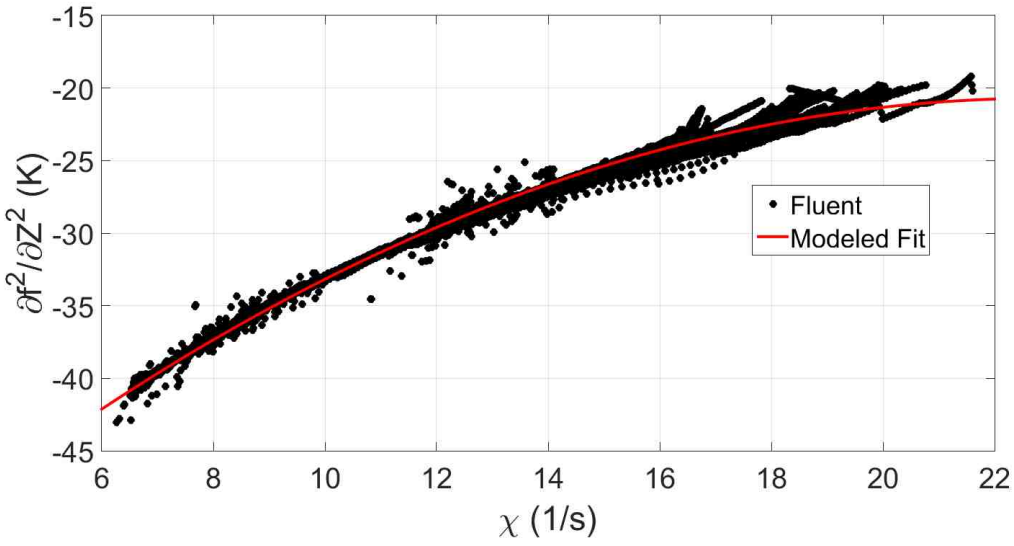

Figure 7.6: $\frac{\partial^2 f}{\partial Z^2}$ plotted against the scalar dissipation rate for multiple inner nozzle velocities and diameters and outer nozzle velocities. The data points, labeled Fluent in the legend, were sampled along the stoichiometric contour in the simulations. A second order polynomial was fit through the data as a model. 30 simulations were used to create this model, which are shown as the symbols, which had varying inner nozzle diameter sizes, inner nozzle velocities, and outer nozzle velocities.

At this point, every term in Eq. (7.6) is known and has been modeled in the counterflow geometry. However, it is not clear yet how to determine where the negative edge exists. Carnell and Renfro [48] showed that negative edge flames stabilized at higher scalar dissipation rates than the one-dimensional extinction scalar dissipation rate which was linearly proportional to the advective heat flux at the edge. The energy equation for standard counterflow diffusion flames along the centerline are simple balances between the diffusive heat loss and chemical heat release. However, negative edge flames have increased heat gain which is simply the advective heat flux at the edge. Therefore, the heat release is less than the diffusive heat loss at the edge. With this in mind, the interpretation can be extended to say that there exists an extinction advective heat flux for a given scalar dissipation rate. If the advective heat flux, which acts as an energy gain, is not sufficiently

high to balance the heat loss then the flame will extinguish for the given scalar dissipation rate.

Beginning at the centerline of the burner there is a perfect balance between diffusive heat loss and chemical heat release which continues until reaching the outer nozzle. Upon reaching the outer nozzle, the scalar dissipation rate rapidly increases and the advective heat flux increases. Both of these quantities increase until reaching a critical value for which the advective heat flux can no longer sustain the flame. This notion can be thought as the limiting extinction advective heat flux at the edge for a given scalar dissipation rate. Therefore, if the extinction advective heat flux for a given scalar dissipation rate can be modeled, then the negative edge location can be predicted. Carnell and Renfro [48] showed that the advective heat flux is linearly proportional to the scalar dissipation rate at the edge. Therefore, Eq. (7.6) can be rewritten in Eq. (7.9), and it can be readily seen that the equation is already in a linear form, where the slope, D, is $\rho c_p \frac{\partial^2 T}{\partial Z^2}$ and the intercept, W, is $\dot{\omega}'''\Delta h$ at the extinction point. Interestingly, when combined, each of these terms are nearly constant at the edge and therefore can be used to calculate the extinction advective heat flux for a given scalar dissipation rate. The modeled values were compared against the actual edge values and are shown in Figure 7.7.

$$\rho c_p V_r \frac{\partial T}{\partial r} = \frac{\partial^2 T}{\partial Z^2} \rho c_p \chi \; + \dot{\omega}''' \Delta h$$
$$A = D\chi + W \tag{7.9}$$

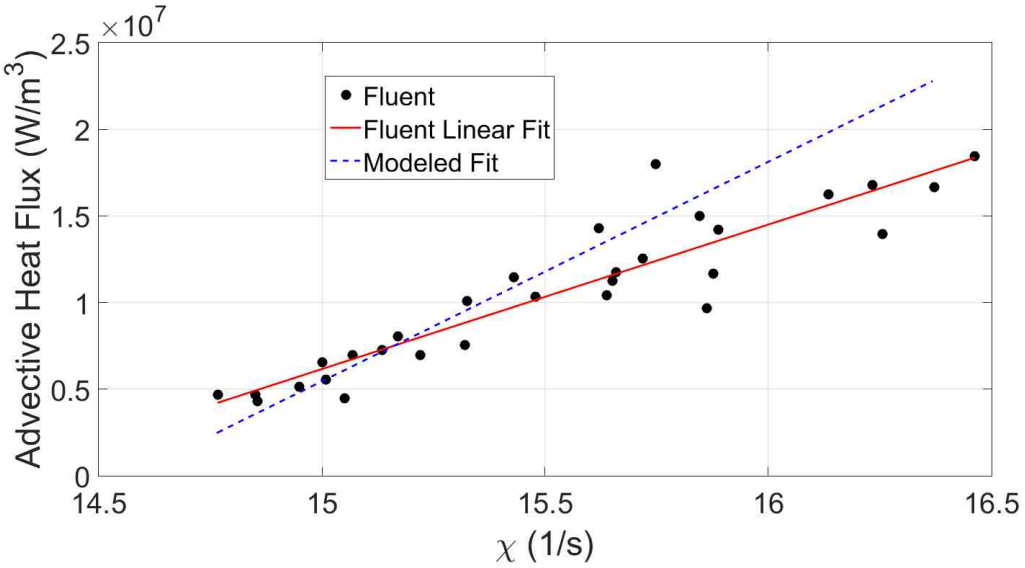

Figure 7.7: Advective heat flux plotted against scalar dissipation rate at the edge plotted as points from Fluent. A linear fit was plotted through the data as a solid red line. The model to predict the advective heat flux and scalar dissipation rate at the edge is plotted as a dotted blue line.

The modeled fit and linear fit from Fluent of the extinction advective heat flux show strong similarity particularly from χ =14.5 to 15.5. However, from χ = 15.5 to 16.5 there is more deviation. Although errors were as high as 40%, the average error was approximately 16%. Interestingly, the data which was fit using the two-dimensional simulations was nearly represented using the simple scaling from Eq. (7.9). It is worth noting that the one-dimensional extinction scalar dissipation rate is approximately 14.5 1/s, which should have nearly zero advective heat flux. This is true when extrapolating both the model and the linear fit from Fluent. However, the slopes of these curves are slightly different. The slope difference can potentially be explained by not using the same extinction criteria. For instance in [48] two different definitions for extinction gave two different extinction advective heat flux slopes, which could potentially account for the difference.

In order to define where extinction occurs, the scalar dissipation rate and advective heat flux are needed. The scalar dissipation rate is easily attainable, but the advective heat flux requires the temperature profile, and subsequently the radial derivative. Unfortunately, the advective heat flux cannot be directly computed since ρ, c_p, and $\dot{\omega}'''$ are all dependent on the temperature. Therefore, the temperature needs to be calculated to determine the negative edge flame conditions. Prior to the temperature calculation, the velocity and scalar dissipation rate profiles were pre-computed and subsequently $\frac{\partial^2 f}{\partial Z^2}$ was calculated computed since it is only dependent on the scalar dissipation rate.

The governing equation, Eq. (7.6), can be rearranged to the form given in Eq. (7.10). Each of the terms on the right hand side are all either predetermined or are a function of the temperature, therefore an implicit numerical scheme can be used to iterate and solve for the temperature profile. Trapezoidal integration method is a simple and robust numerical scheme which can be used to compute the temperature using this ordinary differential equation and is given in Eq. (7.11). The inputs for this code were the inner and outer nozzle velocities, centerline scalar dissipation rate, and fuel dilution. The radial temperature profile was initialized with uniform 50 μm grid resolution at the centerline temperature. Although this simulation was initialized with the correct temperature, any reasonable flame temperature could have been used and the temperature would recover to the correct temperature over a few grid points since it would balance the diffusive heat loss and reaction rate. The modeled and Fluent temperature profiles for a 20:40 case were compared and is shown in Figure 7.8 (a). Clearly, the modeled temperature nearly perfectly follows the Fluent output. Figure 7.8 (b) shows the post-processed advective heat flux using both Fluent and the model. There is near identical agreement here as well. The

extinction advective heat flux using both the model and linear fit were overlaid on this graph. Along the centerline the advective heat flux is greater than the extinction advective heat flux, which stabilizes a flame. As the temperature begins decreasing the advective heat flux rapidly rises, however, the extinction advective heat flux also rises. There is a point at which the extinction advective heat flux is greater than the advective heat flux, which is the point at which extinction occurs. Even though the modeled and linear fit from Figure 7.7 did not match well throughout the entire range, it seems that both do sufficiently well at locating extinction for this case. Therefore, the energy equation for this specific negative edge flame can be well characterized using two-dimensional flow simulations.

$$\frac{\partial T}{\partial r} = \frac{\frac{\partial^2 f}{\partial Z^2} T \rho c_p \chi \ + \dot{\omega}''' \Delta h}{\rho c_p V_r} \tag{7.10}$$

$$\frac{T_i - T_{i-1}}{\Delta r} = \int \frac{\frac{\partial^2 f}{\partial Z^2} T \chi \ + \frac{\dot{\omega}''' \Delta h}{\rho c_p}}{V_r} \tag{7.11}$$

$$T_i = T_{i-1} + \frac{\Delta r}{2} \left(\left. \frac{\frac{\partial^2 f}{\partial Z^2} T \chi \ + \frac{\dot{\omega}''' \Delta h}{\rho c_p}}{V_r} \right|_i + \left. \frac{\frac{\partial^2 f}{\partial Z^2} T \chi \ + \frac{\dot{\omega}''' \Delta h}{\rho c_p}}{V_r} \right|_{i-1} \right)$$

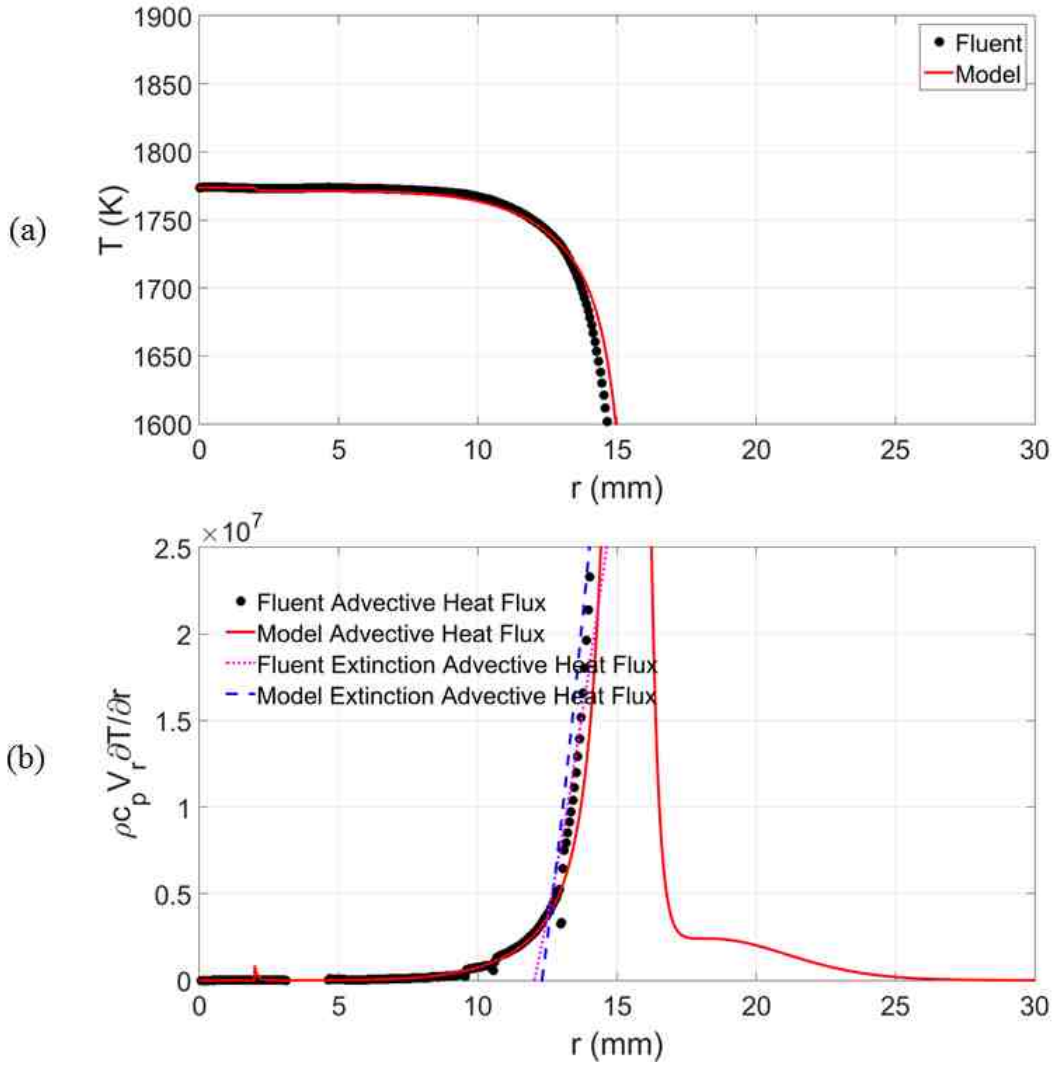

Figure 7.8: Temperature (a) and advective heat flux (b) plotted along the stoichiometric line in the radial direction for the 20:40 case. For both cases the dots represent the output from Fluent whereas the solid red line is the model prediction. In (b) the dotted magenta and dashed blue lines are the extinction advective heat flux for the respective scalar dissipation rate calculated from the linear fit at the edge and model respectively.

7.1.2.2 Model Development Using Global Counterflow Extinction Results

The previous analysis was used solely to understand the behavior of each term in the energy equation and to validate that the important quantities in the energy equation could be calculated. The goal, however, is to use less computationally expensive simulations to model the negative edge flame. For instance, centerline opposed-flow diffusion flames can be easily calculated using CHEMKIN [119] or Cantera [116] chemical

software packages since they are one-dimensional simulations which can provide useful information about the quantities modeled in the previous sub-chapter. In order to bridge this gap, similar counterflow simulations were performed in Fluent, but instead the inner and outer nozzle velocities were kept the same. This provides similar information as OPPDIFF and CHEMKIN simulations, while not changing the numerical flow scheme which was used in the previous sub-chapter. Instead of running numerous negative edge flame studies, the terms in the energy equation will be modeled using the centerline data until global extinction occurs to see how well the model behaves using centerline information. Interestingly, there should not be a large difference in the results since extinction is occurring in both cases, however, in the negative edge case there is an influence of the advective heat flux.

The inner and outer nozzle velocities were initialized at 10 cm/s and increased by 1 cm/s until global extinction occurred. Once extinction occurred, the last converged solution was used to increase the velocities by 0.1 cm/s until extinction occurred again. Similar to Carnell and Renfro [48], extinction occurred at nearly 1712 K with a scalar dissipation rate of approximately 14.5 1/s. The following modeled terms result from analyzing each centerline solution at the stoichiometric location.

Figure 7.9 shows the temperature plotted against heat release at the stoichiometric location using the centerline counterflow simulations. Far from extinction, the temperature is relatively high and decreases as extinction is approached. Conversely, the heat release is relatively low prior to extinction and increases as extinction is approached. This is similar behavior as through the negative edge flame, where close to the centerline there is a perfect balance between the diffusive heat loss and heat release until the reaching the

outer nozzle where the diffusive heat loss becomes much larger which increases the heat release. Through the negative edge the heat release peaks and subsequently decreases as reactions cannot keep up with the diffusive heat loss and the temperature continuously decreases. Similarly in the 1-D case, there is a perfect balance between heat release until extinction is approached. Close to extinction the heat release slope becomes smaller since it cannot keep up with the diffusive heat loss as the temperature continues to decrease. The heat release begins to turn over and decreases slightly as extinction is approached. This region is extremely important to characterize well, since this is where the negative edge flame exists. For instance, in Carnell and Renfro [48] two definitions of extinction were used, maximum reaction rate and the extinction temperature (1712 K), which are both characterized in this set of cases. Therefore, as long as the heat release through the extinction region in the centerline counterflow cases are well characterized, then the remainder of the model can be extrapolated to lower temperatures past extinction to obtain a smooth profile. However, it needs to be clearly stated that past this point the negative edge flame no longer exists.

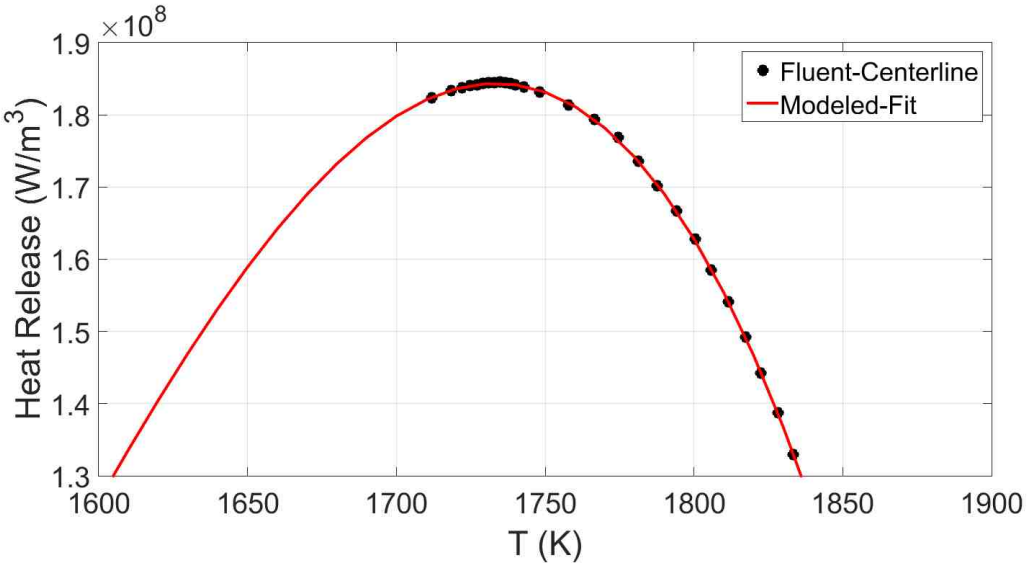

Figure 7.9: Heat release plotted against temperature along the burner centerline for varying boundary condition velocities. The points represent data from Fluent and the solid red line is a third order polynomial fit used for modeling purposes.

Although the data for the model is only needed up until (and slightly past) extinction it is interesting to note both similarities and differences between Figure 7.5 and Figure 7.9. The data points at higher temperatures than extinction seem to correlate very well between the negative edge and centerline cases, as expected. Past extinction however, it is clear that the centerline model in Figure 7.9 reaches lower heat release values than the full negative edge flame values, although only slightly. Therefore, there will be differences past the negative edge when using the 1-D centerline information.

The only other term which needs to be modeled is the $\frac{\partial^2 f}{\partial Z^2}$ term, which again is essentially the flame thermal thickness response to mixture fraction gradients. Similarly, $\frac{\partial^2 f}{\partial Z^2}$ can be calculated using the counterflow centerline data at the stoichiometric location, which was plotted versus scalar dissipation rate in Figure 7.10. Points prior to and near extinction show similar behavior as in the negative edge flames simulations. At approximately χ = 15 1/s, $\frac{\partial^2 f}{\partial Z^2}$ is approximately -25 K using both the centerline and negative

edge flame data. Therefore, it seems that both the heat release and $\frac{\partial^2 f}{\partial Z^2}$ terms have similar behavior until extinction using both the full negative edge flame simulations and centerline simulations. Therefore, the radial temperature profile should be able to be calculated.

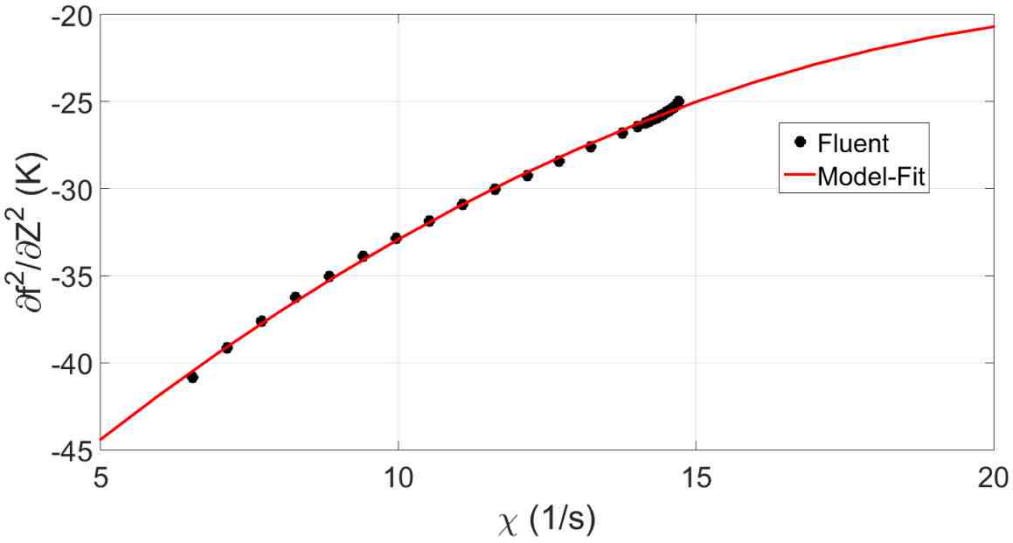

Figure 7.10: $\frac{\partial^2 f}{\partial Z^2}$ plotted against χ where the dots represent points along the centerline for varying nozzle velocities. The solid red line is a second order polynomial fit used for modeling purposes.

Similarly, the radial temperature profile was calculated with the same numerical scheme as previously described and shown in Figure 7.11 (a) and subsequently the advective heat flux in Figure 7.11 (b). The temperature profile matches well with the Fluent output until approximately 14 mm where the Fluent output decreases faster than the modeled temperature. Since the governing equation is still the same, there must be a small imbalance between the heat gain and heat loss, which is obviously not accurately modeled. In this case, the modeled heat gain is higher than the heat loss, leading to a slightly higher temperature than what Fluent calculated. The advective heat fluxes are similarly slightly different between the Fluent output and modeled results, since the temperature profiles are different. The extinction advective heat flux was calculated using Eq. (7.9), but instead the

slope and intercept was calculating using the last centerline case prior to extinction. All of the values which were calculated at the last stabilized simulation were nearly identical to the values calculated in Figure 7.7, and therefore are nearly identical to the values calculated using the negative edge simulation. Using this line as the marker for extinction, the modeled advective heat flux extinguishes slightly before the Fluent output, but is nearly the same even though the temperature profiles and advective heat flux profiles differ. Interestingly, the profiles vary much more significantly after extinction occurs. As noted early, especially in the centerline heat release model, the model past extinction cannot perform well, but will likely work well prior to extinction. This is evident when noticing how the temperature and advective heat fluxes behave prior to extinction and post extinction.

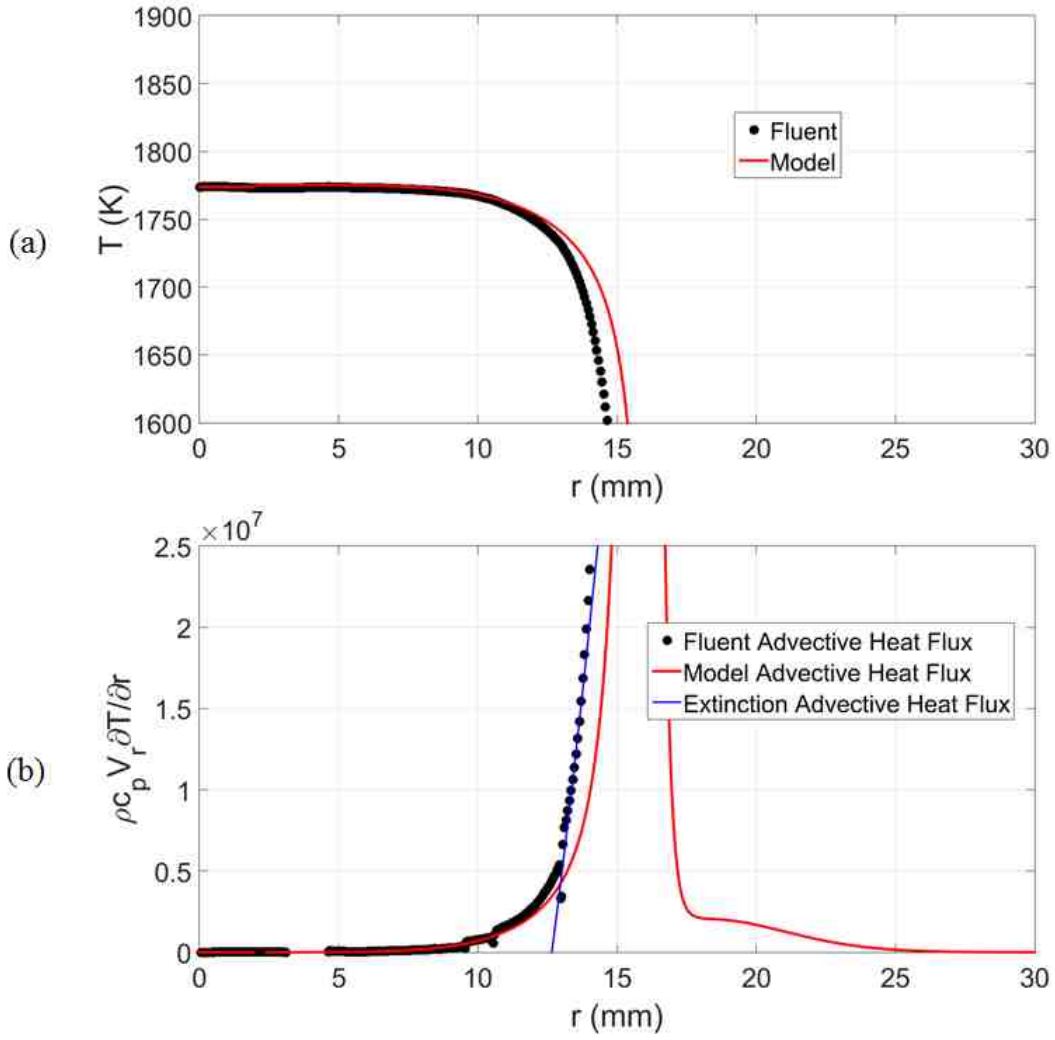

Figure 7.11: Temperature (a) and advective heat flux (b) calculations along the stoichiometric line where the dots are points extracted from the Fluent output and the solid red line is the prediction from the model. The solid blue line in (b) is the modeled extinction advective heat flux.

7.1.3 Summary and Conclusions

Typically, negative edge flames are calculated using two-dimensional simulations, but data is only collected along the stoichiometric line, and therefore can be modeled as a one-dimensional problem. Since the energy equation only has a few terms in it, each individual term in the energy equation was modeled along the stoichiometric line. The model was developed and validated using the two-dimensional numerical outputs along the

stoichiometric line. Particularly the velocity, scalar dissipation rate, thermal width, and heat release were modeled. Subsequently, the one-dimensional temperature field was numerically solved in the radial direction which correlated well with the two-dimensional output. A new approach to determine extinction in negative edge flames was determined and used to find when the negative edge is formed. As a step forward, centerline simulations were computed in a counterflow diffusion flame with relevant boundary conditions. The information at the centerline was used to model the terms in the energy equation again. The centerline extinction simulations approached extinction to simulate how a negative edge flame behaves as extinction is approached. Similarly the terms in the energy equation were modeled and the temperature profile matched reasonably well with the two-dimensional flow simulation. However, differences do exist particularly after extinction occurred.

Future work will examine using detailed chemistry OPPDIFF simulations to compare against detailed chemistry negative edge simulations. The individual energy equation terms will be modeled again using only the centerline data to compare against two-dimensional flow simulations using detailed chemistry. The goal of this work overall has been to develop a model such that OPPDIFF simulations could be calculated and used to calculate negative edge flames sufficiently well, and is one step away from achieving this goal.

7.2 Unsteady and Laminar Negative Edge Flames

7.2.1 Motivation

Steady negative edge flames were well characterized in a series of work by Carnell and Renfro [47,48,77]. As a step toward understanding turbulent negative edge flame

behavior, unsteady and laminar negative edge flames need to be studied. This sub-chapter will examine similar negative edge flames which were formed in [48], but imposes unsteady boundary conditions at different frequencies to identify the edge flame response to different frequencies. The energy budget will also be reassessed to determine the differences between the steady and unsteady cases. Furthermore, this sub-chapter will attempt to understand what role the unsteady energy term plays in unsteady negative edge flame dynamics.

7.2.2 Numerical Setup

7.2.2.1 Computational Domain

The same modified counterflow burner which was previously described in Chapter 5.2 and nearly the same numerical scheme as described in Chapter 5.2.2 was used to simulate unsteady negative edge flames. The axisymmetric computational domain is shown in Figure 7.12. Low velocity fuel and air were injected through the inner nozzles in opposing directions to create a flat diffusion flame near the centerline. The air was modeled as 21 % O_2 and 79% N_2 by volume while the fuel stream was nitrogen diluted methane modeled with 20% CH_4 and 80% N_2 by volume. Higher velocity fuel and air at the same concentrations were injected in a coannular region, representing an outer nozzle. The increase velocity led to an increase in scalar dissipation rate along the flame with increasing radial position. At some point, as shown in Figure 7.12 (b), the flame is locally extinguished. In prior work [48], both the inner and outer flows were modeled by supplying a steady state velocity from the respective regions. In this work, the inner flow was a constant 10 cm/s, but the outer flow was represented by a sinusoidal velocity

fluctuation which ranged from 40 – 100 cm/s. The velocity fluctuations were simulated with varying cycle periods ranging from 0.625 to 50 ms.

The inner nozzle radius for this work was 60 mm, which was chosen to lessen the effect of radial diffusion through the edge [48]. A 1 mm wall separated the inner and outer nozzles, to match conditions from previous steady-state experiments. The outer nozzle region extended an additional 25 mm in the radial direction. A cooling jacket from the experimental burner design [47] was included, which had walls which extended 2.5 mm in the axial direction and 14 mm in the radial direction. Therefore, the total radial length was 100 mm. The upper and lower nozzles were separated by 15 mm in the axial direction. Three different grid resolutions were used, similar to [48], which had 250, 125, and 62.5 μm grid resolution in sections (G1), (G2), and (G3) respectively, shown in Figure 7.12 (a). These three regions were meant to resolve the (G1) flow, (G2) temperature gradient, and (G3) reaction layer. Each section length was 2.5 mm in the axial direction.

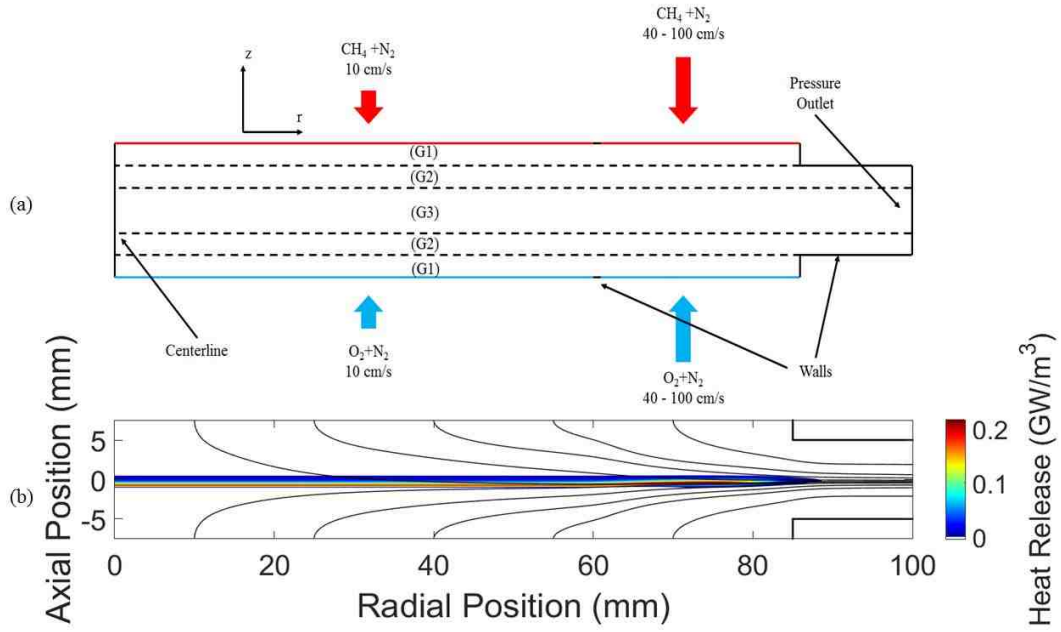

Figure 7.12: (a) Modified counterflow geometry used for unsteady negative edge flame simulations. Three grid resolutions were used labeled (G1) – (G3). (b) shows the heat release field with streamlines issuing from the boundaries.

7.2.2.2 Numerical Formulation

Fluent 16.1 was used with a transient, segregated, implicit solver. The Semi-Implicit Method for Pressure Linked Equations (SIMPLE) [106] scheme with PRessure STaggered Option (PRESTO!) for pressure interpolation was used to couple the velocity and pressure calculations. Fluid properties were modeled as laminar incompressible ideal gases. Therefore, the mixture thermal conductivity, viscosity, and specific heat capacity were calculated via ideal gas mixing. The thermal conductivity and viscosity of individual species were calculated via kinetic theory. The L-J characteristic length and energy parameter were supplied from the GRI transport database [108]. Multicomponent and thermal diffusion were calculated by solving the Maxwell-Stefan equations for the diffusive flux vector. Mass diffusive fluxes were calculated using binary diffusion coefficients, while thermal diffusion was empirically modeled using composition equations derived from Kuo [107]. One-step chemistry was modeled using exponents from

Westbrook and Dryer [105] to calculate the volumetric reaction rate for methane. One-step chemistry was previously used [48,120] to calculate negative edge flames and was shown to sufficiently capture the extinction edge location and response to boundary conditions. The c_p values were altered, similar to [48], using suggestions from [109] to obtain realistic flame speeds. This same procedure was used here for more direct comparison to the previous studies. Detailed chemistry could be included to improve the quantitative prediction of the flame edge structure, but one-step chemistry is sufficient for the flame edge response studies reported here.

50 μs time steps were used in the calculations, which were chosen by assuming the flame motion would be approximately 1 m/s, and therefore would move approximately one grid point per iteration. Temporal convergence was verified using 25 μs time steps for a case with a 5 ms cycle period, shown in Figure 7.13. There are minimal differences between the two time step sizes. Iterations between the time steps reached residual values which were nearly the same as the steady converged case. The numerical simulation began with the converged steady solution with 10 cm/s inner nozzle velocity and outer 40 cm/s velocity. The unsteady boundary conditions were imposed and the simulations were run at the given time step sizes until the time-dependent radial location of the negative edge flame showed periodic behavior. One cycle period was sampled by outputting relevant terms for post-processing. Figure 7.13 shows one example of the time-dependent radial location of the edge (b) and the corresponding unsteady energy term at the edge (a).

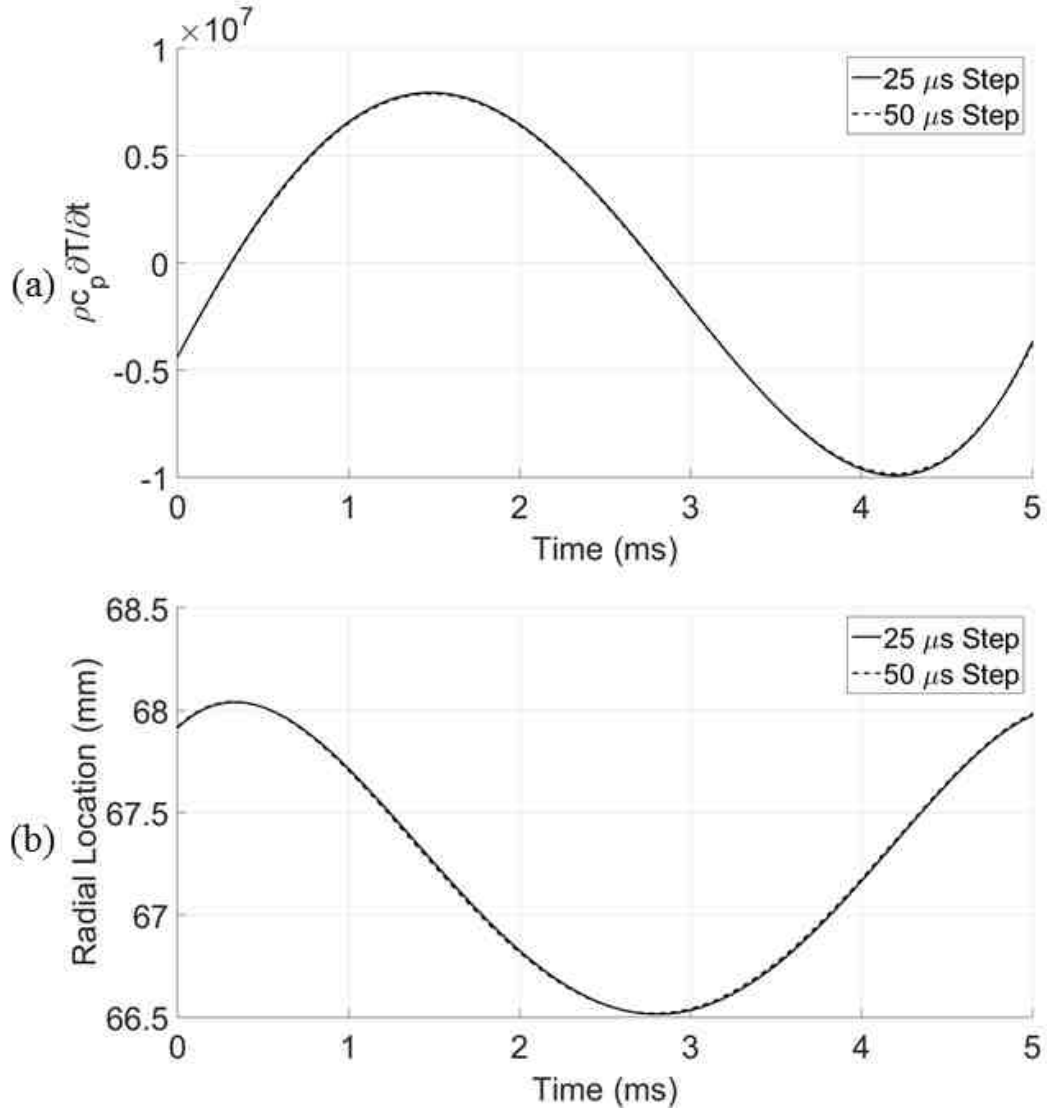

Figure 7.13: $\rho c_p \frac{\partial T}{\partial t}$ at the flame edge (a) and radial location of the edge determine by the 1712 K contour (b) for a negative edge case with a 5 ms cycle period. Two time steps were used, which show minimal differences.

7.2.3 Results and Discussion

7.2.3.1 Unsteady Energy Budget Analysis

The analysis presented in this work was calculated along the stoichiometric mixture fraction line using Z, defined in Eq. (7.2) [118], where Y_i is the i^{th} elemental mass fraction and superscripts F and O refer to the values at the fuel and oxidizer boundary conditions respectively. Figure 7.14 shows the radial position of the negative edge with a 20 ms cycle

period, defined by the radial position of the 1712 K temperature isocontour along the stoichiometric mixture fraction [48]. This isocontour of T was chosen to characterize the edge location in prior work for this fuel mixture since it corresponds to the limiting temperature for a one-dimensional counterflow flame undergoing extinction [48]. The radial position of the edge oscillates approximately 9.5 mm over the duration of the cycle and is periodic. Interestingly, the difference in time between the minimum and maximum radial points is larger for the outward motion than inward motion showing a hysteresis in the flame behavior. The maximum radial position occurs at 18.2 ms, while the minimum radial position occurs at 7.1 ms. Therefore, it takes approximately 11 ms to transition from the minimum to maximum radial position, but only 9 ms to move from the largest to smallest radial position.

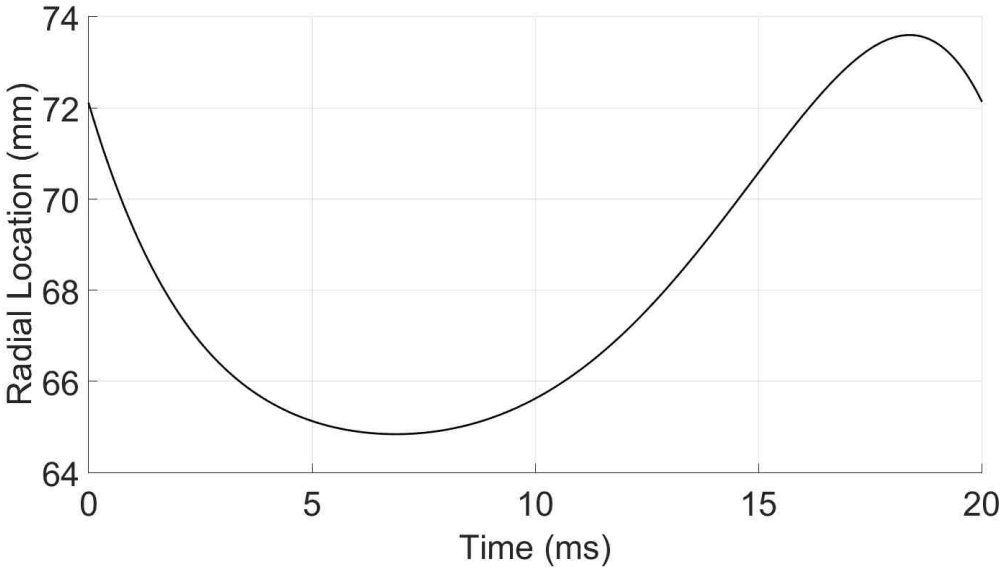

Figure 7.14: Radial location defined by the radial position of the 1712 K temperature along the stoichiometric mixture fraction contour using a 20 ms cycle period. Energy analysis of locations marked (a) – (d) is shown in Figure 7.15.

The individual terms of the full energy equation are shown in Eq. (7.12). In Eq. (7.12) ρ refers to the density, c_p is the mixture specific heat capacity at constant pressure,

T is the temperature, t is time, V is the velocity with subscripts referring to the direction, λ is the thermal conductivity, J_i is the species diffusive flux, $\dot{\omega}'''$ is the volumetric rate of reaction, Δh is the enthalpy of combustion, and r and a are the radial and axial directions respectively The individual energy terms along the stoichiometric contour for four time steps are shown in Figure 7.15 using a cycle period of 20 ms. The four time steps represent (a) the minimum radial position, (b) outward flame motion toward the maximum radial position, (c) the maximum radial position, and (d) inward flame motion toward the minimum radial position.

$$\rho c_p \frac{\partial T}{\partial t} = -\rho c_p \left(V_r \frac{\partial T}{\partial r} + V_a \frac{\partial T}{\partial a} \right) + \lambda \left(\frac{\partial^2 T}{\partial r^2} + \frac{\partial^2 T}{\partial a^2} + \frac{1}{r} \frac{\partial T}{\partial r} \right) + \frac{\partial \lambda}{\partial r} \frac{\partial T}{\partial r} + \frac{\partial \lambda}{\partial a} \frac{\partial T}{\partial a} - \sum_i \nabla \mathrm{h}_i \cdot \vec{J}_i + \dot{\omega}''' \Delta h \tag{7.12}$$

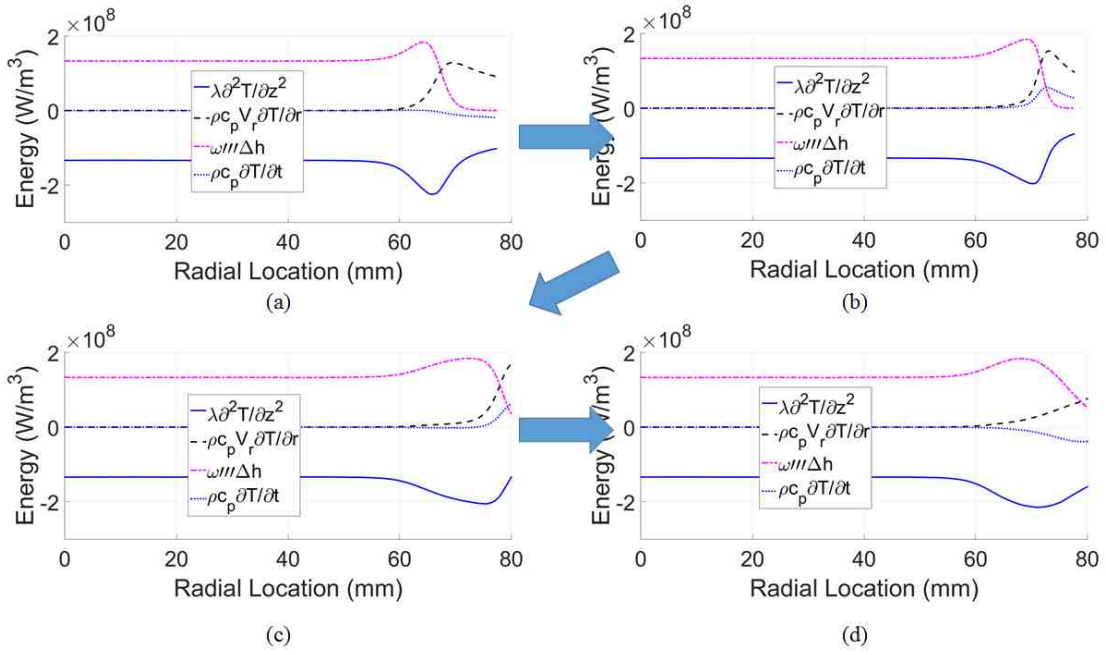

Figure 7.15: Energy budget along the stoichiometric line for the 20 ms cycle period case at four times in the cycle. The time steps represent times at (a) the minimum radial position, (b) moving from the minimum to maximum radial location, (c) the maximum radial location, and (d) moving from the maximum to minimum radial location.

Four energy terms are important in the energy budget: the axial diffusive heat loss ($\lambda \frac{\partial^2 T}{\partial a^2}$), radial advective heat flux ($\rho c_p V_r \frac{\partial T}{\partial r}$), chemical heat release ($\dot{\omega}''' \Delta h$), and unsteady energy ($\rho c_p \frac{\partial T}{\partial t}$) terms. All other terms are negligible at all times and positions along the flame. This is identical to the steady results in [48] except for the expected importance of the unsteady term in the present simulations. At each time step, there is a balance between only the diffusive heat loss and chemical heat release until the outer nozzle is reached (~ 60 mm) where the scalar dissipation rate begins to increase radially. Therefore the unsteady behavior is not effecting the inner counterflow diffusion flame. Upon reaching the outer nozzle the diffusive heat loss and heat release both increase in magnitude with scalar dissipation rate. In the steady case, the diffusive heat loss is larger in magnitude than the heat release through the negative edge which is balanced by the advective heat flux term [48]. In these unsteady simulations, the advective heat flux clearly plays a role in the energy budget, however, there is also a relatively large influence of the unsteady energy term. Interestingly, the advective heat flux is always positive in the energy budget ($v \cdot \nabla T$ is always negative) and therefore the flame is continuously a negative edge flame or extinction front throughout the entire cycle. The diffusive heat loss is greater in magnitude than the heat release with the unsteady energy term having both positive and negative values. Thus, when it advances in radial position, it merely has an extinction velocity that is less than the bulk velocity such that the extinction point is pushed outwards.

At the minimum radial position (Figure 7.15 (a)), the flame is similar to a steady negative edge flame with an outer nozzle velocity of 100 cm/s. When the flame feels the influence from the 100 cm/s outer nozzle velocity, the largest scalar dissipation rate is present, leading to the flame residing at the lowest radial position. At this time the unsteady

term is negligible at the edge. As the outer nozzle velocity decreases, the scalar dissipation rate is relaxed and the flame proceeds outward to a larger radial location. The unsteady energy term, Figure 7.15 (b), is positive at this point and the temperature is increasing in time. At the maximum radial position, Figure 7.15 (c), the unsteady energy term is again zero since the flame has essentially reached the steady state condition of a 40 cm/s outer nozzle velocity. As the flame recedes, Figure 7.15 (d), the unsteady term becomes negative as the temperature is decreasing and the minimum radial position is approached.

The energy terms were tracked at the negative edge location, defined by the same 1712 K isocontour as in [48], and plotted in time shown in Figure 7.16. At the beginning of this periodic sequence the diffusive heat loss magnitude, shown as a dashed line in Figure 7.16, is greater than the heat gain from the advective heat flux and heat release, shown as a dotted line. Therefore there is an imbalance between the heat loss and heat gain which results in the flame receding to reach conditions with lower scalar dissipation rates, consistent with Figure 7.14. At approximately 7 ms, there is an instance when there is a balance between the diffusive heat loss and heat gain. At this time the radial position is the smallest since the diffusive heat loss is the greatest and is therefore the largest magnitude extinction event. Transitioning through this point the heat gain is greater than the heat loss, and therefore the flame can withstand higher scalar dissipation rates, and thus moves to larger radial positions. At approximately 18 ms, there again is a balance between the heat gain and heat loss, and therefore the flame position is not moving, consistent with observations in Figure 7.14. Conversely, the flame is at the largest radial position at this instance since the heat loss is lower than at 7 ms. The solid line represents the diffusive

heat loss and unsteady energy term added together, which balance the heat gain from the advective heat flux and chemical heat release.

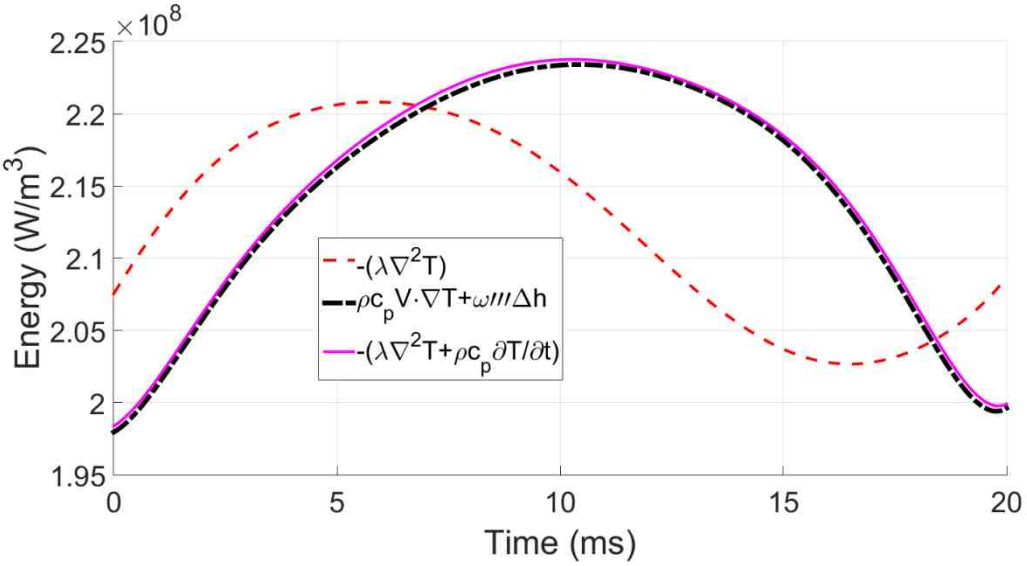

Figure 7.16: Energy budget at the negative edge with a cycle period of 20 ms case. The red dashed line is the diffusive heat loss, dotted black line is the combined advective heat flux and chemical heat release, and solid magenta line is the diffusive heat loss and unsteady energy term.

The radial location in Figure 7.14 was observed to recede faster than proceed. However, Figure 7.17 shows the unsteady energy term at the edge which reaches higher magnitudes while the flame is proceeding (positive $\rho c_p \frac{\partial T}{\partial t}$) than when it is receding (negative $\rho c_p \frac{\partial T}{\partial t}$). This is counterintuitive since the unsteady energy term represents the edge velocity, and therefore higher unsteady energy magnitudes would intuitively suggest higher edge velocities. Therefore, there is clearly another influence which impacts the edge velocity other than simply the imbalance between the heat gain and heat loss which can explain this behavior.

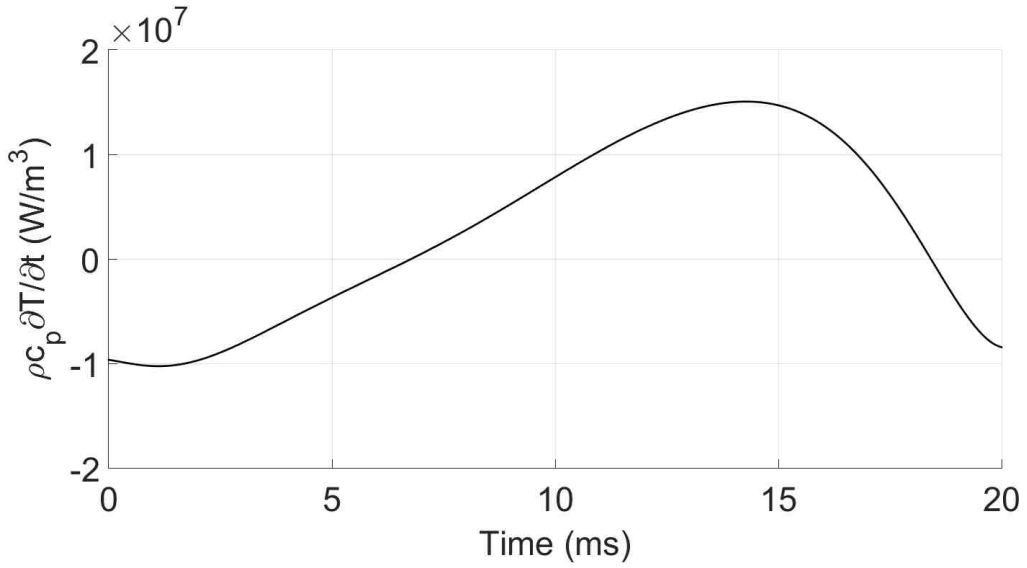

Figure 7.17: Unsteady energy term plotted in time for the 20 ms cycle period case.

7.2.3.2 Edge Velocity

One of the most important parameters for negative edge flames is the edge velocity, which is the relative speed of the flame with respect to the flow, since it determines flame hole growth rates. If the edge velocity can be better understood, flow conditions can be designed to better control flame hole development. The local flame edge velocity is defined as shown in Eq. (7.13), where V_e is the edge velocity relative to the flow, V_{flame} is the flame velocity in fixed coordinates, and V_{flow} is the flow velocity in fixed coordinates. The flame velocity was calculated by taking the derivative of the radial and axial positions of the flame with respect to time. The difference between the flame and flow velocities was computed and this value was used as the edge flame velocity. The edge velocity is the speed at which a negative edge flame would recede in a stationary fluid [39], or the bulk velocity that would be needed to balance the negative edge to create a stationary extinction front [48].

$$V_e = V_{flame} - V_{flow} \tag{7.13}$$

The edge velocity is plotted against the radial edge location in Figure 7.18 for several different velocity fluctuation frequencies. In [48] it was shown that there is no single edge velocity for a given scalar dissipation rate. In the unsteady cases, the flame experiences a range of scalar dissipation rates that are dictated by the outer nozzle velocities, and clearly there is a variation in the range of edge velocities and radial locations experience at different oscillation frequencies. Beginning with the 1.25 ms cycle period case, the fluctuations are sufficiently fast that the flame does not move far from its initial location but still experiences a range of negative edge velocities. As the cycle period is increased, the flame has more time to propagate over a larger radial change in position and the flame also experiences a larger range of edge velocities. These observations are true until a cycle period of 20 ms where further increases in the cycle period lead to the same range of radial positions and a smaller ranges of edge velocities. The symbols in Figure 7.18 represent the steady state solution for outer nozzle velocities of 40, 50, 60, 70, 80, 90, and 100 cm/s. At increasing cycle periods, the unsteady flames are converging toward these steady state solutions.

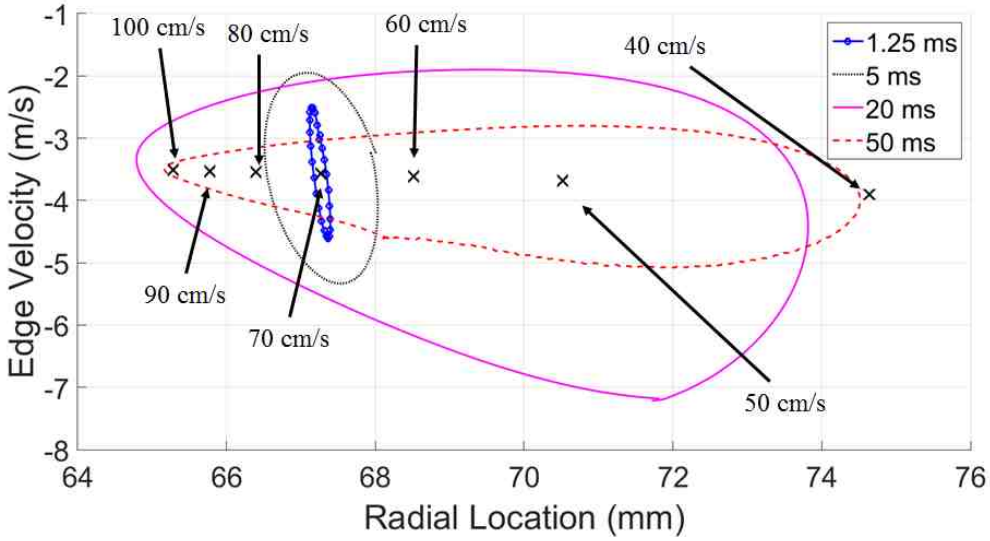

Figure 7.18: Edge velocity plotted against the edge location for four cycle periods. The symbols represent the edge location and velocity under steady-state conditions.

The flow velocity for the same oscillation cycle periods are shown in Figure 7.19. The symbols again show the flow velocity at flame edge for steady-state solutions with outer nozzle velocities from 40 – 100 cm/s. Beginning with the 1.25 ms cycle period case, the flame again does not have sufficient time to move during the oscillation, but the change in outer nozzle velocity still causes variation in the flow through the flame at the edge. Because the flame motion is small, the flow velocity is approximately the same as the flame edge velocity in Figure 7.18 for this case. As the cycle period is increased, the range of radial locations and flow velocities also increase. This trend holds until the 20 ms cycle period case, after which further increases in the cycle period lead to a decreasing range of flow velocities. The flow velocities through the edge converge to the flow velocities experienced by the steady-state solutions. Interestingly, for the cases around 20 ms with large changes in both velocity and position, the flow velocities at the extreme radial positions are not the extreme flow velocities. Thus, there is a phase difference between the

outer nozzle boundary effect and the flow which goes through the edge, as discussed in more detail in the next sub-chapter.

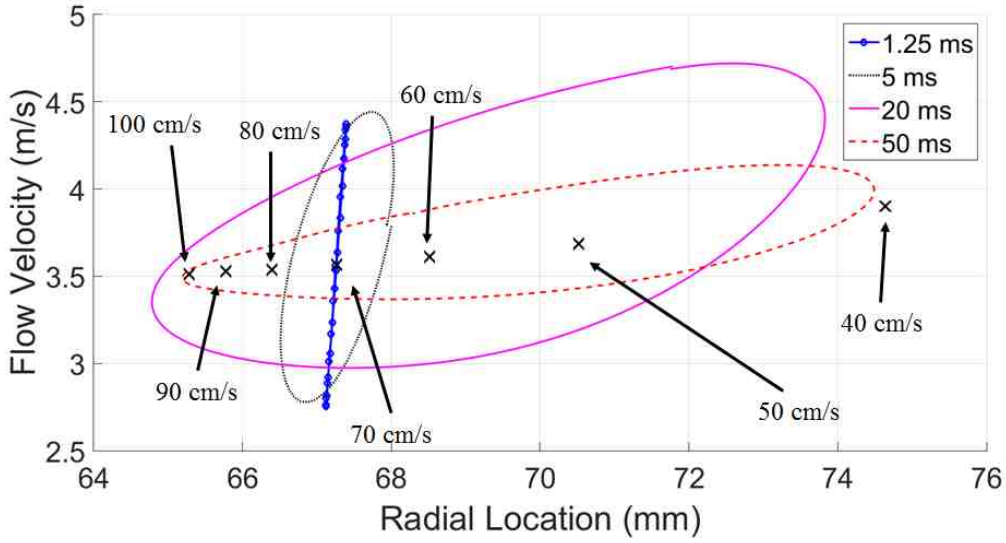

Figure 7.19: Flow velocity plotted against the edge location for four cycle periods. The symbols show the flow velocity at the edge location using steady-state simulations.

Figure 7.18 and Figure 7.19 show that the average radial position of the flame at shorter cycle periods is lower than that of longer cycle periods. This can be explained by the radial positions of the steady-state solutions. Decreasing the outer nozzle velocity leads to a nonlinear increase in radial location. Larger cycle periods can experience the full range of radial positions from the steady solution of the 40 and 100 cm/s case, but at small cycle periods the flame nominally resides at the radial position of the steady 70 cm/s case, which is the average velocity of the outer nozzle. Since the 70 cm/s case has a flame position that is smaller than the average of the 40 and 100 cm/s cases, the short cycle period case resides at a smaller average radial position than the long cycle period cases.

As seen in Figure 7.18 and Figure 7.19, the edge velocity depends significantly on the frequency of the unsteady flow fluctuations and is not single valued. However, further analysis of the energy balance through the edge during these oscillations can be used to

describe these variations in behavior. First, the unsteady energy term in Eq. (7.12) can be related to the flame velocity and spatial temperature gradient as given in Eq. (7.14). The left and right hand sides of Eq. (7.14) are plotted in Figure 7.20 for several cycle periods. Nearly all times of all the cases fall along the line of equality, supporting the simplification of Eq. (7.14).

$$\rho c_p \frac{\partial T}{\partial t} = -\rho c_p V_{flame} \cdot \nabla T \tag{7.14}$$

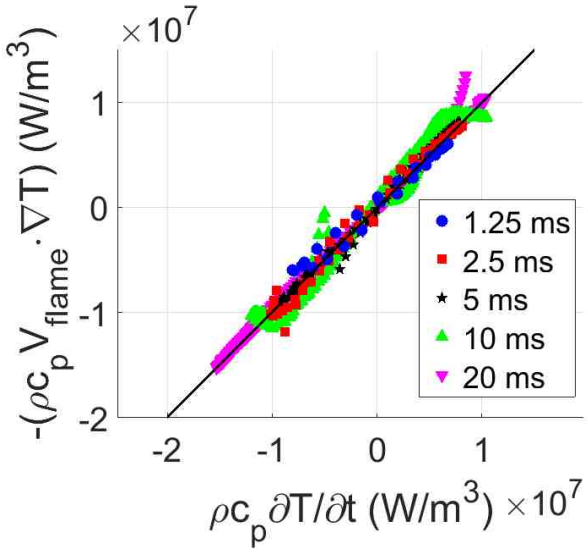

Figure 7.20: Flame velocity energy characterization plotted against unsteady energy term. The legend depicts the cycle period, whereas the solid black line represents the equality line defined by Eq. (7.14).

Equations (7.13) and (7.14) can then be combined to give Eq. (7.15), where $\partial_t T$ and $\partial_r T$ are the derivatives of temperature in time and radial direction, respectively. Since the flow velocity is negligible in the axial direction at the flame, Eq. (7.15) for this geometry only requires the radial velocity for V_{flow}, but this could be expanded to include additional terms for other geometries. Similarly, only the radial temperature gradient was included since the axial gradient is negligible. The left and right hand sides of Eq. (7.15) are plotted against each other in Figure 7.21 for several different frequencies and this

simplification of the edge velocity is valid for all times in each case in this study. Other flowfields may require axial velocity and temperature gradient terms, but Eq. (7.15) is valid for the unsteady flames in this study.

$$\frac{\partial T}{\partial t} = -(V_e + V_{flow}) \cdot \nabla T$$
$$V_e = -\left(\frac{\partial_t T}{\partial_r T} - V_r\right) \tag{7.15}$$

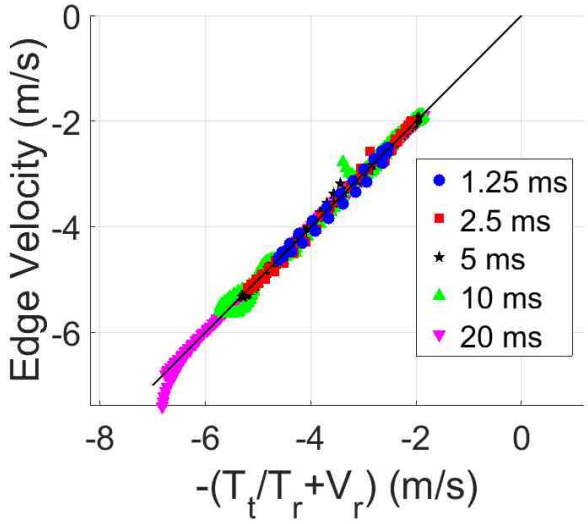

Figure 7.21: Left and right hand side of Eq. (7.15). T The legend represents the symbols used for each case, and the black line represents points which satisfy equality between the left and right hand sides.

From the energy equation, the unsteady energy term is the imbalance between heat loss and gain, which is simply written in (7.16) for this geometry removing terms shown to be negligible. Equation (7.16) can be rearranged and combined with Eq. (7.15) to yield Eq. (7.17), where Q is defined as the right hand side.

$$\rho c_p \partial_t T = \dot{\omega}''' \Delta h - \rho c_p V_r \partial_r T + \lambda \partial_a^2 T \tag{7.16}$$

$$V_e = -\left(\frac{\dot{\omega}''' \Delta h + \lambda \partial_a^2 T}{\rho c_p V_r \partial_r T}\right) V_r \equiv Q \tag{7.17}$$

The left and right hand side of Eq. (7.17) is shown in Figure 7.22, which again confirms good agreement and justifies the use of Eq. (7.17) to describe the extinction behavior. The small departure from equality in Figure 7.22 is due to terms neglected in the derivation, such as the axial advective heat flux and radial diffusive heat loss, which are small but not exactly zero. These terms can be important in other geometries and could be included in the analysis if needed. Equation (7.17) gives rise to a simple interpretation of the edge velocity in the counterflow geometry. In Eq. (7.17) the numerator is the difference between diffusive heat loss and chemical heat release gain, both of which scale with the local scalar dissipation rate, and the denominator is the advective heat flux. Therefore, the edge velocity can be interpreted as the net heat gain from mixing dominated terms, scaled by the rate at which this gain can be advected by flame motion. For negative edge flames, the diffusive heat loss is greater in magnitude than the chemical heat release. Therefore the numerator will always be negative and since the advective heat flux is also negative, the edge velocity will also subsequently be negative. In steady cases, the difference in the heat and diffusive heat loss exactly balances the advective heat flux. Therefore, the bracketed terms becomes unity and the edge velocity is simply the negative of the flow velocity, as was demonstrated in the steady simulations of [48]. In the unsteady case, the bracketed value will vary from unity and therefore will change the edge velocity.

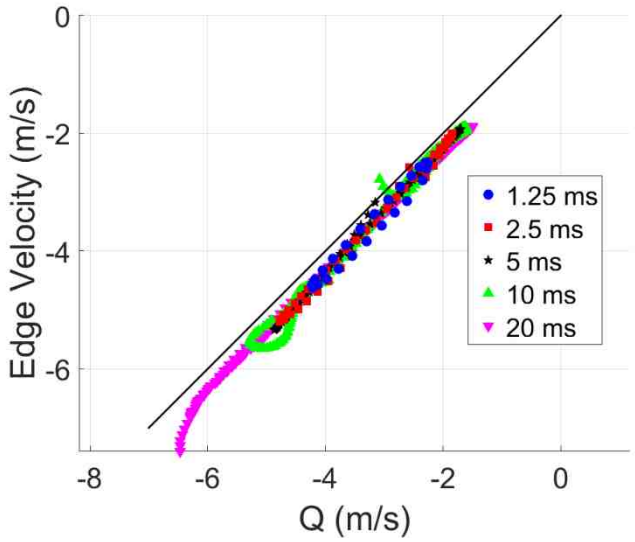

Figure 7.22: Left and right hand sides of Eq. (7.17). The solid black line represents equality being satisfied.

7.2.3.3 Edge Response to Different Frequencies

The negative edge flame response to different imposed boundary condition frequencies is further examined using the maximum radial change in flame position, shown in Figure 7.23. The radial position changes from steady state simulations with outer nozzle velocities of 40 and 100 cm/s were also calculated and plotted as a solid line in Figure 7.23. At relatively large cycle periods, greater than 20 ms, the flame responds closely to the changes expected at the steady state conditions. However, as the cycle period deceases, or the frequency increases, the flame no longer reaches the steady state conditions. Therefore, there is a frequency response time associated with unsteady negative edge flames. At very short cycle periods, the flame is nearly stationary, having little movement as shown previously. This has implications to negative edge flame motion in turbulent flows which have a large frequency spectrum. These results indicate that small eddies with higher fluctuation frequencies should not affect negative edge flame motion as much as larger

scale lower frequency fluctuations and that this critical time scale can be used to understand the flame response.

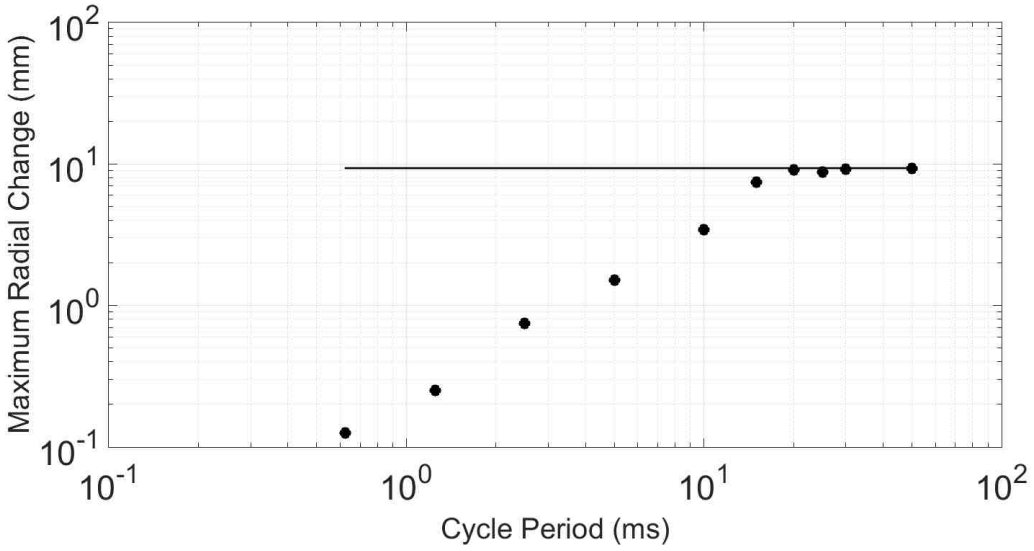

Figure 7.23: Edge flame radial position difference response. The steady cases have a radial position difference of 9.35 mm, shown as the solid black line.

The energy budget at the edge for several cycle frequencies is shown in Figure 7.24. The time in each sequence was normalized by the cycle period for comparison. Figure 7.24 (c) shows the energy budget for the case with a cycle period of 50 ms. The heat loss and gain terms nearly follow the velocity fluctuation from the nozzle exit, shown in Figure 7.24 (d). Therefore, this case is approaching quasi-steady-state conditions where the velocity fluctuation imposes a change in heat loss at the edge and the heat gain (heat release and advection) terms have ample time to respond and nearly reach steady conditions. This case does not have a large difference between the heat loss and gain, and therefore has relatively small unsteady energies. Figure 7.24 (b) shows the energy budget for the 5 ms cycle period case. In this case, the heat loss, indicated by the dashed line, nearly follows the velocity fluctuation. However, the heat gain terms no longer follow the heat loss terms well and therefore display a longer response time than the diffusive heat loss. Since the

flame is no longer at near quasi-steady-state conditions, the flame can no longer reach the same radial locations that are expected from the steady solution, consistent with Figure 7.23. Figure 7.24 (a) shows the energy budget for the case with a 1.25 ms cycle period. At this point, the heat losses also no longer keep up with the velocity fluctuations and therefore have reached conditions at which both the heat loss and gain display a lag relative to the velocity fluctuations. This leads to the flame residing at nearly a constant radial location since the heat loss and gain are no longer in phase with each other.

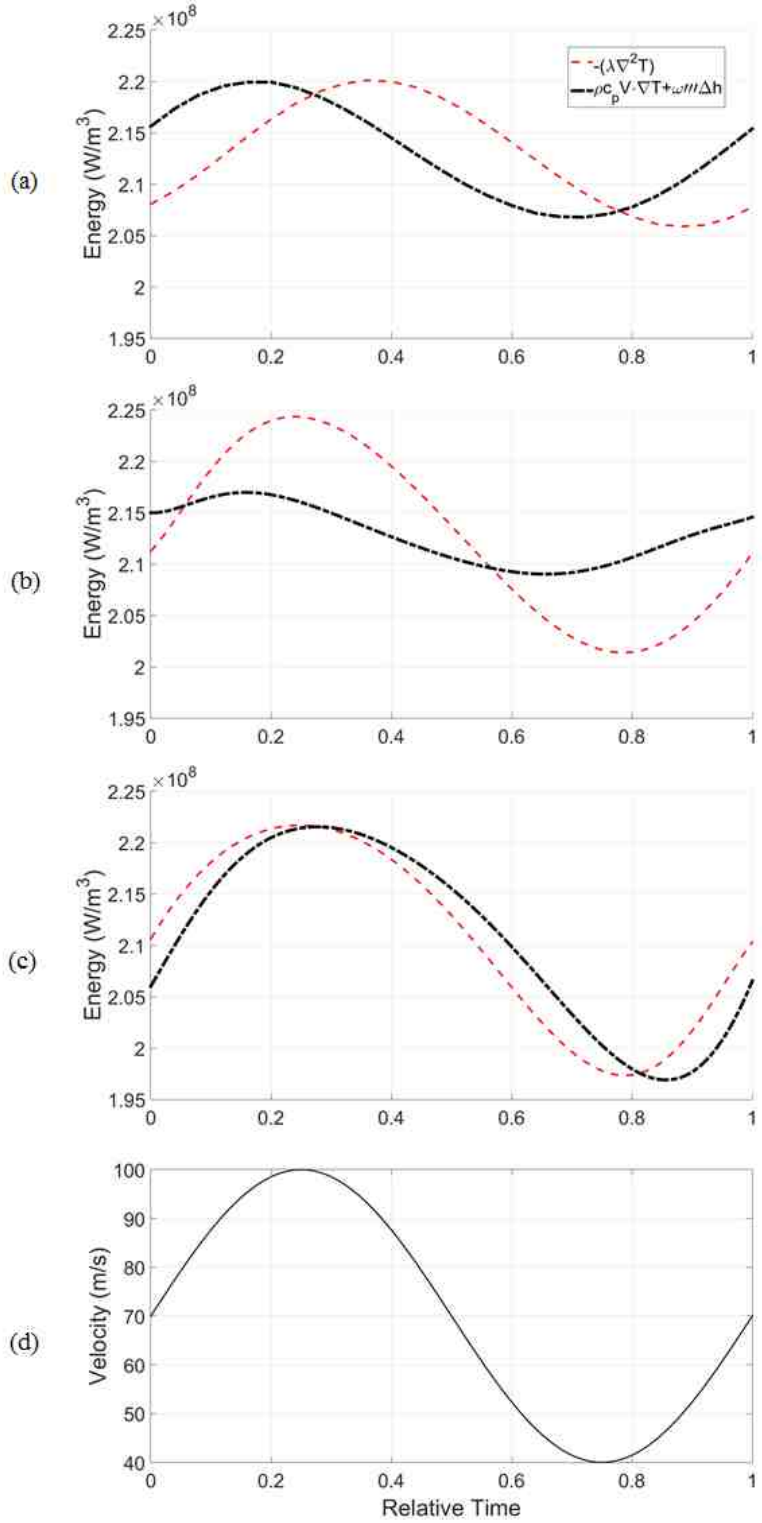

Figure 7.24: Energy budget for cycle periods of (a) 1.25 ms, (b) 5 ms and (c) 50 ms. The velocity change at the outer nozzle exit is also plotted in (d). The time in each sub-figure has been normalized by the cycle period for comparison. The red dashed lines in (a) – (c) are the heat loss and the dotted black lines are the heat gain.

This time lag can be further examined by computing the time delay from the maximum velocity amplitude to the maximum heat gain or loss term in a frequency normalized time unit, which was then converted into radians. The same calculation was conducted for the minimum values which were averaged with the maximum phase delays and are shown in Figure 7.25. At relatively long cycle periods the phase delay is rather small for both the heat gain and loss terms. As the cycle period decreases, the heat gain delay begins to slowly rise until approximately the 20 ms case. Further cycle time decrease leads to the phase lag significantly increasing and therefore being out of phase with both the velocity fluctuation and diffusive heat loss. The heat loss term has nearly constant phase lags approximately until the 2.5 ms case which then leads to higher lags with decreasing cycle period time.

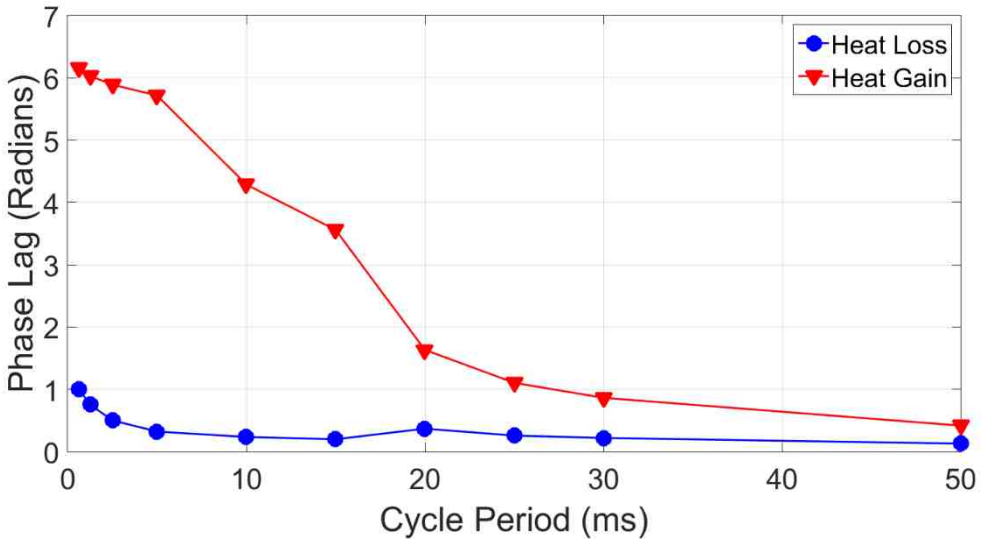

Figure 7.25: Phase delay between extreme velocity and energy terms. The calculations were conducted between the maximum and minimum extremes which were subsequently averaged.

7.2.4 Summary and Conclusions

Unsteady negative edge flames were simulated with imposed oscillating boundary conditions. The edge flame exhibited unsteady inward and outward motion in the

counterflow burner. Compared to earlier simulations of a steady negative edge flame in this geometry, the same simplified analysis of the energy balance through the flame was applied with the addition of an unsteady energy term. The dynamics of the flame motion were tracked at the edge and analysis of the unsteady energy term in the form of a flame velocity fully described the flame motion.

The negative edge flame velocity was calculated using a simplified energy equation which showed the edge flame speed to be governed by the imbalance between heat release and diffusive heat loss scaled by the advective heat flux and flow velocity. This equation provides a simplified description of edge flame speed response. The edge response with respect to different oscillation frequencies was also characterized and a negative edge flame response time was found from the simulations. For this fuel and combustor geometry, the flame reaches approximate steady state conditions for fluctuations slower than approximately 20 ms (50 Hz), but has minimal response to the fluctuations for frequencies above 1.25 ms (1000 Hz).

There are two competing time scales which influence the behavior of the flame. At rather long timescales above 20 ms, the heat loss and gain terms nearly follow the velocity fluctuations. Therefore, these conditions are in quasi-steady-state and match flame behavior from steady-state solutions. However, below 20 ms the heat gain from heat release and advection can no longer keep up with the velocity fluctuations, while the diffusive heat loss term continues to follow the velocity fluctuations. In this range, the flame no longer reaches the same radial locations as the steady-state cases. Further decrease in the cycle period below 2.5 ms reaches a critical value at which the heat losses

also is out-of-phase with the velocity fluctuation, and at this point the flame resides at a near constant radial location.

7.3 Negative Edge Flame Velocities in a Turbulent Flow

7.3.1 Background and Motivation

Although significant progress has been made with respect to negative edge flames, most findings in [48] could not be compared to experiments because it would require multiple geometries to be used. In order to alleviate this problem, a new burner was built which separates the stable flame strength from the flow velocity. In the previous design, if the inner nozzle velocity was increased, in an attempt to increase the flow velocity and advective heat flux through the edge, the flame strength would decrease and therefore change the advective heat flux at the edge. This burner was designed such that increases in flow velocity would not alter the flame strength drastically, allowing the advective heat flux to be easily controlled. This geometry also has the ability to go to higher advective heat flux values since higher velocities were attainable. In this sub-chapter negative edge flames are formed in turbulent environments. Specifically, experimental measurements of the edge flame velocity will be measured with respect to different boundary conditions.

7.3.2 Experimental Setup

7.3.2.1 Combustor Design

The burner used in this work, shown in Figure 7.26, was able to create statistically stationary negative edge flames in flows with varying levels of turbulence. The main channel cross sectional area was 15.7 mm deep (into the page) by 34.8 mm wide. Fuel and air flowed from the bottom of the burner on opposing sides of a 9.5 mm wide splitter plate which was 50.4 mm in length and was placed in the center of the channel. While flowing

on the respective side of the splitter plate, the gases went through steel mesh pieces to distribute the flow and subsequently a 3.2 mm cell size, 12.7 mm thick aluminum honeycomb to straighten the flow. The flow exiting either side of the splitter plate is referred to as the "slot flow" in this paper. The fuel and air mixed in an 88.9 mm long test section where the splitter plate ended, leading to the formation of a two dimensional flame sheet stabilized in the wake of the splitter plate. Square, 15.7 mm wide, jets were introduced perpendicular to the flame sheet 19 mm downstream of the splitter plate, which supplied the same fuel and air mixtures from the respective sides but at higher velocities. The jets introduced perpendicular to the flame sheet will be referred to as "side jets" in this paper. The side jets caused an increase in scalar dissipation rate along the flame sheet in the flow direction and led to local extinction. The flow then went through an exhaust section, shown in Figure 3.4, to vent the products and allow laser access to the test section.

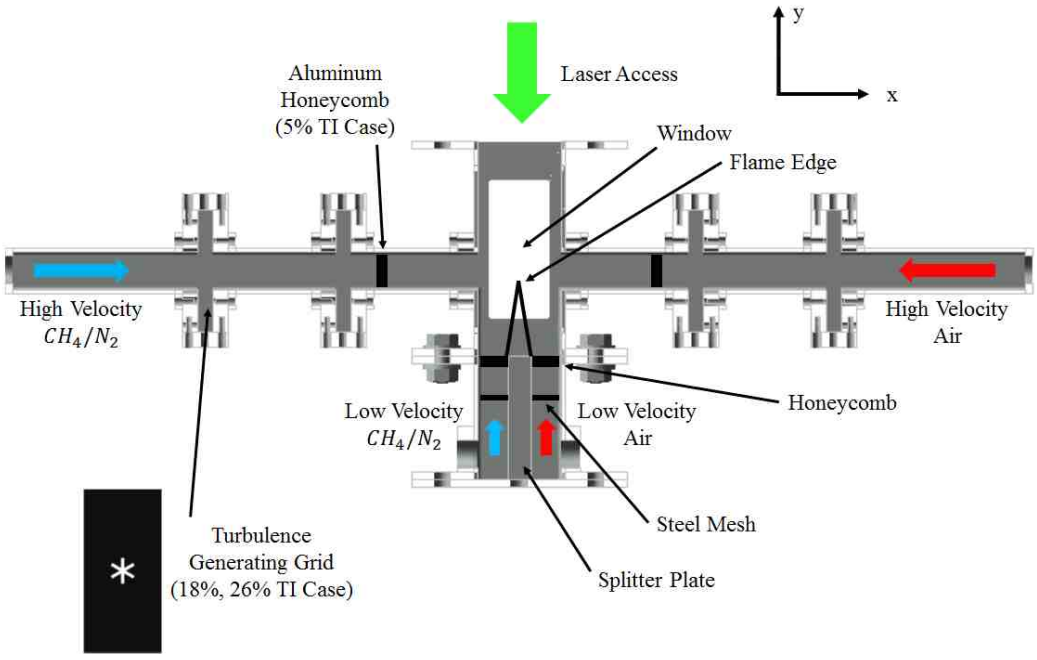

Figure 7.26: Experimental schematic of the turbulent negative edge burner. An example turbulence generating grid is also shown. Items appearing on both sides of the burner are only labeled on one side due to limited space. A depiction of a flame has also been drawn in.

The side jets had varying levels of turbulence intensities. Low (~5%) turbulence intensities were achieved by simply placing an aluminum honeycomb flow straightener in the channel. Higher turbulence intensities (18 and 26%) were achieved by removing the honeycomb and instead placing turbulence generating grids in the flow, which were 3D printed using polylactic acid (PLA) filament. The turbulence generating grid, shown inset in Figure 7.26, was designed to have a central jet with 6 slots extending outward, similar to the design used in [78,79]. The grids each had 1 mm wide slots and were 7 mm and 3 mm long from the center of the jet, leading to 84% and 94% blockage ratios, which generated 18 and 26% turbulence intensities, respectively. The integral length scales were measured to be approximately 5 mm for each case. The turbulence properties were measured using particle image velocimetry (PIV), which will be introduced in the next sub-chapter, with a side jet separately flowing air into the room at the set velocities used in the experiments. The turbulent Reynolds number, calculated using the integral length scale and root-mean-square of the velocity fluctuations were 52, 141, and 164 for the 5, 18, and 26% turbulent intensity cases.

In this work, methane diluted with nitrogen was used as the fuel with two different fuel concentrations, 25% and 30% by volume. Incoming slot velocities were varied between 60 and 120 cm/s for the 30% fuel case and between 60 and 100 cm/s for the 25% fuel case. The maximum slot velocity with 25% fuel was lower since the flame could not stabilize, due to the flame being weaker. Variations in both the fuel concentration and slot velocity led to different bulk advective heat fluxes flowing through the negative edge. Higher fuel concentrations led to stronger flames, and therefore higher bulk advective heat flux; likewise higher velocities also led to higher advective heat fluxes. Side jet velocities

were held constant at 3 m/s leading to similar scalar dissipation rate fields on average. In order to simply refer to different cases in this paper, the notation V_{slot}:V_{side} will be used where V_{slot} and V_{side} are the slot and side jet velocities in cm/s, respectively.

7.3.2.2 Diagnostics

The main result of interest for this work is the flame edge velocity relative to the flow. Therefore, both the flow and flame velocities were measured in laboratory coordinates. The relative edge velocity could then be calculated using Eq. (7.18), where V_{edge} is the edge velocity relative to the flow, V_{flame} is the flame velocity in laboratory coordinates, and V_{flow} is the flow velocity.

$$V_{edge} = V_{flame} - V_{flow} \tag{7.18}$$

The flow velocity was measured with PIV by using aluminum oxide particles with a nominal diameter of 1 μm as tracer particles which were illuminated using a Photonics high repetition rate, dual cavity Nd:YLF laser. Dual frame Mie scattering images were captured at 2 kHz using a Phantom V611 high speed camera equipped with a f = 105 mm Sigma compound lens. A constant 100 μs time delay between laser pulses was used for each case. LaVision Davis 8.3 was used to control the timing of both the PIV measurements and separate chemiluminescence imaging, but also to process images and calculate velocity vectors. The Mie scattering images had a resolution of approximately 22.8 pixels/mm. A multipass algorithm successively worked from 128 × 128 pixel to 32 × 32 pixel sized interrogation windows with 50% overlap, leading to a vector spacing of approximately 0.7 mm.

Flame chemiluminescence images were captured using a Phantom Miro 310 equipped with a f = 50 mm Nikon compound lens. The flame chemiluminescence was used to measure the flame velocity in laboratory coordinates. The exposure time of the camera was set to 385 μs to maximize the chemiluminescence signal while avoiding Mie scattering from PIV. The chemiluminescence resolution was approximately 0.13 mm/pixel. Based on the frame rate and pixel resolution, the flame velocity resolution was approximately 26 cm/s.

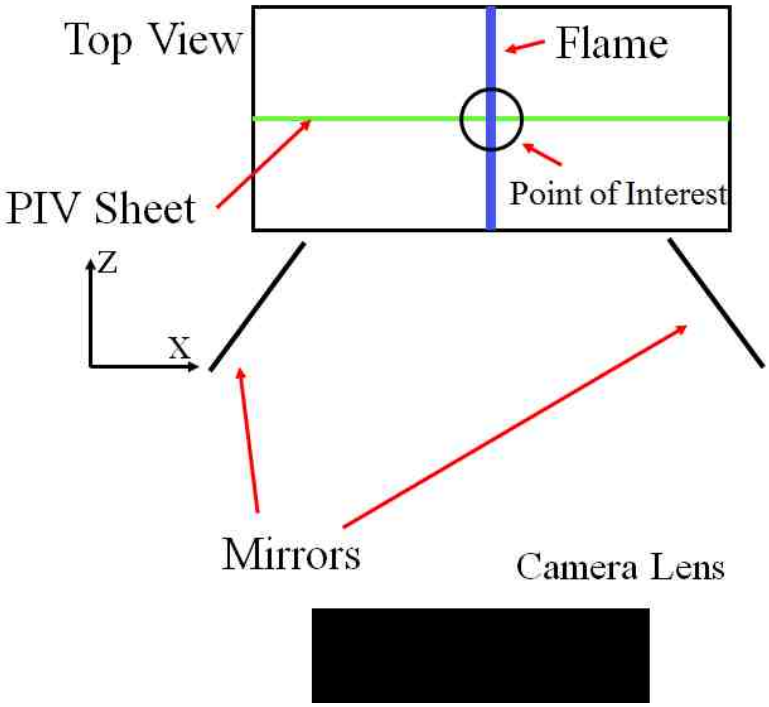

Figure 7.27: Optical setup including PIV laser sheet, flame nominal position and camera from the top view of the test section.

Since the flow velocity is only acquired in a single plane in the center of the burner, the flame velocity also needs to be at the same location. Figure 7.27 shows a top-view of the combustor section which also has drawn in the PIV laser sheet and nominal flame position. The flame position which intersects the PIV sheet is the point of interest and needs to be tracked in time.

Three views of the flame sheet were acquired in order to extract the flame edge location at the same depth as the PIV sheet. An end on view down the length of the flame sheet (the same view as in Figure 7.26) was taken along with two views each at 30 degrees from normal in the x-z plane by placing two mirrors near the test section which were angled such that all three views were obtained using a single camera, shown in Figure 7.27. The three views were projected into the x-y coordinates shown in Figure 7.26 using a known calibration plate placed in the plane of the PIV laser sheet. The three views were separately processed using a nonlinear anisotropic filter to smoothen out small variations in the signal while maintaining large gradients [121]. The Otsu method [122] was then used to determine the threshold between chemiluminescence signal and background noise, which was used to find the flame contour. Examples of the three contours from single frames are shown in Figure 7.28. In typical stereoscopic imaging, characteristic points need to be found in order to compute depth. For the purpose of this work, only the flame position at the center of the combustor section, where the PIV laser sheet was located, was needed. Therefore, only contour points from the two side views with the same projected spatial location that also overlap the end on view were classified as being in the same plane as the PIV laser sheet. An example of an identified flame edge in the PIV sheet is shown in Figure 7.28. Points which did not overlap at the same spatial location were typically points which were out of plane from the PIV laser sheet and these frames were removed and not included in the resulting statistics.

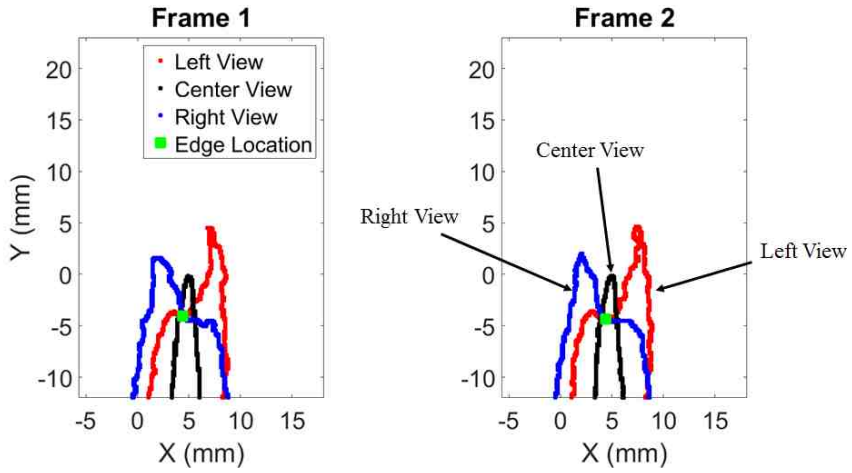

Figure 7.28: An example of neighboring frames with flame contours from three views projected into the coordinates of Figure 7.26, along with the valid edge location. Contours have been plotted with different colors and leader lines have been added in frame 2 for print versions.

The PIV system only measures velocity in the x-y plane of Figure 7.26, thus, conditions with large out of plane flame motion (z-direction) must be discarded from the statistics. Therefore, a check was performed at each edge point identified, for instance in Figure 7.28, to determine whether the flame edge was locally flat in the out of plane direction. Flat in this regard was defined as being parallel with the x-direction. The angle of the flame contour was calculated at the edge point using the two angled views by fitting a third order polynomial to a 1 mm wide region at the edge point. Only edges which were within 15 degrees of being flat were kept for velocity characterization. The example flame in Figure 7.28 shows a flame which has a higher stabilization point closer to the front of the burner and a lower stabilization point in the back of the burner, by observing the left and right views. The center region, however, is locally flat even though other regions along the flame were not.

Frames with valid edge points which pass the criteria given above were then used to obtain flame velocities. The flame velocity was calculated in laboratory coordinates by

simply measuring the distance in both the x and y directions for the translation of the identified flame edge between chemiluminescence frames and dividing by the frame rate. The flow velocity was obtained by probing the vector field which occurred between the two chemiluminescence images at the mean location between the two edge points. Since the stoichiometric line through the edge was not measured in the experiment, an estimate of the stoichiometric line was needed for valid velocities [15,48]. The stoichiometric line is essentially the normal direction of the flame surface, and since the flame has already been conditioned to be flat, the direction of the flame in the x-y direction was needed at the edge. A skeleton morphological operation [123] was performed using the end on view flame contour to approximate the x-y flame direction. The stoichiometric contour is estimated from the chemiluminescence signal, which is dominated by CH* and only present in the thin reaction layer. Therefore, we expect the center of the chemiluminescence signal to approximate the stoichiometric contour well. The skeleton fit approximates the center of the chemiluminescence contour, where only the longest feature of the skeleton fit is used and spurious lines are removed. A fifth order polynomial was fit to the skeleton and the angle of the polynomial was probed at the same spatial location as the velocity measurement. By keeping the out of plane angle flat and measuring the flame direction at the edge, the negative edge flame speed normal to the edge flame surface was sufficiently captured. Equation (7.18) was computed in both the x and y directions, projected into the normal direction of the flame obtained from the skeleton fit, and the magnitude was then computed giving a single negative edge flame speed relative to the flow. Approximately 25,000 images from each case were obtained and processed, and approximately 1,000 data points were retained after filtering the edge points for overlap

in the plane of the laser, and flame edge flatness. These 1,000 data points were confirmed to provide statistical convergence of the edge velocity. After sampling half of the data points (approximately 500 frames), the mean velocity was a maximum of 10% different than the mean velocity of the entire data set, or 16 cm/s.

7.3.3 Results and Discussion

Edge velocities for each case were calculated using the procedure outlined above. Figure 7.29 shows results for the 30% CH_4 case. Negative edge flames do exist for all conditions studied, even at high turbulence intensities. Although these flames are weaker due to the high dilution levels, the edge velocity magnitudes are significantly higher than the laminar premixed propagation flame speed for undiluted fuel. Examining each turbulence intensity case independently, there is a clear shift to higher negative flame speeds with increased slot velocity. Based on work in [48], this is believed to be an influence of increased advective heat flux through the edge, simply through an increased velocity with similar flame strengths. In [48], a trend of increased gas velocity, or increased advective heat flux, led to a linear increase in negative flame speed for laminar edge flames. This linear increase in negative flame speed with flow velocity is also observed for the turbulent flames. The turbulence level also modifies the negative edge speed with an increase in the turbulence intensity leading to a decrease in the negative edge speed. At each slot velocity, the percent difference between the highest and lowest turbulence case were all above 25%, and as high as 50%.

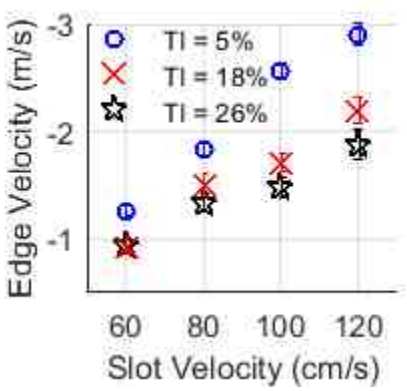

Figure 7.29: Averaged edge velocity plotted against the incoming slot velocities at the respective turbulence intensities (TI) for the 30% CH_4 fuel case. Error bars were calculated using the t-test 95% confidence interval.

Similar measurements were performed for the 25% fuel case, shown in Figure 7.29, up to a slot velocity of 100 cm/s. Similar trends are found for this case as well; as the slot velocity is increased, the negative edge velocity increased linearly for each turbulence intensity case. Also, on the whole, increasing turbulence seems to have an effect on the edge velocity. As the turbulence intensity is increased, the average edge velocity decreases; however the difference between the 18% and 26% turbulence intensity cases are not statistically significant compared to the 30% fuel case. The negative edge velocities in the 80:300 to 100:300 cases are both over 30% different between the highest and lowest turbulence intensity cases.

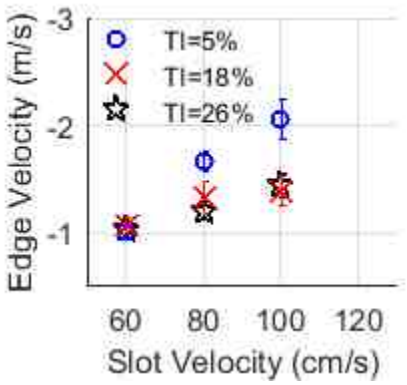

Figure 7.30: Edge velocities plotted against the incoming slot velocities for the respective turbulence intensities (TI) for the 25% CH_4 fuel case. Error bars were calculated similarly as in Figure 7.29.

The impact of advective heat flux on the edge can be studied by comparing the two fuel dilution cases. For the lowest turbulence intensity, the 25% fuel case has lower velocities than the 30% fuel case. The velocities of the low turbulence intensity 25% fuel case were 1.02, 1.66, and 2.05 m/s for the 60:300, 80:300, and 100:300 cases respectively, while the 30% fuel case were 1.25, 1.84, and 2.56 m/s. This is consistent with the understanding of steady, laminar negative edge flames discussed in [48]. The higher dilution in the 25% fuel case creates a weaker flame, as characterized by the lower peak flame temperature and the lower one dimensional scalar dissipation rate required for local extinction, as compared to the 30% fuel case. One would expect a weaker flame exposed to the same bulk flow field to stabilize in an environment with a smaller scalar dissipation rate, because of the lower one-dimensional extinction scalar dissipation rate and advective heat flux. If the flame stabilizes at a location with a lower scalar dissipation rate, the negative edge speed will also be reduced since these parameters are linearly related. Therefore, a weaker flame existing in the same bulk velocity field (as in this work) should lead to a lower negative edge flame speed which is consistent with Figure 7.29 and Figure 7.30. As pointed out in [48], there is no single negative edge flame speed for a given scalar

dissipation rate, which is also apparent here as the negative edge velocity depends significantly on the advective heat flux through the edge as a function of both the slot velocity and flame strength.

As shown in Figure 7.29 and Figure 7.30, turbulence also plays a role on the negative edge flame speed, but one would not necessarily expect this result. In [48], it was shown that the scalar dissipation rate is proportional to the advective heat flux at the negative edge, and that the negative edge speed is proportional to the excess scalar dissipation rate above the one dimensional extinction value. Therefore, it is expected that for a given slot velocity and fuel concentration, the advective heat flux at the edge would be similar for all three turbulence intensity cases, and that flow fluctuations would cause the flame to find a dynamic balance at a similar value of the local scalar dissipation rate, leading to a constant edge velocity. However, as turbulence levels increase, the results indicate that the negative edge flame speed is lower, which requires a lower scalar dissipation rate. This implies the advective heat flux through the edge is also lower. One explanation for this is that the flame may be subject to fluctuations which could weaken the flame upstream of the negative edge. This implies that the local conditions ahead of the negative edge flame may play a critical role in the negative edge speed. Yoo *et al.* [46] showed that scalar dissipation rates as well as the transient history affects the negative edge flame speed. The edge flame speeds in [46] were eventually correlated using a density weighted scalar dissipation rate using the local density compared to the boundary condition density. This is the same effect as exposing a flame to a steady scalar dissipation rate field which does not extinguish the flame quickly. The flame will be weakened by the longer residence time in the increased scalar dissipation rate field, which will lead to a lower scalar

dissipation rate at the edge than if it were extinguished quickly. The scalar dissipation rate at the edge will decrease and therefore the edge velocity will as well. Both of these concepts are ways the flame may weaken upstream of the edge, but the interpretation is different because one is transient while the other is in steady conditions.

It should be noted that there are several significant difference between this sub-chapter and Chapter 7.2. First, the flame significantly upstream of the negative edge may be effected in a non-periodic way, which leads to different statistically stationary negative edge flame speeds. Also, the highly turbulent side jets have a large range of frequency spectrum which are likely on either side of the negative edge flame response time. Therefore, this can leads to very different results when comparing turbulent and non-turbulent behavior. For instance, turbulent conditions will have higher probability of higher frequency content, and therefore have more eddies which do no interact with the negative edge flame. Moreover, Chapter 7.2 described a tendency for negative edge flames to recede toward the stabilization point much quicker than proceeding outward. From a diagnostic standpoint, more edge points may be sampled which are proceeding in the y-direction and lead to different statistically stationary edge velocities.

7.3.4 Summary and Conclusions

Statistically stationary negative edge flames in a turbulent flow were produced by introducing high velocity turbulent jets perpendicular to a stabilized non-premixed flame sheet. The high velocity jets increased the scalar dissipation rate along the flame sheet in the flow direction which created negative edge flames. Different levels of bulk advective heat flux were supplied through the negative edge, by varying both fuel dilution (flame

temperature) and incoming bulk velocities. For each case, differing levels of jet turbulence intensity were examined.

The flame edge velocity was measured by simultaneously measuring the flame and flow velocity in laboratory coordinates, and taking the algebraic difference normal to the flame edge to obtain the relative edge velocity. The negative edge flame velocities varied with slot velocities, fuel concentration, and turbulence levels. As the slot velocities or fuel concentration increased, the advective heat flux through the flame also increased leading to a larger negative edge flame speed. This result matches prior work in laminar flames. As the turbulence level increased, the negative edge speed decreased. This result implies that the flame is stabilizing in locations of lower instantaneous scalar dissipation rate with increasing turbulent intensity. The prior work in steady laminar flames shows this only results when the advective heat flux through the flame is decreased. Thus these results imply that the flame is weakened upstream of the flame edge and that the time history of scalar dissipation rate along the flame sheet affects the negative edge flame speed.

8 Premixed Jet in Hot Coflow

8.1 Motivation

Modern gas turbine engines have been subject to strict pollutant emission regulations which has led to design changes to either improve efficiency or reduce pollutant production. Efficiency can be improved by increasing the pressure ratios [5], while pollutant reduction can be achieved by distributing the heat release throughout the combustor such that high temperatures are reduced [4,5]. The Pratt and Whitney Technology for Advanced Low NO_x (TALON) combustor utilizes both of these methods [7]. The design utilizes a rich swirl burner which provides a stable burning flame in which staged air injectors are used downstream to locally extinguish the flame. Downstream of the air injectors burning occurs again under lean conditions. The working principle in this combustor is to avoid burning in stoichiometric regions by quickly quenching the flame such that the mixture transitions from rich to lean conditions quickly with minimal high temperature heat release. This reduces the overall temperature in the combustor which also reduces pollutant emissions. Although the combustor is designed to not burn at stoichiometric conditions, it is still likely that reactions are occurring at high peak temperatures leading to high pollutant production. One way to totally alleviate this would be going to a fully premixed combustor where premixed jets are injected into a flow of hot vitiated products. Safety has been a major factor keeping combustors fully non-premixed, like the TALON combustor, because premixed combustion has the potential for flashback to occur which leads to burning in unwanted regions [5]. Although safety is a concern, premixed combustion does allow the temperature to be better controlled since lean equivalence ratios can avoid high temperature burning altogether. General Electric has

produced the Twin Annular Premixed Swirler (TAPS) combustor which utilizes a low flow rate, non-premixed pilot to stabilize premixed swirl burning flames [124]. Since the peak temperature inside the combustor can be changed based on the equivalence ratio, pollutant emissions can be significantly reduced.

When a premixed mixture is issued into a sufficiently hot environment, autoignition is a potential stabilization mechanism and the conditions for autoignition are complicated by non-homogeneous mixture and temperature distributions, as shown in Figure 8.1. In Figure 8.1 the mixture fraction was defined as unity in the reactants and zero in the vitiated products. Therefore, there is a tradeoff between the temperature and mixture fraction, and likewise fuel concentration. High temperatures have low fuel concentrations producing low amounts of heat, while low temperatures have high mixture fractions and increased heat release. This creates a very difficult problem when conceptualizing autoignition behavior with both species and temperature gradients. Studies related to fuel jets in hot environments generally found that autoignition occurred at the so-called most reactive mixture fraction both using single-step [125] and detailed chemistry [126] defined as the mixture fraction which has the shortest ignition delay time. This dissertation examines a representative problem where a premixed jet is issued into a sufficiently hot coflow such that the mixture can autoignite. Analysis near a stable autoigniting point are conducted to develop an understanding of how the flame is stabilizing in this non-homogeneous environment.

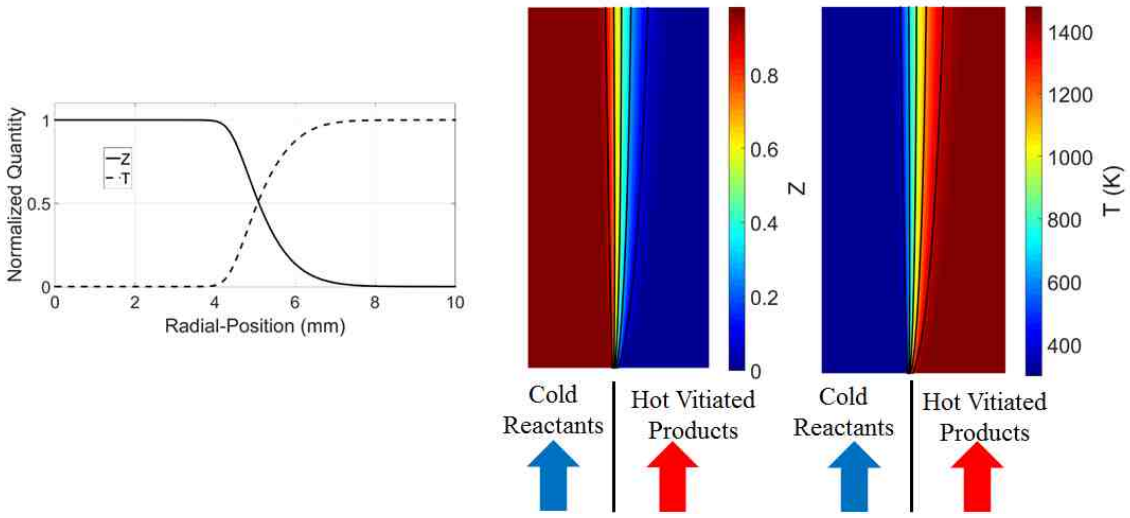

Figure 8.1: Mixture fraction and temperature contour plot and horizontal slice depicting tradeoff between mixture fraction and temperature.

8.2 Setup

8.2.1 Burner Design

The first generation of this burner was built, and a schematic is shown in Figure 8.2. The burner consists of two coannular nozzles in which the outer nozzle provides vitiated products, while the inner nozzle provides premixed cold reactants. A 264.7 mm diameter cylinder was refractory lined with Kast-O-Lite 97L to form a converging nozzle for the coflow. The refractory lining is used due to the low thermal conductivity and low thermal expansion properties which will not transfer much heat from the hot flow or expand during the different thermal cycles. The fuel and air entering both the jet and coflow were well mixed before entering the bottom of the burner. A connector which held the jet and perforated plates in place allowed different jet diameters to be used. The current study utilizes a 3.81 mm diameter jet which runs straight through the center of the burner. The coflow fluid enters through four ports on the bottom of the burner and flows through a series of flow distributors before passing through a final steel perforated plate with an 87%

blockage ratio and 1.5 mm diameter holes to stabilize a coflow flame and to act as a flame arrestor. The coflow diameter is 122.5 mm in this region, which then passes through a converging nozzle to create a nearly plug flow velocity profile at the jet exit. The coflow diameter is 50 mm at the exit, leading to a contraction ratio of 6:1 over 70 mm in length. In work by [47], it was found that a large contraction ratio will give a fairly uniform velocity profile. After passing through the converging nozzle, both the jet and coflow exit the burner and are allowed to mix. The burner is unconfined in the laboratory. All cases in this experiment produced a laminar and steady lifted flame allowing low speed diagnostics to be used.

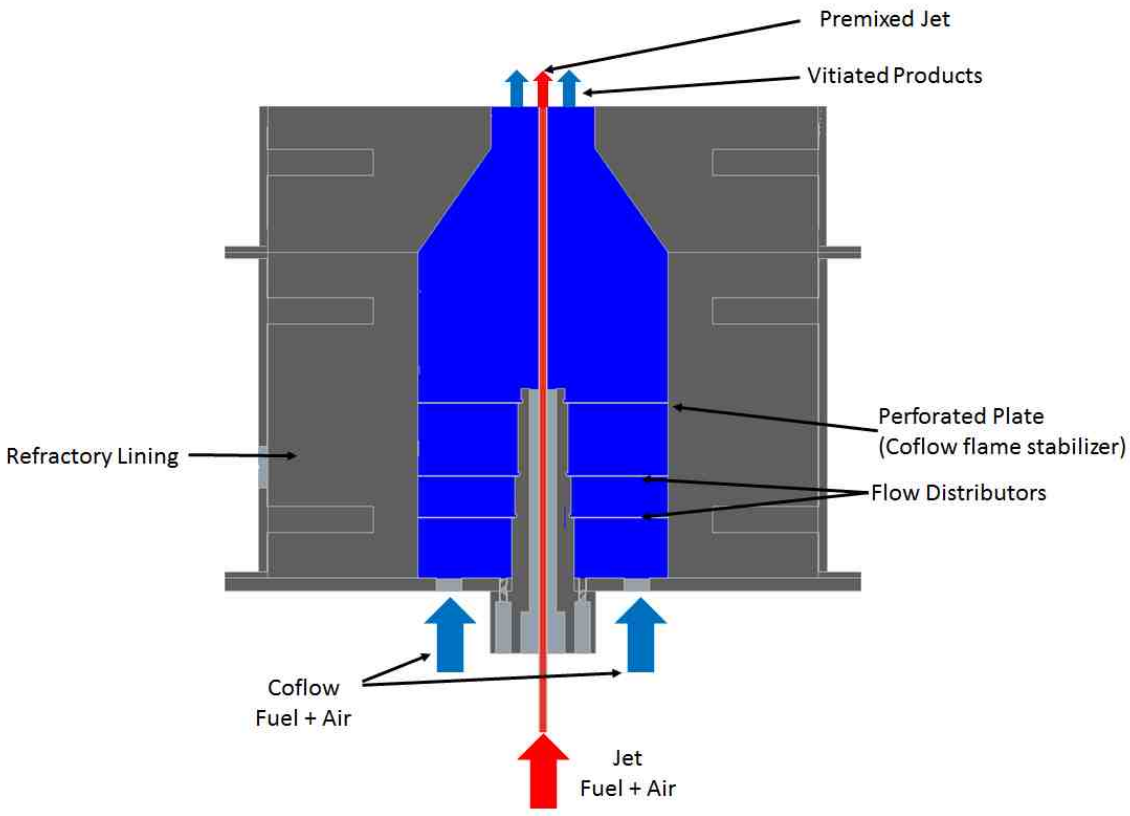

Figure 8.2: Jet in coflow burner design. Slice shown is through the center of the burner.

Several boundary conditions were varied in the experiments including ϕ_J and V_J. ϕ_J was varied from 0.75 – 1, while the ϕ_{Co} was held constant at 0.7 for these experiments.

Ethylene was used as the jet fuel due to the molecular weight being similar to air, while propane was used to create the vitiated products in the coflow. V_{Co} was set to 6 m/s for each case, while V_J was varied from 6 – 8 m/s. Rayleigh scattering has been used to measure the coflow temperature with ϕ_{Co} at 0.7, which is nominally 1500 K. While many boundary conditions were used, only one case was studied in depth using numerical simulations.

8.2.2 Diagnostics

Both OH and CH_2O PLIF were conducted in this experiment, shown in Figure 8.3. CH_2O can be utilized to identify the preheat region ahead of the reaction layer, while OH is present in the reaction and post reaction regions [127]. CH_2O PLIF was performed by using the frequency tripled output of the Nd:YAG to excite the $^1_0 4$ transition in the $A \leftarrow X$ band. The beam was directed towards the burner and a 15 mm long sheet was created using both an f = 500 and f = -60 mm cylindrical lens. OH PLIF was performed by using the frequency doubled output of the Nd:YAG to pump a Sirah tunable dye laser circulating a Rhodamine 590 and ethanol solution. The laser was tuned to approximately 283 nm to excite the $Q_1(5)$ transition in the $X \leftarrow A(1,0)$ band of OH. A sheet was formed using both an f = 500 and f = -30 mm cylindrical lens system.

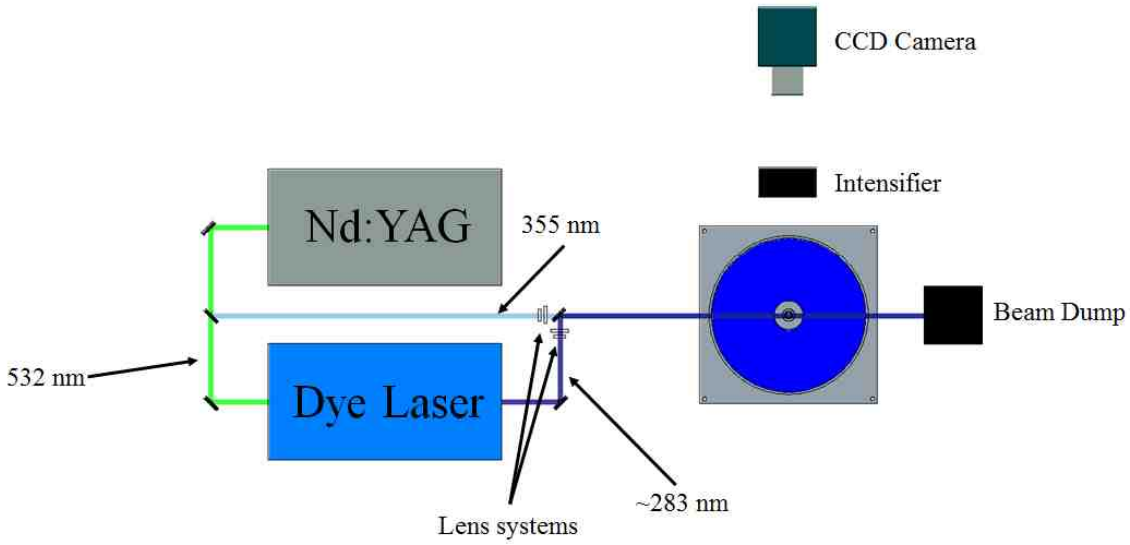

Figure 8.3: OH and CH_2O PLIF laser and imaging setup.

Fluorescence signal from OH and CH_2O was collected one after another using the same Universe Kogaku UV 1054B compound lens to project the light onto a Photonis XX1950LP image intensifier. The intensifier was gated for 400 ns to reduce the chemiluminescence and background light signal. The intensifier phosphor screen was imaged using a Mightex CGN-B013-U camera. For OH PLIF, a 320 ± 20 nm filter was placed ahead of the compound lens, while a 455 ± 25 nm filter was used for CH_2O PLIF.

Since the compound lens used to collect light was subject to chromatic aberrations, a translation stage was used to image the fluorescence signal from two different locations for the respective species. One PLIF beam was first blocked and images were collected, then both beams were blocked and background images with only the flame running were taken. The same procedure was completed for the other PLIF measurement after adjusting the lens position to correct for focusing length. Both a laser and dark background were also collected at the respective positions. Images were processed by averaging the fluorescence signals as well as the flame, dark, and laser background images. The actual

PLIF signal was obtained by subtracting both the flame and laser background images from the fluorescence signal and adding the dark background since the dark background was subtracted twice. The images were then calibrated into x-y coordinates using a known calibration plate aligned with both PLIF beams with LaVision Davis 8.3.

8.2.3 Numerical Setup

A premixed jet in vitiated coflow was simulated in a similar environment for further analysis, and the computational domain is shown in Figure 8.2. The domain size was altered in order to reduce the computational time. The jet was modeled as 2.5 mm wide and the coflow as 5 mm wide, while the domain was 20 mm high in the axial direction. For simplicity, the jet wall was not included in the calculations. The domain height was chosen since the flame was observed to stabilize at approximately 10 mm. The left edge of the computational domain was modeled as an axis of symmetry and the top and right portions were modeled with pressure outlets. The bottom of the domain had both the jet and coflow inlets. The mesh had a uniform 30.25 μm resolution, however, a simulation with double the grid resolution was also computed to ensure grid convergence and will be shown later in this Chapter. Both the jet and coflow were modeled at 5 m/s with a plug-flow velocity profile. The jet was simulated with a premixed ϕ = 0.75 ethylene-air mixture and the coflow was simulated using the chemical equilibrium state of a ϕ = 0.7 propane-air mixture which underwent heat loss to bring it to 1500 K. This temperature boundary condition was chosen to match the experimental boundary condition. The individual species concentrations and temperatures were input at the coflow exit as well as both pressure outlets.

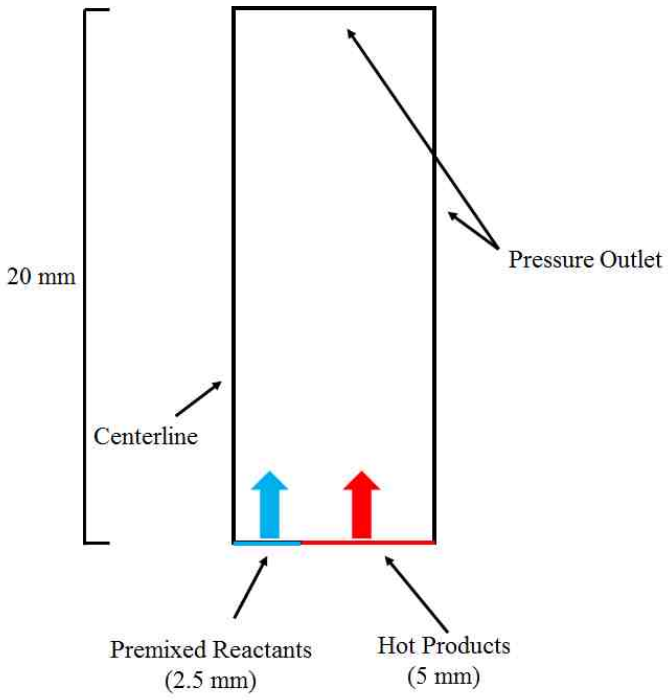

Figure 8.4: Computational domain for modified jet-in-coflow geometry.

ANSYS Fluent 16.1 was used to compute the numerical simulation with a steady, segregated, implicit solver. The Semi-Implicit Method for Pressure Linked Equations (SIMPLE) [106] scheme with PREssure Staggering Option (PRESTO!) was used to interpolate the pressure for pressure-velocity coupling. Multicomponent species and thermal diffusion were used to solve the Maxwell-Stefan equations for diffusive mass flux vectors, using binary mass diffusion coefficients and empirical thermal diffusion models [107], respectively. The fluid was modeled as a laminar incompressible ideal gas, and therefore the mixture thermal conductivity, viscosity, and specific heat capacity was calculated using ideal gas mixing. Mass and thermal diffusivities, viscosity, and thermal conductivity were all calculated with kinetic theory for each species. The full GRI transport and thermodynamic database were used for fluid properties [108]. Detailed chemistry was calculated with Arrhenius chemistry using the GRI-3.0 [108] chemical mechanism which has 53 species and 325 reactions. Fluent calculates chemistry by

invoking User-Defined-Scalars for each species, and is limited to 50 species in total. Therefore, three species were removed: Ar, C_3H_8, and C_3H_7. Thus, 50 species and 309 reactions were used after removing these species and their respective reactions.

8.3 Results and Discussion

8.3.1 General Ignition Observations

Example PLIF images of both CH_2O and OH are shown in Figure 8.5. The CH_2O laser sheet is approximately 15 mm long ranging from 4 – 19 mm in the Y direction. The jet center is at X = Y = 0 and is flowing in the positive Y direction. Clearly the high heat release is occurring at significantly lifted regions, approximately 10 mm downstream of the jet exit, shown in the OH signal. There is also CH_2O production far upstream of the OH signal, which indicates significant preheating ahead of the high heat release region [68]. Therefore, since there is CH_2O production sufficiently far upstream of OH, the stabilization is expected to be altered by autoignition characteristics. If autoignition was not playing a role in the stability behavior, CH_2O would be expected to be present in the nearfield of OH production and quickly consumed. Therefore, these flames are thought to at least be autoignition assisted, however, it is unclear whether the flame is stabilized only by autoignition or also assisted by flame propagation. It should be noted, however, that the CH_2O production is likely just an effect of the hot mixing layer present between the cold premixed jet and hot vitiated coflow.

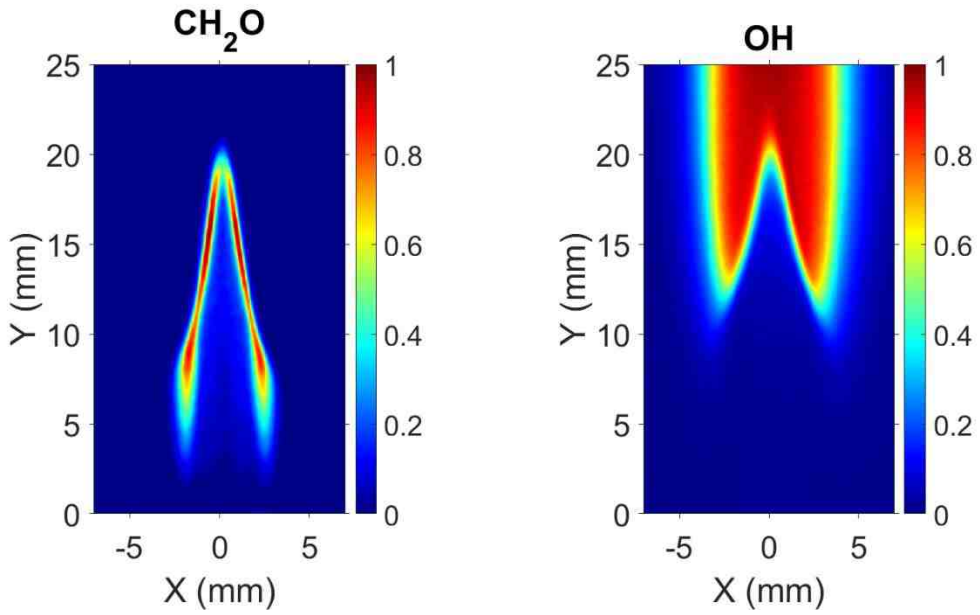

Figure 8.5: Example PLIF images of CH_2O and OH for ϕ_{Co} = 0.7, V_{Co} = 6 m/s, ϕ_J = 0.75, and V_J = 6 m/s.

By assuming that the velocity is a constant 6 m/s upstream of the flame (the jet and coflow boundary condition) and the flame base is approximately 10 mm above the jet exit, then the flow time to the reacting region is approximately 1.6 ms. Chemical simulations were performed using Cantera [116] with GRI Mech 3.0 [108] consistent with the mechanism used in Fluent to characterize the ignition delay time. The chemical calculation sequence is depicted in Figure 8.6, which is a simplified version of the experiment where mixing occurs instantaneously and does not further diffuse in the axial direction. The coflow mixture was simulated by calculating the chemical equilibrium state of the coflow inlet boundary conditions, the jet fluid was initialized and a portion, defined by Z given in Eq. (8.1), was adiabatically mixed with the vitiated coflow fluid. The mixture was then simulated in a perfectly stirred reactor (PSR) where a time marching scheme was used to compute the time evolution of the reacting fluid. The ignition delay time was defined based on the time to reach the maximum heat release for each Z with the results shown in Figure

8.7 for the case of ϕ_{Co} = 0.7 and ϕ_J = 0.75. The simulations show the homogenous ignition delay time for Z less than 0.2 is approximately 100 μs or less, which is at least 10 times faster than the suggested experimental timescale. The low Z values have short ignition delay times due to the high mixture temperature, but do not release much heat due to low fuel concentrations. Conversely, large Z values have more fuel which releases a larger amount of heat, but requires a longer ignition delay time. Therefore, the actual stabilization point in the experiment with gradients in Z is impacted by this trade off.

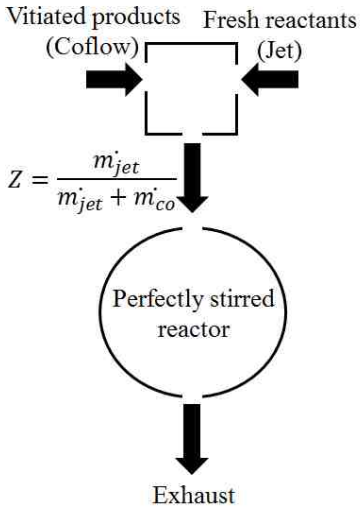

Figure 8.6: Visual depiction of the chemical simulations.

$$Z = \frac{\dot{m}_J}{\dot{m}_J + \dot{m}_{Co}} \tag{8.1}$$

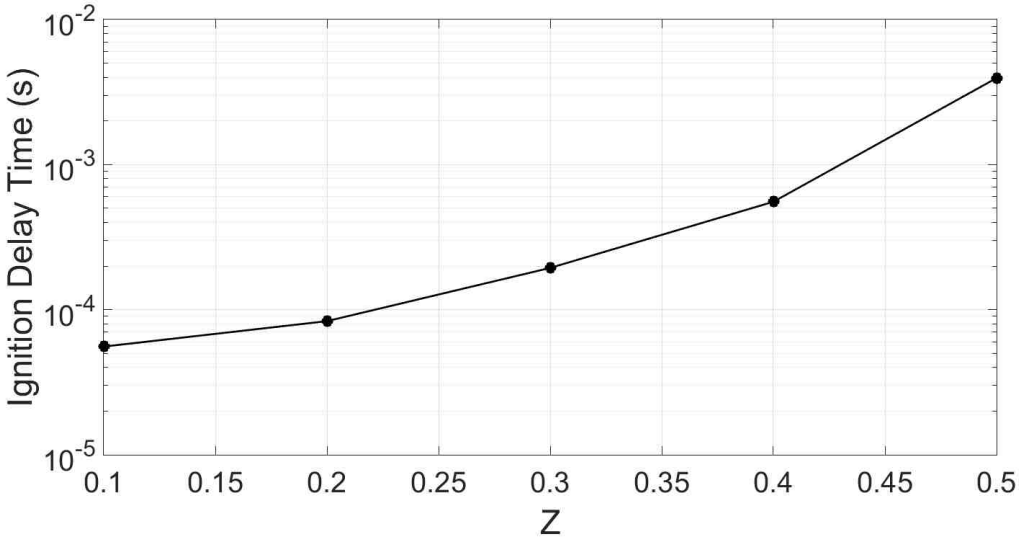

Figure 8.7: Ignition delay times simulated using a perfectly stirred reactor (PSR) for different mixture fractions between the premixed jet and vitiated coflow products.

Since CH_2O and OH are important in understanding the stability behavior for these flames, CH_2O and OH concentrations from the PSR calculations are shown in Figure 8.8 as dashed and solid line respectively. H_2O_2 was also plotted as a dotted line and will be discussed later. These simulations show the large range of time scales present at the different Z values in the mixing layer between the jet and coflow. For all Z values, CH_2O is rapidly produced in the earliest timescales of the simulation. Conversely, OH is produced slower, especially with larger Z values, and is typically representative of high temperature heat release and post-combustion products [127]. The Z = 0.1 simulation seems to produce CH_2O and OH almost simultaneously, therefore CH_2O is quickly consumed in the resulting flame. OH is likely produced very quickly since the mixture temperature is still high. For the larger Z values, there is a duration of time where the peak CH_2O concentrations are essentially constant, exemplified in the Z = 0.5 case. The temperature at this condition is much lower than for low mixture fractions and the ignition delay is notably longer; however the peak concentration of formaldehyde is reached much

sooner. During the time when CH_2O is relatively constant, there is rapid production of H_2O_2 as well. However, H_2O_2 is produced in low concentrations at lower mixture fractions. Therefore, H_2O_2 seems to be produced only at relatively low temperatures prior to ignition. It is interesting to note that by using the same scaling from earlier, if the autoignition stabilization is dominated by $Z = 0.5$, then the liftoff height would be approximately 24 mm and would be much higher than observed. Therefore, either the non-idealized mixing layer or smaller mixture fractions are dominating the stability.

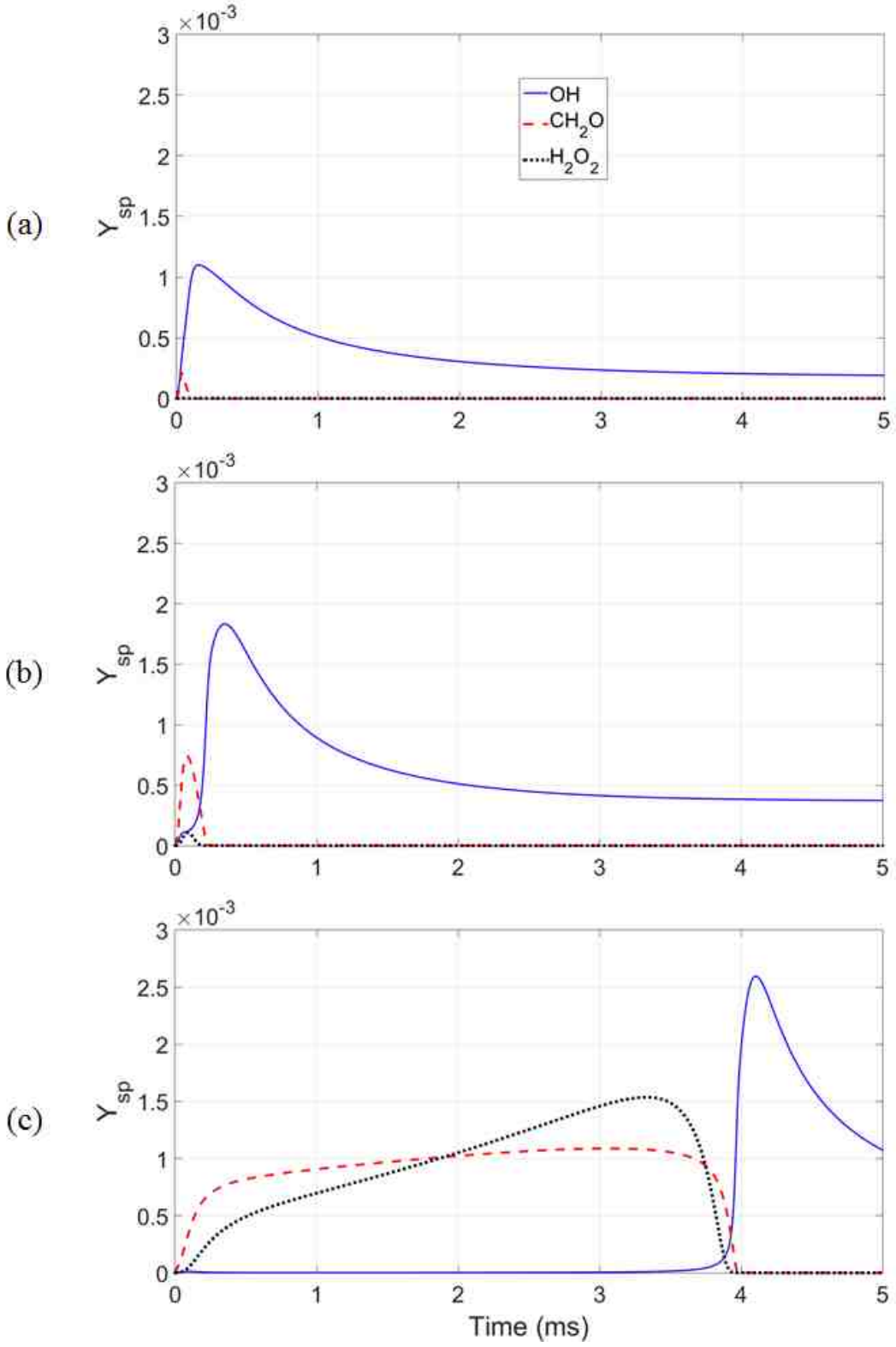

Figure 8.8: Mass fraction samples of OH, CH_2O, and H_2O_2 in time from the 0-D PSR chemical simulations.

Peak concentrations of OH, CH_2O, and H_2O_2 as well as the initial temperature of the mixture are plotted in Figure 8.9. As Z increases, peak values of OH and CH_2O monotonically increase when chemical reactions take place ($Z < 0.5$), likely due to higher fuel concentrations. The last ignitable mixture is the mixture fraction of 0.5, which is the last mixture which produces OH, and correlates to an initial mixture temperature of approximately 950 K. Mixture fractions larger than 0.5 still produce CH_2O and H_2O_2 since the mixture is still relatively hot, but at smaller concentrations than the 0.5 mixture fractions. Therefore, formation of CH_2O and H_2O_2 do not necessarily indicate mixtures which can react and produce heat, but rather mixtures that can still undergo preheat-type reactions.

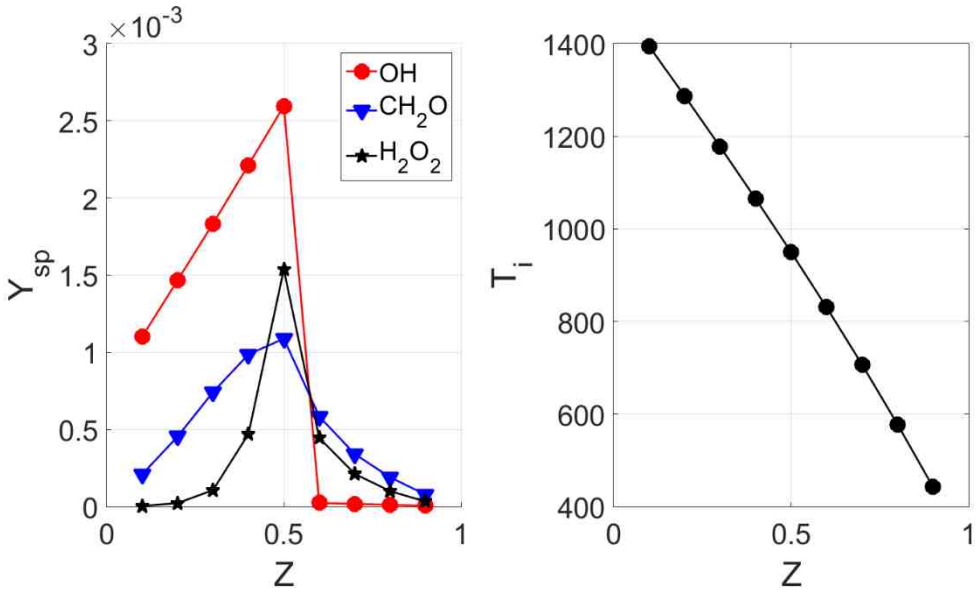

Figure 8.9: Maximum concentrations of OH, CH_2O, and H_2O_2 as well as initial mixture temperature plotted versus mixture fraction using an idealized PSR calculation.

These trends were used to better understand conditions in the jet in coflow experiment. Numerical simulations were performed with plug flow velocities at 5 m/s for both the jet and coflow with relevant conditions to the experiment. The standard mesh resolution was 31.25 μm which was also compared to a simulation with doubled grid

resolution, leading to 16.125 μm cell sizes. Figure 8.10 shows a comparison of the standard and doubled mesh resolution by obtaining radial profiles of (a) CH_2O and H_2O_2 mass fractions and (b) temperature at 3, 4, and 5 mm above the jet exit. These profiles were used since they have been indicated as important species in autoignition-type behavior. Each of the respective profiles show very good similarity and therefore indicates grid independence using mesh cell sizes of 31.25 μm.

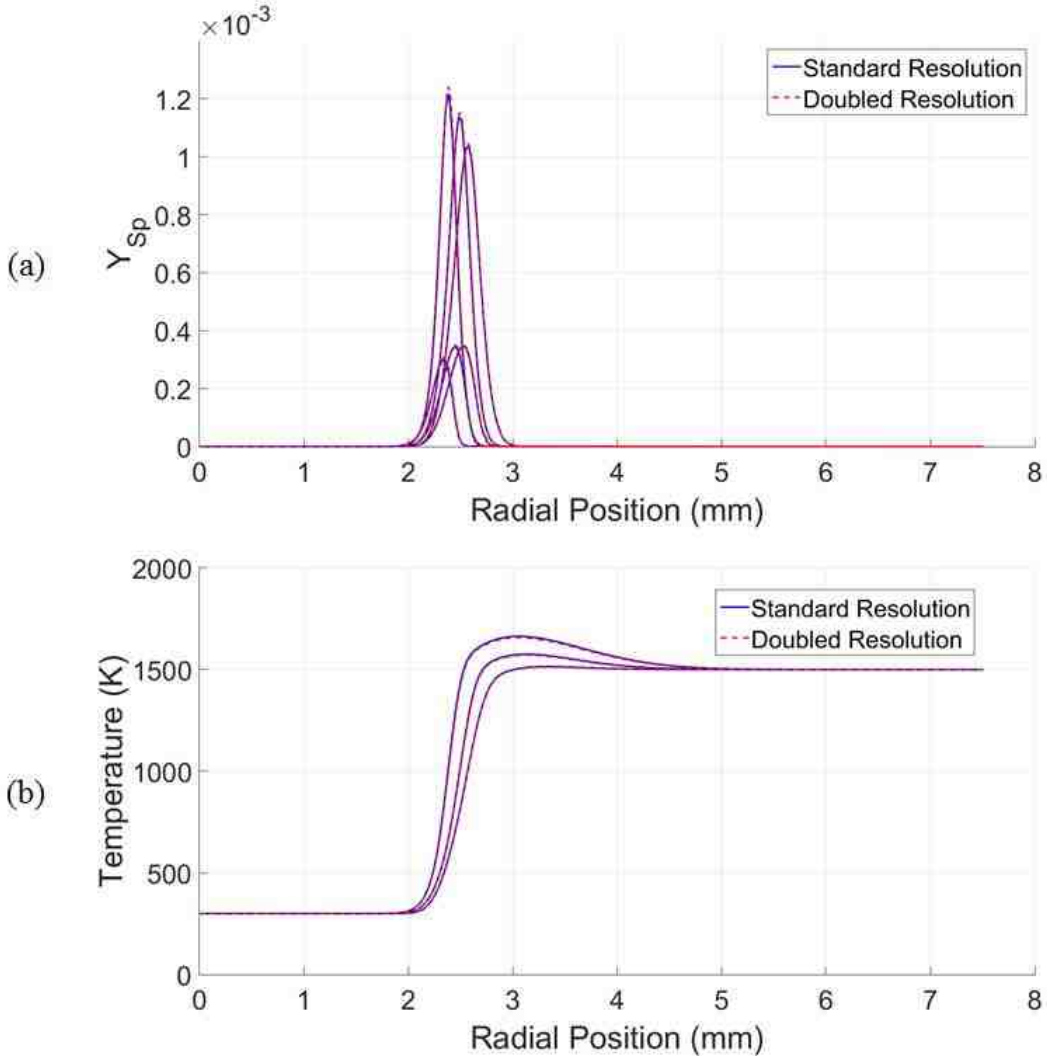

Figure 8.10: Horizontal (radial) profiles of (a) CH_2O and H_2O_2 mass fractions and (b) temperature at 3, 4 and 5 mm above the jet exit.

The heat release was calculated by using the reaction rates for each reaction and multiplying by the enthalpy of combustion for each individual reaction. The heat produced from each reaction was summed and is plotted in Figure 8.11 both in the whole flowfield (a) and around the location of flame stabilization (b). The computational domain is depicted in Figure 8.4, where the bottom edge from 0 to 2.5 mm is the jet exit and from 2.5 to 7.5 mm is the hot coflow. Both the jet and coflow are flowing in the positive axial direction with the same velocity magnitude. The white line in Figure 8.11 (b) follows the maximum heat release at each axial height. The magenta lines plotted in both (a) and (b) are the streamlines which intersect the maximum heat release (white) line at the location of 10%, 30%, 50% and 90% of the maximum heat release rate, respectively. The flame is relatively highly lifted above the jet exit, where the 90% heat release contour begins at approximately 7.5 mm in the axial direction. Beyond 7.5 mm the flame nearly acts as a lifted premixed flame, maintaining a nearly constant Bunsen angle with the same constant shape and heat release magnitude. The region between the 10% and 90% heat release is considered the stabilization region for this flame since this is where the flame transitions to a lifted premixed flame. Therefore, the stabilization region is between 2 and 7.5 mm in the axial direction.

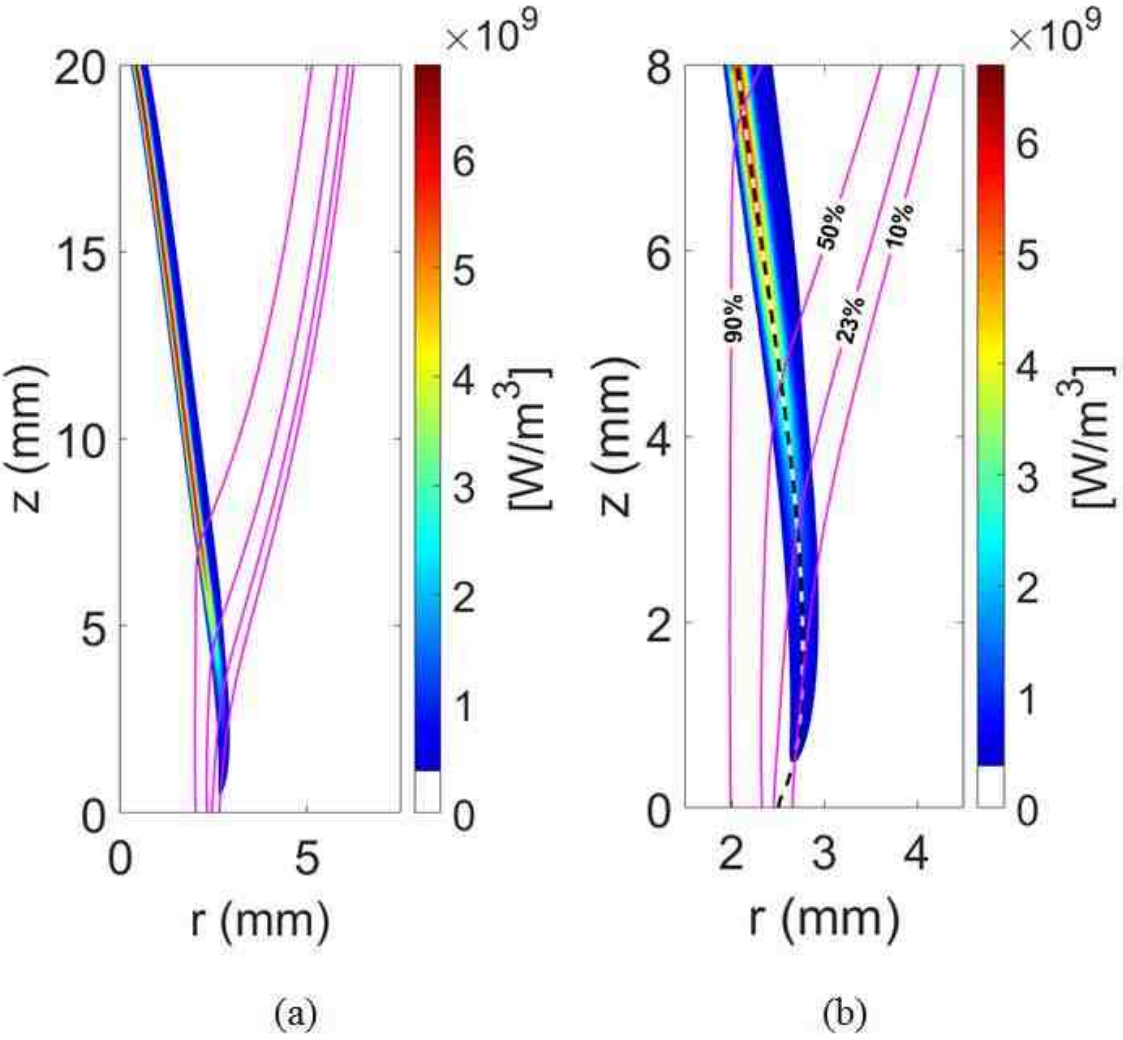

Figure 8.11: Heat release contour plot for the jet in coflow simulation showing the (a) full field and (b) zoomed in view. Magenta lines are calculated streamlines which pass through the minimum axial height of the 10%, 30%, 50%, and 90% maximum heat release contours. In (b) the white line is the line of local maximum heat release.

Upstream of the 10% maximum heat release contour, there is still heat being released all the way to the burner exit, but is very small when compared to the heat which is released from the premixed region. Therefore, this inherently brings up a question for these flames: what is the location of the beginning of the flame? Observations from Figure 8.5 show the flame highly lifted which is consistent with Figure 8.11 if the flame is defined as regions with high amounts of heat release. However, since there is heat being produced

on the order of 10^8 W/m^3 near the jet exit, it is questioned whether this flame is lifted or actually attached. One distinguishing feature is that the low heat release reactions near the burner exit likely cannot sustain high heat release rates without the presence of the coflow providing suitable heat transfer, whereas the downstream premixed flame provides sufficient feedback of heat and species to the incoming jet reactants to allow the mixture to ignite. A key question to be addressed in this research is therefore: where do the reactions transition from being supported by the coflow to self-sustaining and what is the role of autoignition in that transition?

Flow times to different percentages of the maximum heat release were sampled in the flow simulation by calculating a streamline which passes through the respective heat release contour, and subsequently calculating the residence time along the streamline to the maximum heat release. These values were compared against the chemical time scales for different mixture fractions and is shown in Figure 8.12. The flow ignition times are shown as red triangles and correspond to the red axis along the top and right side of the figure. For low heat release values, the flow ignition time is approximately 200 μs and is longer than the most reactive mixture fraction from the chemical simulations. The flow ignition times is rather flat, while the chemical ignition time has a much larger range. This may be due to only a portion of the sampled streamlines being dominated by autoignition. Once autoignition occurs, there could be a fairly quick transition which allows the downstream mixtures to all undergo premixed flame behavior, leading to a relatively flat line. There is a single crossing point where the flow time is lower than the chemical ignition delay time at larger mixture fractions. This would be expected also by noting from earlier that if the

flame was dominated by the ignition delay time from Z = 0.5, the flame would remain outside of the computational domain.

Although low heat release values are comparable to smaller mixture fractions, there is still a difference in the ignition delay time. There are two main reasons why this may be the case. First, the homogenous reactor assumes instantaneous idealized mixing and also assumes that the streamlines follow lines of constant mixture fraction, which is likely not the case since the streamlines will be near vertical and diffusive effects from the coflow will lead to curved mixture fraction iso-lines, shown in Figure 8.1. Therefore, streamlines will likely pass through many mixture fractions prior to reacting. The second main reason can be observed from the 10% heat release streamline in Figure 8.11. The streamline originates from the coflow and therefore needs time to mix with the jet to obtain fuel. Not only that, but the streamline actually passes through the maximum heat release line layer twice. Therefore, the fluid parcel likely diffuses with the jet, reacts while still diffusing reactants, and increases in heat release again. This leads to a non-homogenous mixing effect and an inherent mixing time which is needed for this streamline to reach an ignitable mixture which could cause a longer ignition delay time. Also, since the mixture has two local maximum heat releases, it clearly has non-homogenous effects which elongate the ignition delay time.

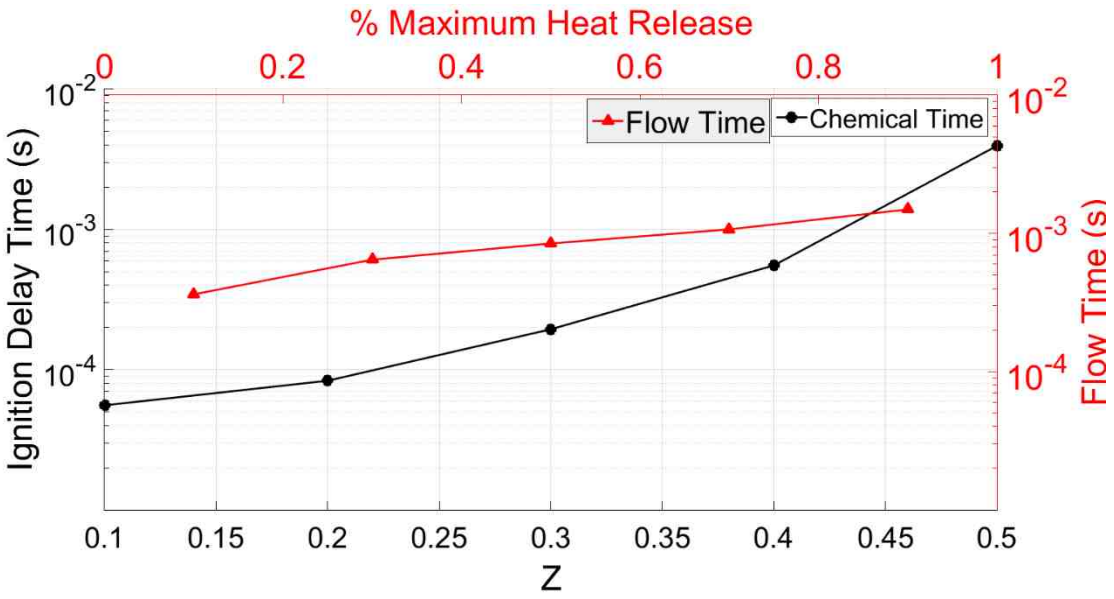

Figure 8.12: Ignition delay time plotted from the chemical simulations and points extracted from the flow simulation with a given amount of heat release. Both of the delay times were defined as the time to reach the maximum heat release.

8.3.2 Species and Temperature Simulated Observations

Mass fractions of OH, CH_2O, and H_2O_2 were plotted in Figure 8.13 with similar streamline and local maximum heat release line as in Figure 8.11. Axial heights greater than 10 mm show consistencies for each species, but are different at lower axial heights. Axial heights greater than 10 mm show consistent behavior with premixed flames. There is a small region where both CH_2O and H_2O_2 are produced and are quickly consumed, where large concentrations of OH are present in the reaction layer and post-combustion products region. Therefore, this region should be dominated by the premixed jet only, and should have little influence from the coflow itself. The streamlines ahead of the reaction layer have little influence from the coflow and produce low amounts of preheat radicals until the flame is approached, also consistent with premixed flame behavior.

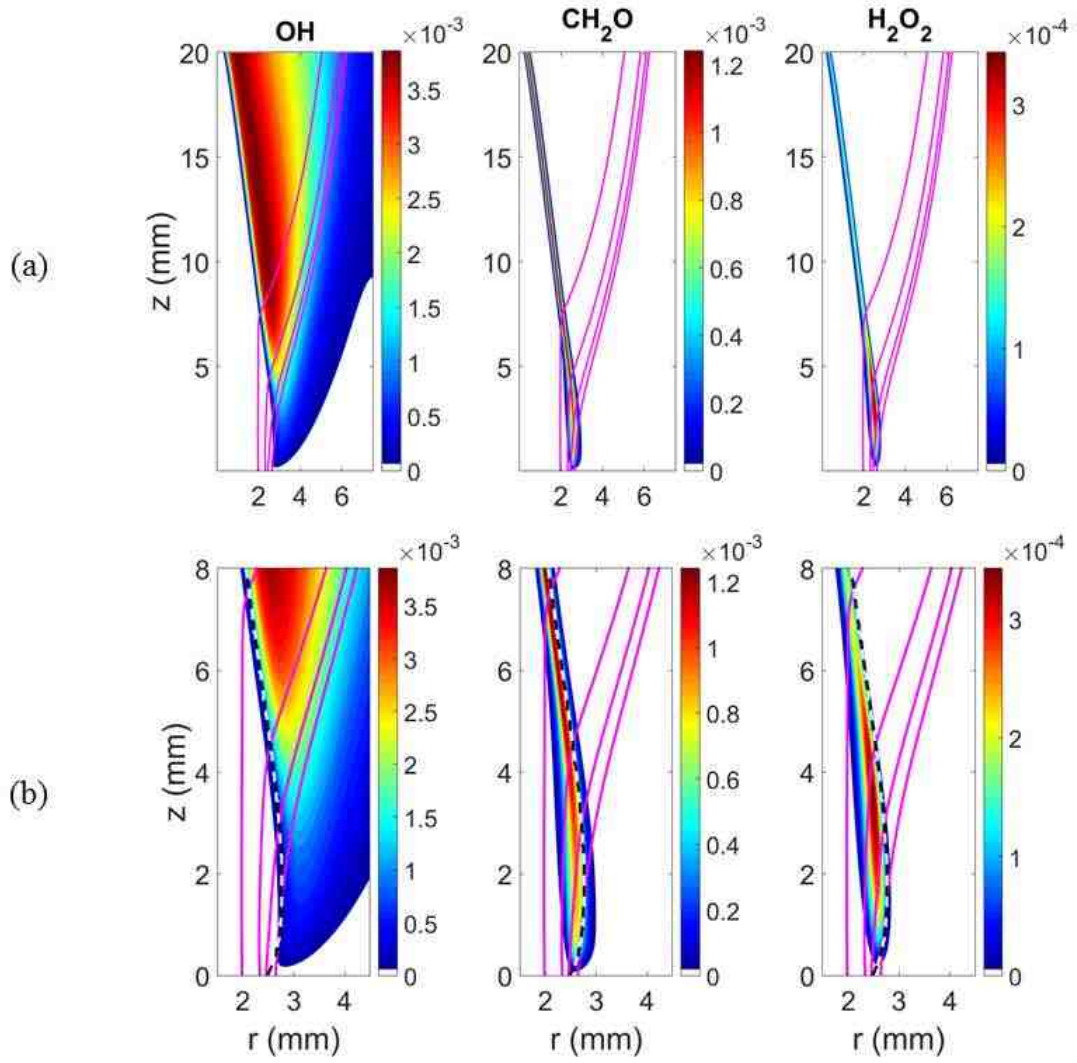

Figure 8.13: Mass fractions of OH, CH_2O, and H_2O_2 on the full computation domain (a) and near the stabilization location (b). Magenta lines represent streamlines through 10%, 30%, 50%, and 90% of the maximum heat release and the white line in (b) is the local maximum heat release.

Axial heights less than 8 mm, shown in Figure 8.13 (b) have very different behavior. OH is produced in very small quantities upon passing through the reaction layer at lower axial heights, and therefore likely are being stabilized by mixtures closer to the coflow. At higher axial locations, more OH is produced and is likely stabilized by mixture fractions closer to the jet. CH_2O is produced in very high quantities and even reaches near peak values at an axial position of approximately 4 mm. Since CH_2O is a radical present

in the preheat region, there are significant preheating effects ahead of the high heat release region in the streamwise direction.

H_2O_2 similarly is produced upstream of the high heat release reaction layer, however, H_2O_2 concentration decreases when approaching the premixed region. Interestingly, the streamline which passes through the maximum H_2O_2 mass fraction also flows through less than 50% of the maximum heat release, and therefore may indicate that more premixed behavior is occurring with streamlines which pass through greater than or equal to 50% of the maximum heat release. In Figure 8.9 it was also shown that non-negligible amounts of H_2O_2 are produced between 700-1100 K which indicates that low temperature chemistry is playing a role in the stability behavior of this flame. However, the maximum values of OH and CH_2O are on the same order of magnitude as the chemical simulations, but H_2O_2 reaches much larger concentrations in the chemical simulations than the flow simulation. This is likely due to the flame transitioning to premixed flame behavior at lower mixture fractions than the $Z = 0.5$, where maximum H_2O_2 concentrations were produced. The species contour plots and streamline information indicates that there is autoignition type behavior in streamlines which pass through less than 50% of the maximum heat release, and premixed flame behavior in streamlines with larger maximum heat release rates.

Temperature contour plots are shown in Figure 8.14 with similar streamlines and maximum heat release lines as previous figures. Similarly, at axial locations higher than 10 mm, there are premixed flame characteristics. Conversely, at axial positions lower than 8 mm, there is very different behavior. Temperatures along the streamlines through different regions of the maximum heat release were plotted in Figure 8.15 for comparison.

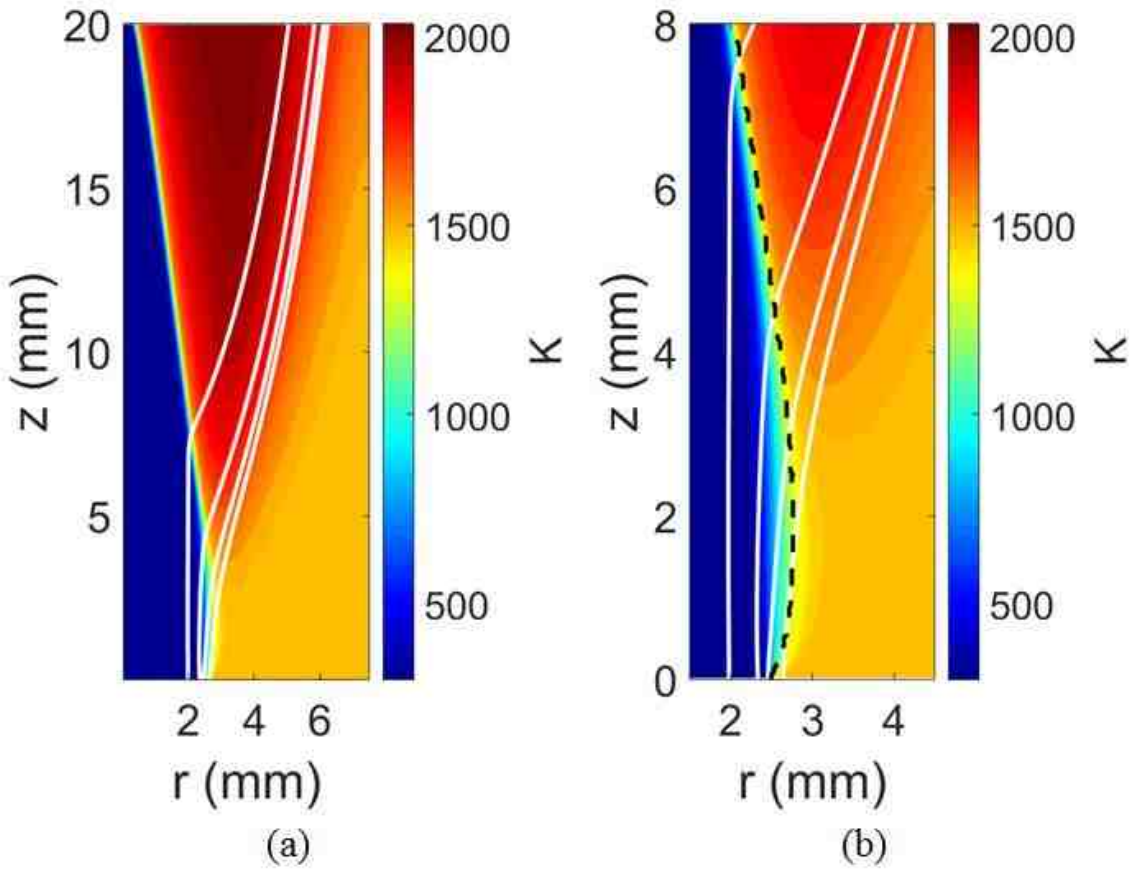

Figure 8.14: Temperature plots in the full computational domain (a) and zoomed in view (b) with streamlines and maximum heat release lines shown in magenta and black respectively.

Since the 10% heat release streamline originates from the coflow, the temperature initially decreases as it passes through the mixing layer. Subsequently, the temperature increases by either reactions or diffusion from the coflow. All other streamlines originate from the jet and essentially linearly increase in temperature prior to a rapid rise in temperature. The regime where the temperature increases in a linear way is likely dominated by diffusive heat transfer from the coflow and the fast rise in temperature is likely either diffusion or chemical heat release. Interestingly, the 0.3 line in Figure 8.15 reaches temperatures around 900 K with a nearly linear temperature rise before the rapid rise occurs. Streamlines with greater heat release maximums have lower temperatures prior

to the quick rise in temperature. Therefore, it is unlikely that the plotted streamlines which pass through 50% of the maximum heat release or greater autoignite, since they do not reach suitable temperatures prior to the quick rise in temperature. The temperature which are referred to as suitable to ignite is the last temperature which autoignites in the PSR calculation from Figure 8.9, which was approximately 950 K.

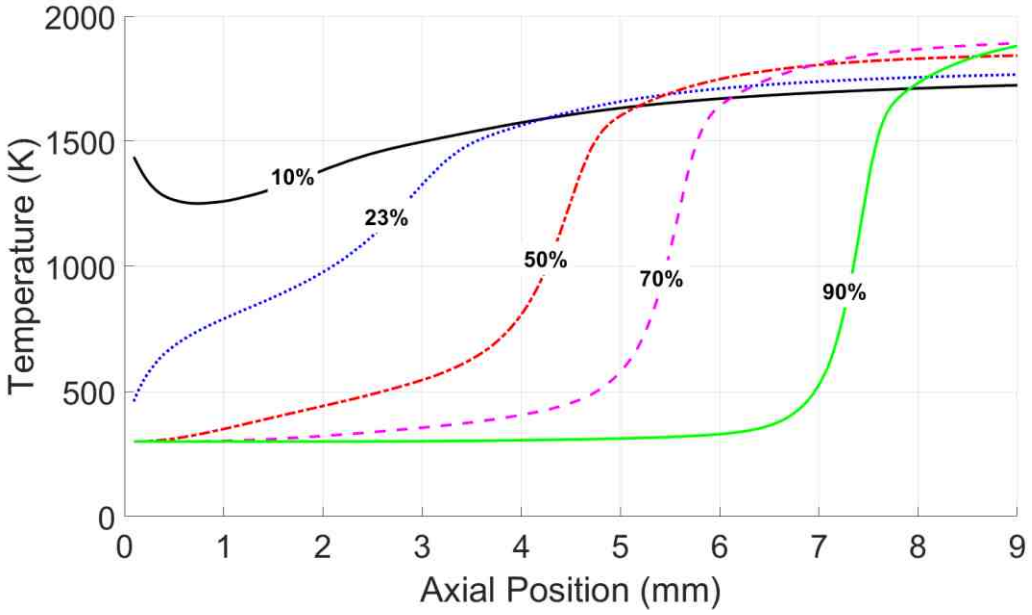

Figure 8.15: Temperatures sampled along different streamlines which pass through different percentages of the maximum heat release, indicated by the legend.

8.3.3 Energy Equation Analysis

The energy budget for individual terms of the energy equation can be calculated to determine the relative contribution of each process. The steady-state energy equation is given in Eq. (8.2) in cylindrical coordinates, where ρ is the density, c_p is the specific heat capacity at constant pressure, V_r is the radial velocity, T is the temperature, V_a is the axial velocity, λ is the thermal conductivity, J_i is the flux of energy due to mass diffusion, $\dot{\omega}'''$ is the reaction rate, Δh is the enthalpy of combustion, and r and a are the radial and axial directions respectively. The energy budget along a streamline can help understand the

process for a fluid particle approaching the flame. The energy balance in Eq. (8.2) can be transformed into the local normal and tangential components along the streamline, shown in Eq. (8.3), where η is the normal direction and τ is the tangential direction. It should be noted that only a partial transformation was invoked. The $\frac{\lambda}{r}$ and the enthalpy transport by species diffusion are negligible as verified in calculations; thus these were neglected from Eq. (8.3).

$$0 = -\rho c_p \left(V_r \frac{\partial T}{\partial r} + V_a \frac{\partial T}{\partial a}\right) + \frac{\partial}{\partial r}\left(\lambda \frac{\partial T}{\partial r}\right) + \frac{\partial}{\partial a}\left(\lambda \frac{\partial T}{\partial a}\right) + \frac{\lambda}{r}\frac{\partial T}{\partial r} - \sum_i \nabla \mathrm{h}_i \cdot \vec{J}_i + \dot{\omega}''' \Delta h \tag{8.2}$$

$$0 = -\rho c_p \left(V_\tau \frac{\partial T}{\partial \tau}\right) + \frac{\partial}{\partial \tau}\left(\lambda \frac{\partial T}{\partial \tau}\right) + \frac{\partial}{\partial \eta}\left(\lambda \frac{\partial T}{\partial \eta}\right) + \dot{\omega}''' \Delta h \tag{8.3}$$

This analysis along the streamline was conducted to help identify whether the specific fluid element is influenced by autoignition or premixed flame behavior. In the PSR calculations, the 0-D reactor is simulated as a homogeneous point, and has no spatial flowfield information. Therefore, the energy budget should simply be a balance between the unsteady energy term (in an unsteady energy equation) and heat release ($\dot{\omega}''' \Delta h$). However, autoignition can also be simulated in a plug flow reactor (PFR), which represents a one-dimensional fluid particle convected in the streamwise direction [62]. Autoignition in a PFR can be interpreted slightly different as a balance between advective heat flux ($\rho c_p V \cdot \nabla T$) and heat release. Conversely, in premixed flames, specifically a laminar freely propagating flat premixed flame, in the preheat region there should be a balance between diffusive heat gain ($\nabla \cdot (\lambda \nabla T)$) from the flame and advective heat loss toward the flame. As the temperature rises along this streamline, heat release will begin, and the diffusive term will decrease eventually becoming negative representing heat loss to other fluid

elements upstream of the flame. These characteristics are important to distinguish between the two stability modes in the more complex jet in coflow geometry.

The energy budget which passes through the 90% heat release contour is shown in Figure 8.16. Far upstream of the reaction layer there is no energy transport in the isothermal flow. However, in the nearfield of the reaction layer, where heat is being released, the preheat region exists where the fluid element is being diffusively heated by the reaction layer which is balanced by the advective heat flux. Upon reaching the reaction layer the fluid is heated by the chemical heat release and diffusive heat flux, however, at a critical point, the diffusive term becomes a heat loss term which when combined with the advective heat loss balance the heat gain from the chemical heat release. Therefore, the energy budget along this streamline shows very similar trends as a typical premixed flame. This streamline and those farther downstream can be classified as having near classic premixed flame behavior since the reactants are being preheated by the reaction layer itself and can self-sustain chemical reactions.

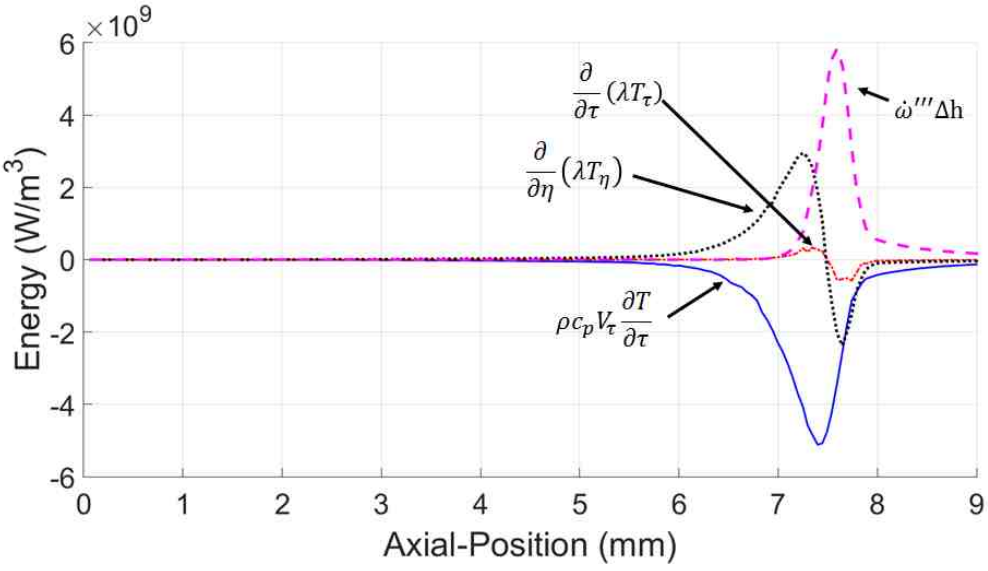

Figure 8.16: Energy budget along the 90% maximum heat release contour.

Figure 8.16 is also broken into individual directional terms. The advective heat flux along the streamline is dominated by the tangential component, since flow normal to the streamline is zero. The diffusive term, however, is dominated by the normal component with only a small amount from the component along the streamline. Therefore, the fluid is being heated by neighboring streamlines. From Figure 8.11, it can be seen that the streamlines enter the premixed flame at an angle, which leads to this dominant diffusion in the cross-stream direction.

The streamline entering the 50% of maximum heat release energy budget is shown in Figure 8.17. Far upstream of the reaction layer, the mixture is being diffusively heated normal to the streamline from the hot coflow. The heat gain is nearly constant and is balanced by the tangential advective heat flux, for similar reasons as in Figure 8.16. In the region where the diffusive heating is nearly constant, Figure 8.15 shows the temperature increasing nearly linearly. Near the reaction layer, there is an increase in the diffusive heating which is likely from the higher temperature reaction layer. Therefore, this fluid is being aided by the flame to diffusively heat the mixture past the critical point at which heat release can dominate. The axial locations where the diffusive heating increases correspond to the locations with a rapid temperature rise in Figure 8.15. Therefore, the fluid along this streamline is still aided by the chemical heat release from the flame. However, the flame did not add a large amount of heat and preheating by the coflow upstream of the reaction layer was necessary for this streamline to transition to a flame. Therefore, this region could be classified as a premixed flame aided by preheating from the hot coflow.

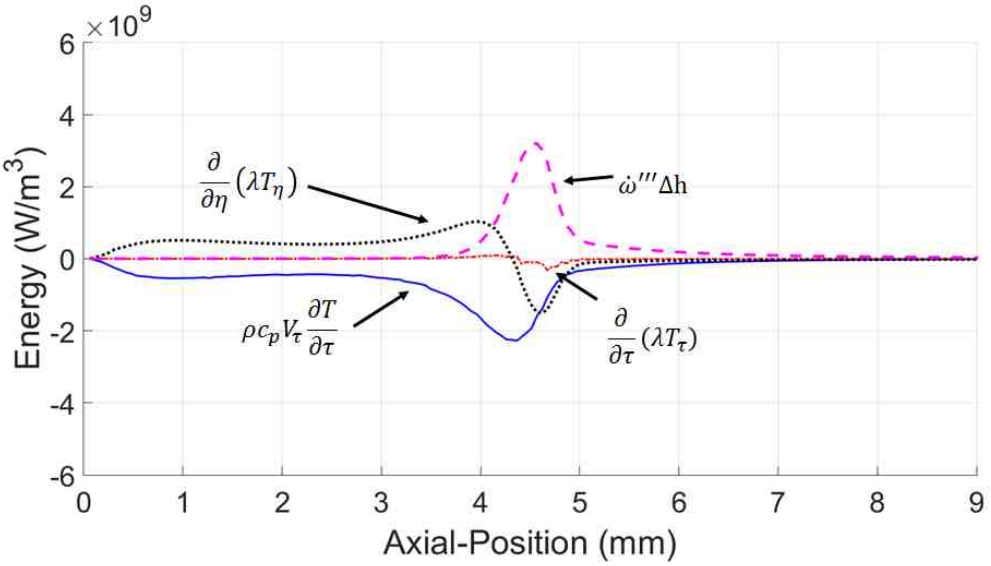

Figure 8.17: Energy budget along the 50% maximum heat release contour.

The streamline which passes through the 30% maximum heat release contour energy budget is shown in Figure 8.18. Similar to Figure 8.17 the flame is diffusively heated normal to the streamline upstream of the reaction layer and is balanced by tangential advective heat flux. The diffusive heat gain at locations very close to the jet exit (~ 0.5 mm) have very high heating rates in comparison to Figure 8.17, which is likely due to the streamline originating closer to the coflow and therefore having higher diffusive heating rates. The diffusive heat flux remains nearly constant from approximately 1 – 3 mm in the axial direction before decreasing in magnitude when chemical reactions begin. Therefore, the fluid along this particular streamline is not aided by heat transfer from the heat release region, but rather is being diffusively heated at a nearly constant rate by the coflow until the heat release occurs. However, the heat release profiles are broader than the 50% and 90% cases and the peak heat release is substantially lower (as expected since the streamline is going through the 30% of maximum heat release contour). This streamline has strong similarities to an autoigniting mixture since the fluid element traveling along this streamline feels little-to-no effect from the flame and spontaneously ignites once

sufficiently heated. However, the mixture would not ignite if the mixture was not preheated by the coflow. Similar to the 50% streamline, the mixture is nearly linearly increasing in temperature, as shown in Figure 8.15, until the temperature rapidly rises which coincides with the high heat release locations. In this case the rapid temperature increase is only by the coflow heating and chemical reactions, as opposed to the flame, coflow, and chemical heat release in Figure 8.17.

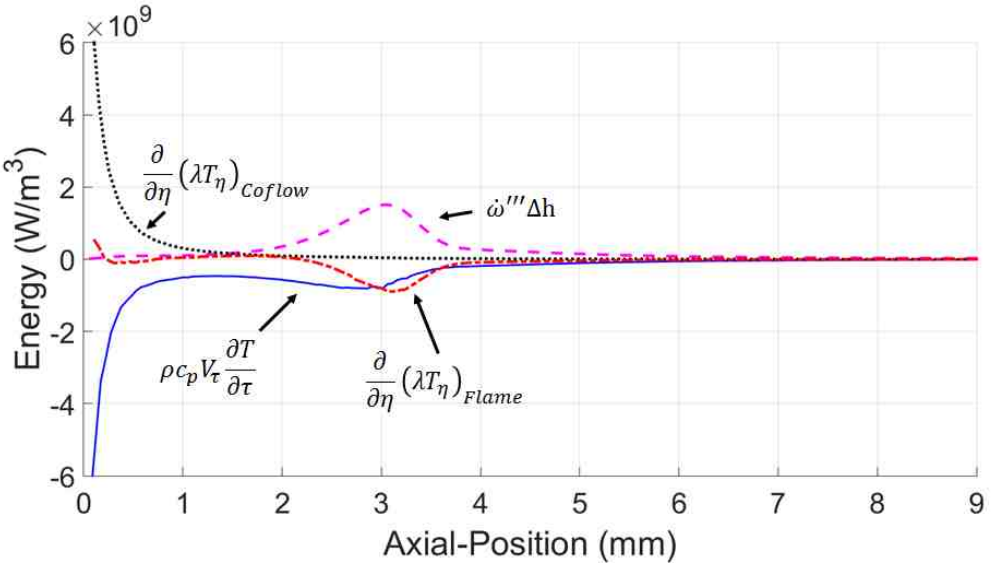

Figure 8.18: Energy budget along the 30% maximum heat release contour.

The energy budget along the 10% maximum heat release contour is shown in Figure 8.19. The fluid element originates from the coflow in this case. Therefore, upon entering the domain the temperature decreases by diffusive heat loss from the jet and is balanced by advective heat gain. Nearly immediately upon entering the domain heat release begins. There is a short time in which the fluid mixes with the jet to obtain reactants, but begins reacting within the first 0.5 mm. Interestingly, the high chemical heat release rate is fairly long, almost ranging 3 mm in the axial direction. Since diffusive heat loss is also occurring along this entire region, diffusive species transfer is also occurring. It was observed in Figure 8.11 that the streamline passes through the maximum heat release line twice.

Therefore, there are two local peaks in the heat release plot in Figure 8.19. Therefore, it is likely that the reaction layer along this streamline is being sustained by reactants continually diffusing into the reaction layer, allowing reactions to continue. This is dissimilar to the autoigniting and premixed flame behavior. Typically, the fluid along a streamline reaches critical conditions and reacts quickly, which consumes the reactants. However, this streamline continuously reacts, similar to a non-premixed diffusion flame. This streamline has very similar properties of a diffusion flame, but cannot be at stoichiometric conditions.

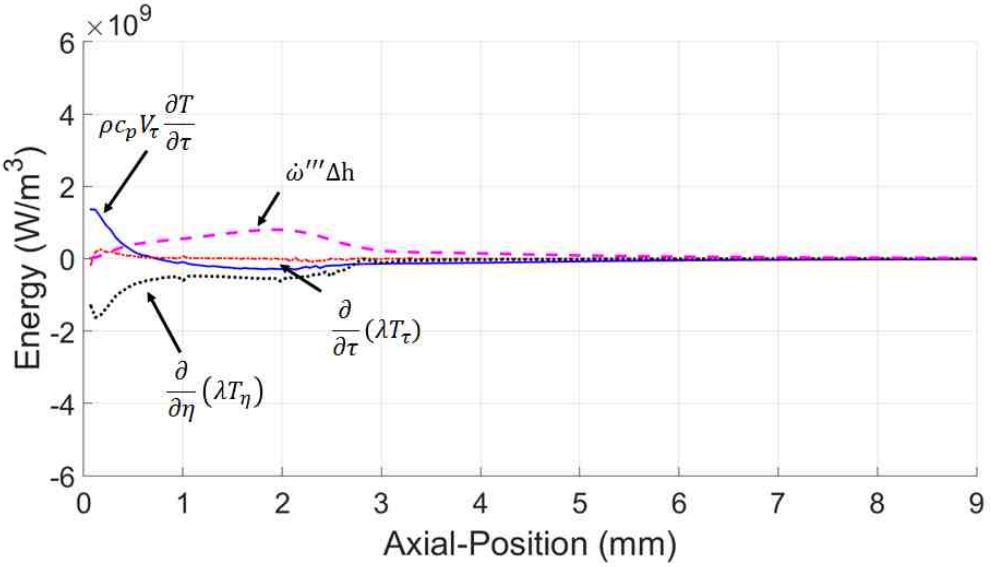

Figure 8.19: Energy budget along the 10% heat release contour.

These observations support an understanding of the stability of this flame. Each fluid element along the streamline needs to be sufficiently heated to a critical point (with sufficient species concentration and temperature) such that chemical reactions can occur. Streamlines originating close to the mixing layer (larger radial positions than the 30% heat release streamline origin) are continually heated by the coflow until the critical conditions are met such that high reaction rates can occur. Streamlines between the 30% and 50% maximum heat release contours are still preheated by the coflow, but begin feeling affects

from the flame which increase the heating rates slightly near the flame and brings the fluid to a critical point for existence of the flame. Since the flame is heating the fluid, as opposed to the coflow, the fluid is not diluted with vitiated products and leads to more heat release. Transitioning from the 50% to 90% maximum heat release streamlines, the fluid elements feel less of an effect from the coflow and are heated more by the presence of the flame, which again leads to less fuel dilution. Near the 90% maximum heat release streamlines and beyond, the fluid is only heated by the flame, and nearly has no interaction with the coflow. Therefore the jet fluid is essentially no longer diluted by the coflow and has maximum heat release rates. However, the fluid is heated by neighboring streamlines to bring the mixture to a critical point such that reactions can occur. The given fluid element which reacts diffusively heats the fluid normal to the flame surface and preheats the neighboring streamlines which originate closer to the centerline and self-sustains reactions.

The overall description of the flame behavior is that the autoignition behavior at lower axial points is dominated by heating from the coflow which provide heat release and slightly increases the fluid temperature. Mixtures closer to the jet begin feeling effects from this flame which permits these streamlines to reach a point of significant heat release faster. Since the flame is interacting with these mixtures, as opposed to the coflow, the mixture is not diluted as much and therefore releases more heat. This continually occurs in the axial direction along the reaction layer which feedbacks information to incoming streamlines. The mixture begins feeling a larger effect from the flame and less from the coflow. This is when the fluid-flame feedback interaction finally reaches self-sustaining conditions and is acting as a premixed flame.

One other interesting observable that has not been fully explained yet is that the autoignition delay time from the PSR is different than the flow times to various regions along the flame. The energy analysis has a key characteristic along the streamline which is different than the PSR calculations. The energy analysis shows that the fluid element is continually heated by the coflow until reactions occur. This is different than the PSR calculations since the PSR mixture is adiabatically mixed and held constant for the remainder of the calculations. Therefore, the behavior along the streamline in the flow simulation is not captured at all in the 0D reactor. As diffusion occurs in the mixing layer, the temperature is increasing, but the equivalence ratio decreases and the dilution increases. Therefore, the mixture along the streamline which interacts with the coflow will continually have this tradeoff which is not represented in the 0D reactor. Therefore, the ignition delay times from the PSR calculations and the flow times from the numerical simulations indeed should not be the same since there is significantly different physics occurring along a fluid streamlines.

8.4 Summary and Conclusions

A premixed jet in vitiated coflow burner was used to help understand autoignition stabilized flame behavior. Lifted flames were observed with significant CH_2O production ahead of OH production, indicating autoignition characteristics ahead of the stabilization point in both experiments and simulations. Ignition delay times from homogenous reactor chemical simulations were approximately an order of magnitude shorter than the observed flow time to the stabilization point, indicating further analysis was needed to understand the stability behavior. Rapid CH_2O production was found at short time scales in the chemical simulation while OH was produced near the reaction layer. However, CH_2O was

produced at high quantities and were nearly constant for a long duration with high mixture fractions. H_2O_2 was found to exist at low temperatures and increased in concentration when the CH_2O concentrations were constant. Therefore, observations of H_2O_2 were likely low temperature chemistry dominated.

Ignition delay times from the homogenous reactor simulations were compared to flow times to different regions in the reaction layer using numerical flow simulations. The flow times to the reaction layer were larger than the homogenous ignition delay time indicating again that further analysis was needed. Fairly large concentrations of both CH_2O and H_2O_2 were observed upstream of the high heat release rates indicating potential lower temperature chemistry effects. High temperatures and heat release rates were observed to be highly lifted, consistent with experimental observations. However, heat was being released nearly to the jet exit at low rates. Terms in the energy equation were calculated and compared and different points in the flame. Streamlines passing through high heat release rates had similar behavior as typical premixed flames. However, streamlines which pass through lower heat release rates showed effects of coflow preheating. At very low heat release rates, the streamline essentially only had heating effects from the coflow prior to reacting. Conversely, streamlines which passed through half of the maximum heat release rates were preheated by the coflow and subsequently were also heated by the flame which led to suitable conditions for reactions to occur. Therefore, a feedback from the flame was felt at a critical point which continuously led to higher heat release rates until finally reaching self-sustaining conditions.

9 Concluding Remarks and Future Work

The work in this dissertation has implications for fundamental understanding of mechanisms which are present and may be used in future practical systems which utilize stratified flow fields, involving a concentration or temperature gradient. The following will briefly conclude each topic discussed and will outline potential future work related to the respective Chapter.

9.1 Advective Heat Flux Estimation

The advective heat flux ($\rho c_p v \cdot \nabla T$) is important to both distinguish the type of edge flame present in a flowfield, but also can measure the strength of an extinction wave. Modern laser techniques make it possible to measure the $v \cdot \nabla T$ term, but require extensive complicated setups and are challenged by spatial resolution required to accurately estimate the temperature gradient. The flow dilatation was theoretically, numerically, and experimentally shown to be an estimate for the advective heat flux under low molecular weight and pressure gradient approximations. Future work should utilize and verify this measurement in a practical turbulent flowfield with small molecular weight changes, such as with ethylene or ethane fuels, to determine the impact of the $\frac{\partial w}{\partial z}$ term which is not measured in two-dimensional particle image velocimetry (PIV) measurements. Tomographic or dual-plane stereo PIV should also be conducted in similar environments to extract the third out of plane gradient. Different geometries which may inherently create different out of plane velocity gradients should be tested, such as a turbulent jet diffusion flame issuing into a cold environment, a jet in crossflow experiment, and a turbulent premixed propagation flame in a duct. Different fuels should also be studied to understand

the utility of the technique in the presence of larger molecular weight changes by using alternative fuels, such as hydrogen or propane.

9.2 Positive Edge Flames

Propagation speeds for interacting triple flames using three different fuels were measured and modeled with respect to the flame base curvature (which is linearly related to the equivalence ratio gradient) and stoichiometric separation distance. These parameters were used to characterize the propagation speed with respect to the equivalence ratio gradient ahead of the flame base and was modeled based on the level of interaction between neighboring triple flames. The model sufficiently captured the propagation speed for all of the tested fuels leading to the conclusion that only aerodynamic interactions occurred between neighboring triple flames. It was also found that each interacting triple flame case nearly maximized the propagation speed of an infinitely wide triple flame, not attainable with a single triple flame. Future work should test the validity of the limits for interacting triple flames reaching the zero gradient propagation speed of a single triple flame. This can be conducted by using a small diameter fuel jet which creates very close stoichiometric distances which flows at relatively high velocities such that there is a low equivalence ratio gradient ahead of the flame base. This flame should propagate nearly at the zero gradient propagation speed of a single triple flame if it maximizes the interaction between the two flames.

9.3 Negative Edge Flames

Negative edge flames were studied by: modeling the steady energy equation along the stoichiometric contour, describing dynamics in unsteady flows, and measuring the edge velocity in turbulent flows.

Terms in the energy equation were modeled first by using two dimensional simulations to calculate each term in the energy equation and subsequently calculate the temperature profile. The edge location was sufficiently captured using a one-dimensional calculation. Furthermore, centerline counterflow simulations were used to obtain one-dimensional data long the centerline for various cases which could be used to calculate the energy equation again and sufficiently resolved the temperature profile and edge location. Further analysis should be conducted with various burner geometries and fuel concentrations with one-step chemistry and should also be verified to work with detailed chemistry. Obvious next steps also include using different fuels to determine the impact of differing fuel diffusivities. Ideally, a generalized model could be produced which could then be implemented into turbulent simulations to determine if and when a negative edge flame exists. Responses to unsteady boundary conditions would also prove useful to have both a steady and unsteady negative edge flame model.

Unsteady negative edge flames were studied with respect to different oscillating velocity frequencies. The energy equation was calculated along the stoichiometric line and the flame edge dynamics could be fully described by the unsteady energy term. The negative edge flame velocity was calculated and a new interpretation of the edge velocity was derived and calculated. A negative edge response time was found where larger cycle periods led to near steady state behavior, while smaller cycle periods led to the flame not fully reaching steady conditions. Future work should look at different amplitudes of the velocity fluctuations to determine the impacts on the response time and how the unsteady energy term is affected. Other work could include sufficiently reducing the velocity

amplitude such that the edge becomes an ignition front to track the behavior and characterize the two regimes.

Turbulent negative edge velocities were measured in a newly designed burner. A stereo-view chemiluminescence imaging setup was used to track the flame in time and was used to determine the flame speed in the plane of velocity measurements. The combination of flame and flow velocities were used to measure the edge flame speed with respect to the flow. Different turbulent conditions and bulk advective heat fluxes were used to determine the impact on the edge velocity. Increased advective heat flux through the edge led to higher negative edge velocity magnitudes, however increased turbulence levels led to smaller edge velocity magnitudes. Therefore it was concluded that turbulence had an effect on the edge velocity. Future analysis will be conducted by examining the turbulent characteristics of the side jets to understand how the velocity fluctuations could impact the edge velocity using knowledge from the unsteady negative edge flame work. Other future work could include imaging the edge flame by using a laser scanning approach which would allow the flame volume to be reconstructed. In this experiment, the edge velocity could be captured in multiple planes and could generate a large amount of data regarding the negative edge.

9.4 Premixed Jet in Vitiated Coflow

A steady and laminar premixed jet in vitiated coflow was studied both experimentally and numerically. The high temperature heat release region was found to be stabilized at a liftoff height which correlates to approximately an order of magnitude longer ignition delay time than predicted from chemical simulations. Autoignition characteristics were found upstream of the high temperature heat release indicating that

autoignition was aiding the flame stability. Low temperature chemistry species were present ahead of the high temperature heat release indicating low temperature chemistry was present. Furthermore, an energy budget was conducted and the flame stabilization behavior was described. The logical next steps for this work is to examine how different boundary conditions effect the flame stabilization behavior, particularly the jet equivalence ratio as well as the coflow species composition and temperature. Moreover, transient fuel injection should be studied to understand how the flame dynamics change from the steady state case. Lastly, turbulent conditions should be studied in the various boundary conditions to understand the role turbulence has on the stabilization point. Similar to the turbulent negative edge burner, multi-view imaging could be used in order to reconstruct the entire three-dimensional volume which could identify different burning regimes and also identify flow structures which aid autoignition behavior.

A. Appendix

The following Chapter covers short studies which are still within the scope of this dissertation. The first study will cover a diagnostic investigation to use only velocity information to calculate the flowfield temperature. The second study will cover measurements of steady negative edge flame scalar dissipation rates and advective heat fluxes, which were only simulated in previous studies.

A.1 Temperature Estimation from Velocity Measurements

Motivation

Combustion diagnostics have significantly evolved over the years, especially since the invention of the laser. However, important quantities cannot be measured simultaneously without the use of multiple lasers and complicated experimental setups. For instance, non-intrusive temperature measurements using Rayleigh scattering in conjunction with particle image velocimetry (PIV) is very difficult to perform since Rayleigh scattering measurements rely on low-level scattering signal which are inaccurate when particles are in the flow since Mie scattering interferes with the signal. This sub-chapter is an extension of Chapter 5, which attempts to calculate the temperature using only velocity measurements.

Theory, Numerical Scheme and Procedure

Similar to Eq. (5.1), beginning with the ideal gas law substituted into the continuity equation, Eq. (9.1) can be obtained, where p is pressure, R is the mixture averaged gas constant, T is temperature, and v is the velocity vector. However, this time steady state will not be assumed. The pressure and molecular weight terms will still be assumed to be constant in both space and time, similar to Chapter 5.1.2, and Eq. (9.2) can be derived. By

examining Eq. (9.2) it should be noted that the velocity can be directly measured using PIV, leaving only temperature as an unknown. Therefore, the temperature can be computed using a proper numerical scheme.

$$\frac{\partial}{\partial t}\left(\frac{p}{RT}\right) + \nabla \cdot \left(\frac{pv}{RT}\right) = 0 \tag{9.1}$$

$$\frac{\partial}{\partial t}\left(\frac{1}{T}\right) + \nabla \cdot \left(\frac{v}{T}\right) = 0 \tag{9.2}$$

Equation (9.2) is in a conservative form which is appealing from a numerical standpoint since there are a few numerical schemes which can be used. For this study, the two-dimensional Lax-Wendroff scheme was used since the equation is a linear hyperbolic equation. Hyperbolic functions transfer information along characteristics lines, and in this case is the velocity streamlines, which convects the temperature information. A fourth order dissipation term was added such that the large oscillations do not grow due to decoupling of neighboring points. The dissipation term was meant to not be larger than the error accrued in the discretized form of the actual governing equation.

Similar to Chapter 5, both a positive and negative edge flame were simulated in Fluent and experiments were also performed with similar conditions. The details of the geometry, numerical formulation, and experiments are given in Chapter 5. The only information from the numerical simulation which was needed was the velocity and temperature fields. The particle image velocimetry (PIV) measurements were also used to compute the temperature, but were only assessed qualitatively for now. Temperature measurements were performed, however, were not necessarily needed at this time.

To solve the temperature with velocity information, the boundary conditions were modeled by setting the inlet streams to a constant value, and the outlets by using a backward

differencing scheme. The temperature field was initialized with a constant 300 K field prior to calculations. Since the experiments and simulations are conducted in steady conditions, the temperature temporal derivative should converge to zero. Therefore, the unsteady term will be utilized, which was not used in Chapter 5.1.2 in order to estimate the residuals of the current time step and converge the solution by approaching steady state conditions. It should also be noted that although this technique is being used for only steady-state flowfields, it is straightforward to extend this analysis to unsteady flows if the technique works properly. Details regarding the numerical scheme, such as the time step and dissipation term, will need to be further analyzed to ensure accurate results in time resolved measurements.

Results and Discussion

The estimation was first tested with similar numerical simulations as in Chapter 5. The temperature output from Fluent, which will be referred to as 'Fluent temperature', was used as the true solution to compare to the temperature calculated with the Fluent velocity field, referred throughout this sub-chapter as 'calculated temperature.' This gives an easy way to compare how the technique behaviors without the uncertainty that would be present in the experimental measurements. Equations (9.3) and (9.4) show the Cartesian representation of the numerical scheme where the superscript denotes the time step and the subscript denotes the spatial location, T is temperature, t is time, x is the x-coordinate, u is the x-component velocity, y is the y-coordinate, and v is the y-component of velocity. A fourth order numerical dissipation term was also added to the scheme to prevent decoupled neighboring nodes from creating large errors.

$$\left(\frac{1}{T}\right)_{i,j}^{*} = \left(\frac{1}{T}\right)_{i,j}^{n} - \frac{\Delta t}{2\Delta x}\left(\left(\frac{u}{T}\right)_{i+1,j}^{n} - \left(\frac{u}{T}\right)_{i-1,j}^{n}\right) + \frac{(\Delta t)^2}{2(\Delta x)^2}\left(\left(\frac{u}{T}\right)_{i-1,j}^{n} - 2\left(\frac{u}{T}\right)_{i,j}^{n} + \left(\frac{u}{T}\right)_{i+1,j}^{n}\right) \tag{9.3}$$

$$\left(\frac{1}{T}\right)_{i,j}^{n+1} = \left(\frac{1}{T}\right)_{i,j}^{*} - \frac{\Delta t}{2\Delta y}\left(\left(\frac{v}{T}\right)_{i+1,j}^{*} - \left(\frac{v}{T}\right)_{i-1,j}^{*}\right) + \frac{(\Delta t)^2}{2(\Delta y)^2}\left(\left(\frac{v}{T}\right)_{i-1,j}^{*} - 2\left(\frac{v}{T}\right)_{i,j}^{*} + \left(\frac{v}{T}\right)_{i+1,j}^{*}\right) \tag{9.4}$$

Numerical Positive Edge Comparison

A similar numerical output from Chapter 5.3.1.1 was used in this Chapter, and the Fluent and calculated temperature are shown in Figure A.1 (a) and (b) respectively. There is striking similarity between the two temperature fields from a qualitative standpoint. Along the premixed flame base there is a well resolved temperature gradient where the premixed flame base resides. Downstream of the premixed flame base there is a fairly symmetric temperature field which has maximum temperatures along the diffusion tail for the Fluent temperature field. The estimated temperature field has similar characteristics, however, there are oscillations of the overall trend which tend to skew the interpretation of the temperature field. It is also clear that the temperature order of magnitude is well represented in the estimated temperature as well.

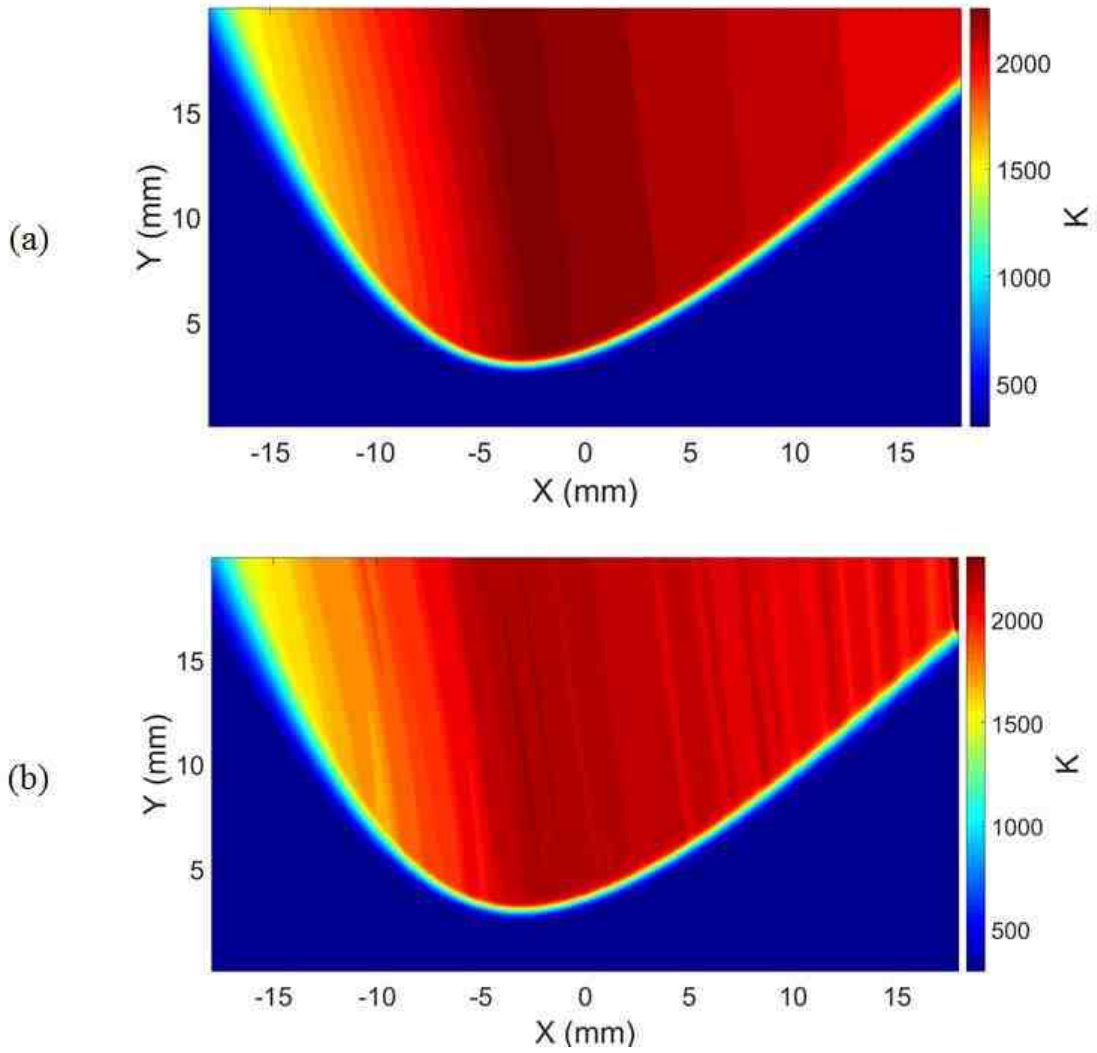

Figure A.1: Fluent (a) and calculated (b) temperatures using Eqs. (9.3) and (9.4).

Quantitative samples were also compared along streamlines through the diffusion tail and points through the rich and lean premixed branches, shown in Figure A.2. Again, there is very good agreement between the Fluent and calculated temperatures. The profile which increases in temperature at the lowest y-location is along the diffusion tail, while the other two profiles are through the premixed branches. The calculated temperature is slightly lower in magnitude than the Fluent temperatures, but agree very well with the Fluent temperature. Figure A.3 compares three horizontal slices of the Fluent and calculated temperatures. The trends of each profile is nearly the same, having almost

identical local temperatures. However, the calculated temperature profiles have oscillations on the order of 1 mm in width. The oscillations seem to have largest magnitudes changes on the outer-edges of the temperature profiles than toward the centers. This is likely a numerical error which was not sufficiently dissipated with the numerical dissipation term and likely could be optimized in future work. Thus far, the calculated temperature from the velocity field well represents the Fluent temperature field.

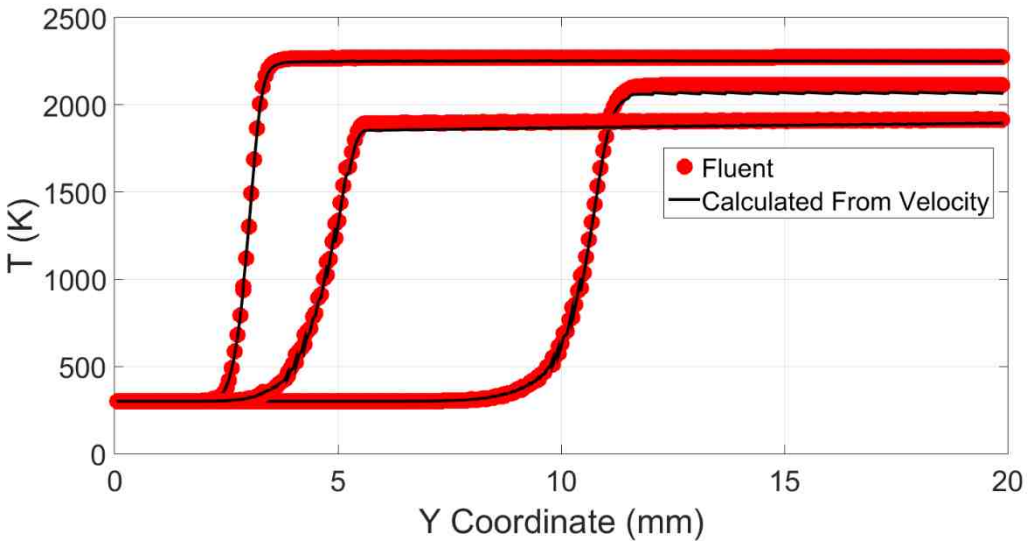

Figure A.2: Temperature streamlines at three different locations comparing the Fluent and calculated temperatures.

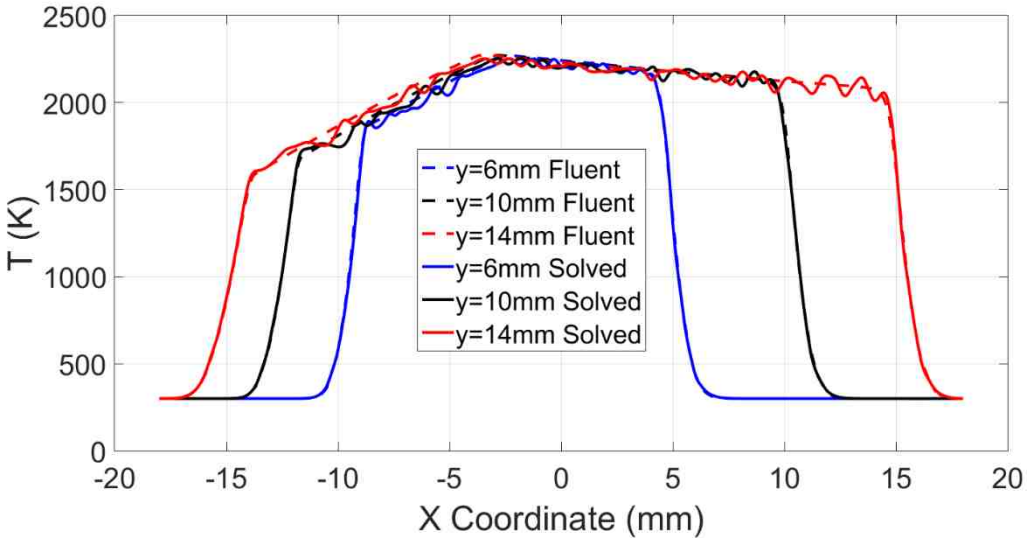

Figure A.3: Horizontal profiles from Fluent and calculated temperatures at three different heights.

Numerical Negative Edge Comparison

Similarly, a similar negative edge flame Fluent temperature field was compared to calculated temperatures using the velocity information. Since this flowfield is axisymmetric, cylindrical coordinates were used and therefore a slight variation of Eq. (9.3) and (9.4) were used to account for the $\frac{1}{r}$ term which needs to be included. The Fluent and estimated temperature fields are shown in Figure A.4. Because of the $\frac{1}{r}$ term, large errors were calculated at smaller radial locations and were not plotted. Qualitatively, there is very good agreement with the two temperature fields again. The order of magnitudes between the two flames are very similar, however, the calculated temperature may be slightly higher than the Fluent temperature. Also, there is an observable oscillation in the high temperature width in the calculated temperature field, which might be caused by the numerical errors again. Overall, the qualitative temperature fields look very similar.

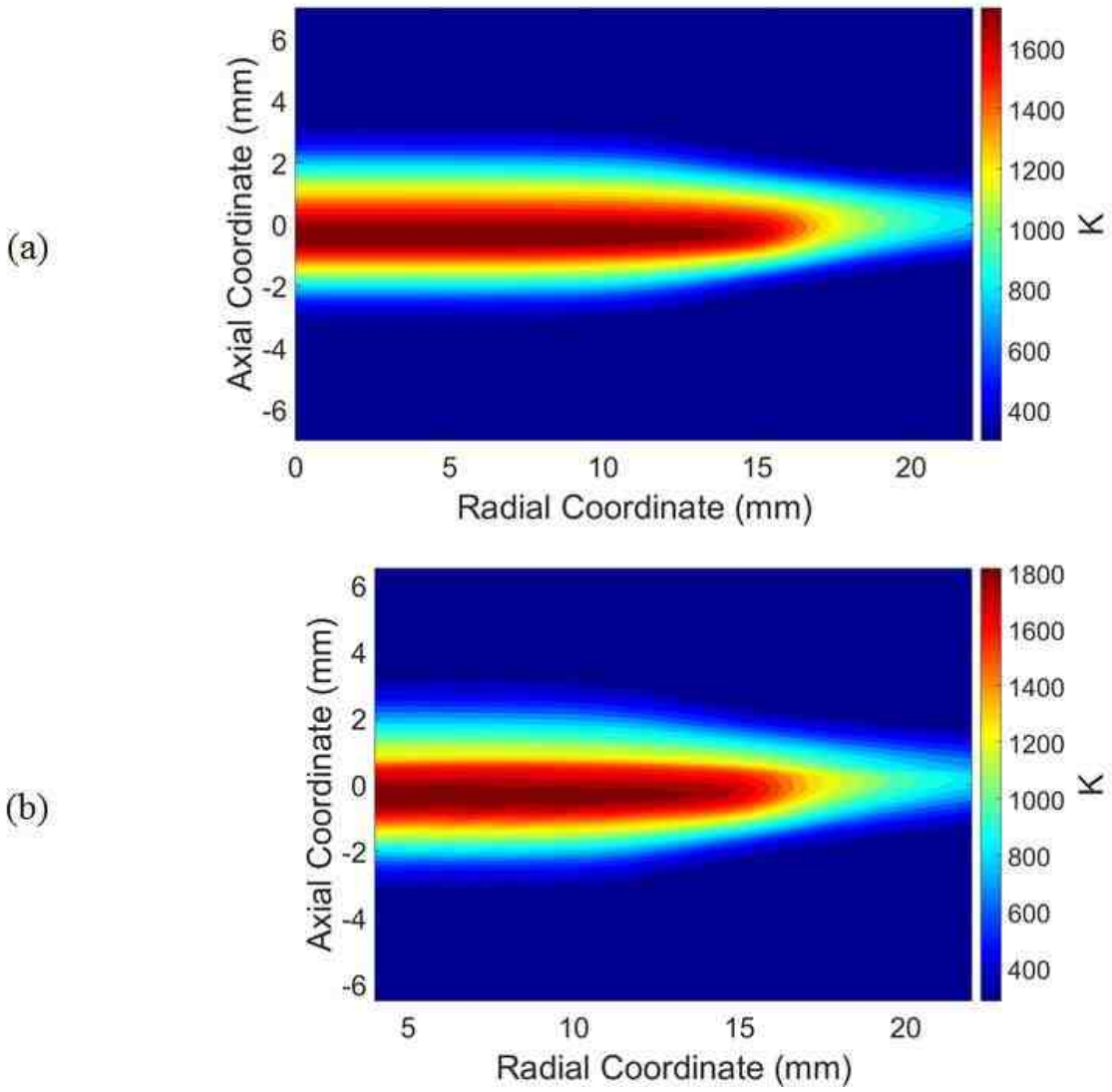

Figure A.4: Fluent (a) and calculated (b) temperature fields in the negative edge flame case.

As a more rigorous comparison, the temperatures were quantitatively compared in the axial (Figure A.5) and radial (Figure A.6) directions. The axial profile was sampled at a r = 10 mm and the profiles look nearly identical, reaching nearly the same peak temperature. There is very small variations on either side of the maximum temperature, from about 500 – 1000 K, specifically in the positive axial direction where the calculated temperature is slightly lower than the Fluent temperature. Also, there is a fairly large

oscillation near the peak temperature around an axial position of zero. This again is likely due to the numerical scheme decoupling neighboring points and is likely why the high temperature width has oscillations in Figure A.4 (b).

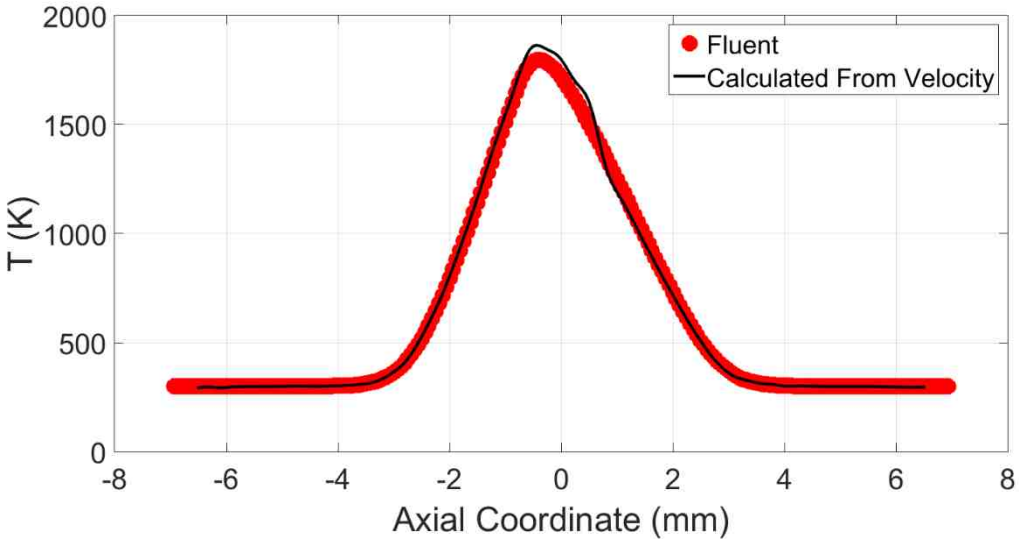

Figure A.5: Axial temperature profile comparing Fluent and the calculation.

The radial temperature profiles are shown in Figure A.6 and show very similar trends. The profile was sampled by obtaining the maximum temperature at the respective radial location in both outputs. Clearly, the calculated temperature is slightly higher than the Fluent temperature again, by approximately 50 K on average. However, the calculated temperature nearly follows the same trend as the Fluent temperature, but has a slightly higher magnitude. Also, there is an oscillation with an amplitude change of approximately 10 K along the inner nozzle portion of the flame and has an approximately 2 mm width. Again, this is likely due to numerical error, and should be further analyzed. At this point, there is still good agreement between the Fluent and calculated temperature using numerical simulations, even though the calculated temperature only relies on velocity information.

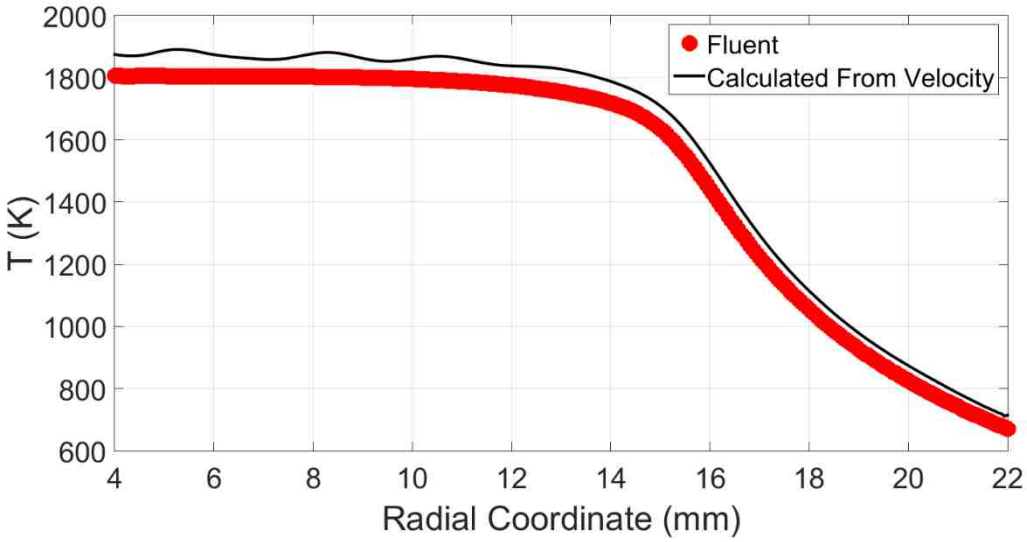

Figure A.6: Radial profile temperature comparison. The temperature was sampled using the maximum temperature at the respective radial location.

Experimental Positive Edge Comparison

The goal of this work is to calculate the temperature field in experiments without the need additional diagnostics. Figure A.7 shows the estimated temperature field using only velocity measurements from Chapter 5. There are some clear similarities between the expect temperatures and the estimated temperature shown here. First, there is a large temperature gradient along the premixed branches, consistent with the numerical work. Also, the maximum temperature order of magnitudes are similar to what is expected for this fuel and flowfield. However, there are many differences which need to be addressed. Downstream of the premixed branches, there is little dilatation and therefore the temperature should stay nearly constant along the streamline, similar to Figure A.2. Also, there should be a near symmetric temperature profile similar to Figure A.3 with a maximum temperature toward the center of the flowfield. Both of these are not consistent with the experiments. Downstream of the rapid temperature rise along the premixed branches, the temperature is continuously rising by over 100 K which is not realistic. Also, there are

very large oscillations in the horizontal direction which cannot be easily explained. The oscillations should be very small if they are numerical errors, which does not seem to be the case. Also interestingly, the center of the flame should be the highest temperature since it is where the diffusion flame resides. However, the temperature at the center of this flame actually seems to be a local minimum, contrary to what is expected.

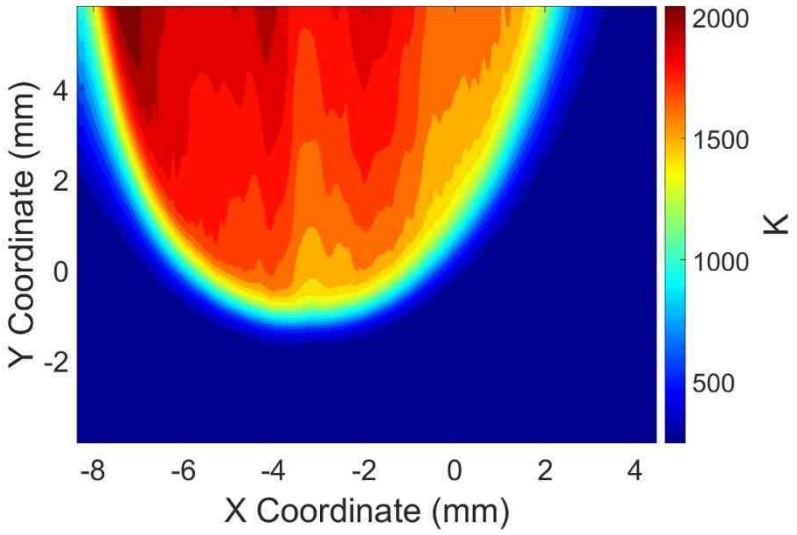

Figure A.7: Temperature calculation using experimental PIV measurements.

Experimental Negative Edge Comparison

Unfortunately, the experimental calculated temperatures from PIV measurements in the negative edge counterflow burner gave unrealistic temperatures, peaking at 6000 K near where the flame surface was likely located. The extremely high temperatures could not be avoided, even though the exact numerical scheme and code were used to calculate the temperature in Figure A.4 (b). Further discussion of the experiments will be detailed in the next sub-chapter.

Experimental Discussion

Clearly, the experimental calculated temperature measurements from PIV do not work nearly as well as the calculated temperature in the numerical simulations. There are

a few reasons for why the technique might not have worked. The resolution of the numerical simulations were 62.5 μm near the reaction layer, whereas the PIV measurements were approximately 0.75 mm, and therefore were approximately an order of magnitude different. This is a problem when trying to resolve the high temperature gradients present in flames which are typically on the order of 1 mm wide. The PIV measurements could be interpolated onto a smaller grid to obtain higher spatial resolution but was not successful. Therefore, higher spatial resolution measurements without interpolation may be required to successfully estimate the temperature. Also, there is inherent uncertainty in the PIV measurements which are likely much larger than the numerical error in Fluent. This effect could also be a reason for the inaccurate temperatures. Both of these potential error sources can be amplified since the numerical scheme is a time marching-type scheme along the characteristic lines. Therefore, small errors along the whole streamline could lead to very large downstream errors since they are being accumulated starting from the streamline inlets.

It is suggested for future work to reexamine this technique using a simple lifted jet in coflow geometry where two-dimensional measurements can be easily made using well-defined boundary conditions. The measurements should be highly accurate and have high spatial resolution near 50 μm to obtain similar resolutions as the numerical simulations. Single shots measurements should also be examined to see the utility of using a single flowfield as opposed to the averaged PIV measurements. Since flames such as the positive edge flame have small oscillations in time, the average flowfield and therefore temperature measurement could be significantly affected. Also a different geometry other than the counterflow burner should be used since measurements near the stagnation plane may be

highly inaccurate, especially when trying to calculate quantitative temperature measurements. When and if this technique is possible in experiments, time resolved steady and laminar measurements should be conducted to determine the utility of this technique in unsteady flows.

Summary and Conclusions

The utility of an unsteady equation via the continuity equation and ideal gas law was used to attempt to calculate the temperature in both positive and negative edge flames using only velocity information. The calculated temperature was in agreement to numerical temperature fields extracted from Fluent when computed velocities were used for the analysis. Both a positive and negative edge flame were examined which showed strong qualitative and quantitative agreement. However, the calculated temperature in the experiments using PIV measurements did not produce reasonable temperatures. There are several factors which may play a role in the temperature calculations which were explained, but were not further explored.

A.2 Experimental Negative Edge Scalar Dissipation Rate and Advective Heat Flux Measurements

Motivation

Work in [48] simulated negative edge flames in the modified counterflow geometry shown in Figure 5.2 and found a linear relationship between scalar dissipation rate and advective heat flux at the extinction edge. Although the scalar dissipation rate was a measureable quantity, the advective heat flux was not easily measureable prior to this dissertation (Chapter 5). This sub-chapter will utilize the diagnostic technique developed

in Chapter 5 to measure the advective heat flux and use the formaldehyde width as an approximation for the scalar dissipation rate to experimentally validate findings from [48].

Experimental Setup

A similar burner setup was used in this Chapter as used in Chapter 5.2.1. The inner nozzle velocity was varied from 10 – 20 cm/s and the outer nozzle velocity was varied from 30 – 50 cm/s to create different stable negative edge conditions. Two diagnostics were used to measure both the scalar dissipation rate and advective heat flux. Particle image velocimetry (PIV) was used, similar to the description given in Chapter 5.2.3, and the dilatation was used as a scaled advective heat flux. The scalar dissipation rate was measured in a similar procedure as outlined in [128], where formaldehyde planar laser induced fluorescence (CH_2O PLIF) signal was shown to be related to the scalar dissipation rate. In [128], the width of the CH_2O fluorescence was inversely related to the scalar dissipation rate. CH2O PLIF was performed in the counterflow burner by taking the third harmonic of an Nd:YAG laser at 355 nm with approximately 125 mJ per pulse and redirecting it toward the burner. The beam was not expanded, but was converged in one direction to form an approximately 9 mm long sheet. Both laser sheets (PIV and CH_2O PLIF) were spatially overlapped using a dichroic mirror. The PLIF signal was imaged using a similar intensifier unit setup as described in Chapter 5.2.3. The main difference between this experiment and past experiments in this dissertation, which performed OH PLIF instead, was the spectral filter placed in front of the image intensifier. In this experiment a 430 – 480 nm spectral filter was used and in previous experiments a 300 – 340 nm filter was used.

Results and Discussion

Two quantities needed to be measured in this study, the scalar dissipation rate and advective heat flux at the edge. Therefore, the first thing to find was the location of the edge. Figure A.8 shows an example of the (a) averaged CH_2O PLIF, (b) chemiluminescence, and (c) processed CH_2O PLIF images as described subsequently. The processed CH_2O image also shows a black dot which represents the processed edge location. There are some observations which can be made in determining the edge. First, the CH_2O signal is preferentially higher in low temperatures due to Boltzmann fraction effects [128]. Therefore, the high signal counts represent lower temperatures. Along the centerline there is a steady counterflow diffusion flame, as shown in Figure A.8 (b) from the chemiluminescence. CH_2O is produced on the upper portion of the diffusion flame and therefore the flame resides on the bottom portion of the signal. This is also apparent since the bottom of the CH_2O signal will have higher temperatures since it is closer to the reaction layer, and therefore has lower signal counts. Radially outward through the negative edge, the temperature decreases because reactions are no longer taking place and the entire CH_2O signal increases as well. Therefore, the low CH_2O PLIF signal can be used to determine the high temperature region. These observations are important to determine the flame edge and will be subsequently discussed.

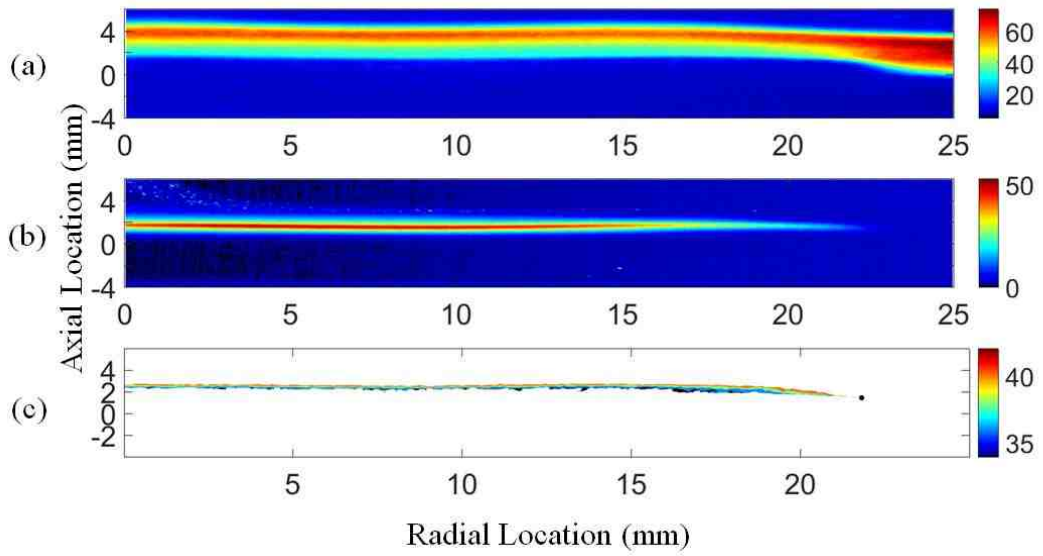

Figure A.8: Averaged negative edge signals of (a) CH_2O PLIF, (b) chemiluminescence, and (c) processed CH_2O signal. The black dot in (c) is the edge location.

Figure A.9 shows the processing steps used to obtain the edge location. Figure A. 9 (a) is the same image as Figure A.8 (a), however, at each radial location, the maximum fluorescence signal was measured and the intensities which were less than the half-maximum were removed from the image, leaving the data shown in Figure A.9 (a). Next, the remaining high signal level represented low temperatures, and therefore needed to be removed. The Otsu method [122] was used to determine the threshold which separates the low and high temperature regions. Points which were above the threshold were removed since they represent low temperatures and the remaining data is shown in Figure A.9 (b). At this point, the remaining signal is nearly only the high temperature regions, however, there is clearly leftover low temperature pixels remaining through the edge. Therefore, the Otsu method was recalculated and similarly the signal with higher pixels than the threshold were removed. The remaining signal is shown in Figure A.9 (c) and was the final processed image. There is residual data left from the top-half of the flame which was subsequently removed and the point residing at the largest radial location was chosen as the negative

edge location. This procedure was used for each case and was used throughout the analysis as the sample location.

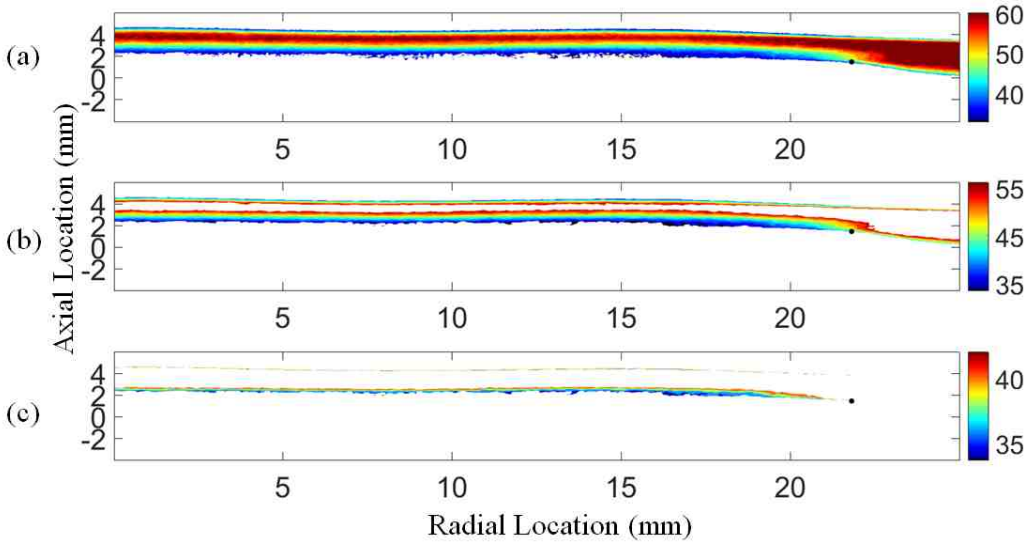

Figure A.9: Processing steps to obtain edge location, depicted by the black dot in (c).

The scalar dissipation rate was shown to be inversely proportional to the CH_2O PLIF width in negative edge flames [128]. Similar analysis was conducted to obtain the scaled scalar dissipation rate at the edge in this experiment. Figure A.10 shows the CH_2O width, using the full width at half maximum (FWHM) for several different cases, where (a) has constant inner nozzle velocities and (b) has constant outer nozzle velocities. With constant inner nozzle velocities, it is expected that the scalar dissipation rate is nearly constant along the stable counterflow diffusion flame. This is evident in Figure A.10 (a), where the FWHM of CH_2O PLIF is nearly constant from 0 to 10 mm in the radial direction. As the flow passes through the outer nozzle, the CH_2O width decreases, and therefore the scalar dissipation rate increases. The vertical lines represent the radial location where the respective edge is located based on the previous analysis. Conversely, in Figure A.10 (b) the outer nozzle velocities are constant. Therefore the three cases will have different CH_2O

widths from 0 to 10 mm and is clearly shown. The blue dots, which is the case with the largest CH_2O width is the lowest inner nozzle velocity case and therefore has the lowest scalar dissipation rate along the counterflow diffusion flame. A polynomial was fit through the data to obtain a smooth profile which was used to extract the CH_2O width at the edge location, and therefore the scaled scalar dissipation rate. In [128], it was noted that the scalar dissipation rate correlated well with the CH_2O width while the CH_2O width was decreasing. Past this, where the CH_2O width increases, the flame has completely extinguished and no longer represents the scalar dissipation rate. All of the edge locations determined from the previous analysis were ahead of this point and therefore are valid for scalar dissipation rate measurements.

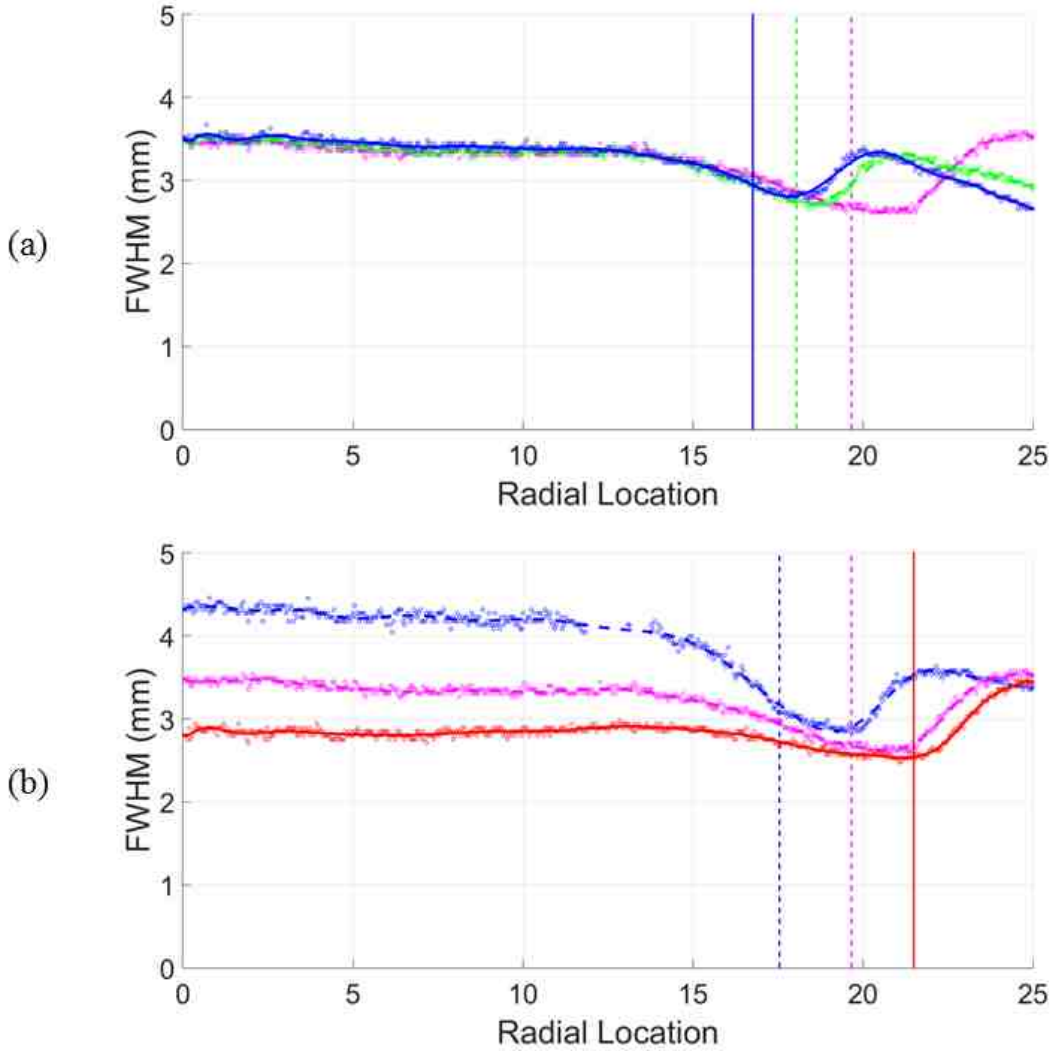

Figure A.10: CH_2O PLIF full width at half maximum values in the radial direction for (a) constant inner nozzle velocities and (b) constant outer nozzle velocities.

The CH_2O width was sampled using the polynomial fit at the edge location for each case and was converted to a scaled scalar dissipation rate using Eq. (9.5) [128], where χ is the scalar dissipation rate and W is the CH_2O full width at half maximum. Since the scalar dissipation rate is inversely proportional to the CH_2O FWHM, the actual scalar dissipation rate was not obtained. A calibration could have been performed to obtain the scaling constant, however. The dilatation was computed using the PIV measurements, and the same edge location was sampled in the dilatation field to obtain a scaled advective heat

flux, via the analysis from Chapter 5. It should be noted that the dilatation measurement was very sensitive to the edge location. Small changes in the edge location drastically changed the magnitudes of the dilatation. A sensitivity analysis should be conducted in future work. The points were all sampled and are plotted in Figure A.11. This plot is similar to the advective heat flux plotted against scalar dissipation rate plot as in [48] which showed that negative edge flames resided at linearly higher values of scalar dissipation rate, proportional to the advective heat flux. Therefore, this figure experimentally shows that the advective heat flux and scalar dissipation rate are linearly proportional at the negative edge in this geometry, which was previously only shown numerically.

$$W \propto \chi^{-0.45} \tag{9.5}$$

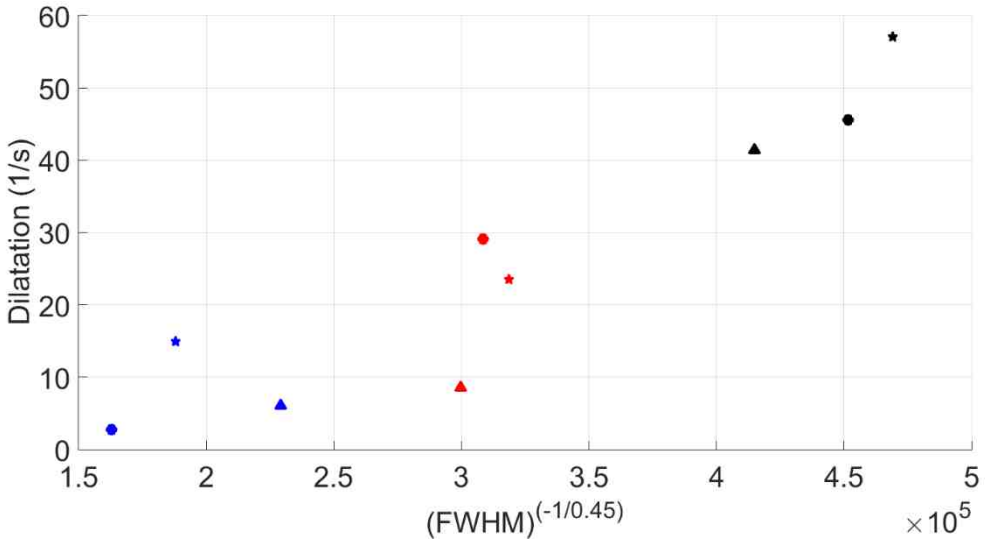

Figure A.11: Dilatation plotted against scaled scalar dissipation rate.

There are some subtle differences between Figure A.11 and the one shown in [48]. The figure in [48] shows the radial advective heat flux plotted against the scalar dissipation rate. However, the dilatation includes both the axial and radial advective heat flux components which could show slightly different results. Also interestingly, the plot shown here is nearly linear, which is slightly different than expected. The points in [48] which

were in the linear regime were mostly cases with larger inner nozzle diameters which lessened the effects from radial diffusion. Therefore, since these experiments were conducted with smaller inner diameters, there should be an influence of the radial diffusion and therefore should not necessarily follow a linear fit. However, the dilatation measurements are very close to zero, which could have introduced more error than the difference from radial diffusion. Therefore, these effects may be present but are masked by inherent experimental error.

Summary and Conclusions

Numerical simulations from Carnell and Renfro [48] showed that the advective heat flux and scalar dissipation rate at the edge of negative edge flames in a modified counterflow burner geometry were linearly proportional which led to the flame residing at higher scalar dissipation rates than the one-dimensional extinction scalar dissipation rate. This was a significant finding which showed that these extinction waves have an added influence of the advective heat flux through the edge. Prior to this dissertation, the advective heat flux was a difficult quantity to measure, and therefore the findings from [48] were not experimentally shown. This sub-chapter provided experimental evidence to suggest that the scaled advective heat flux (measured using the flow dilatation) and scalar dissipation rate (measured using CH_2O PLIF widths) were linearly proportional.

References

[1] U.S. Energy Information Administration, Electricity Data Browser, n.d.

[2] U.S. Energy Information Administration, Annual Energy Outlook 2016, n.d.

[3] Nitrogen Oxides (NOx), Why and How They Are Controlled, 1999.

[4] S. Samuelsen, Rich Burn, Quick-Mix, Learn Burn (RQL) Combustor, in: Gas Turbine Handb., National Energy Technology Laboratory, 2006: pp. 227–233.

[5] W. Bender, Lean Pre-mixed Combustion, in: Gas Turbine Handb., National Energy Technology Laboratory, 2006: pp. 217–227.

[6] T. Lieuwen, H. Torres, C. Johnson, B.T. Zinn, A mechanism of combustion instability in lean premixed gas turbine combustors, ASME 123 (2001) 182–189.

[7] R.G. McKinney, D. Sepulveda, W. Sowa, A.K. Cheung, The Pratt & Whitney TALON X Low Emissions Combustor : Revolutionary Results with Evolutionary Technology, Am. Inst. Aeronaut. Astronaut. Meet. 45 (2007) 1–8.

[8] V. Favier, L. Vervisch, Edge flames and partially premixed combustion in diffusion flame quenching, Combust. Flame 125 (2001) 788–803.

[9] T.R. Meyer, G.J. Fiechtner, S.P. Gogineni, J.C. Rolon, C.D. Carter, J.R. Gord, Simultaneous PLIF/PIV investigation of vortex-induced annular extinction in H2-air counterflow diffusion flames, Exp. Fluids 36 (2004) 259–267.

[10] C.K. Law, Combustion Physics, 1st ed., Cambridge University Press, 2006.

[11] V. Bergmann, W. Meier, D. Wolff, W. Stricker, Application of spontaneous Raman and Rayleigh scattering and 2D LIF for the characterization of a turbulent CH4/H2/N2 jet diffusion flame, Appl. Phys. B 66 (1998) 489–502.

[12] K.A. Watson, K.M. Lyons, J.M. Donbar, C.D. Carter, Simultaneous Rayleigh imaging and CH-PLIF measurements in a lifted jet diffusion flame, Combust. Flame 123 (2000) 252–265.

[13] J. Hult, U. Meier, W. Meier, A. Harvey, C.F. Kaminski, Experimental analysis of local flame extinction in a turbulent jet diffusion flame by high repetition 2-D laser techniques and multi-scalar measurements, Proc. Combust. Inst. 30 (2005) 701–709.

[14] I. Boxx, C. Heeger, R. Gordon, B. Bohm, M. Aigner, A. Dreizler, W. Meier, Simultaneous three-component PIV/OH-PLIF measurements of a turbulent lifted, C3H8-Argon jet diffusion flame at 1.5 kHz repetition rate, Proc. Combust. Inst. 32 (2009) 905–912.

[15] S. Karami, M. Talei, E.R. Hawkes, J.H. Chen, Local extinction and reignition mechanism in a turbulent lifted flame : A direct numerical simulation study, Proc. Combust. Inst. 36 (2017) 1685–1692.

[16] J.C. Rolon, F. Aguerre, S. Candel, Experiments on the interaction between a vortex and a strained diffusion flame, Combust. Flame 100 (1995) 422–429.

[17] G. Amantini, J.H. Frank, A. Gomez, Experiments on standing and traveling edge flames around flame holes, Proc. Combust. Inst. 30 (2005) 313–321.

[18] J. Buckmaster, Edge-flames and their stability, Combust. Sci. Tech 115 (1996) 41–68.

[19] P.N. Kioni, B. Rogg, K.N.C. Bray, A. Linan, Flame spread in laminar mixing layers: the triple flame, Combust. Flame 95 (1993) 276–290.

[20] P.N. Kioni, K.N.C. Bray, D.A. Greenhalgh, B. Rogg, Experimental and numerical studies of a triple flame, Combust. Flame 116 (1999) 192–206.

[21] V.S. Santoro, A. Liñán, A. Gomez, Propagation of edge flames in counterflow mixing layers: Experiments and theory, Proc. Combust. Inst. 28 (2000) 2039–2046.

[22] J. Boulanger, L. Vervisch, J. Reveillon, S. Ghosal, Effects of heat release in laminar diffusion flames lifted on round jets, Combust. Flame 134 (2003) 355–368.

[23] H.G. Im, J.H. Chen, Structure and propagation of triple flames in partially premixed hydrogen-air mixtures, Combust. Flame 119 (1999) 436–454.

[24] J. Lee, S.H. Won, S.H. Jin, S.H. Chung, Lifted flames in laminar jets of propane in coflow air, Combust. Flame 135 (2003) 449–462.

[25] T. Plessing, P. Terhoeven, N. Peters, M.S. Mansour, An experimental and numerical study of a laminar triple flame, Combust. Flame 115 (1998) 335–353.

[26] I.K. Puri, S.K. Aggarwal, S. Ratti, R. Azzoni, On the similitude between lifted and burner-stabilized triple flames: A numerical and experimental investigation, Combust. Flame 124 (2001) 311–325.

[27] X. Qin, I.K. Puri, S.K. Aggarwal, Characteristics of lifted triple flames stabilized in the near field of a partially premixed axisymmetric jet, Proc. Combust. Inst. 29 (2002) 1565–1572.

[28] G.R. Ruetsch, L. Vervisch, A. Liñán, Effects of heat release on triple flames, Phys. Fluids 7 (1995) 1447–1454.

[29] S. Kostka, W.F. Carnell, Jr., M.W. Renfro, Propagating edge-flame response to multiple stoichiometry gradients, Combust. Flame 154 (2008) 82–95.

[30] H. Philips, Flame in a buoyant methane layer, Symp. (Int.) Combust. 10 (1965) 1277–1283.

[31] Y.S. Ko, S.H. Chung, G.S. Kim, S.W. Kim, Stoichiometry at the leading edge of a tribrachial flame in laminar jets from Raman scattering technique, Combust. Flame 123 (2000) 430–433.

[32] Y.S. Ko, S.H. Chung, Propagation of unsteady tribrachial flames in laminar non-premixed jets, Combust. Flame 118 (1999) 151–163.

[33] N.I. Kim, J.I. Seo, K.C. Oh, H.D. Shin, Lift-off characteristics of triple flame with concentration gradient, Proc. Combust. Inst. 30 (2005) 367–374.

[34] J. Lee, S.H. Won, S.H. Jin, S.H. Chung, O. Fujita, K. Ito, Propagation speed of tribrachial (triple) flame of propane in laminar jets under normal and micro gravity conditions, Combust. Flame 134 (2003) 411–420.

[35] M.K. Kim, S.H. Won, S.H. Chung, Effect of velocity gradient on propagation speed of tribrachial flames in laminar coflow jets, Proc. Combust. Inst. 31 (2007) 901–908.

[36] M. Hirota, T. Yokomori, K. Yasuda, Y. Nagai, M. Mizomoto, G. Masuya, Burning velocity of triple flames with gentle concentration gradient, Proc. Combust. Inst. 31 (2007) 893–899.

[37] Y.S. Ko, T.M. Chung, S.H. Chung, Characteristics of propagating tribrachial flames in counterflow, KSME Int. J. 16 (2002) 1710–1718.

[38] J.W. Dold, Flame propagation in a nonuniform mixture: analysis of a slowly varying triple flame, Combust. Flame 76 (1989) 71–88.

[39] M.S. Cha, P.D. Ronney, Propagation rates of nonpremixed edge flames, Combust. Flame 146 (2006) 312–328.

[40] H. Song, P. Wang, R.S. Boles, D. Matinyan, H. Prahanphap, J. Piotrowicz, P.D. Ronney, Effects of mixture fraction on edge-flame propagation speeds, Proc. Combust. Inst. 36 (2017) 1403–1409.

[41] G. Amantini, J.H. Frank, B.A.V. Bennett, M.D. Smooke, A. Gomez, Comprehensive study of the evolution of an annular edge flame during extinction and reignition of a counterflow diffusion flame perturbed by vortices, Combust. Flame 150 (2007) 292–319.

[42] Y.C. Chen, R.W. Bilger, Stabilization mechanisms of lifted laminar flames in axisymmetric jet flows, Combust. Flame 123 (2000) 23–45.

[43] R. Daou, J. Daou, J. Dold, Effect of volumetric heat loss on triple-flame propagation, Proc. Combust. Inst. 29 (2002) 1559–1564.

[44] C. Pantano, D.I. Pullin, A statistical description of turbulent diffusion flame holes, 137 (2004) 295–305.

[45] S.Y. Yang, S.K. Ryu, B.K. Lee, S.H. Chung, Extinction of interacting nonpremixed flames and existence of stationary retreating edges in twin-jet counterflow, Combust. Theory Modelling 13 (2009) 235–250.

[46] C.S. Yoo, H.G. Im, Transient dynamics of edge flames in a laminar nonpremixed

hydrogen-air counterflow, Proc. Combust. Inst. 30 (2005) 349–356.

[47] W.F. Carnell, Jr., M.W. Renfro, Stable negative edge flame formation in a counterflow burner, Combust. Flame 141 (2005) 350–359.

[48] W.F. Carnell, Jr., M.W. Renfro, Influence of advective heat flux on extinction scalar dissipation rate and velocity in negative edge flames, Combust. Theory Modelling 10 (2006) 815–830.

[49] M.L. Shay, P.D. Ronney, Nonpremixed edge flames in spatially varying straining flows, Combust. Flame 112 (1998) 171–180.

[50] N. Peters, F.A. Williams, Liftoff characteristics of turbulent jet diffusion flames, AIAA 21 (1983).

[51] D.A. Everest, D.A. Feikema, J.F. Driscoll, Images of the strained flammable layer used to study the liftoff of turbulent jet flames, Twenthy-Sixth Symp. Combust. (1996) 129–136.

[52] K.A. Watson, K.M. Lyons, J.M. Donbar, C.D. Carter, On scalar dissipation and partially premixed flame propagation, Combust. Sci. Tech 175 (2003) 649–664.

[53] K. Wohl, N.M. Kapp, G. Gazley, The stability of open flames, Third Symp. Combust. (1949) 3–21.

[54] L. Vanquickenborne, A. Van Tiggelen, The stabilization mechanism of lifted diffusion flames, Combust. Flame 10 (1966) 59–69.

[55] K.M. Lyons, Toward an understanding of the stabilization mechanisms of lifted turbulent jet flames : Experiments, Prog. Energy Combust. Sci. 33 (2007) 211–231.

[56] A. Upatnieks, J.F. Driscoll, C.C. Rasmussen, S.L. Ceccio, Liftoff of turbulent jet flames — assessment of edge flame and other concepts using cinema-PIV, Combust. Flame 138 (2004) 259–272.

[57] Y. Mizobuchi, S. Tachibana, J. Shinio, S. Ogawa, T. Takeno, A numerical analysis of the structure of a turbulent hydrogen jet lifted flame, Proc. Combust. Inst. 29 (2002) 2009–2015.

[58] D. Han, M.G. Mungal, Simultaneous measurements of velocity and CH distributions . Part 1 : jet flames in co-flow, Combust. Flame 132 (2003) 565–590.

[59] G. Mittal, M. Chaos, C.J. Sung, F.L. Dryer, Dimethyl ether autoignition in a rapid compression machine: Experiments and chemical kinetic modeling, Fuel Process. Technol. 89 (2008) 1244–1254.

[60] S. Dooley, S.H. Won, M. Chaos, J. Heyne, Y. Ju, F.L. Dryer, K. Kumar, C.J. Sung, H. Wang, M.A. Oehlschlaeger, R.J. Santoro, T.A. Litzinger, A jet fuel surrogate formulated by real fuel properties, Combust. Flame 157 (2010) 2333–2339.

[61] D.F. Davidson, B.M. Gauthier, R.K. Hanson, Shock tube ignition measurements of

iso-octane/air and toluene/air at high pressures, Proc. Combust. Inst. 30 (2005) 1175–1182.

[62] E. Mastorakos, Ignition of turbulent non-premixed flames, Prog. Energy Combust. Sci. 35 (2009) 57–97.

[63] R. Cabra, T. Myhrvold, J.-Y. Chen, R.W. Dibble, A.N. Karpetis, R.S. Barlow, Simultaneous laser Raman-Rayleigh-LIF measurments and numerical modeling results of a lifted turbulent H2/N2 jet flame in vitiated coflow, Proc. Combust. Inst. 29 (2002) 1881–1888.

[64] R. Cabra, J.-Y. Chen, R.W. Dibble, A.N. Karpetis, R.S. Barlow, Lifted methane – air jet flames in a vitiated coflow, Combust. Flame 143 (2005) 491–506.

[65] A.M. Steinberg, R. Sadanandan, C. Dem, P. Kutne, W. Meier, Structure and stabilization of hydrogen jet flames in cross-flows, Proc. Combust. Inst. 34 (2013) 1499–1507.

[66] S.M. Al-noman, S.K. Choi, S.H. Chung, Numerical study of laminar nonpremixed methane flames in coflow jets : Autoignited lifted flames with tribrachial edges and MILD combustion at elevated temperatures, Combust. Flame 171 (2016) 119–132.

[67] C.M. Arndt, M.J. Papageorge, F. Fuest, J.A. Sutton, W. Meier, M. Aigner, The role of temperature, mixture fraction, and scalar dissipation rate on transient methane injection and auto-ignition in a jet in hot coflow burner, Combust. Flame 167 (2016) 60–71.

[68] R.L. Gordon, A.R. Masri, E. Mastorakos, Simultaneous Rayleigh temperature, OH- and CH2O-LIF imaging of methane jets in a vitiated coflow, Combust. Flame 155 (2008) 181–195.

[69] D.J. Micka, J.F. Driscoll, Stratified jet flames in a heated (1390 K) air cross-flow with autoignition, Combust. Flame 159 (2012) 1205–1214.

[70] E. Oldenhof, M.J. Tummers, E.H. V Veen, D.J.E.M. Roekaerts, Ignition kernel formation and lift-off behaviour of jet-in-hot-coflow flames, Combust. Flame 157 (2010) 1167–1178.

[71] R. Sullivan, B. Wilde, D.R. Noble, J.M. Seitzman, T.C. Lieuwen, Time-averaged characteristics of a reacting fuel jet in vitiated cross-flow, Combust. Flame 161 (2014) 1792–1803.

[72] C.S. Yoo, R. Sankaran, J.H. Chen, Three-dimensional direct numerical simulation of a turbulent lifted hydrogen jet flame in heated coflow: flame stabilization and structure, J. Fluid Mech. 640 (2009) 453–481.

[73] D. Schmitt, M. Kolb, J. Weinzierl, C. Hirsch, T. Sattelmayer, Ignition and flame stabilization of a premixed jet in hot cross flow, Proc. ASME Turbo Expo 2013 Turbine Tech. Conf. Expo. (2013) 1–10.

[74] J.A. Wagner, S.W. Grib, M.W. Renfro, B.M. Cetegen, Flowfield measurements and flame stabilization of a premixed reacting jet in vitiated crossflow, Combust. Flame 162 (2015) 3711–3727.

[75] J.A. Wagner, S.W. Grib, J.W. Dayton, M.W. Renfro, B.M. Cetegen, Flame stabilization analysis of a premixed reacting jet in vitiated crossflow, Proc. Combust. Inst. 36 (2017) 3763–3771.

[76] J.A. Wagner, M.W. Renfro, B.M. Cetegen, Premixed jet flame behavior in a hot vitiated crossflow of lean combustion products, Combust. Flame 176 (2017) 521–533.

[77] W.F. Carnell, Jr., M.W. Renfro, Measurement of temperature gradients through local extinction using Raman scattering spectroscopy, Int. J. Altern. Propuls. 1 (2007) 135–153.

[78] G. Coppola, A. Gomez, Experimental investigation on a turbulence generation system with high-blockage plates, Exp. Therm. Fluid Sci. 33 (2009) 1037–1048.

[79] G. Coppola, B. Coriton, A. Gomez, Highly turbulent counterflow flames : A laboratory scale benchmark for practical systems, Combust. Flame 156 (2009) 1834–1843.

[80] M. Raffel, C.E. Willert, S.T. Wereley, J. Kompenhans, Particle image velocimetry: a practical guide, Springer, 2007.

[81] J. Luque, D.R. Crosley, LIFBASE: Database and Spectral Simulation Program, (1999).

[82] S. Kostka, S. Roy, P.J. Lakusta, T.R. Meyer, M.W. Renfro, J.R. Gord, R. Branam, Comparison of line-peak and line-scanning excitation in two-color laser-induced-fluorescence thermometry of OH., Appl. Opt. 48 (2009) 6332–6343.

[83] I. Grant, Particle image velocimetry: a review, Proc. Instn. Mech. Engrs 211 (1997) 55–76.

[84] A.C. Eckbreth, Laser diagnostics for combustion temperature and species, Overseas Publishers Association, 1996.

[85] J.M. Seitzman, R.K. Hanson, P.A. DeBarber, C.F. Hess, Application of quantitative two-line OH planar laser-induced fluorescence for temporally resolved planar thermometry in reacting flows, Appl. Opt. 33 (1994) 4000–4012.

[86] A. Omrane, P. Petersson, M. Alden, M.A. Linne, Simultaneous 2D flow velocity and gas temperature measurements using thermographic phosphors, Appl. Phys. B 92 (2008) 99–102.

[87] G.S. Elliott, N. Glumac, C.D. Carter, Molecular filtered Rayleigh scattering applied to combustion, Meas. Sci. Technol. 12 (2001) 452–466.

[88] N. Chakraborty, S. Cant, Unsteady effects of strain rate and curvature on turbulent premixed flames in an inflow-outflow configuration, Combust. Flame 137 (2004) 129–147.

[89] N. Chakraborty, R.S. Cant, Influence of Lewis number on curvature effects in turbulent premixed flame propagation in the thin reaction zones regime, Phys. Fluids 17 (2005) 105105.

[90] N. Chakraborty, E. Mastorakos, Numerical investigation of edge flame propagation characteristics in turbulent mixing layers, Phys. Fluids 18 (2006) 105103.

[91] N. Chakraborty, R.S. Cant, Effects of strain rate and curvature on surface density function transport in turbulent premixed flames in the thin reaction zones regime, Phys. Fluids 17 (2005) 65108.

[92] L. Cifuentes, C. Dopazo, J. Martin, P. Domingo, L. Vervisch, Local volumetric dilatation rate and scalar geometries in a premixed methane-air turbulent jet flame, Proc. Combust. Inst. 35 (2015) 1295–1303.

[93] C. Dopazo, L. Cifuentes, J. Martin, C. Jimenez, Strain rates normal to approaching iso-scalar surfaces in a turbulent premixed flame, Combust. Flame 162 (2015) 1729–1736.

[94] M. Gamba, N.T. Clemens, O.A. Ezekoye, Volumetric PIV and 2D OH PLIF imaging in the far-field of a low Reynolds number nonpremixed jet flame, Meas. Sci. Technol. 24 (2013) 24003.

[95] P.S. Kothnur, M.S. Tsurikov, N.T. Clemens, J.M. Donbar, C.D. Carter, Planar imaging of CH, OH, and velocity in turbulent non-premixed jet flames, Proc. Combust. Inst. 29 (2002) 1921–1927.

[96] P.G. Mehta, M.C. Soteriou, A. Banaszuk, Impact of exothermicity on steady and linearized response of a premixed ducted flame, Combust. Flame 141 (2005) 392–405.

[97] C.J. Mueller, J.F. Driscoll, D.L. Reuss, M.C. Drake, Effects of unsteady stretch on the strength of a freely-propagating flame wrinkled by a vortex, Symp. (Int.) Combust. 26 (1996) 347–355.

[98] J.A. Mullin, W.J.A. Dahm, J.M. Donbar, Combined PLIF and PIV laser imaging measurements of heat release effects at the small scales of turbulent reacting flows, 10th Int. Symp. Appl. Laser Tech. to Fluid Mech. (2000).

[99] M.G. Mungal, L.M. Lourenco, A. Krothapalli, Instantaneous velocity measurements in laminar and turbulent premixed flames using on-line PIV, Combust. Sci. Tech 106 (1995) 239–265.

[100] H.N. Najm, P.H. Paul, C.J. Mueller, P.S. Wyckoff, On the adequacy of certain experimental observables as measurements of flame burning rate, Combust. Flame 113 (1998) 312–332.

[101] A.M. Steinberg, J.F. Driscoll, N. Swaminathan, Statistics and dynamics of turbulence-flame alignment in premixed combustion, Combust. Flame 159 (2012) 2576–2588.

[102] N. Swaminathan, K.N.C. Bray, Effect of dilatation on scalar dissipation in turbulent premixed flames, Combust. Flame 143 (2005) 549–565.

[103] A. Upatnieks, J.F. Driscoll, S.L. Ceccio, Cinema particle imaging velocimetry time history of the propagation velocity of the base of a lifted turbulent jet flame, Proc. Combust. Inst. 29 (2002) 1897–1903.

[104] ANSYS Fluent User Manual, (2015).

[105] C.K. Westbrook, F.L. Dryer, Simplified reaction mechanisms for oxidation of hydrocarbon fuels in flames, Combust. Sci. Tech 27 (1981) 31–43.

[106] S. V. Patankar, D.B. Spalding, A calculation procedure for heat, mass, and momentum transfer in three-dimensional parabolic flows, Int. J. Heat Mass Transf. 15 (1972) 1787–1806.

[107] K.K. Kuo, Principles of combustion, Wiley, New York, 1986.

[108] G.P. Smith, D.M. Golden, M. Frenklach, N.W. Moriarty, B. Eiteneer, M. Goldenberg, C.T. Bowman, R.K. Hanson, S. Song, W.C. Gardiner, V. V. Lissianski, Z. Qin, GRI-Mech 3.0, GRI Mech. (1999). http://www.me.berkeley.edu/gri_mech/.

[109] J.W. Rose, J.R. Cooper, H.M. Spiers, Technical data on fuels, Wiley, 1977.

[110] A. Brockhinke, S. Haufe, K. Kohse-Hoinghaus, Structural properties of lifted hydrogen jet flames measured by laser spectroscopic techniques, Combust. Flame 121 (2000) 367–377.

[111] P. Domingo, L. Vervisch, Triple flames and partially premixed combustion in autoignition of non-premixed turbulent mixtures, Symp. (Int.) Combust. 26 (1996) 233–240.

[112] A. Wason, W.F. Carnell, Jr., M.W. Renfro, Velocity and scalar measurements in neighboring lifted edge flames, Combust. Sci. Tech 178 (2006) 789–811.

[113] K. Yamamoto, Y. Isobe, N. Hayashi, H. Yamashita, S.H. Chung, Behaviors of tribrachial edge flames and their interactions in a triple-port burner, Combust. Flame 162 (2015) 1653–1659.

[114] M. Sneep, W. Ubachs, Direct measurement of the Rayleigh scattering cross section in various gases, J. Quant. Spectrosc. 92 (2005) 293–310.

[115] J.I. Seo, N.I. Kim, H.D. Shin, An experimental study of the fuel dilution effect on the propagation of methane – air tribrachial flames, Combust. Flame 153 (2008) 355–366.

[116] D.G. Goodwin, H.K. Moffat, R.L. Speth, Cantera: An object- oriented software

toolkit for chemical kinetics, thermodynamics, and transport processes., (2017). http://www.cantera.org.

[117] S.W. Grib, M.W. Renfro, Propagation speeds for interacting triple flames, Combust. Flame 187 (2018) 230–238.

[118] R.W. Bilger, S.H. Starner, R.J. Kee, On reduced mechanisms for methane-air combustion in nonpremixed flames, Combust. Flame 80 (1990) 135–149.

[119] R. J. Kee, F.M. Rupley, J.A. Miller, M.E. Coltrin, J.F. Grcar, E. Meeks, H.K. Moffat, A.E. Lutz, G. Dixon, M.D. Lewis, Smooke, J. Warnatz, G.H. Evans, R.S. Larson, R.E. Mitchell, L.R. Petzold, W.C. Reynolds, M. Caracotsios, W.E. Stewart, P. Glarborg, C. Wang, O. Adigun, CHEMKIN Collection, (2000).

[120] S.W. Grib, M.W. Renfro, Two dimensional advective heat flux estimation from velocity measurements, Combust. Flame 184 (2017) 261–272.

[121] H. Malm, G. Sparr, J. Hult, C.F. Kaminski, Nonlinear diffusion filtering of images obtained by planar laser-induced fluorescence spectroscopy, J. Opt. Soc. Am. A 17 (2000) 2148–2156.

[122] N. Otsu, A Tlreshold Selection Method from Gray-Level Histograms, IEEE 9 (1979) 62–66.

[123] R.C. Gonzalez, R.E. Woods, Digital Image Processing, Pearson, 2007.

[124] H.C. Mongia, TAPS-A 4th Generation Propulsion Combustor Technology for Low Emissions, Am. Inst. Aeronaut. Astronaut. 1 (2003) 1085–1095.

[125] E. Mastorakos, T.A. Baritaud, T.J. Poinsot, Numerical Simulations of Autoignition in Turbulent Mixing Flows, Combust. Flame 109 (1997) 198–223.

[126] R. Hilbert, D. Thevenin, Autoignition of Turbulent Non-Premixed Flames Investigated Using Direct Numerical Simulations, Combust. Flame 128 (2002) 22–37.

[127] P.H. Paul, H.N. Najm, Planar laser-induced fluorescence imaging of flame heat release rate, Symp. Combust. 27 (1998) 43–50.

[128] K.R. Gosselin, W.F. Carnell, Jr., M.W. Renfro, Formaldehyde Fluorescence as a Marker for Scalar Dissipation Through Local Extinction, Combust. Sci. Tech 187 (2015) 1742–1758.

Vita

Stephen W. Grib

Education

University of Kentucky, Lexington, Kentucky, 2018
Ph.D Mechanical Engineering

- Dissertation Title: "Laminar and turbulent study of combustion in stratified environments using laser based measurements"

University of Connecticut, Storrs, Connecticut, 2013-2015
Ph.D Candidate Mechanical Engineering

Bloomsburg University, Bloomsburg, Pennsylvania, 2013
B.S. Physics, B.S. Mathematics

Experience

University of Kentucky, Lexington, KY

- Research Assistant, 2015-Present
- Teaching Assistant, 2015-2016

University of Connecticut, Storrs, CT

- Graduate Research Assistant, 2013-2015

Publications and Presentations

Journal Publications

10. **S.W. Grib**, M.W. Renfro, "Negative edge flame velocities in a turbulent flow," (in preparation).
9. **S.W. Grib,** T.C. Owens, M.W. Renfro, "Stabilization of a steady and laminar premixed jet in vitiated coflow," (in preparation).
8. **S.W. Grib**, M.W. Renfro, "Unsteady negative edge flame response to periodic oscillations," *Combustion and Flame* (submitted).
7. **S.W. Grib**, M.W. Renfro, "Fuel effects on interacting triple flame propagation velocities," *Combustion and Flame* (in review).
6. J.E. Wilson, **S.W. Grib**, A.D. Ahmad, M.W. Renfro, S. Adams, A.A. Salaimeh, "Study of near-cup droplet breakup of an automotive electrostatic rotary bell (ESRB) atomizer using high-speed shadowgraph imaging," *Coatings*, v. 8 (2018) 174.
5. S. Poozesh, **S.W. Grib**, M.W. Renfro, P.J. Marsac, "Near-field dynamics of high-speed spray dryer nozzle: effects of operational conditions and formulation," *Powder Technology*, v. 333 (2018), 230-238.
4. **S.W. Grib**, M.W. Renfro, "Propagation speeds for interacting triple flames," *Combustion and Flame*, v. 187 (2018), 230-238.
3. **S.W. Grib**, M.W. Renfro, "Two dimensional advective heat flux estimation from velocity measurements," *Combustion and Flame*, v. 184 (2017), 261-272.
2. J.A. Wagner, **S.W. Grib**, J.W. Dayton, M.W. Renfro, B.M. Cetegen, "Flame stabilization analysis of a premixed reacting jet in vitiated crossflow," *Proceedings of the Combustion Institute*, v. 36 (2017), 3763-3771.

1. J.A. Wagner, **S.W. Grib**, M.W. Renfro, B.M. Cetegen, "Flowfield measurements and flame stabilization of a premixed reacting jet in vitiated crossflow," *Combustion and Flame,* v. 162 (2015), 3711-3727.

Conference Proceedings and Presentations

11. **S.W. Grib**, T.C. Owens, M.W. Renfro, "Stabilization of a premixed jet in vitiated coflow," 2018 Spring Technical Meeting of the Central States Section of the Combustion Institute (2018).
10. T.C. Owens, **S.W. Grib**, M.W. Renfro, "Temperature effect on autoignition for a premixed jet in vitiated coflow," 2018 Spring Technical Meeting of the Central States Section of the Combustion Institute (2018).
9. **S.W. Grib**, M.W. Renfro, "Unsteady negative edge flames in a periodic flow," 2018 Spring Technical Meeting of the Central States Section of the Combustion Institute (2018).
8. **S.W. Grib**, M.W. Renfro, "Negative edge flame velocities in a turbulent flow," 43rd Dayton-Cincinnati Aerospace Sciences Symposium (2018).
7. **S.W. Grib**, M.W. Renfro, "Autoignition stabilization of a premixed jet in vitiated coflow," *AIAA SciTech* (2018).
6. J. Wilson, **S. Grib**, M. Renfro, S. Adams, A. Salaimeh, "Study of near-cup water droplet breakup of a rotary bell atomizer using shadowgraph and high-speed imaging," Institute for Liquid Atomization and Spray Systems (2017).
5. **S.W. Grib**, M.W. Renfro, "Propagation velocities for neighboring triple flames," 10th U.S. National Combustion Meeting (2017).
4. **S.W. Grib**, M.W. Renfro, "Propagation velocities for neighboring triple flames," 42nd Dayton-Cincinnati Aerospace Sciences Symposium (2017).
3. **S.W. Grib**, M.W. Renfro, "Calculation of Advective heat flux and temperature from particle image velocimetry measurements," 2016 Spring Technical Meeting of the Central States Section of the Combustion Institute (2016).
2. J.A. Wagner, **S.W. Grib**, M.W. Renfro, B.M. Cetegen, "Experimental studies of a reacting jet in a vitiated crossflow," 9th U.S. National Combustion Meeting (2015).
1. **S.W. Grib**, J.A. Wagner, M.W. Renfro, B.M. Cetegen, "Ignition of a reacting jet in vitiated crossflow," 9th U.S. National Combustion Meeting (2015).

Honors and Awards

Graduate Student Awards

- *Mechanical Engineering Outstanding Ph.D Student*, Department of Mechanical Engineering, University of Kentucky, March 2018
- *Outstanding Student Poster,* Department of Mechanical Engineering, University of Kentucky, March 2017

Undergraduate Student Awards

- *Outstanding Student in Physics*, Department of Physics and Engineering Technology, Bloomsburg University, May 2013
- *Levi-Gray Award - Outstanding Sophomore Physics Student*, Department of Physics and Engineering Technology, Bloomsburg University, May 2011